UNIVERSITÉ DE STRASBOURG

ÉCOLE DOCTORALE DE PHYSIQUE ET CHIMIE PHYSIQUE (ED 182)

Institut Charles Sadron (UPR 22)

THÈSE présentée par :

Christophe HIGY

soutenue le : **1er avril 2015**

pour obtenir le grade de : **Docteur de l'université de Strasbourg**

Discipline/ Spécialité : Physique - Chimie physique

Conformation des polyélectrolytes dans des films nanométriques assemblés couche-par-couche

THÈSE dirigée par :

M. DECHER Gero	Professeur, Université de Strasbourg
Mme FRAGNETO Giovanna	ILL Senior Fellow, Institut Laue-Langevin, Grenoble

RAPPORTEURS :

Mme von KLITZING Regine	Professeur, Université technique de Berlin
Mme GLINEL Karine	Professeur, Université catholique de Louvain

---

AUTRES MEMBRES DU JURY :

M. BALL Vincent	Professeur, Université de Strasbourg
M. GUTFREUND Philipp	ILL Scientist, Institut Laue-Langevin, Grenoble

Résumé de la thèse en français

Conformation des polyélectrolytes dans des films nanométriques assemblés couche-par-couche

La technique d'assemblage couche-par-couche (LbL, pour Layer-by-Layer) [1] est une véritable approche "bottom-up" qui permet la nanofabrication de couches minces multimatériaux sur des surfaces de tailles et de formes (plane, sphérique) et de nature (or, verre, silicium,...) différentes à partir d'un grand nombre de molécules (polymères, colloïdes, protéines, cellules, nanoparticules, ...) en utilisant un processus unique. Elle est basée sur un concept simple (interaction intermoléculaire attractive, principalement électrostatique) et combine une simplicité expérimentale avec un faible coût de fabrication et un respect de l'environnement (peu polluante). La préparation de films multicouches peut être réalisée par trempage [1], par pulvérisation [2] ou par assemblage LbL assisté par spin-coating [3] consécutif de composés cationiques et anioniques, en particulier des polyélectrolytes, avec une étape intermédiaire de rinçage. La Figure 1 montre une représentation du processus de déposition couche-par-couche, ainsi que les méthodes de trempage, pulvérisation et assemblage LbL assisté par spin-coating.

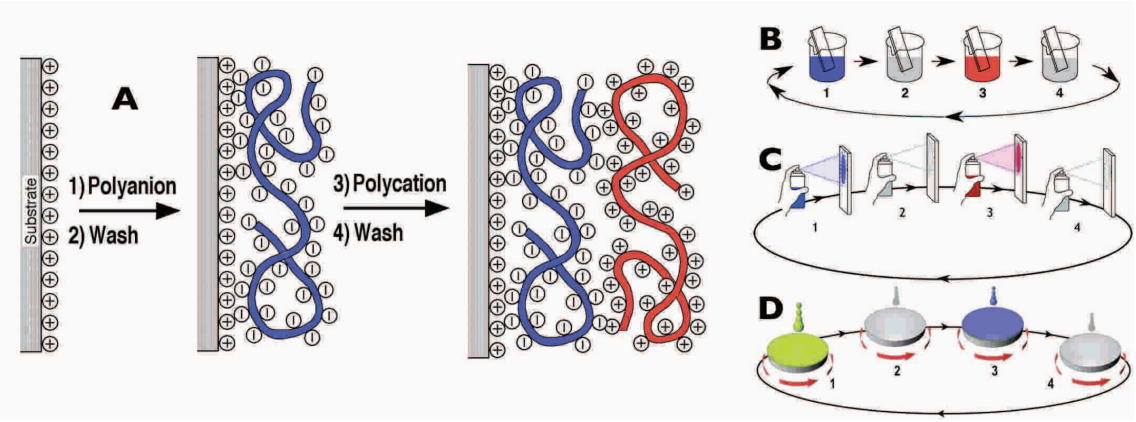

Figure 1: Représentation schématique de la construction d'un film multicouche (A) réalisée par trempage (B), par pulvérisation (C) ou par assemblage LbL assisté par spin-coating (D).

Les propriétés des films multicouches découlent de leur composition, des conditions de dépôt et de leur architecture. Ces films peuvent être considérés comme des complexes de polyélectrolytes aux interfaces. Alors que les complexes de polyélectrolytes en solution possèdent une structure "ladder-like" ou "scrambled egg" en fonction de divers paramètres, il n'est pas clair comment la structure interne des films LbL est obtenue à travers un processus d'assemblage par étape et en fonction des conditions de dépôt. Seules des investigations par des techniques de diffusion neutronique ont permis d'obtenir des détails structuraux sur ces films, incluant par exemple, la structure stratifiée, l'interpénétration des couches ainsi que le contenu en sel et en eau [4–6]. Par ailleurs, nous avons montré récemment qu'il y avait des différences structurales (épaisseur, rugosité, propriétés) considérables entre des films préparés par trempage et pulvérisation dont l'origine est loin d'être comprise [2]. A

notre connaissance, aucune étude n'a été réalisée sur la conformation des chaînes de polymères (taille et forme) dans les films multicouches. Les informations sur les paramètres moléculaires et de dépôt contrôlant la structure des films LbL sont d'une importance primordiale pour leur application en science des matériaux et dans les sciences de la vie.

L'objectif de mon travail a consisté à étudier la structure interne et la conformation des chaînes de polyélectrolytes dans les multicouches de polyélectrolytes en fonction de la nature chimique des polymères et des conditions de préparation en utilisant les techniques de réflectométrie des neutrons (détermination de la structure (épaisseur, rugosité, densité de longueur de diffusion SLD) des films perpendiculairement à la surface) [7, 8] et de diffusion de neutrons aux petits angles par incidence rasante (GISANS, détermination du rayon de giration moyen des chaînes de polymères dans la direction parallèle à la surface du film) [9]. Ces études nous ont permis de mieux comprendre les mécanismes d'adsorption des polyélectrolytes et de formation des films, ainsi que l'influence des différents paramètres de préparation des films.

Mon travail de thèse a porté essentiellement sur 3 parties :

- L'effet du vieillissement sur des films multicouches composés de poly(styrene sulfonate) sel de sodium (PSS) et de poly(allylamine hydrochlorure) (PAH).
- L'amélioration des fits des courbes de réflectivité spéculaire en utilisant le "fit global", un processus de fit en parallèle de courbes de réflectivité spéculaire de plusieurs films préparés selon les même conditions en considérant certains paramètres structuraux comme égaux pour tous les films. Nous avons aussi étudié l'influence du substrat et de l'air à la surface sur les couches de polyélectrolytes proches en considérant une structure inhomogène perpendiculairement à la surface.
- L'étude de la conformation de chaînes de polyélectrolytes pour un film composé de PSS et de PAH.

1. Effet du vieillissement sur les films multicouches

Pour étudier l'effet du vieillissement sur les films multicouches, nous avons effectué des mesures de réflectométrie des neutrons en 2012-2013 sur des échantillons composés de PSS et de PAH mesurés par notre équipe en 1998 [10], c'est-à-dire après 14-15 ans, et en 2007 [11], c'est-à-dire après 5-6 ans.

a) Evolution après 15 ans

Trois échantillons vieux de 15 ans ont été remesurés à l'ILL. Chacun présente un nombre différent de paires de couches (PSS-PAH) non-deutérées séparant les paires de couches (PSS-PAH) deutérées : zéro paire de couche (échantillon A3), c'est-à-dire l'échantillon est complètement deutéré ; une paire de couches (échantillon A1) et deux paires de couches (échantillon A2). Il est important de

noter que ces échantillons ont été stockés sans contrôle des conditions de stockage (humidité, température, etc...). Une mesure préliminaire de l'épaisseur des films par ellipsométrie a montré une forte augmentation de l'épaisseur des films en 16 ans, allant de 1,75 à 3,2 fois la taille initiale, en fonction du film.

Des mesures de réflectométrie des neutrons ont alors été effectuées à l'ILL et montrent des courbes très différentes de celles observées initialement, ce qui indique un important changement de structure dans ces films avec le temps. Après analyse, on peut noter les points suivants :

- Une inhomogénéité dans le changement structurel du film. En effet, on peut voir que la SLD des couches non-deutérées et deutérées n'est pas la même selon leur position dans le film et qu'une structure en 2 "blocs" apparait. Une explication serait que les polymères sont plus mobiles au niveau de l'interface avec l'air alors qu'ils sont moins mobiles à l'interface avec le substrat.

- Une augmentation de l'épaisseur totale du film, en accord avec les mesures par ellipsométrie.

- Une diminution de la SLD moyenne dans le film, indiquant soit un changement dans la composition du film, soit un changement de densité, ce qui coïncide avec l'augmentation d'épaisseur.

- Une augmentation de l'interpénétration des polyélectrolytes entre les couches. En effet, nous ne pouvons plus distinguer les couches deutérées et non-deutérées dans l'échantillon A1, mais c'est encore possible pour l'échantillon A3 (présence d'un pic de Bragg représentant le contraste entre les couches deutérées et non-deutérées) (Figure 2).

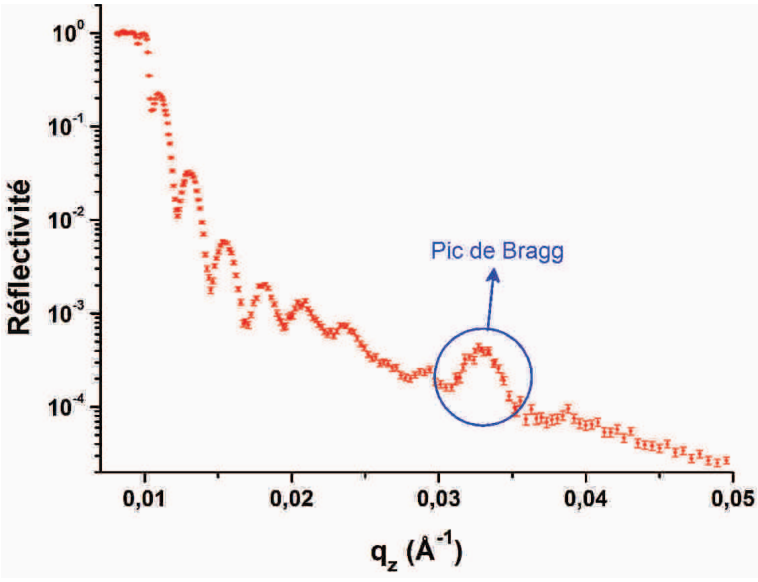

Figure 2: Courbe de réflectivité spéculaire de l'échantillon A2 mesuré à l'ILL en 2012-2013.

A l'heure actuelle, nous n'avons pas pu identifier qu'elle est l'origine exacte de ces changements, mais nous pouvons suggérer trois scénarios : 1) une oxydation des polyélectrolytes dans les films ; 2) une contamination des films ; 3) une importante absorption d'eau dû à l'humidité ambiante. Des mesures préliminaires de XPS ont montré une certaine oxydation à la surface, mais une étude de la composition des films sur toute la profondeur est nécessaire.

Le point important à noter est que malgré le changement important dans la structure des films, la structure en couche est toujours visible, même de manière très faible. Néanmoins, la limite de stockage des films et la limite d'analyse des données expérimentales ont été atteintes.

b) Evolution après 5 ans

Après mesure de 7 échantillons vieux de 5 ans, nous avons constaté qu'ils présentent tous la même évolution structurale. C'est la raison pour laquelle seulement deux de ces échantillons seront décrits ici. Il s'agit d'un film ayant la structure $Si/SiO_2/PEI/[(PSS_{h7}\text{-}PAH)_3/(PSS_{d7}\text{-}PAH)]_6/(PSS_{h7}\text{-}PAH)_3$ (échantillon C, PSS_{h7} représente le PSS non-deutéré et PSS_{d7} le PSS deutéré) et d'un film ayant la structure $Si/SiO_2/PEI/[(PSS_{h7}\text{-}PAH)_4/(PSS_{d7}\text{-}PAH)]_8/(PSS_{h7}\text{-}PAH)_4$ (échantillon E), déposés tous les deux par pulvérisation. L'analyse des courbes de réflectivité obtenues en 2007 et en 2012-2013 et des profils SLD (Figure 3) permet de comparer les paramètres structuraux des films (Tableau 1).

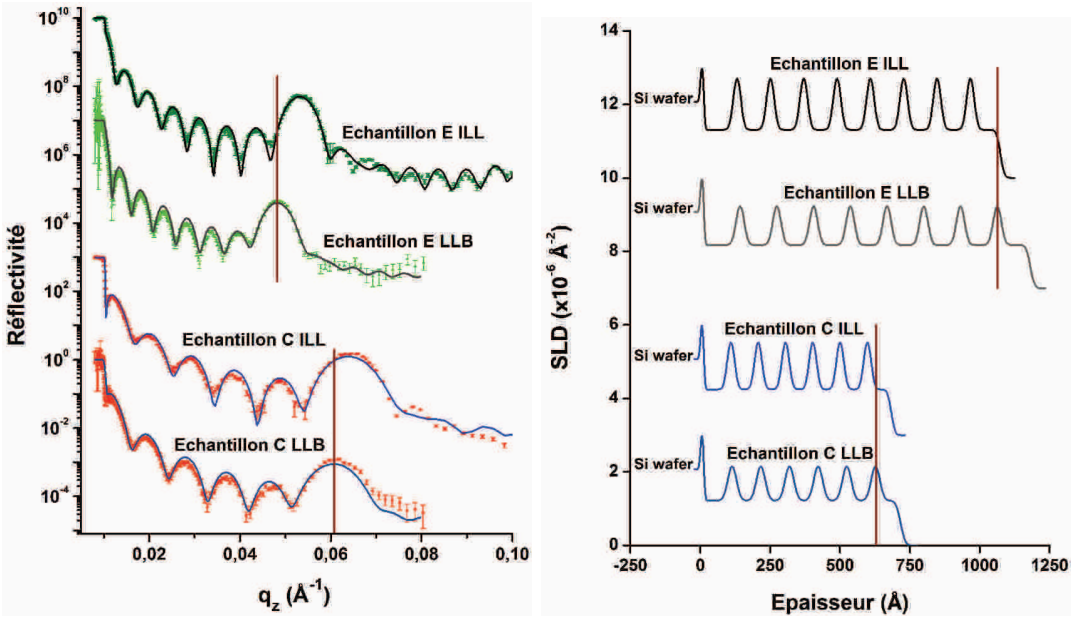

Figure 3: A gauche, les courbes de réflectivité spéculaire (points) des échantillons C et E mesurée au LLB en 2007 et à l'ILL en 2012-2013, ainsi que les modèles théoriques correspondants (lignes). A droites, les profils SLD extraits des fits. Les courbes sont décalées pour plus de clarté.

Après 5 ans, on observe une légère diminution de l'épaisseur et de la rugosité ainsi qu'une légère augmentation de la SLD, qui correspond à une augmentation de

	LLB en 2007				ILL en 2012-2013			
	Epaisseur par paire de couches (Å)	SLD non-deutérée ($\times 10^{-6}$ Å^{-2})	SLD deutérée ($\times 10^{-6}$ Å^{-2})	Rugosité (Å)	Epaisseur par paire de couches (Å)	SLD non-deutérée ($\times 10^{-6}$ Å^{-2})	SLD deutérée ($\times 10^{-6}$ Å^{-2})	Rugosité (Å)
Echantillon C	25,7 ± 2,5	1,22 ± 0,22	2,63 ± 0,57	13,5 ± 10,5	24,4 ± 6,5	1,24 ± 0,14	2,97 ± 0,40	10,8 ± 7,1
Echantillon E	26,3 ± 2,5	1,18 ± 0,22	2,62 ± 0,57	12,0 ± 10,5	23,9 ± 0,3	1,31 ± 0,04	3,27 ± 0,18	11,3 ± 10,1

Table 1: Valeurs des paramètres structuraux pour les films C et E mesuré au LLB en 2007 et à l'ILL en 2012-2013, déterminées à partir des fit des réflectivités spéculaires.

la densité. Ces observations suggèrent une légère compression des films due probablement à une plastification des polyélectrolytes dans les films causée par l'humidité de l'air.

Nous pouvons en déduire que la structures de ces films est stable sur une période de quelques mois à 2-3 ans.

2. Fit global et inhomogénéité

Il a été observé lors de l'analyse des réflectivités speculaires mesurées au LLB en 2007 [11] que les valeurs des paramètres structuraux déterminées à partir des fits ne sont pas exactement les mêmes pour des films multicouches préparés dans les même conditions. En particulier, seize films préparés par spray avaient été mesurés. Les réflectivités spéculaires de ces seize films ont été analysées indépendemment, puis en utilisant le "fit global", qui est un processus permettant de fitter en même temps plusieurs courbes et de considérer certains paramètres structuraux des différents films comme égaux, par exemple il est possible de forcer les épaisseurs par paires de couches de tous les films à être identiques. Nous avons effectué quatre fits globaux différents, le premier où les épaisseurs par paires de couches des seize films sont identiques, le deuxième pour lequel les SLDs sont identiques, le troisième où les rugosités sont égaux et le quatrième où les épaisseurs, les SLDs et les rugosités sont les mêmes. Nous avons pu observer que les SLDs et les rugosités, qui présentent des différences avec les fits individuels, donnent de très bons fits en considérant les même valeurs pour tous les films. Nous pouvons donc considérer que les SLDs et les rugosités sont identiques pour des films préparés selon les même conditions et déterminer des valeurs moyennes pour les paramètres structuraux grâce aux fits globaux. Par contre, il n'est pas possible de calculer une épaisseur moyenne pour les seize films, on observe des différences qui sont probablement dues aux conditions de préparation non-contrôlées, comme la température.

Les structures des films, dont l'effet du vieillissement a été étudié et qui ont été analysés avec les fits globaux, ont été considérés comme homogènes perpendiculairement à la surface. De nouveaux films ont été préparés et mesurés par réflectométrie

des neutrons, mais les fits effectués en considérant une structure homogène ne sont pas de bonnes qualités. Nous avons montré que les films possèdent des structures inhomogènes, avec des différences structurelles pour les couches proches du substrat ou de la surface, c'est-à-dire des épaisseurs, SLDs et rugosités différentes de celles des couches en volume (composant la majeur partie du film). Ceci indique une influence du substrat et de l'air aux extrémités des films multicouches de polyélectrolytes. La Figure 4 montre le cas d'un film préparé par pulvérisation. Les modèles théoriques pour une structure homogène et une structure inhomogène sont comparés. Nous pouvons voir que le modèle théorique pour une structure inhomogène correspond mieux à la réflectivité spéculaire mesurée par réflectométrie des neutrons. Toutefois, le fit peut encore être amélioré et la structure du film est probablement plus complexe que celle utilisée dans cette étude.

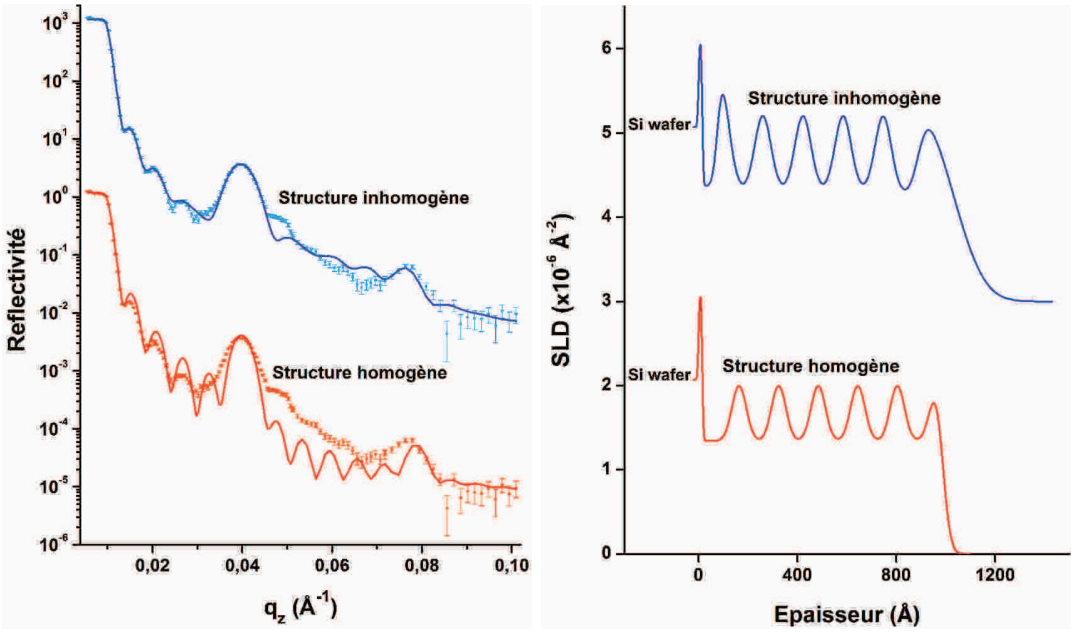

Figure 4: A gauche, la courbe de réflectivité spéculaire (points) et les fits pour une structure homogène et une structure inhomogène (lignes). A droites, les profils SLD extraits des fits. Les courbes sont décalées pour plus de clarté.

3. Etude de la conformation des polyélectrolytes

L'étude de la conformation des polyélectrolytes dans les films multicouches nécessite de combiner les techniques de réflectométrie des neutrons et de GISANS. Ainsi, il est possible de déterminer une taille moyenne des chaînes de polymères perpendiculairement à la surface en combinant l'épaisseur et la rugosité obtenue par réflectométrie et le rayon de giration des chaînes de polymères dans le plan par GISANS.

Un seul film multicouche de polyélectrolytes a pu être mesuré par GISANS, et par conséquent la conformation des chaînes de polyélectrolytes n'a pu être déterminée

que pour ce film. Il s'agit d'un film composé de PSS et PAH et préparé par trempage. Des mesures de réflectométrie de neutrons ont été effectué à l'ILL, les valeurs des paramètres structuraux déterminés à partir du fit de la réflectivité spéculaire sont indiquées dans le Tableau 2.

	Epaisseur par paire de couches (Å)	SLD non-deutérée (x 10^{-6} Å^{-2})	SLD deutérée (x 10^{-6} Å^{-2})	Rugosité (Å)
Couches du haut	10,3 ± 8,9	X	7,78 ± 3,48	18,2 ± 9,1
Couches en volume	52,2 ± 2,1	1,04 ± 0,29	3,28 ± 0,33	17,4 ± 9,7
Couches du bas	52,2 ± 5,8	0,98 ± 0,42	X	17,5 ± 15,5

Table 2: Valeurs des paramètres structuraux pour le films multicouche préparé par trempage, déterminées à partir du fit de la réflectivité spéculaire.

Pour calculer la tailles moyennes maximales des chaînes de PSS dans le film dans la direction perpendiculaire à la surface, il suffit d'additionner la valeur d'épaisseur avec trois fois la valeur de rugosité. Dans le cas du film étudié, les "couches en volume" constituent la majeur partie du film multicouche, la taille des chaînes de polymères est donc calculée selon les valeurs d'épaisseur et de rugosité de ces couches. La tailles moyennes maximales pour des chaînes de PSS de poids moléculaire M_w = 80 800 g/mol dans le film étudié est de 10,4 nm dans la direction perpendiculaire à la surface, c'est-à-dire un rayon de giration maximal de 4,3 nm.

Les films utilisés pour les mesures GISANS doivent être composés d'un mélange de polyélectrolytes deutérés et non-deutérés. Pour ce faire, nous avons préparé notre film avec un mélange de polyanions non-deutérés et deutérés de 1:1. Après mesure et traitement des données expérimentales, nous obtenons des courbes suivant la fonction de Debye [12, 13] :

$$I = \frac{2}{q_y^2 R_{gy}^2}\left[1 - \frac{1}{q_y^2 R_{gy}^2}\left(1 - exp(-q_y^2 R_{gy}^2)\right)\right] \quad (1)$$

où I est l'intensité, q le vecteur de diffusion et R_{gy} le rayon de giration en direction y.

Un ajustement des courbes à l'aide d'une courbe théorique suivant la fonction de Debye nous a permis de déterminer le rayon de giration des polyanions dans le plan. La Figure 5 représente les courbes expérimentales pour trois longueur d'onde, 4 Å, 5 Å et 7 Å, ainsi que le fit des courbes expérimentales. Le rayon de giration calculé est 15,6 nm ± 1,8 nm.

En comparant le rayon de giration des chaînes de polymères dans le plan à la taille des chaînes de polymères perpendiculairement à la surface, nous observons une taille plus faible perpendiculairement à la surface que parallèlement. Ceci indique que les chaînes de PSS ont une conformation de pelotes aplaties dans le type de films étudiés, alors que la conformation est sphérique en solution.

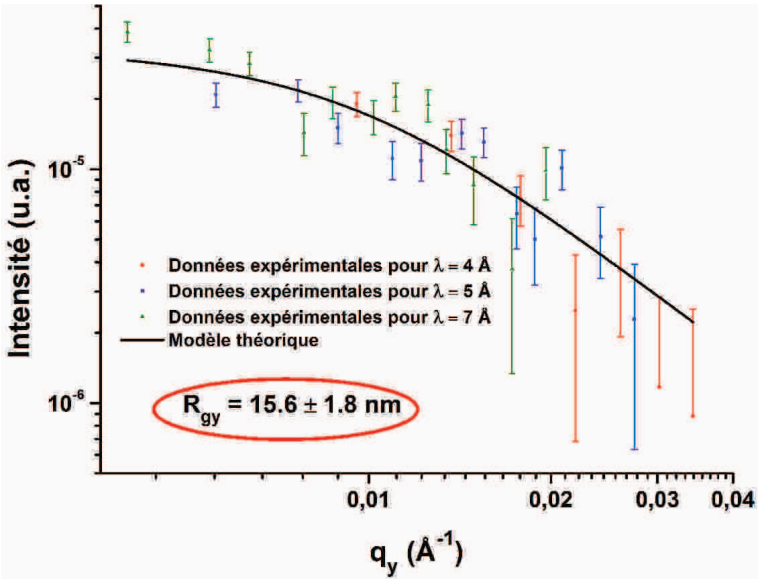

Figure 5: Courbes expérimentales GISANS pour un film multicouche contenant 50% de PSS deutéré. Les données expérimentales (points) pour les longueurs d'onde de 5 Å, 7 Å et 9 Å, ainsi que la fonction de Debye correspondante (ligne) sont représentées.

4. Conclusions

Au cours de ce travail, des études réalisées par réflectométrie des neutrons et GISANS ont permis d'obtenir des informations supplémentaires sur la structure interne des films multicouches en fonction des conditions de préparation et du vieillissement.

En ce qui concerne l'effet du vieillissement sur les films LbL, nous avons montré par réflectométrie des neutrons que les films préparés il y a 15 ans sont considérablement affectés : une augmentation significative de l'épaisseur, une augmentation du degré d'interpénétration des polyélectrolytes entre les couches voisines et une inhomogénéité de la densité des couches selon la profondeur dans le film. L'oxydation des polyélectrolytes avec le temps est une des causes possibles.La limite de stockage est atteinte.

Après un stockage de 5 ans, les films subissent un léger tassement due à une plastification des polyélectrolytes. Nous pouvons en déduire que les films multicouches de (PSS-PAH) sont stables sur une périodes de quelques mois à 2-3 ans.

Nous avons aussi montré l'utilité du processus de "fit global", permettant de déterminer des valeurs moyennes des paramètres structuraux pour des films préparés selon des conditions identiques. Nous avons observé que les valeurs de SLD et de rugosité sont identiques pour ces films, mais que les épaisseurs présentent une variation selon les films. Ceci est probablement dû aux conditions de préparation non-contrôlées, comme la température.

Nous avons aussi observé que les films présentent une structure inhomogène

dans la direction perpendiculaire à la surface. Les épaisseurs, SLD et rugosité ne sont pas les mêmes pour les couches proches du substrat ou de l'air à la surface comparé aux couches au milieu des films. Ceci nous indique une influence de l'environnement sur la structure aux extrémités des films.

La troisième partie de ce travail nous a permis de montrer qu'il est possible d'effectuer des mesures de GISANS sur nos films multicouches dans le but de déterminer le rayon de giration des chaînes de polyélectrolytes parallèle à la surface du film. En comparant les résultats de ces mesures avec ceux obtenus par réflectométrie, où nous avons été capable de déterminer la taille moyenne des chaînes de polyélectrolytes perpendiculaire à la surface du film, nous avons pu déterminer la conformation des polymères dans un film multicouche. En particulier, les chaînes de PSS présentes dans un film multicouche composé de PSS et PAH adopte une conformation de pelotes aplaties. Des études de conformations sur d'autres films, préparés dans des conditions différentes ou présentant des structures particulières, seront à effectuées à l'avenir

Polyelectrolyte conformation in Layer-by-Layer assembled nanoscale films

PhD thesis presented by

Christophe HIGY

The 1^{st} of April 2015

Supervisors :	Pr. Gero DECHER
	Dr. Fragneto GIOVANNA
Rapporteurs :	Pr. Regine von KLITZING
	Pr. Karine GLINEL
Examinators :	Pr. Vincent BALL
	Dr. Philipp GUTFREUND

Remerciements

Ce travail a été effectué à l'Institut Charles Sadron (ICS) et à l'Institut Laue-Langevin (ILL) d'octobre 2011 à mars 2015. Je voudrais d'abord remercier Jean-François Legrand et Jean-Michel Guenet, directeurs successifs de l'ICS, et Andrew Harrison, directeur de l'ILL pour l'accueil au sein de leurs laboratoires.

J'aimerais remercier Regine von Klitzing, Karine Glinel et Vincent Ball pour avoir accepté de faire partie de mon jury et d'avoir jugé mon travail.

Un grand merci à Gero Decher et Giovanna Fragneto pour m'avoir offert l'opportunité d'effectuer ma thèse dans leurs équipes et d'avoir supervisé mon travail pendant ces 3,5 années. J'ai beaucoup appris sous leur direction, autant d'un point de vue scientifique que d'un point de vue gestion d'un projet de recherche. J'aimerais aussi remercier Philipp Gutfreund, qui était comme un troisième superviseur en m'aidant à effectuer les mesures de diffusion de neutrons, à traiter les données et à analyser les résultats. Enfin, merci à Olivier Félix et Kate Tschopp pour l'aide technique dans les laboratoires.

Il est important d'avoir un bon encadrement pour une thèse, mais il est aussi important de travailler dans une bonne ambiance et j'aimerais remercier toute l'équipe, ceux qui sont là depuis un moment, ceux qui sont déjà partis et ceux qui viennent d'arriver, pour l'ambiance de folie qu'il y avait dans notre couloir. On a passé de super moments et de super soirées, on a bien rigolé et on a bien déliré, surtout les derniers mois de ma thèse où je pense qu'on a fait peur à nos voisins de bureau avec nos blagues pourries et nos rires débiles. Ce fut un plaisir de tous vous rencontrer et je ne vous oublierai pas : le Justicier masqué (ou pas), PauPaul, MichMich, le Bleu, Trampoline, Obélix, Marco, Cruella, Marek, Sri, Seydina, Rémi, Rebecca, Maria, Heveline, Teru, Alliny, Souvik, ... et tous les autres, vous êtes trop nombreux pour que je vous cite tous.

J'ai eu la chance que cette bonne ambiance soit présente dans tout l'institut et pour ça, je vous remercie tous. Là encore, il y a trop de monde à remercier, mais j'ai passé de bonnes soirées (Noël, été, ...) et de très bons moments avec vous. Entre autre, merci au BJC pour l'organisation des activités (sport, soirée) qui permettaient de se changer les idées, merci aux babyfooteux pour ces parties endiablées qui me permettaient de me défouler, et merci d'être venu nombreux au café du vendredi matin.

Bien sûr, merci aux vieux amis qui me permettaient de m'amuser en dehors du labo autant que je m'amusais dans le labo : Nono, Marsou, Marc mon gros nounours, Pierre, Arthur senior et Arthur junior, Papillon, Aurore, Camille, les Manus, Julie,

Cilou, Amina, Chachatte, Max, Laura, Alex, Marie-Laure, ... En particulier, merci aux parigos pour l'accueil, la bonne bouffe et les parties de Borderland, et merci aux fidèles des soirées pizzas-jeux vidéos.

Pour finir, j'aimerais remercier ma famille. C'est toujours agréable de retourner chez ses parents de temps en temps, de se vautrer sur le canapé devant la télé, un verre à la main et les pieds sur la table, et de ne rien faire de tout le weekend, à part jouer avec ses neveu/nièces, très (trop ?) bien manger et prendre des kilos, et bien s'amuser en discutant ou devant un jeu. Merci à vous et merci à ceux qui se sont occupés de préparer et d'organiser le pot de thèse, j'ai pu me concentrer sur finir ma thèse.

Contents

List of Figures

List of Tables

List of abbreviations

FRMII	Forschungs-Neutronenquelle Heinz Maier-Leibnitz
GISANS	Grazing Incidence Small Angle Neutron Scattering
ILL	Institut Laue-Langevin
KCl	Potassium chloride
LbL	Layer-by-Layer
LLB	Laboratoire Léon Brillouin
M_w	Molecular weight
NaCl	Sodium chloride
PAH	Poly(allylamine hydrochloride)
PDADMAC	Poly(diallyldimethylammonium chloride)
PdI	Polydispersity index
PEI	Poly(ethyleneimine)
PMAA	Poly(methacrylic acid)
PMeVP	Poly(4-vinyl-N-methylpyridinium) iodide
PSS_{d7}	Deuterated poly(styrene sulfonate) sodium salt
PSS_{h7}	Non-deuterated poly(styrene sulfonate) sodium salt
SANS	Small Angle Neutron Scattering
SLD	Scattering length density
TOF	Time-of-flight
XPS	X-ray Photoelectron Spectrometry

Motivation

The study of the conformation of polyelectrolyte chains is possible by measuring the sizes (radius of gyration or hydrodynamic radius) of polyelectrolyte coils by scattering experiments (light, X-ray, neutron). Scattering measurements were already used to determine the conformation of polyelectrolyte chains in solution (see for example references [27–32]), of polyelectrolyte chains in complexes (see for example references [33–36]) and of polyelectrolyte complexes particles (see for example references [37, 38]), and to study the influence of the physico-chemical parameters on this conformation. We will quickly describe here works on poly(styrene sulfonate) (PSS) chain conformation, as it is the polyelectrolyte studied in this thesis.

Several studies of the radius of gyration and the conformation of PSS chains in solutions were performed using Small Angle Neutron Scattering (SANS) [39–42]. The effect of various physico-chemical parameters were probed, as the salt concentration and nature or the PSS concentration. In the four references cited above, it was determined that PSS chains in solutions have a more or less spherical coil conformation depending on the parameters, with radii of gyration from 4.7 nm to 22.9 nm.

One study of the conformation of PSS chains in a complex of polyelectrolytes was performed by M. Z. Markarian *et al.* [33]. The radius of gyration of PSS chains in a PSS/(diallyldimethylammonium chloride) (PDADMAC) complex was determined by SANS, for two different molecular weights of the PSS (M_w = 14,000 g/mol and M_w = 104,000 g/mol) and for concentration of salt (sodium chloride, NaCl) in the solutions from 0.1 M to 1.5 M. The conformations were determined to be more or less spherical, and the sizes were 2.5 nm to 2.7 nm for the low PSS molecular weight and 10.5 nm to 11.0 nm for the high PSS molecular weight. These sizes are in the same order of magnitude than the ones for PSS in solution.

For now, no measurements of the conformation of polyelectrolyte chains in multilayer films prepared by the Layer-by-Layer (LbL) process were performed. But observations of the change of structure of the films were done. A. Pallandre *et al.* [14] have studied the deposition of multilayer films of PSS and PDADMAC on structured substrates, composed of repellent and attracting stripes. Whereas the end-to-end distances of the polyelectrolytes were determined to be 38 nm for PSS and 80 - 115 nm for PDADMAC, the width of the adsorbing stripes were set to values ranging from 10 nm to 100 nm. It was shown that the multilayer films adsorbed only on the attracting stripes, even for the narrow ones. As the width were smaller than the sizes of the polyelectrolytes, this indicates a deformation, a change of con-

formation of the polyelectrolytes in the films due to the constraints. This effect is sketched in Figure 6. But no measurements of the sizes of polyelectrolyte chains in the films were carried out, in different direction (in-plane and out-of-plane), to determine the exact conformation.

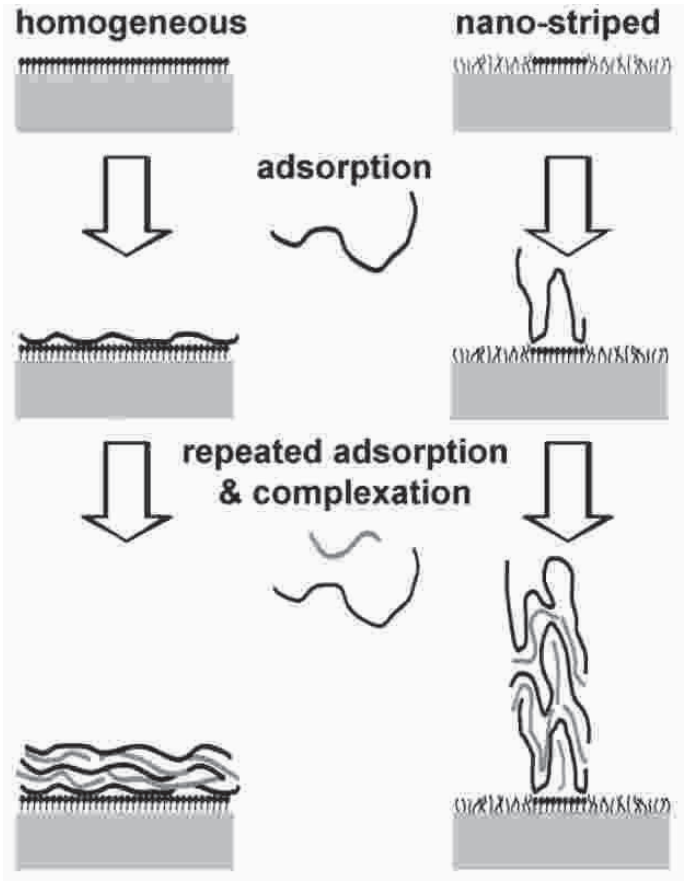

Figure 6: Schematic representation of the build-up of multilayer films of polyelectrolytes on homogeneous and nanostriped surfaces. Reproduced from reference [14].

Observations of the change of film thicknesses depending on the build-up parameters were also performed (see for example references [2, 43–45]). This change of thickness indicates a change of structure, maybe due to a change of polyelectrolyte conformation in multilayer films. One interesting effect was observed by M. Lösche *et al.* [10] on a multilayer film composed of PSS and poly(allylamine hydrochloride) (PAH). This film was prepared by dipping during two days, and was stored in water during the night (around 12 h). Neutron reflectometry measurements showed that the three last layer pairs deposited before the storage in water were thinner than the other layers. This is shown on the scattering length density (SLD) profile of the film in Figure 7. This change of thickness is due to a plastification, a relaxation of the polyelectrolytes due to the water. We may assume a change of conformation of the polyelectrolyte chains.

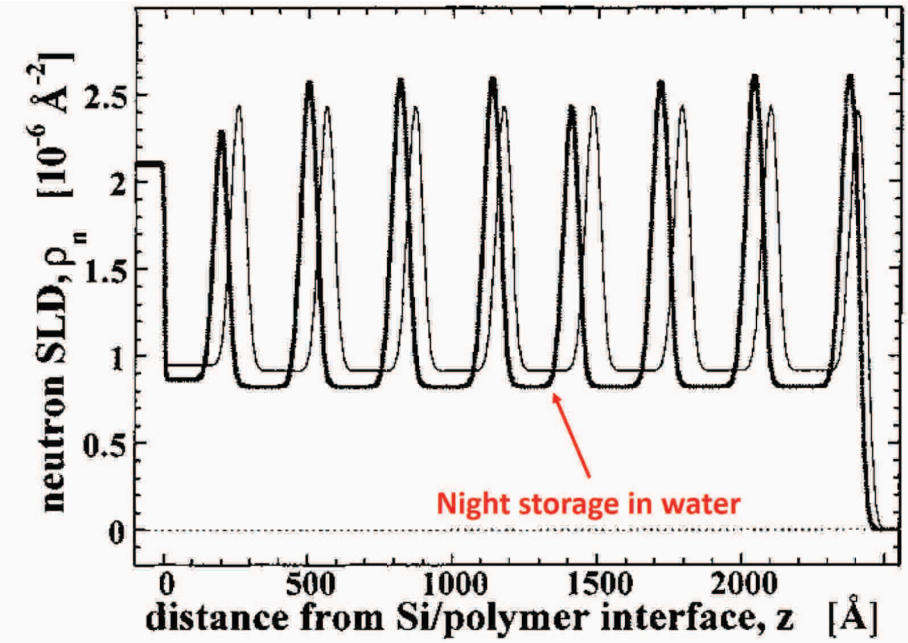

Figure 7: Scattering length density profile of a dipped multilayer film of PSS and PAH. The storage in water is indicated. Adapted from reference [10].

The aim of the present work was to study the conformation of polyelectrolyte chains in multilayer films of polyelectrolytes prepared by the LbL process. We will show the first study of conformation of polyelectrolyte chains performed on a multilayer film using neutron scattering measurements. As pointed out above, the sample preparation conditions as well as storage may have an influence on the structure of the films. Unfortunately, due to limited time of measurements, we had to know if the films are enough stable to be prepared at the same time and stored several months or years before the measurements, or if we had to prepare new films just before the experiments. We therefore studied the structural reproducibility of LbL preparation under the same conditions. In addition, we performed a study of the ageing of the films, described in this thesis. We will also discuss the quality of the structures determined from the measurements and of the model used.

Chapter 1

Introduction

1.1 Physical chemistry of polymers and polyelectrolytes

A polymer is a macromolecule which is composed of repetitions of individual molecules, called monomers, which are linked together by covalent bonds. The properties of polymers depend mainly on three parameters : the properties of the monomers ; the way of formation of the covalent bonds between the monomers ; the degree of polymerization, which correponds to the number of monomers.

Polyelectrolytes are charged polymers. The interactions of polyelectroytes with the oppositely charged polyelectrolytes in solution or at interfaces are complex, driven by different forces and depending on various parameters.

1.1.1 Polymers in solution

The concept of polymers appears at the beginning of the 1910's and since then the physical chemistry of polymers has been studied [46–49].

The conformation of a polymer in solution is described by a random walk in three dimensions. The simplest model, the freely jointed chain model, describes a polymer as being composed of N+1 monomers connected by N covalent bonds with a fixed length "a", as shown in Figure 1.1(A).

Each bond can be considered as a vector and the end-to-end vector $\overrightarrow{r_c}$ of a polymer chain is given by the addition of all bond vectors :

$$\overrightarrow{r_c} = \sum_{i=1}^{N} \overrightarrow{r_i} \tag{1.1}$$

The mean distance between the starting point and the end point is given by :

$$\sqrt{< \overrightarrow{r_c}^2 >} = aN^{0.5} \tag{1.2}$$

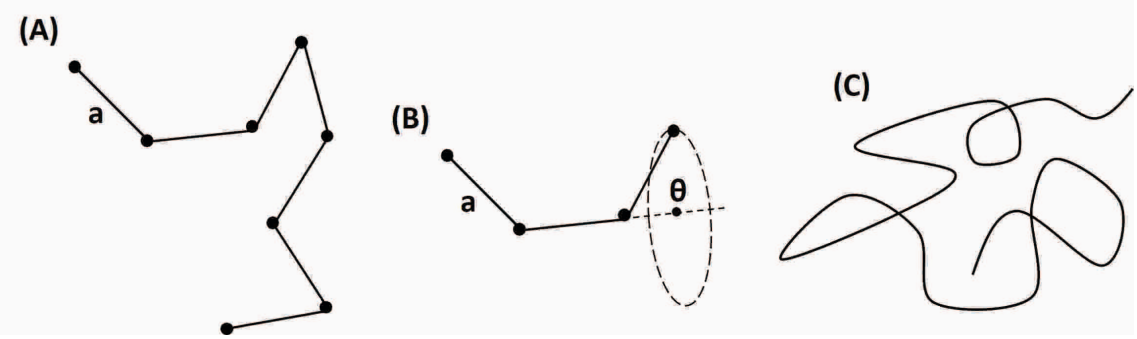

Figure 1.1: Models for a polymer chain in solution : the freely jointed chain model (A), the freely rotating chain model (B) and the worm-like chain model (C).

Chemical bonds do not have arbitrary angles. The backbone of many polymers consists of long alkane chains and the bond angle is fixed (for example, a tetrahedral angle is equal to 109.5°). Due to this restriction, we can correct the freely jointed chain model by introducing fixed bond angles, giving the freely rotating chain model (see Figure 1.1(B)). The mean end-to-end distance become :

$$\sqrt{< \overrightarrow{r_c}^2 >} = a(c_\infty N)^{0.5} \tag{1.3}$$

with c_∞ the characteristic ratio, which depends on the bonding angle in the backbone and on the existence of bulky side groups which might reduce the rotation around the bonds. For a tetrahedral angle, c_∞ is equal to 2, showing that such a chain has a bigger extension than the one predicted by the freely jointed chain model.

Another effect has to be taken into account, the interactions of the polymer with itself and with the solvent, called excluded volume interactions. There are three different cases : the polymer is dissolved in a good solvent, in a poor solvent or in an ideal solvent.

In a good solvent the interactions of the polymer with the solvent are favored. So, the random walk is more extended and the mean end-to-end distance becomes :

$$\sqrt{< \overrightarrow{r_c}^2 >} = a(c_\infty N)^{0.6} \tag{1.4}$$

In a poor solvent, it is the inverse, the interactions of the polymer with itself are favored and an attraction between the monomers is present. The mean end-to-end distance is given by :

$$\sqrt{< \overrightarrow{r_c}^2 >} = a(c_\infty N)^{\nu} \quad \text{with} \quad 0.33 < \nu < 0.5 \tag{1.5}$$

For $\nu < 0.5$, the chain is collapsed to a globule. The volume of this globule is linear in N and its radius is proportional to V and N : $R \sim V^{1/3} \sim N^{1/3}$ [49].

Finally, the attractive and repulsive forces compensate each other in an ideal solvent. So, Equation (1.3) is not changed.

The end-to-end distance $\sqrt{<\overrightarrow{r_c}^2>}$ is difficult to measure, so the conformation of a polymer chain is usually characterized by the radius of gyration R_g, which can be measured, for example, by scattering measurements (light, X-ray or neutron scattering). R_g is the average distance that a monomer has from the center of mass of the polymer chain :

$$R_g = \frac{\sum_i m_i r_i^2}{\sum_i m_i} = \frac{<\overrightarrow{r_c}^2>}{6} \tag{1.6}$$

The flexibility of the polymer chain is located at the connection points of the monomers in the freely jointed chain model and the freely rotating chain model. But a rotation by a finite angle as described by the freely rotating chain model is not likely to appear for a rigid polymer, because of the energy cost. These polymers can be described by an elastic chain that obeys Hook's law for small deformation. The worm-like chain model is used (see Figure 1.1(C)), for which the polymer is described by a continuous chain with step length, a, approaching zero, and number of bonds, N, approaching infinity. The boundary condition of a constant contour lenght, L = Na, is used.

In this model, the polymer is described by the characteristic bending constant, κ_b. The typical length scale over which the correlation between two polymer segments is lost, called persistence length L_p, can be calculated using Hook's law and the thermal average of all the possible polymer conformations :

$$< \cos\theta(s) >= \exp\left(-\frac{s}{L_p}\right) \tag{1.7}$$

with s the distance along the contour of the chain and θ the angle between a vector that is tangent to the polymer at position 0 and a vector tangent to the polymer at a distance s away from position 0. For the worm-like chain model, we have :

$$L_p = \frac{\kappa_b}{kT} \tag{1.8}$$

1.1.2 Polymers on surfaces

Most polymers adsorb irreversibly on surfaces, whereas small molecules usually do not form a permanent layer but adsorb and desorb in a reversible way. This is due to the fact that polymers adsorb on the surface with several segments. Moreover, a polymer adsorbed on a surface keeps its entropy by not binding completely, but it has "loops" which are not conformationally restricted. The number of loops depends also on the solvent. In a good solvent, the polymer is slightly adsorbed on the surface with loops extending over a distance over which is in the same order of magnitude of the radius of gyration. For a poor solvent, the polymer forms a dense layer on the surface.

1.1.3 Polyelectrolytes in solutions

Polyelectrolytes are charged polymers. Their charges come from the dissociation of ionic bonds in solution, giving charges of equal sign along the polymer chain and ions of the oppositely charge in the solution. The conformation of polyelectrolytes in solution is strongly dependent on the interactions between these charges together and with the solvent [47, 48, 50, 51]. For example, electrostatic repulsion of the charges along the chain will cause a bigger radius of gyration of the polyelectrolytes than for uncharged polymers. The charges also cause the solubility of polyelctrolytes in water whereas most of the uncharged counterparts are only soluble in organic solvent. Of course, the electro-neutrality has to be preserved. The physical chemistry of polyelectrolytes in solution depends on several parameters, like counterion nature or pH.

1.1.3.1 The Manning condensation

The Bjerrum length, l_B, is the distance over which two interacting elementary charges in a dielectric medium, with a dielectric constant ε, have an electrostatic energy equal to the thermal energy (kT) :

$$l_B = \frac{e^2}{4\pi\varepsilon kT} \tag{1.9}$$

Polyelectrolytes have often a high charge density, with a distance between the charges shorter than the Bjerrum length. So, the counterions present in the solution condensate on the polyelectrolyte to compensate the energy loss due to the charge distance smaller than l_B. This is called the Manning condensation. Considering a rod-like polyelectrolyte as defined in Figure 1.2, the potential of the rod is given by :

$$\phi(r) = \frac{\nu}{2\pi\varepsilon} \ln\left(\frac{r}{b}\right) \tag{1.10}$$

with ν = -e/a the linear charge density and b the diameter of the rod-like polyelectrolyte.

The electrostatic energy, E, needed for moving a counterion with a charge eZ at a distance r_i away from the polyelectrolyte is equal to :

$$E = \frac{\nu}{2\pi\varepsilon} eZ \ln\left(\frac{r_0}{b}\right) \tag{1.11}$$

The entropy gain by a counterion exploring an area of radius r_0 is equal to :

$$S = k \ln\left(\frac{\pi r_0^2}{\pi b^2}\right) = 2k \ln\left(\frac{r_0}{b}\right) \tag{1.12}$$

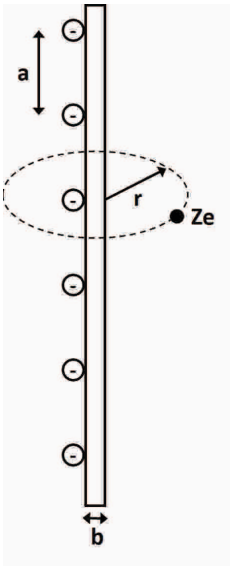

Figure 1.2: A rod-like polyelectrolyte with a diameter a and a linear charge density ν = -e/a. A counterion of charge eZ is at a distance r of the polyelectrolyte in a medium of dielectric permittivity ε.

We can calculate the free energy, F, of a counterion in solution :

$$F = E - TS = \left(\frac{\nu e Z}{2\pi\varepsilon} - 2kT\right)\ln\left(\frac{r_0}{b}\right) = 2kT\left(\frac{\nu e Z}{4\pi\varepsilon kT} - 1\right)\ln\left(\frac{r_0}{b}\right) \qquad (1.13)$$

A counterion dissociates from the polyelectrolyte only with a gain of entropy higher than the electrostatic attraction it has to overcome to dissociate, that is F $\leq$ 0. There are counterion bounds at any time, so the polyelectrolyte has a reduced, effective charge density ν_{eff} :

$$\frac{eZ\nu_{eff}}{4\pi\varepsilon kT} - 1 = 0$$
$$\nu_{eff} = \frac{4\pi\varepsilon kT}{eZ} = \frac{e}{l_B Z} \qquad (1.14)$$

We can see that there are enough counterion bounds to have a distance between two charges equal to the Bjerrum lenght l_B.

1.1.3.2 Debye length and electrostatic persistence length

Polyelectrolyte solutions can also contain salt. The ions of the salt screen the electrostatic interactions of the polyelectrolyte charges. For ideal dilute solutions, this screening is called Debye Hückel theory. In this case, the characteristic length

is the Debye length, κ, defined as :

$$\kappa = \sqrt{\frac{e^2}{\varepsilon kT} \sum_i c_i Z_i^2} = \sqrt{4\pi l_B \sum_i c_i Z_i^2} \tag{1.15}$$

with Z_i and c_i the valency and concentration of the i^{th} ion species in solution.

The Debye length corresponds to the distance over which the potential of a Coulombic interaction has decayed to 37% of its initial value. The potential of a charge q in a dilute solution is :

$$\phi = \frac{q}{4\pi\varepsilon r} e^{-\kappa r} \tag{1.16}$$

Of course, the screening of charge has an influence on the polyelectrolyte structure. The effective linear charge density of a polyelectrolyte becomes :

$$\nu_{eff} = \frac{4\pi\varepsilon kT}{eZ} = \frac{e}{\kappa l_B b K_1(\kappa; b)} \tag{1.17}$$

with K_1 the first order modified Bessel function.

We can see that ν_{eff} depends on the Debye length, and through it on the salt concentration. By increasing the salt concentration, the Debye length increases and ν_{eff} decreases. With a smaller effective charge density, the repulsion interactions between the charges on the polyelectrolyte chain are smaller, so the size of the polyelectrolyte coil decreases.

The persistence length, L_p, describes the bending rigidity of a polymer chain. In the case of a polyelectrolyte chain, the electrostatic repulsion of the chain charges contributes to the bending rigidity. Furthermore, contrary to an uncharged polymer, the charge screening reduces the bending rigidity. In the case of polyelectrolytes, the persistence length is defined as :

$$L_p = L_p^0 + L_p^e \tag{1.18}$$

with L_p^0 the persistence length of an uncharged polymer, defined above, and L_p^e the electrostatic persistence length. Using the Odijk-Skolnick-Fixman theory, we can defined L_p^e [52] as :

$$L_p^e = \frac{l_B}{4b^2\kappa^2} \tag{1.19}$$

L_p^e is proportional to the inverse of κ^2, and so proportional to the inverse of the salt concentration. If the salt concentration increases, the electrostatic persistence length decreases, i.e. the polyelectrolyte chain is less "rigid". The charge valency of the counterions has also an effect on the conformation. This effect is represented in Figure 1.3, the conformation of a polyelectrolyte chain is more globular (we talk about coils) for counterions with a higher charge valency.

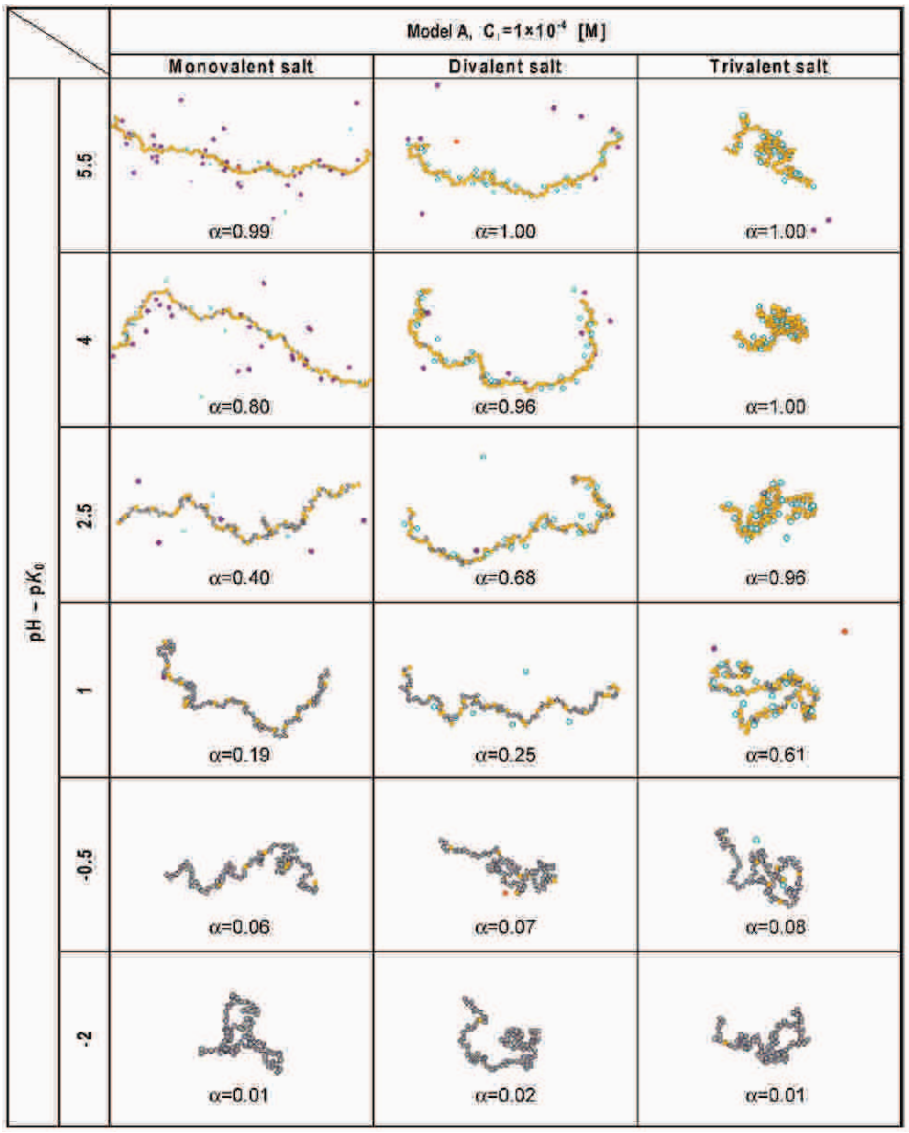

Figure 1.3: Conformation of a polyanion chain as a function of its degree of ionization, α, and the salt valency. Reproduced from reference [15].

1.1.3.3 Effect of the pH

Polyelectrolytes are also influenced by the pH of the solutions. We can define two kinds of polyelectrolytes depending on their response to the pH. Strong polylectrolytes do not respond to the change of pH. For weak polylectrolytes, the degree of ionization, the ratio of ionized and non-ionized groups, changes with the change of pH of the solutions. This is usually described by the pK_a value, defined by the Hendersson Hasselbach equation :

$$pK_a = -\log \frac{[H^+] \times [A^-]}{[HA]} = pH - \log \frac{[A^-]}{[HA]} \tag{1.20}$$

with [HA] the concentration of undissociated groups, [A^-] the concentration of deprotonated acid groups, [H^+] the concentration of protons and pH = -log[H]. This equation is for polyacids (i.e. polyanions). For polybases (i.e. polycations) :

$$pK_b = -\log \frac{[OH^-] \times [B]}{[BH^+]} = pOH - \log \frac{[B]}{[BH^+]} \tag{1.21}$$

with [OH^-] the concentration of OH^- groups, [B] the concentration of the base, [BH^+] the concentration of the conjugated acid of the base B and pOH = -log[OH^-]. We have the following relations at 25°C :

$$pH + pOH = 14 \tag{1.22}$$
$$pK_a + pK_b = 14 \tag{1.23}$$

The degree of ionization, α, is defined as :

$$\alpha = \frac{1}{1 + 10^{pH - pK_a}} \quad \text{for polycations} \tag{1.24}$$
$$\alpha = \frac{1}{1 + 10^{pOH - pK_b}} = \frac{1}{1 + 10^{pK_a - pH}} \quad \text{for polyanions} \tag{1.25}$$

A polyelectrolyte is 50% ionized, $\alpha = 0.5$, when the pH of the solution is equal to the pK_a of the polyelectrolyte. In Figure 1.4, curves of the ionization degree as a function of the pH are represented for a polyanion and a polycation with a pK_a of 7.

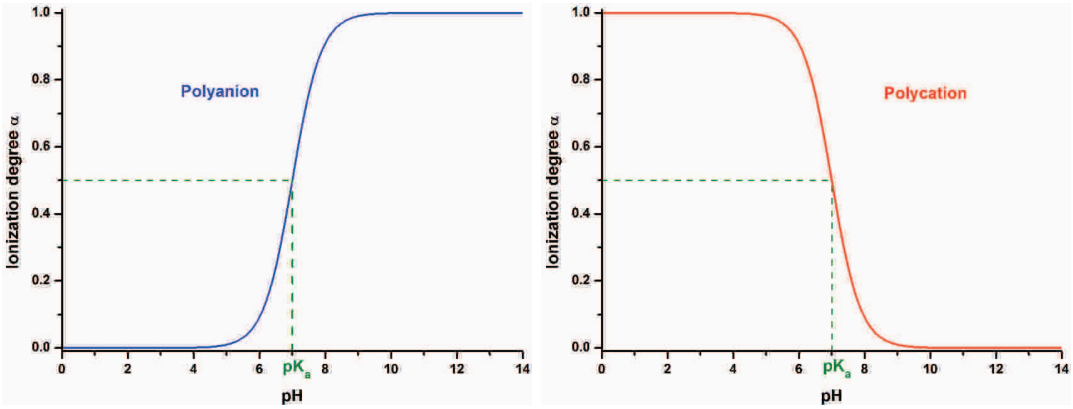

Figure 1.4: Example of ionization degree of polyelectrolytes with pK_a of 7 as a function of the pH of the solutions. On the left, the curve for a polyanion and on the right, the curve for a polycation.

As mentioned above, strong polyelectrolytes are not influenced by the pH of the solutions. This is due to the fact that the pK_a is below 1 for the strong polyanions and above 14 for the strong polycations. So, the strong polyelectrolytes are fully ionized in water for every pH. This is not the case for weak polyelectrolytes. So it is possible to tune the ionization of polyelectrolytes by changing the pH of solutions. The degree of ionization can be decrease with pH $<$ pK_a and increase with pH $>$ pK_a for weak polyanions, and it is the inverse for weak polycations.

It is therefore possible to change the charge density of weak polyelectrolytes by changing the pH of solutions. As the persistence length depends on the charge density, it is possible to vary the conformation of polyelectrolytes by modifying the pH. The effect of the degree of ionization on the conformation of polyanions is represented in Figure 1.3. The decrease of α gives more globular polyelectrolyte chains.

1.1.3.4 The pearl-necklace model

A model to describe hydrophobic polyelectrolytes in water is the pearl-necklace model [16,53–55]. Spheres of diameter d_{str} are composed of several monomers. These spheres form two elements : spherical pearls of diameter d_p which are separated by cylindrical strings of length l_{str} and diameter d_{str}, as represented in Figure 1.5.

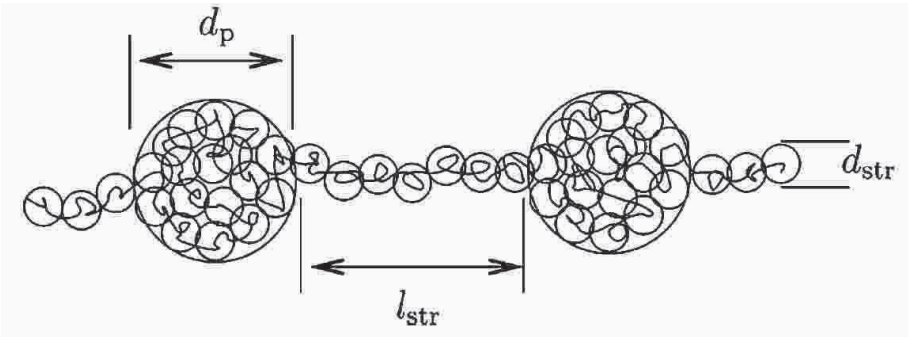

Figure 1.5: Schematic representation of a pearl-necklace structure. Reproduced from reference [16].

The numbers of monomers in a string, m_{str}, and in a pearl, m_p, are given by :

$$m_{str} = \frac{l_{str}}{a} \tag{1.26}$$

$$m_p = \frac{4\pi d_p}{24 v_0} \tag{1.27}$$

with a the length and v_0 the volume of a monomer. The pearl size scales as :

$$d_p \sim a \left(\frac{l_B}{a}\right)^{-1/3} \nu_{eff}^{-2/3} \tag{1.28}$$

and the pearl density as :

$$\rho_p \sim (a^2 \xi_T)^{-1} \tag{1.29}$$

with ξ_T the thermal blob size. The string length is given by :

$$l_{str} \sim a \left(\frac{l_B \xi_T}{a^2}\right)^{-1/2} \nu_{eff}^{-1} \tag{1.30}$$

1.1.4 Polyelectrolyte complexes in solutions

The mixing of a polyanion and a polycation solutions leads to the formation of polyelectrolyte complexes due to electrostatic interactions. The formation of such complexes is studied since the 1930's [56] and is governed by the polyelectrolyte characteristics (charge density, rigidity of the polyelectrolyte chains, ...) and the environment (solvent, counterions, pH, ...) [17, 57–59].

1.1.4.1 Thermodynamics of polyelectrolyte complex formation

The formation of polyelectrolyte complexes is driven by two forces, the attraction between the polyanions and polycations and the increase of entropy due to the counterions released. Indeed, polyelectrolytes in solutions are surrounded by an electrical double layer which is composed of counterions and co-ions. The double layer has a lower energy and a lower entropy than for a random mixing. When two oppositely charged polyelectrolytes form a complex, this double layer is destroyed and the counterions are released by forming a salt solution. This complex formation is represented in Figure 1.6.

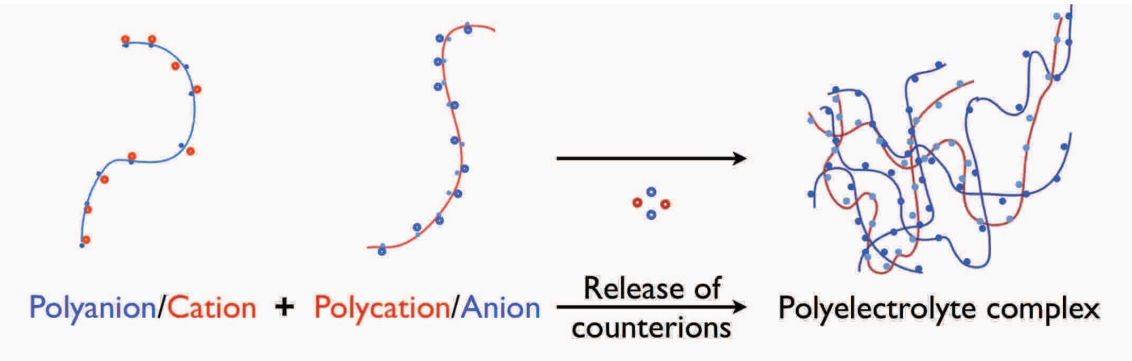

Figure 1.6: Schematic representation of the formation of a polyelectrolyte complex by mixing a polyanion and a polycation solutions.

This formation of complexes changes the enthalpy and entropy of the system and both vary with the salt concentration. The effect of the salt concentration is shown in Figure 1.7. We can see an increase of the Coulombic energy, ΔE, with the increase of the salt concentration. At low salt concentration, the energy of the system decreases upon complexation, due to a stronger decrease of energy coming from the interpolyelectrolyte ion pairing than the increase of energy originated from the release of counterions. The complexation is exothermic ($\Delta E < 0$). The increase of the salt concentration causes a decrease of the Debye length, the screening of the polyelectrolyte charges. So at high salt concentration, the energy gained from the formation of ion pairs between ionic groups of polyanions and polycations decreases. The increase of energy by counterion release is therefore bigger than the energy decrease due to polyelectrolyte charge pairing. The complexation is endothermic ($\Delta E > 0$). In this case, the interactions polyelectrolyte-counterion are favored over the

interactions polyelectrolyte-polyelectrolyte. The entropy of complexation is always positive, but for very high ionic strength, $\Delta E > \Delta S$ (the free energy of the system, ΔF, is positive), so there is no complexation.

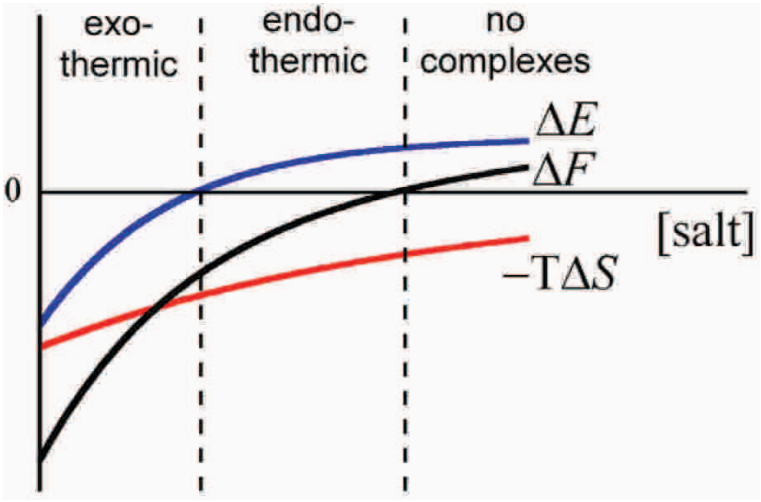

Figure 1.7: Schematic picture showing the influence of the salt cconcentration on the free energy of complexation, ΔF, on the Coulomb energy, ΔE, and on the counterion release entropy, $-T\Delta S$. Reproduced from reference [17].

1.1.4.2 Structure of polyelectrolyte complexes

Two models of polyelectrolyte complex structure are considered : the ladder model and the scrambled-egg model [60–62]. These models are represented in Figure 1.8.

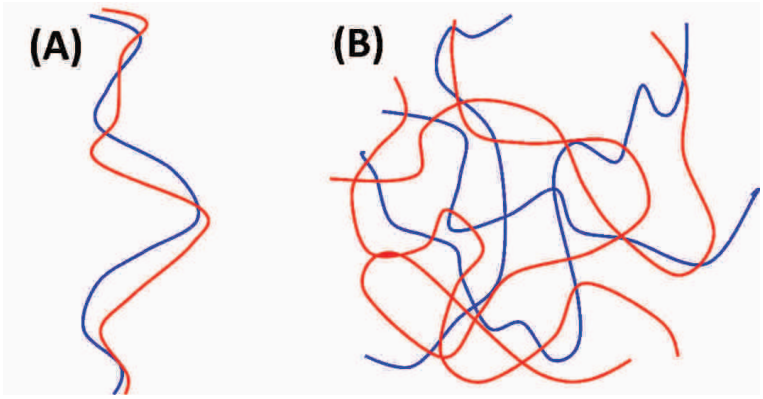

Figure 1.8: Schematic structures of polyelectrolyte complexes, the ladder model, (A), and the scrambled-egg model, (B). Polyanions are represented in blue and polycations in red.

In the ladder model, polyanions and polycations form complexes on a molecular levels, with polyelectrolytes parallel to each other. The complexes are organized in such manner that all oppositely charged groups of the two polyelectrolytes are situated facing each other and form ion pairs. In the scrambled-egg model, the

monomer units of oppositely charged polyelectrolytes are randomly mixed and the charges are statistically compensated by the opposite charges. These two models are the extremes and polyelectrolyte complex structures are usually a combination of the two models. These structures depend on different parameters, as the ionic strength [63] and the pH of the solutions.

At low ionic strength, the increase of the salt concentration leads to a decrease of the amount of aggregation, due to more flexible chains. At high ionic strength, the repulsion between the primary particles is screened, leading to secondary aggregations between the particles and macroscopic flocculation. These aggregations increase with the increase of salt concentration.

As already mentioned, the pH of the solutions has an effect on the degree of ionization of weak polyelectrolytes, so on the energy due to the polyelectrolyte charge pairing. This means that the pH of the solutions has an influence on the formation of complexes for weak polyelectrolytes and on their structure. However, as the pH has no effect on the degree of ionization of strong polyelctrolytes, it has no effect on the formation and the structure of complexes formed by strong polyelectrolytes.

The polyelectrolyte complexation can lead to soluble complexes or to a phase separation between a solvent rich phase and a polymer-rich phase [57,60,64]. Figure 1.9 shows the schematic phase diagram for a polyelectrolyte complexation depending on the fraction of polycations, and on the salt concentration. At very high salt concentration, no complexation occurs. Complexation occurs for low salt concentration and two cases can be distinguish. For high excess of polyanion (small fraction of polycation) or polycation (high fraction of polycation), the complexes are soluble in the solvent. These complexes are negatively charged for an excess of polyanion and positively charged for an excess of polycation. The complexes become insoluble when the amount of polycations and polyanions are closer and the solution is composed of a solvent-rich phase and a polymer-rich phase. The phase diagram can be different for other parameters.

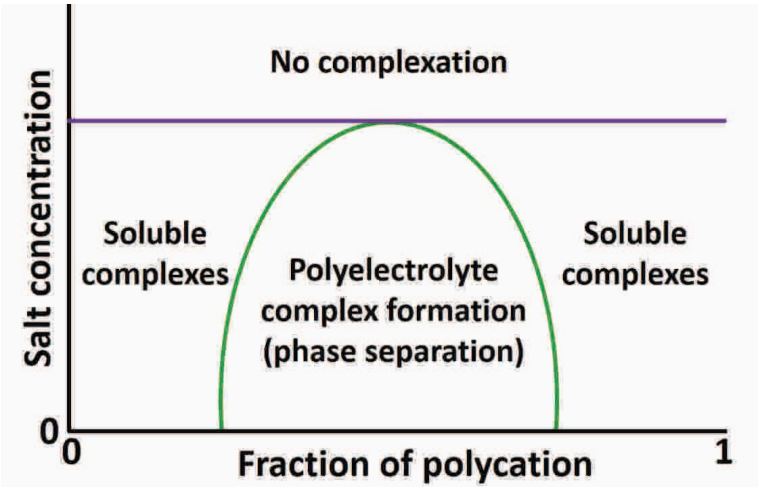

Figure 1.9: Schematic phase diagram of polyelectrolyte complexation. On the vertical axis, the ionic strength or salt concentration. On the horizontal axis, the fraction of polycation.

1.1.5 Complexation at interfaces - The Layer-by-Layer assembly

In the 1980's, Gero Decher discovered the Layer-by-Layer (LbL) technique [1,65, 66], which is a "bottom-up" approach for the build-up of thin multimaterial films on surfaces. It is based on a simple concept, attractive intermolecular interactions, mainly electrostatic, lead to an easy experimental implication and thus low cost and an environmental friendliness (low pollution). This explains the important use of this technique all over the world (in 2010, 3 publications per day) and its versatility allows to use this technique in a broad range of domains.

1.1.5.1 The Layer-by-Layer assembly

The Layer-by-Layer deposition is a bottom-up technique consisting of consecutive depositions of various components. As shown in Figure 1.10, it usually starts with a charged surface, for example positively charged, put in contact with the oppositely charged polyelectrolyte solution, in our example a polyanion, which adsorbed on the surface due to electrostatic interactions. The deposition is followed by a rinsing of the sample to remove the excess of polyelectrolytes, then it is put in contact with the polycation solution, and after the deposition, is rinsed again. Then the procedure is performed several times to have a film with the desired number of layers and the desired thickness. Of course this is not limited to two compounds and specific films can be built up by deposition of several compounds in different sequences.

The representation of the Layer-by-Layer assembly shown in Figure 1.10 is a simplified picture. In fact, multilayer films are not composed of distinct layers separated by well defined interfaces, as represented on the left in Figure 1.11, but the polyelectrolytes interpenetrate within the neighbouring layers to have a charge compensation on the microscopic scale for stoechiometric films. There is a complexation

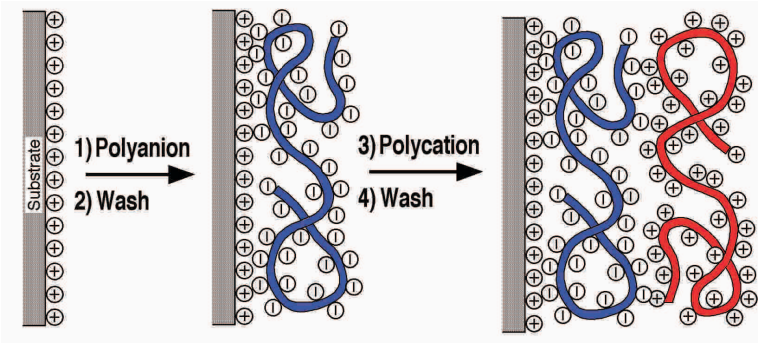

Figure 1.10: Schematic representation of a multilayer film build-up using the Layer-by-Layer process. Counterions are omitted and conformation of polyelectrolyte as well as interpenetration are ideal cases.

at the interfaces. This is illustrated by the relative concentration profils of a polyanion and a polycation in a multilayer film shown on the right in Figure 1.11. We can see the overlap of the two polyelectrolytes at the interfaces of the layers. The relative concentration of the polyanion and the polycation is 1 at any position in the film. The green dots in the figure correspond to deuterated polyanion layers and the concentration profil shows that these layers can be resolved as single layers only if they are separated by at least one non-deuterated layer pair.

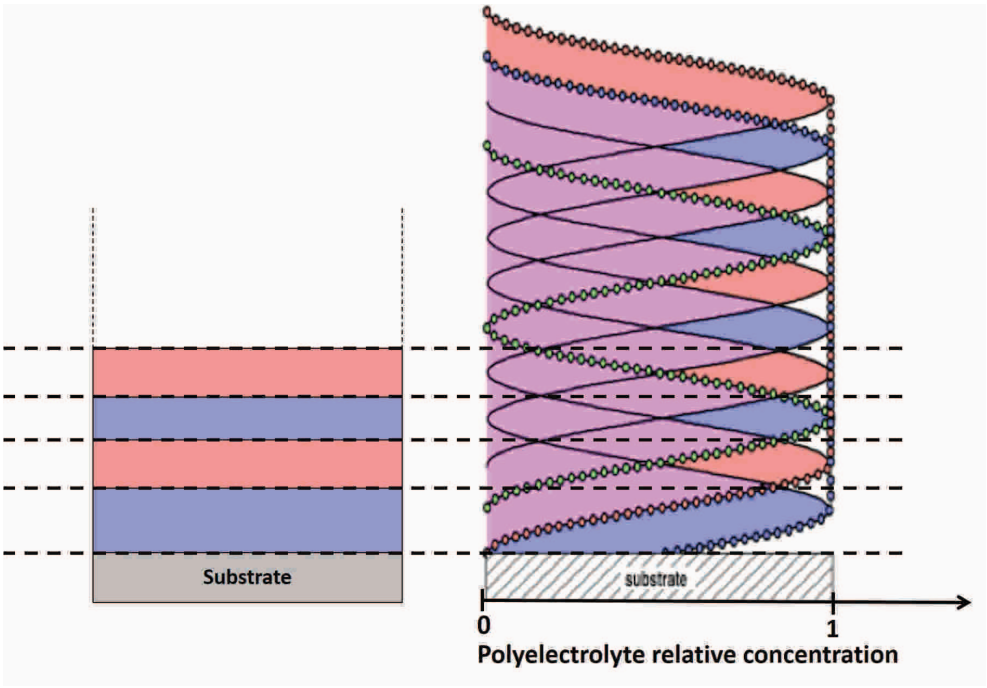

Figure 1.11: Structure of polyelectrolyte multilayer film with a linear growth regime, as determined by X-ray and neutron reflectometry measurements. Polyanion is represented in blue and polycation in red. Adapted from reference [18].

The multilayer films prepared by the Layer-by-Layer assembly can be deposited by three methods : dipping, spraying and spin-assisted LbL assembly, as shown in

Figure 1.12.

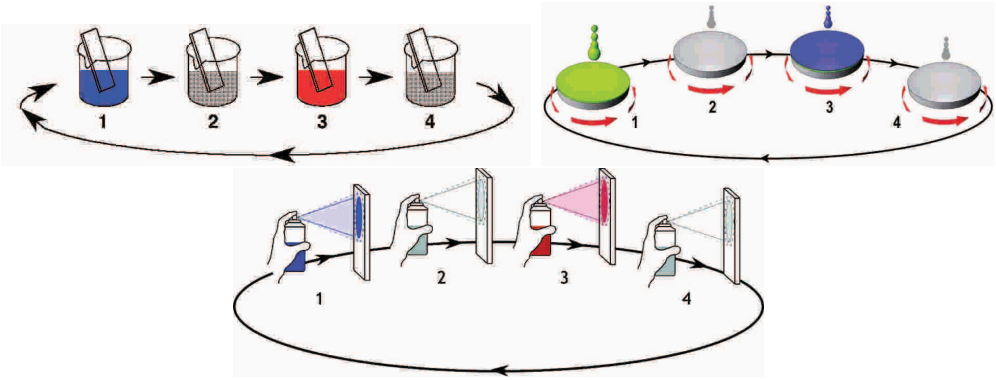

Figure 1.12: Schematic representations of the build-up of multilayer films by dipping (top left), spin-assisted LbL assembly (top right) and spraying (bottom).

The dipping deposition consists of immersing the substrate into the polyelectrolyte solutions for typically 15 min to 20 min, with intermediate rinsing steps of few minutes to remove the non-adsorbed polyelectrolytes [1, 65]. The deposition by spraying [67, 68] is much quicker than the dipping deposition, it usually takes 10 s to 20 s per layer, including the rinsing step, which means that it allows to build up multilayer films with a high number of layers rapidly, for example 100 to 150 layers per day. It is even possible to skip the rinsing steps. Usually, the multilayer films prepared by spraying are thinner than the ones prepared by dipping [2, 69, 70], but more solution is used and there is a bigger amount of waste. It is also possible to spray the two solutions of oppositely charged materials simultaneously on the surface to build up a non-stratified film of complex formed with the two materials [71]. Finally, it is also possible to prepare multilayer films by dropping the solutions and water onto the rotating substrate with the spin-assisted LbL assembly [3, 72]. This method is quick, 20 s to 30 s for the deposition of one layer, but contrary to the spray deposition, consumes a small amount of solution, that is less waste. Unfortunately, the multilayer films are not homogeneous over the surface, the thickness depends on the distance from the center of rotation, and this deposition is not suitable for the coating of large surfaces.

The reason of these differences are not well known, especially the differences between dippping and spraying. An explanation is that the adsorption mechanism is different for dipping (thermodynamic diffusion) and spraying (kinetic diffusion). Another point of view, a difference of solution temperature due to cooling by evaporation during spraying is discussed in Paragraph 2.5.

In addition to the different methods of deposition, a large number of parameters (the conditions of preparation) play a role in the build-up process. We will give here some examples of the influence of the preparation conditions. An important parameter is the salt concentration. Whereas an increase of the salt concentration in polyelectrolyte solutions leads to the decrease of the polyelectrolyte chain size in solution, the increase of the salt concentration of the polyelectrolyte solutions leads to the inverse behaviour in the multilayer films, that is an increase of the thickness

and the roughness of the films [73,74]. K. Büscher *et al.* [45] showed that the nature of the salt has also an influence on the thickness of multilayer films, with thicker films prepared from solutions containing KCl than NaCl for example, and C. C. Buron *et al.* [74] determined that the nature of salt has an effect on the roughness at the surface of the films. The polyelectrolyte charge density also plays a role on the film structure, as it changes the electrostatic interactions which induce the film deposition [43,75,76]. For example, U. Voigt *et al.* showed the case of multilayer films composed of poly(styrene sulfonate) and poly(diallyl-dimethyl-ammoniumchloride-stat-N-methyl-N-vinylacetamide) (P(DADMAC-stat-NMVA)), for which the charge density can be tuned by changing the amount of NMVA in the polycation ; in this case, they showed for example that the maximum thickness of the films is achieved for a degree of charge of the polycation included between 75% and 89% depending on the concentration of the polyelectrolyte solutions. An influence of the pH of the polyelectrolytes solutions was also observed for weak polyelectrolytes on the films thickness and roughness [44, 77], as a change of the pH causes a change of the charge density of weak polyelectrolytes and hence, the electrostatic interactions. All the parameters given above are parameters of the solutions, but the conditions of deposition have an influence on the multilayer films, too. For example, the increase of the temperature of the solutions leads to an increase of the thickness of the films [45, 78] and the use of a drying step after the polyelectrolyte depositions has an effect on the surface morphology compared to film build-up without intermediate drying steps [79,80]. A. Izquierdo *et al.* [2] showed time dependency of the multilayer films thickness for sprayed films, the thickness increases with time until it reaches an equilibrium (the same behaviour is observed also for films prepared by dipping), as well as an effect of repeating depositions of one polyelectrolyte several times before depositing the oppositely charged polyelectrolyte. These parameters are given as examples, but all the deposition conditions have a more or less pronounced effect on the film build-up.

1.1.5.2 Different growth regimes

Two different growth regimes of the multilayer films can be observed : the linear regime and the superlinear regime.

The linear regime corresponds to films with a linear increase of the thickness per layer pair [1, 65]. A typical system exhibiting a linear growth is multilayer films composed of PSS and PAH. An example of a linear growth is shown in Figure 1.13, where the thickness is drawn as a function of the layer pair number, measured by ellipsometry. The film was prepared by dipping a silicon wafer coated with a poly(ethyleneimine) (PEI) layer into solutions of 3 x 10^{-3} monomol/L of PSS and PAH dissolved in 0.5 M NaCl solutions, with three rinsing steps in pure MilliQ water. A total number of ten layer pairs was deposited.

The thickness per layer pair determined from the fit of the experimental curve was 28.76 Å. This corresponds to the typical range of thicknesses observed with the linear regime, which are in the order of few nanometers per layer pair. The thickness per layer pair is smaller than the size of a polyelectrolyte in solution and

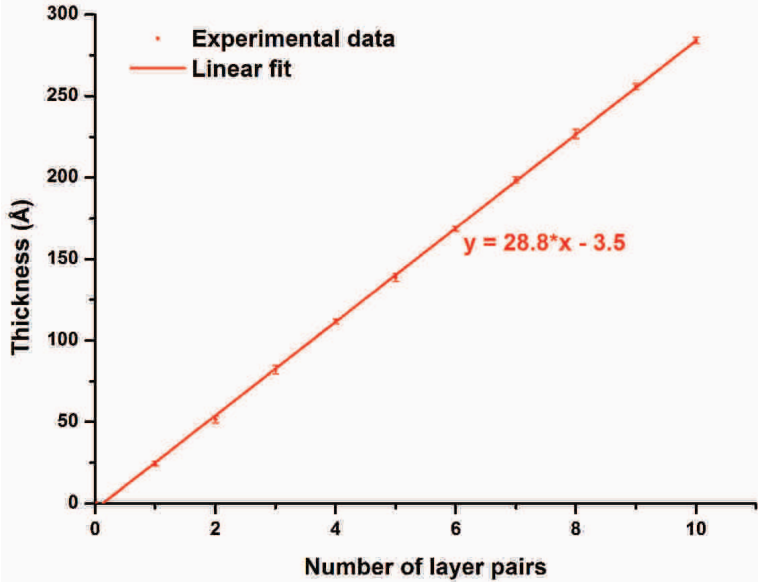

Figure 1.13: Thickness growth of a dipped (PSS-PAH) film with the number of layer pairs.

the polyelectrolyte are fixed in the film, we talk about trapped polyelectrolytes.

The superlinear regime, also called exponential regime, corresponds to films which exhibit an exponential increase of the thickness for the first layers, followed by a linear growth [19, 81].

In Figure 1.14, the thickness growth of a multilayer film composed of PSS and poly(diallyldimethylammonium chloride) with the number of layer pairs measured by ellipsometry is shown. The film was prepared by dipping a silicon wafer coated with a PEI layer into solutions with a concentration of 1 x 10^{-3} monomol/L of PSS and PDADMAC, dissolved in a buffer acetate of 50 mM, 0.2 M NaCl and pH=5.6, with rinsing steps in pure MilliQ water.

We can observe the exponential regime for the six first layer pairs, and the linear regime starting from the seventh layer pair with a thickness increase of 115.36 Å per layer pair. In multilayer films exhibiting a superlinear growth the polyelectrolyte chains are mobile. L. Xu *et al.* showed also the possibility to change the growth regime from linear to superlinear and vice versa by changing the pH of the polyelectrolyte solutions for films composed of poly(2-(dimethylamino)ethyl methacrylate) (PDMA) and poly(methacrylic acid) (PMAA). E. Hübsch *et al.* showed the same change of the growth regime, but by changing the composition of polyelectrolyte mixures. Indeed, they studied multilayer films composed of a mixure of PSS with poly(L-glutamic acid) (PGA) and PAH. By changing the proportion of PSS and PGA, they could build up films with a linear regime for a majority of PSS (films composed of PSS and PAH exhibit a linear growth) and films with a superlinear regime for a majority of PGA (films composed of PGA and PAH exhibit a superlinear growth).

A model for the superlinear growth of multilayer films composed of poly(L-lysine)

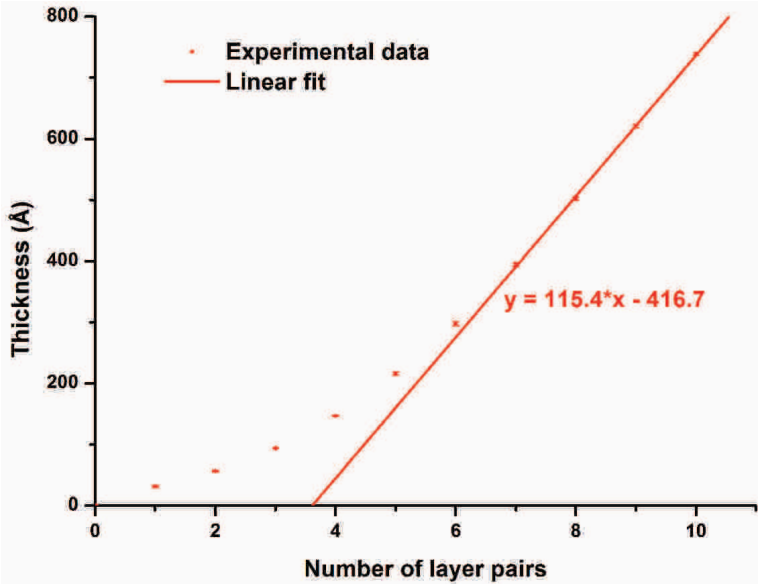

Figure 1.14: Thickness growth of a dipped (PSS-PDADMAC) film with the number of layer pairs.

(PLL) and poly(L-glutamic acid) (PGA) was described by P. Lavalle *et al.* [19] and is represented in Figure 1.15. It was suggested that two kinds of polyelectrolytes constitute the film, strongly adsorbed polyelectrolytes which form the multilayer network and weakly bound polyelectrolytes present in the film. During the deposition of one polyelectrolyte, for example the PGA, this polyelectrolyte adsorb strongly to the film at the surface. Furthermore, the oppositely charged polyelectrolyte, the PLL, which is weakly bound diffuse in the film to the surface, forming complexes with the PGA and leading to an increase of the thickness bigger than just the increase due to the adsorption at the surface. At this time, PGA chains diffuse into the film. With the increase of the thickness, more free polyelectrolytes are contained in the film and can diffuse to form complexes, so we observe an increase of the thickness growth with the number of layers. For a certain thickness, the increase of thickness becomes stable, due to a limitation of the diffusion distance, and so the thickness growth becomes linear. C. Picart *et al.* [81] observed this effect by studying the diffusion of labelled poly(L-lysine) (PLL) in multilayer films composed of PLL and hyaluronan (HA) by fluorescence.

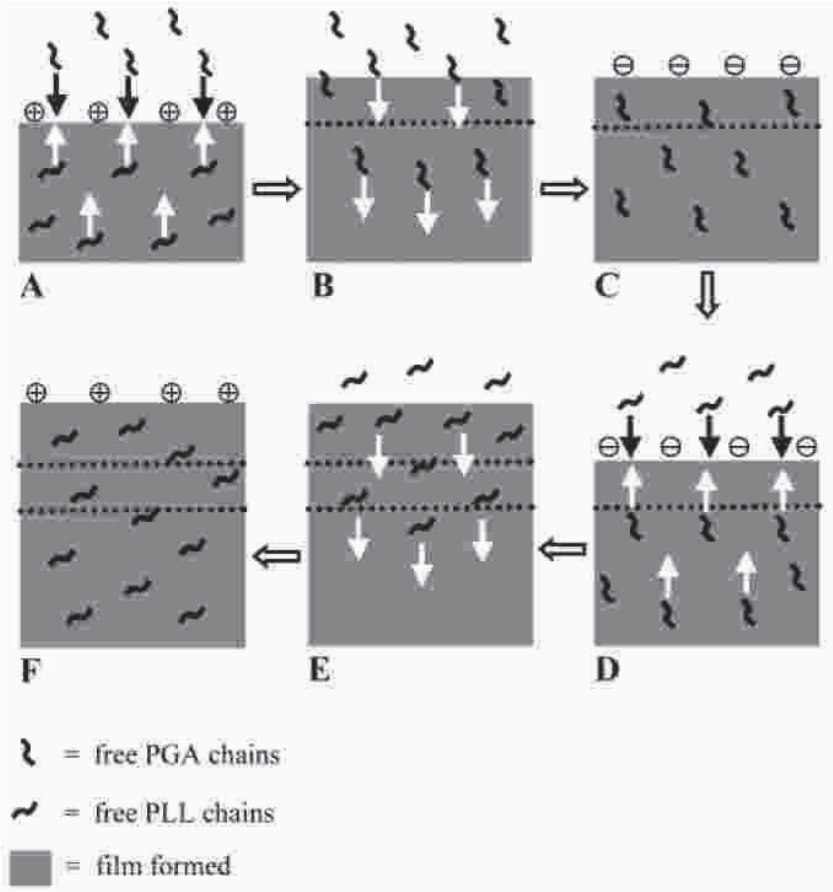

Figure 1.15: Schematic drawing of the build-up mechanism of (PGA-PLL) multilayer films. (A) Beginning of the contact between a $(\text{PGA-PLL})_i$ multilayer film with a PGA solution. (B) Diffusion of PGA chains into the film once all the mobile PLL chains have diffuse out of it. (C) End of step B resulting in a negative charge overcompensation on the film. (D) Beginning of the contact between a $(\text{PGA-PLL})_i$/PGA multilayer film with a PLL solution. (E) Diffusion of PLL chains into the film once all the mobile PGA chains have diffuse out of it. (F) End of step E resulting in a positive charge overcompensation of the $(\text{PGA-PLL})_{i+1}$ film. Reproduced from reference [19].

1.1.5.3 Thermodynamics and kinetics of polyelectrolyte multilayer film formation

The thermodynamics and kinetics of multilayer film formation is a complex subject [18, 21, 82–87]. Whereas polyelectrolyte multilayer film formation can be compared to polyelectrolyte complex formation on some aspects, there are important differences also.

The fact that a couple of polyelectrolytes forms a film which grows linearly or superlinearly seems to depend on the energy of complexation [88]. If the complexation is endothermic, the superlinear growth of the multilayer film is favored, whereas a film grows linearly with an exothermic complexation. As for polyelectrolyte complexes, ionic strength, pH and polyelectrolyte charge density have an influence on multilayer film formation.

The ionic strength, or salt concentration, of the polyelectrolyte solutions has an effect on the thickness of polyelectrolyte multilayer films [73, 89]. As already mentioned, the ionic strength of the polyelectrolyte solutions influences the conformation of the polyelectrolyte chains. At low salt concentration, there is a high repulsion between the polyelectrolyte charges, inducing a stretched conformation. So, when the polyelectrolytes adsorb on a surface, they lie on the surface with a small out-of-plane size, forming layers with a small thickness, as represented in Figure 1.16 (A). Increasing the ionic strength leads to increase the screening of the polyelectrolyte charges. At high ionic strength the conformation is therefore a coil. When adsorbing on a surface the polyelectrolyte chains have a bigger out-of-plane size, forming thicker layer, as represented in Figure 1.16 (A).

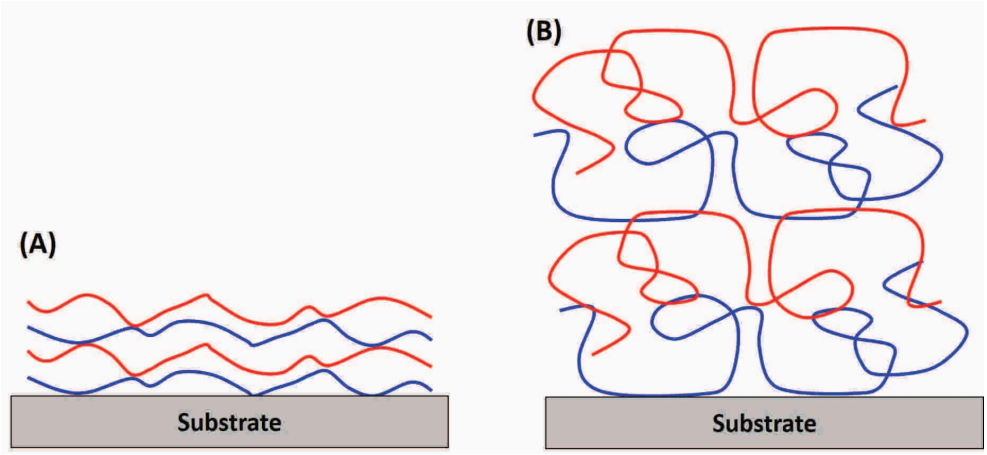

Figure 1.16: Oversimplified representation of polyelectrolyte chain conformation in multiayer films depending on the ionic strength, (A) at low ionic strength and (B) at high ionic strength.

Not only the salt conncentration has an influence on multilayer film build-up, but also the salt nature [20,82,90]. Indeed, the ions are sourrounded by a shell composed of water molecules, called hydration shell, which depends on the nature of the ions, and especially on their electric field. For small ions, the electric field is high and the ions have a large hydration shell. Thus, the ions have a low interaction with the polyelectrolytes. We are in the same case than for a low salt concentration, the repulsion between the polyelectrolyte charges is high, the chains are in a stretched conformation and the adsorbed polyelectrolytes form thin layers. For large ions the hydration shell is small due to a weak electric field and the ions interact highly with the polyelectrolytes. The screening of the polyelectrolyte charges is high and the conformation is a coil. So, the polyelectrolytes form thicker layers. The effect of the counterions nature on the thickness of (PSS-PDADMAC) multilayer films is shown in Figure 1.17.

For strong polyelectrolytes, the pH of the solutions has no effect on the multilayer film build-up, since strong polyelectrolytes are fully ionized and are not influenced by the pH. But when working with weak polyelectrolytes, the pH plays an important role on the build-up of multilayer films [91–93]. First, we already

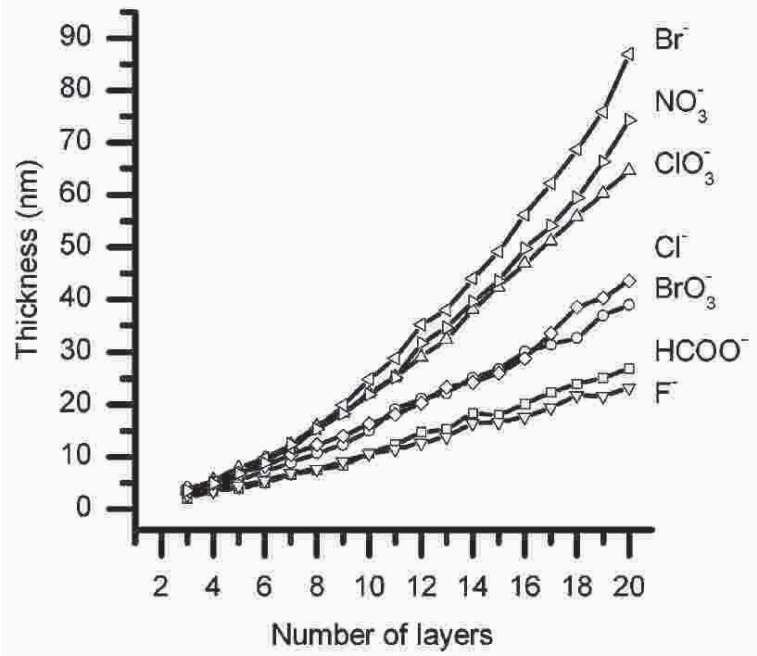

Figure 1.17: Thickness evolution of (PSS-PDADMAC) films versus the number of layers as determined by ellipsometry, for different counterion species. Reproduced from reference [20].

said that the pH of polyelectrolyte solutions has an effect on the conformation of the polymer chains. As for the ionic strength, this has an effect on the layer thickness. But the degree of ionization of the polyelectrolytes has also an influence on their adsorption. If the degree of ionization of a polyelectrolyte decreases, its incorporation in multilayer films increases. Indeed, the number of charges on weak polyelectrolytes depends on its degree of ionization, and so on the pH. By decreasing the degree of ionization of one of the polyelectrolytes (polyelectrolyte A) composing a film without changing the degree of ionization of the second polyelectrolyte (polyelectrolyte B), the number of charges on polyelectrolyte A decreases whereas the number of charges of polyelectrolyte B remains the same. So, to compensate the charges of polyelectrolyte B more polyelectrolyte A is needed in the multilayer film. Of course, the effect of the pH on multilayer film growth is more complex, especially if the weak polyelectrolytes used have different pK_a. The pH can also change the growth regime of the multilayer film from a linear to a superlinear growth depending on the pH, as studied by P. Bieker *et al.* [92].

As for the formation of polyelectrolyte complexes in solution, it is possible to draw a phase diagram to represent the different cases as a function of the parameters [21]. Figure 1.18 shows the schematic phase diagram for the formation of a polyelectrolyte multilayer film depending on the fraction of polycations and on the salt concentration. As for the polyelectrolyte complexes, no complexation occurs at very high salt concentration (region S). At lower salt concentration, for an excess of polyanion or polycation, soluble polyelectrolyte complexes are formed (regions C and C'). For closer proportion of polyanions and polycations, polyelectrolyte multilayer films are formed and two cases can be distinguished. The region L corresponds

to a multilayer in a liquid state, i.e. when polyelectrolytes can diffuse in the multilayer films, leading to the superlinear growth regime. At very low salt concentration, multilayer films are in a glassy state, i.e. the polyelectrolytes are immobile in the film. Of course, like for polyelectrolyte complexation, the phase diagram can be dependent on other parameters than the salt concentration, like the pH.

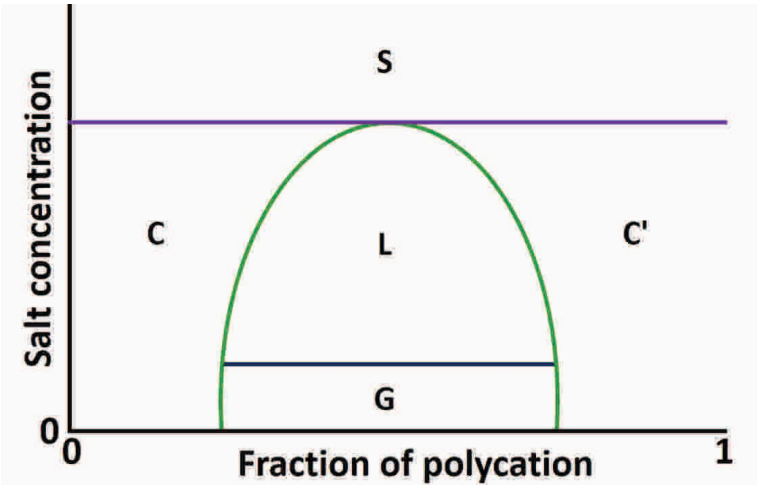

Figure 1.18: Schematic phase diagram of a polyelectrolyte multilayer film adsorption. On the vertical axis, the ionic strength or salt concentration. On the horizontal axis, the fraction of polycation. The L region indicates a multilayer in a liquid state and the G region a multilayer in a glassy state. The C and C' regions corresponds to soluble polyelectrolyte complexes and the S region to a solution with no complexation. Reproduced from reference [21].

1.1.5.4 Polyelectrolyte multilayer film structure

The internal structure of polyelectrolyte multilayer films is not homogeneous but is generally represented by the model of the three zones [94]. This model is represented in Figure 1.19 and takes into account the effect of the substrate and of the environment on the film.

Zone I corresponds to the first layers deposited, which are close to the substrate. The structure of these layers is dependent on the substrate surface, the charge density and the roughness of the surface. Zone III is composed of the last layers, which are close to the surface of the film and are dependent on the environment (air, solution). These two zones are limited in thickness, corresponding to the distance of influence of the substrate and of the environment on the multilayer film. As shown in the figure, for a few number of layers, both the substrate and the environment have an effect on the whole film and zone I and zone III are mixed. By increasing the number of layers, and the thickness of the film, zone I and zone III are defined separately and their thicknesses increase, until their maximal thicknesses are reached. Usually the influence of the substrate and the environment is visible within few layers, that is several nanometers. When zone I and zone III reach their maximal thicknesses, a new zone appear, zone II, which is not influenced by the substrate and the environment. This zone is also named "bulk film". The thickness of zone II in-

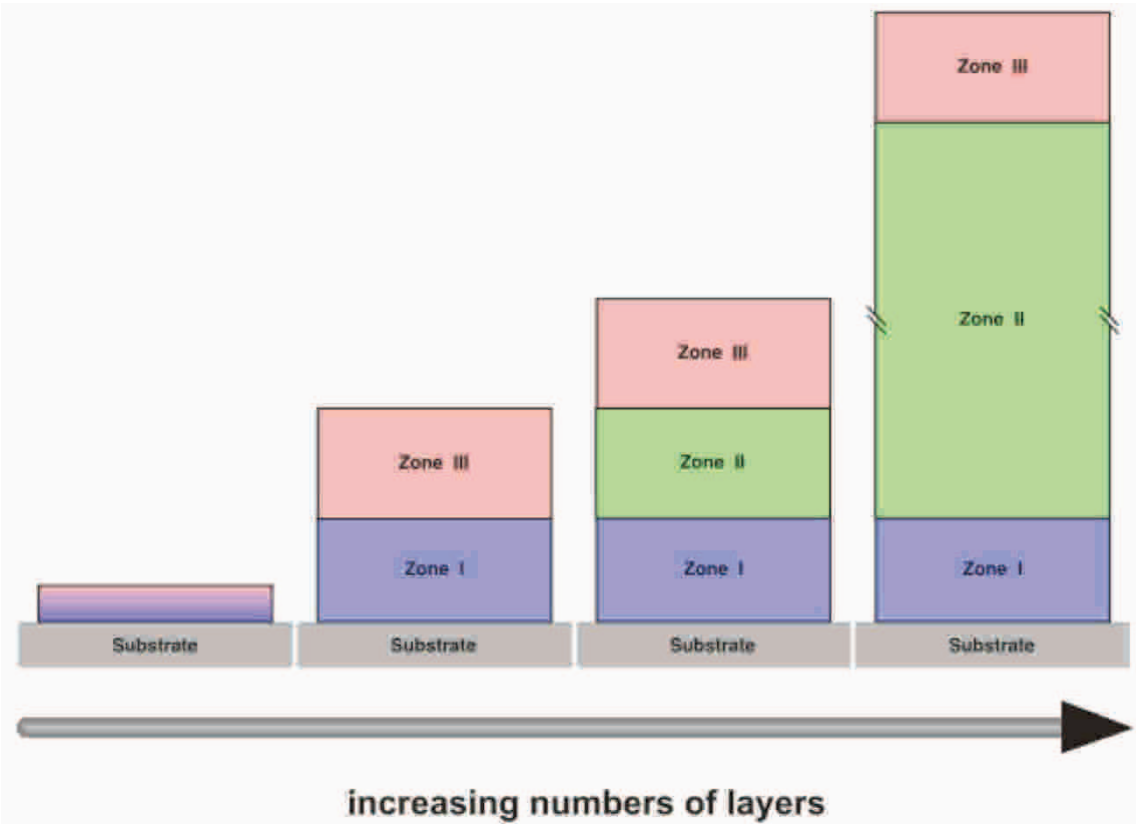

Figure 1.19: Schematic representation of the internal structure of polyelectrolyte multilayer films described by the model of the three zones. Adapted from reference [18].

creases with further layer deposition and, for thick films, is the main part of the film.

The use of this structure or of an homogeneous structure for the analysis of neutron reflectivity is discussed in Paragraph 4.2.

1.1.5.5 A versatile technique

The most common interaction used for the Layer-by-Layer assembly process is the electrostatic interaction. But it is also possible to build up multilayer films of uncharged materials using other kind of interactions, as the hydrogen-bounding [95–97], the covalent bound [98–101] or the Van der Waals interactions [102–105]. For example, W. B. Stockton *et al.* [96] studied the build-up by hydrogen-bounding of multilayer films composed of polyaniline (PA) and several other polymers, like PSS and poly(ethylene oxide), and T. Serizawa *et al.* [102] prepared films with isotactic and syndiotactic PMMA using Van der Waals interactions.

These different interactions allow to deposit a broad range of compounds on surfaces to build up a multilayer film. The most common materials used are the polyelectrolytes [1,65,66,106,107], which are the first compounds used for the preparation of multilayer films assembled by the Layer-by-Layer process. Nanoparticles

can also be incorporated into the multilayer films, as metallic particles (gold [108], iron oxide [109], titanium oxide [110], ...), clay platelets [111], silica particles [112], cellulose nanofibrils [113] or luminescent rare-earth particles [114]. Another kind of materials deposited in multilayer films are biological compounds, for the development of biomedical devices for example, like viruses [115], DNA [116, 117] or proteins [116, 118].

The multilayer films can be deposited on a variety of different surfaces, with different compositions, shapes (the solutions can go everywhere) or sizes, from square centimeters to square meters. For the characterization of the films, plane surfaces are usually used, composed of gold [107], quartz [119] or silicon [77] for example. But the films can also be deposited on nanoparticles [109, 120, 121] or on textile [122] for example.

Due to this broad range of materials and supports which are available for the formation of multilayer films deposited by the Layer-by-Layer assembly, the properties that multilayer films can present are varied and the Layer-by-Layer process is studied and used in a large number of scientific domains. Some examples of properties and potential applications which can be obtained with multilayer films are membrane formation or membrane efficiency enhancement [123–126], coatings of surfaces, like anticorrosion coatings [127], repellent coatings [112], flame-retardant coatings [122] or bioactive coatings [128], formation of fuel cells [129], of capsules for biomedical purpose (drug delivery, ...) [130], of responsive systems under external stimuli (sensors, ...) [101, 131, 132] or of systems presenting specific mechanical properties [126, 132].

1.2 Neutron scattering

Neutrons were discovered in 1932 by James Chadwick and were used in condensed matter since their discovery. They are a perfect probe for the study of the atomic and molecular structure as well as the dynamics of materials. Neutrons interact with the nuclei through the strong interaction.

1.2.1 Neutron radiation

Neutrons are elementary particles which form the nuclei of atoms with the protons. They are electrically neutral and their fundamental properties are listed in Table 1.1.

The lifetime of a free neutron is 886 $\pm$ 10 s and a neutron decays into a proton, an electron and an antineutrino. The neutron penetrates deeply into matter as it is electrically neutral. The only potential experienced by a neutron in scattering experiments is the strong interaction with the nuclei and the magnetic interaction due to the spin. So, neutrons are good probes to study the matter.

Neutrons used for scientific research are produced in reactors by fission of

Mass	M_e = 1.675 x 10^{-27} kg
Spin	s = -$\hbar/2$
Magnetic moment	μ = -9.649 x 10^{-27} J/T
Lifetime (β-decay)	τ = 886 s
Electric charge	Q = 0

Table 1.1: Neutron properties [7]. $\hbar$ is related to the Plank constant h = $2\pi\hbar$.

Uranium-235 or in spallation sources by bombarding a target with particles of high energy produced by an accelerator. Then neutrons are cooled in a moderator to obtain the desired energy for the neutron scattering experiments.

1.2.2 Neutron scattering theory

Neutron scattering consists of illuminating a sample with an incoming neutron beam of a certain momentum, and to measure the intensity of the scattered beam, as shown in Figure 1.20.

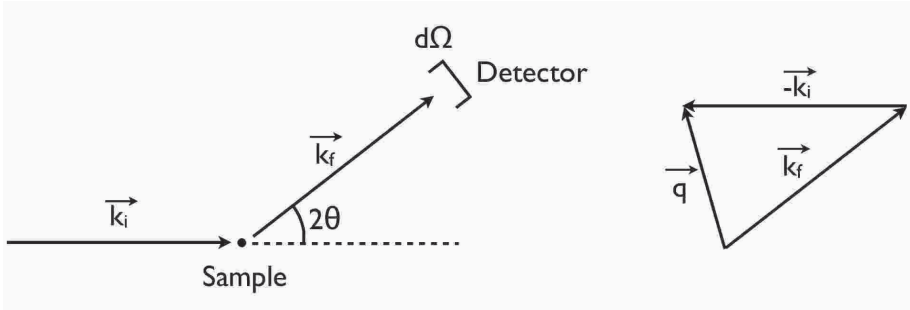

Figure 1.20: Geometry of a scattering experiment. $\vec{k_i}$ and $\vec{k_f}$ correspond to the incoming and the outgoing (scattered) wave vectors and $\vec{q}$ to the momentum transfer or scattering vector.

The scattering is described by the momentum transfer, or scattering vector, $\overrightarrow{q}$ which is calculated by substracting the incoming wave vector from the outgoing wave vector :

$$\overrightarrow{q} = \overrightarrow{k_f} - \overrightarrow{k_i} \tag{1.31}$$

With $k_i = k_f = k = 2\pi/\lambda$ and a scattering angle of 2θ, the value of $\overrightarrow{q}$ is :

$$q = 2k \sin\theta = \frac{4\pi}{\lambda} \sin\theta \tag{1.32}$$

The scattering can be either elastic or inelastic, but we consider no energy transfer between the scattered neutrons and the samples during our studies, so we consider only elastic scattering. This approximation is valid for small momentum transfers and static samples.

Possible inelastic contributions of single particle excitations, like diffusion, lead

to even scattering in all directions (incoherent) and are modeled as a constant background. We can suppose that the quantity measured is the differential elastic cross section

$$\frac{d\sigma}{d\Omega} = \int \frac{d^2\sigma}{d\Omega dE_f} dE_f \tag{1.33}$$

which gives the proportion of the wave intensity with an incident wave number $k_i = 2\pi/\lambda$ and an energy E_f scattered into the solid angle $d\Omega$.

As neutrons interact through the strong interaction, which has a typical range of femtometers, the nuclei of the atoms composing the samples can be considered as points. The total scattering strength of a single nucleus can be described by the scattering length b :

$$\frac{d\sigma}{d\Omega} = b^2 \tag{1.34}$$

The scattering length can be positive and negative, which corresponds to a repulsive or an attractive potential, depending on the isotopes and is in the order of femtometers. Two quantum-mechanical interactions between the neutrons and the nucleus have to be considered in addition to the scattering, the absorption and the spin interactions.

The absorption of neutrons by nuclei depends on the energy of neutrons and is strong if the compound energy of the neutron and the nucleus corresponds to a resonance energy. For cold or thermal neutrons, only few isotopes show resonance absorption of neutrons, and the elements used in our studies have a negligibly small absorption.

The spin interaction comes from the fact that neutrons have a spin of -$\hbar/2$. The overall spin system, which consists of the neutron spin and the nuclear angular moment j, can have two total spin states j - $\hbar/2$ or j + $\hbar/2$, with a probability factor g^+ and g^- respectively. Each of this spin combinations corresponds to a scattering length b^+ and b^-. The average scattering length <b> for one isotope is equal to :

$$< b >= g^+ b^+ + g^- b^- \equiv b_c \tag{1.35}$$

with b_c called coherent scattering length. The standard variation of the scattering length

$$\sqrt{< b^2 > - < b >^2} \equiv b_i \tag{1.36}$$

is called the incoherent scattering length. For a distribution of different isotopes in the material studied, an additional distribution of effective scattering lengths has to be considered.

So, the total cross section σ_{total} can be divided into three parts

$$\sigma_{total} = \int \frac{d\sigma}{d\Omega} d\Omega = 4\pi b^2 = 4\pi b_c + 4\pi b_i + \sigma_{abs} = \sigma_{coh} + \sigma_{inc} + \sigma_{abs} \tag{1.37}$$

with σ_{coh}, σ_{inc} and σ_{abs} the coherent, incoherent and absorption cross sections re-

spectively. The scattering lengths and the cross sections for some elements and their isotopes are listed in Table 1.2 [7, 133].

	Z	A	abundance (%)	b_c (fm)	σ_{coh} (barn)	σ_{inc} (barn)	σ_{abs} (barn)
H	1			-3.74	1.76	80.27	0.33
		1	99.985	-3.74	1.76	80.28	0.33
		2	0.015	6.67	5.59	2.05	5×10^{-4}
		3	$T_{1/2}$ = 12.3 y	4.79	2.89	0.14	$< 10^{-6}$
He	2			3.26	1.34	0	7.5×10^{-3}
		3	0.013	5.75	4.42	1.53	5333
		4	99.987	3.26	1.34	0	0
Li	3			-1.9	0.45	0.92	70.5
		6	7.5	2.01	0.52	0.47	940
		7	92.5	-2.22	0.62	0.78	0.05
B	5			5.3	3.55	1.7	767
		10	19.4	-0.24	0.14	3.04	3835
		11	80.2	6.65	5.57	0.22	5.5×10^{-3}
C	6			6.65	5.55	0.001	3.5×10^{-3}
		12	98.89	6.65	5.56	0	3.5×10^{-3}
		13	1.11	6.2	4.81	0.034	1.4×10^{-3}
N	7			9.36	11	0.5	1.9
		14	99.635	9.37	11	0.5	1.91
		15	0.365	6.44	5.22	5×10^{-5}	2.5×10^{-5}
O	8			5.81	4.23	8×10^{-4}	1.9×10^{-4}
		16	99.75	5.81	4.23	0	1×10^{-4}
		17	0.039	5.65	4.2	0.004	0.24
		18	0.208	5.85	4.29	0	1.6×10^{-4}

Table 1.2: Scattering lengths and cross sections for some elements and their isotopes. Z is the atomic number and A the mass number. The absorption cross section is given for a neutron energy of 25.3 meV. The half lifetime $T_{1/2}$ of unstable nuclei is given.

The scattering lengths may differ significantly, even between two isotopes of the same element. This allows selective isotope replacement in a sample leading to additional contrast for neutron scattering measurements. In particular, the scattering lengths of hydrogen and deuterium differ a lot, which makes neutron scattering a powerful technique for the study of polymer systems [134–136]. But various other materials can be probed by neutron scattering, too. For example, it is possible to characterize the magnetic order and the influence of external conditions on this order in metallic films by neutron diffraction or inelastic neutron scattering, with polarized neutrons [137–139], or to determine the effect of shear stress at the solid/liquid interface (polymer films and different solvent [140,141], aqueous solutions of micelles near silicon wafers [142], etc.). SANS (Small Angle Neutron Scattering) allows for example to measure the persistence length and the radius of gyration of polyelectrolytes in solution [27,39,143,144] or to determine the orientation of nanometric objects in films, like clay platelets [145,146]. Dynamic studies can also be performed [147], as well as studies of the structure of lipid bilayers [148] or of lipid/DNA complexes [149]. These are some examples of the possibilities offered by neutron measurements.

1.2.3 Neutron reflectometry and Grazing Incidence Small Angle Neutron Scattering

In a grazing incidence scattering experiment, a well collimated incident beam arrives on a surface at a small angle. In this case, the approximation that the incident wave is not changed by the sample is not valid anymore. Moreover, as the momentum transfers in scattering experiments at small angle are small, we cannot observe the interferences from individual atoms and the potential describing the interaction between the incident beam and the sample is a mean field of scatterers V_0.

Assuming a step potential $<V(\overrightarrow{r})>$ which is equal to 0 for negative z values and to V_0 for positive z, the Schrödinger equation describing the scattering experiment is :

$$\nabla^2\psi(\overrightarrow{r}) + k^2\psi(\overrightarrow{r}) = 0 \quad \text{with} \quad k^2 = \frac{2m}{\hbar^2}(E - < V(\overrightarrow{r}) >) \tag{1.38}$$

This equation resembles the Helmholtz equation, which describes the propagation of an electromagnetic wave in classical optics [150]. The solution of the equation is the following :

$$\psi(\overrightarrow{r}) = \begin{cases} a_i e^{i\overrightarrow{k_i}\overrightarrow{r}} + a_f e^{i\overrightarrow{k_f}\overrightarrow{r}} & \text{for z}<0 \\ a' e^{i\overrightarrow{k'}\overrightarrow{r}} & \text{for z}>0 \end{cases} \tag{1.39}$$

The wave vectors $\overrightarrow{k_i}$, $\overrightarrow{k_f}$ and $\overrightarrow{k'}$ correspond to the wave vectors of the incoming, the reflected and the transmitted waves. The potential in this case is a Fermi pseudopotentials with an average atomic density ρ_0 :

$$V_0 = \frac{2\pi\hbar^2}{m} b\rho_0 = \frac{2\pi\hbar^2}{m} N_b \tag{1.40}$$

N_b is called the scattering length density (SLD) and corresponds to the average coherent nuclear scattering length density $\rho_0 <b_{coh}>$. Due to the similarity with optics, one can define the refractive index n :

$$n^2 = \frac{k^2}{k_0^2} = 1 - \frac{V_0}{E} = 1 - \frac{\lambda^2}{\pi} N_b \tag{1.41}$$

If we take into account the absorption :

$$n^2 = 1 - \frac{\lambda^2}{\pi} N_b + i\frac{\mu}{k_0} = 1 - \frac{\lambda^2}{\pi} N_b + i\frac{\lambda}{2\pi}\mu \tag{1.42}$$

with the absorption coefficient $\mu = \rho_0(< \sigma_{abs} > + < \sigma_{inc} >)$. The term $\frac{\lambda^2}{\pi} N_b$ is on the order of 10^{-5}, the refractive index is close to one and the absorption is usually

smaller. So we can approximate :

$$n \approx 1 - \frac{\lambda^2}{2\pi} N_b + i \frac{\lambda}{4\pi} \mu \tag{1.43}$$

1.2.3.1 Neutron reflectometry

Specular reflectivity [7,8]

In a neutron reflectometry measurement, the intensity of a neutron wave reflected from the surface of a sample is measured. In a simplified case, just the specular reflectivity is detected, i.e. the incident angle θ_i is equal to the reflected angle θ_f ($\theta_i = \theta_f = \theta$). In this case, the momentum transfer vector $\overrightarrow{q}$ is normal to the surface as shown in Figure 1.21. The amplitudes follow the equations :

$$a_i + a_f = a' \tag{1.44}$$

$$a_i \overrightarrow{k_i} + a_f \overrightarrow{k_f} = a' \overrightarrow{k'} \tag{1.45}$$

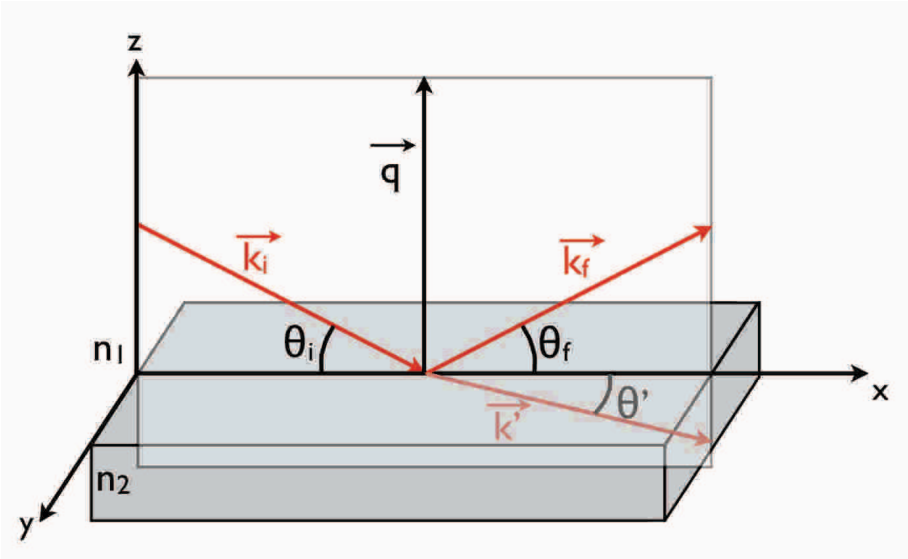

Figure 1.21: Geometry of the reflection and transmission (refraction) of a neutron wave on a plane surface.

If we consider $k = |\overrightarrow{k_i}| = |\overrightarrow{k_f}|$ in vacuum and in the material $nk = |\overrightarrow{k'}|$, thus $n_1 = 1$ and $n_2 = n$, we have :

$$a_i k \cos\theta + a_f k \cos\theta = a' nk \cos\theta' \tag{1.46}$$

$$(a_i - a_f) k \sin\theta = a' nk \sin\theta' \tag{1.47}$$

The projection perpendicular to the surface gives the amplitude of the reflectivity

r and the transmittivity t :

$$r \equiv \frac{a_f}{a_i} = \frac{\sin\theta - n\sin\theta'}{\sin\theta + n\sin\theta'} \tag{1.48}$$

$$t \equiv \frac{a'}{a_i} = \frac{2\sin\theta}{\sin\theta + n\sin\theta'} \tag{1.49}$$

With the Snell-Descartes law ($\sin\theta = n\sin\theta'$) we get :

$$r = \frac{\sin\theta - \sqrt{n^2 - \cos^2\theta}}{\sin\theta + \sqrt{n^2 - \cos^2\theta}} \tag{1.50}$$

If we consider only small angles and absorption :

$$n^2 \approx 1 - 2\frac{\lambda^2}{2\pi}N_b - 2i\frac{\lambda}{4\pi}\mu = 1 - \theta_c^2 - i\frac{\lambda}{2\pi}\mu \tag{1.51}$$

with the critical angle $\theta_c = \lambda\sqrt{\frac{N_b}{\pi}}$. So, for small angles, the reflection amplitude is :

$$r = \frac{\theta - \sqrt{\theta^2 - \theta_c^2 - i\frac{\lambda}{2\pi}\mu}}{\theta + \sqrt{\theta^2 - \theta_c^2 - i\frac{\lambda}{2\pi}\mu}} \tag{1.52}$$

The angles can be converted into momentum transfers q and q_c, and the reflected intensity is equal to :

$$R_F = |r|^2 = \left|\frac{q - \sqrt{q^2 - q_c^2 - i\frac{8\pi}{\lambda}\mu}}{q + \sqrt{q^2 - q_c^2 - i\frac{8\pi}{\lambda}\mu}}\right|^2 \tag{1.53}$$

which is the reflectivity of a sharp interface known as the Fresnel reflectivity. For large momentum transfer $q \gg q_c$:

$$R_F \approx \frac{q_c^2}{16q^4} \tag{1.54}$$

For a stratified sample consisting of N slabs with thicknesses d_j and refractive indexes n_j, as shown in Figure 1.22, the momentum transfer is still normal to the surface and the z-component of the wave has to be considered recursively. The wave function can be written as a superposition of an upwards and downwards traveling wave :

$$\psi(z) = a_j^+ e^{ik_{z,j}z} + a_j^- e^{-ik_{z,j}z} \tag{1.55}$$

with $k_{z,j} = kn_j\sin\theta_j$ the projection of the incident wave vector projected perpendicularly to the interface. As there is a continuity of ψ and $d\psi/dz$ at the depth $z_{j,j+1}$ between the phases j and j+1, we can define the boundary conditions at every

interface :

$$a_j^+ e^{ik_{z,j}z_{j+1}} + a_j^- e^{-ik_{z,j}z_{j+1}} = a_{j+1}^+ e^{ik_{z,j+1}z_{j+1}} + a_{j+1}^- e^{-ik_{z,j+1}z_{j+1}} \quad (1.56)$$

$$k_{z,j}(a_j^+ e^{ik_{z,j}z_{j+1}} - a_j^- e^{-ik_{z,j}z_{j+1}}) = k_{z,j+1}(a_{j+1}^+ e^{ik_{z,j+1}z_{j+1}} - a_{j+1}^- e^{-ik_{z,j+1}z_{j+1}}) \quad (1.57)$$

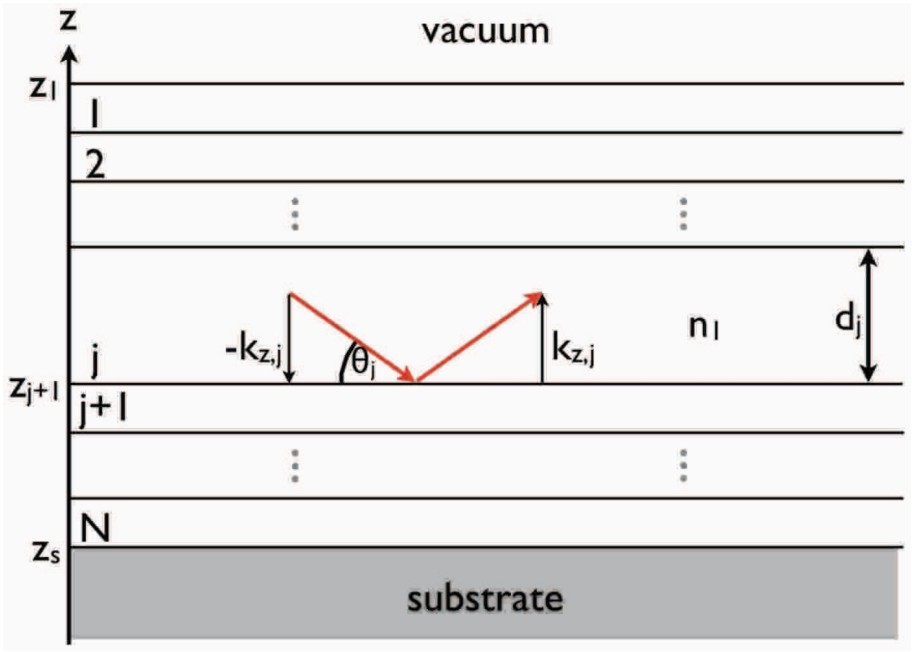

Figure 1.22: Representation of a stratified medium and the reflection geometry.

By combining these two equations, we can write the following matrices :

$$\begin{pmatrix} a_j^+ e^{ik_{z,j}z_{j+1}} \\ a_j^- e^{-ik_{z,j}z_{j+1}} \end{pmatrix} = \begin{pmatrix} p_{j,j+1} & m_{j,j+1} \\ m_{j,j+1} & p_{j,j+1} \end{pmatrix} \times \begin{pmatrix} a_{j+1}^+ e^{ik_{z,j+1}z_{j+1}} \\ a_{j+1}^- e^{-ik_{z,j+1}z_{j+1}} \end{pmatrix} \quad (1.58)$$

with $p_{j,j+1} = \frac{k_{z,j}+k_{z,j+1}}{2k_{z,j}}$ and $m_{j,j+1} = \frac{k_{z,j}-k_{z,j+1}}{2k_{z,j}}$. The matrix composed of $p_{j,j+1}$ and $m_{j,j+1}$ is called refraction matrix $\mathcal{R}_{j,j+1}$ and transforms the wave amplitudes from the medium j to the medium j+1. Furthermore there is a phase shift due to the thickness d_j of the layer and this can be presented in matrix form as well :

$$\begin{pmatrix} a_j^+ e^{ik_{z,j}z_j} \\ a_j^- e^{-ik_{z,j}z_j} \end{pmatrix} = \begin{pmatrix} e^{-ik_{z,j}d_j} & 0 \\ 0 & e^{ik_{z,j}d_j} \end{pmatrix} \times \begin{pmatrix} a_j^+ e^{ik_{z,j}z_{j+1}} \\ a_j^- e^{-ik_{z,j}z_{j+1}} \end{pmatrix} \quad (1.59)$$

The matrix composed of $e^{ik_{z,j}d_j}$ and $e^{-ik_{z,j}d_j}$ is called transition matrix $\mathcal{T}_j$. By combining the two matrices, it is possible to calculate the wave amplitude at the surface ($z = z_1$) out of the amplitude at the substrate interface ($z = z_s$) :

$$\begin{aligned} \begin{pmatrix} a_0^+ e^{ik_{z,0}z_1} \\ a_0^- e^{-ik_{z,0}z_1} \end{pmatrix} &= \mathcal{R}_{0,1}\mathcal{T}_1 ... \mathcal{T}_N \mathcal{R}_{N,s} \times \begin{pmatrix} a_s^+ e^{ik_{z,s}z_s} \\ a_s^- e^{-ik_{z,s}z_s} \end{pmatrix} \\ &= \begin{pmatrix} M_{11} & M_{12} \\ M_{21} & M_{22} \end{pmatrix} \times \begin{pmatrix} a_s^+ e^{ik_{z,s}z_s} \\ a_s^- e^{-ik_{z,s}z_s} \end{pmatrix} \end{aligned} \quad (1.60)$$

with the resulting matrix called the transfer matrix. The reflection coefficient is :

$$r = \frac{a_0^+ e^{ik_{z,0}z_1}}{a_0^- e^{-ik_{z,0}z_1}} = \frac{M_{11}a_s^+ e^{ik_{z,s}z_s} + M_{12}a_s^- e^{-ik_{z,s}z_s}}{M_{21}a_s^+ e^{ik_{z,s}z_s} + M_{22}a_s^- e^{-ik_{z,s}z_s}} \tag{1.61}$$

With a thick one side roughened substrate (>0.1 mm), there is no reflection from the backside of the substrate, and we can assume :

$$a_s^+ e^{ik_{z,s}z_s} = 0 \tag{1.62}$$

and the reflectivity is :

$$R = |r|^2 = \left|\frac{M_{12}}{M_{22}}\right|^2 \tag{1.63}$$

In Figure 1.23 are shown the reflectivity curves and the SLD profiles of one multilayer film fully protonated, which can be considered as one layer on a substrate, and of one multlilayer film composed of a sequence of deuterated and protonated layers, which can be considered as a stratified film. Kiessig fringes and Bragg peaks can be observed, coming from the interference minima due to the layered structure.

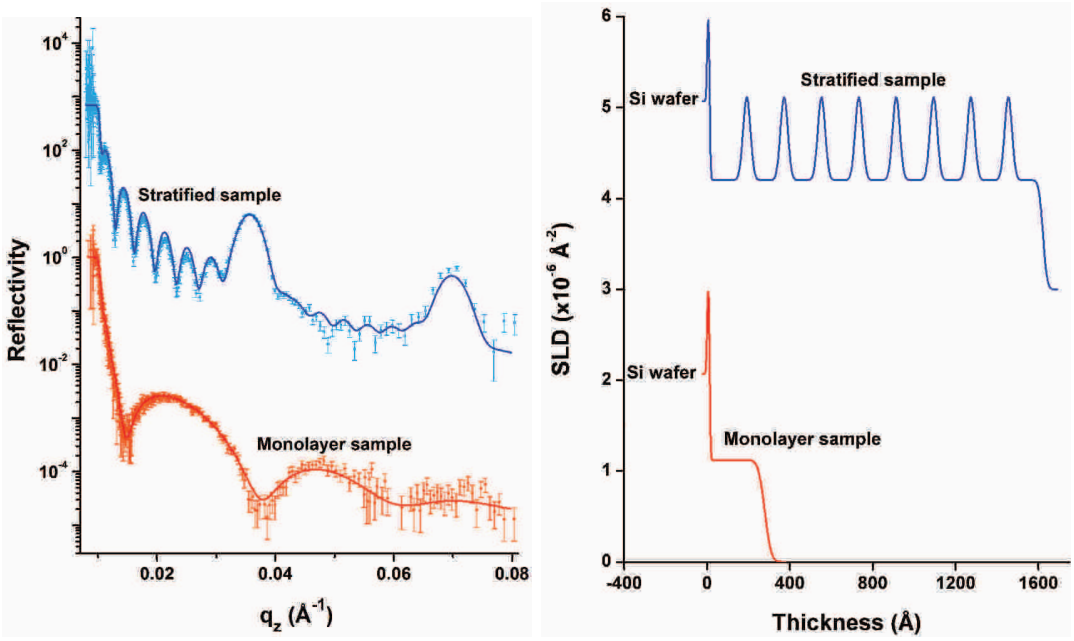

Figure 1.23: Neutron reflectivity curves (left) of a fully protonated (PSS-PAH) multilayer film (monolayer sample) and a (PSS-PAH) film with deuterated layers every six layer pairs (stratified sample). On the right, the SLD profiles corresponding to the fits. The curves are shifted for clarity.

For now, we have assumed perfectly sharp interfaces. But in real samples, this is, of course, not the case and we have to assume rough or diffuse interfaces, as shown in Figure 1.24. In this case, for large momentum transfer ($q_z \gg q_c$), the reflectivity

from a graded interface is :

$$R(q_z) = R_F(q_z) \left| \int_0^\infty \frac{df}{dz} e^{iq_z z} dz \right|^2 \tag{1.64}$$

with the interfacial density function f(z), which is shown in Figure 1.24 (left).

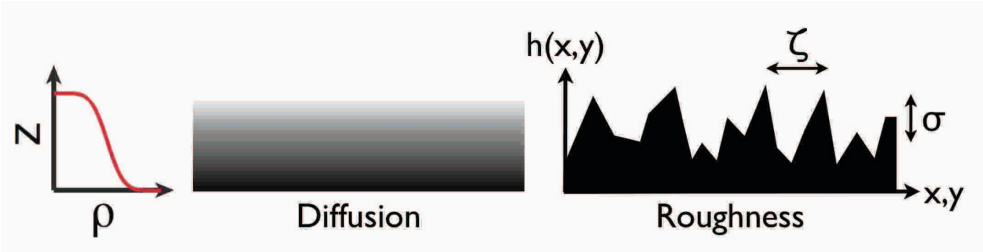

Figure 1.24: Diffuse (middle) and rough (right) interfaces. σ is the Gaussian width of the error function plotted on the left, h(x,y) the height function and ζ the lateral correlation length.

If we assume a Gaussian distribution between two phases, the interfacial density function is an error function erf(z) :

$$f(z) = erf\left(\frac{z}{\sqrt{2}\sigma}\right) \tag{1.65}$$

with σ the Gaussian width. The reflected intensity for a statistical interface is then :

$$R(q_z) = R_F(q_z) e^{-q_z^2 \sigma^2} \tag{1.66}$$

It causes a sharp decrease of the reflectivity. The equation above is valid only if the lateral correlation length ζ is much larger than the corresponding coherence length of the impinging wave, that is the maximal distance within the beam with a well-defined phase relation. For ζ much smaller than the correlation length, the roughness leads to a slightly different reflectivity :

$$R(q_z) = R_F(q_z) e^{-q_z q_{z'} \sigma^2} \tag{1.67}$$

Off-specular reflectivity

We considered above the reflectivity in specular conditions, i.e. when the incident and reflected angles are the same, so when the momentum transfer is normal to the surface. This is valid if no density correlations parallel to the surface are present, but if we consider a rough interface as shown in Figure 1.24 on the right, there are lateral correlations on some length scale ζ. So, there is some non-vanishing signal in the off-specular directions, which is also called diffuse scattering. In this case, the differential cross section is :

$$\frac{d\sigma}{d\Omega} = \left(\frac{\Delta N_b}{q_z}\right)^2 \int_S \int_S' e^{iq_z[h(x,y)-h(x',y')]} e^{iq_x(x-x')} e^{iq_y(y-y')} dx dx' dy dy' \tag{1.68}$$

with ΔN_b the difference of SLD between two adjacent layers and h(x,y) the height function. By assuming that the height function is symmetric and depends only on the distance (x-x',y-y') between two points on the surface, the equation can be simplified :

$$\frac{d\sigma}{d\Omega} = \left(\frac{\Delta N_b}{q_z}\right)^2 \frac{A}{\sin\theta} \int_S < e^{iq_z[h(0,0)-h(x,y)]} > e^{i(q_x x + q_y y)} dxdy \tag{1.69}$$

with A the illuminated area of the sample surface and the angular brackets denote an ensemble average. If we assume that the statistics of the height variations are Gaussian :

$$\frac{d\sigma}{d\Omega} = \left(\frac{\Delta N_b}{q_z}\right)^2 \frac{A}{\sin\theta} \int_S e^{-q_z^2 < [h(0,0)-h(x,y)]^2 > /2} e^{i(q_x x + q_y y)} dxdy \tag{1.70}$$

$< [h(0,0) - h(x,y)]^2 >$ can be written as :

$$\begin{aligned} < [h(0,0) - h(x,y)]^2 > &= 2 < h^2 > -2 < h(0,0) - h(x,y) > \\ &= 2\sigma^2 - 2C(x,y) \end{aligned} \tag{1.71}$$

with C(x,y) the height-height correlation function. So, the scattering cross section can be divided into two parts, the specular and the diffuse part :

$$\begin{aligned} \frac{d\sigma}{d\Omega} &= \left(\frac{d\sigma}{d\Omega}\right)_{spec} \times \left(\frac{d\sigma}{d\Omega}\right)_{diff} \\ &= \left(\frac{\Delta N_b}{q_z}\right)^2 \frac{A}{\sin\theta} e^{-q_z^2\sigma^2} \times \int_S e^{q_z^2 C(x,y)} e^{i(q_x x + q_y y)} dxdy \end{aligned} \tag{1.72}$$

1.2.3.2 Grazing Incidence Small Angle Neutron Scattering

To investigate samples in the direction parallel to the surface, Grazing Incidence Small Angle Neutron Scattering (GISANS) is used [9]. GISANS is performed with the same geometry as reflectometry with a shallow incident angle $\theta_i < 1°$, and a 2D detector is used to measure the whole scattering pattern as a function of the angles θ_f and θ_{in}, as shown in Figure 1.25.

The surface sensitivity in this kind of measurements is given by the penetration depth of the incident beam into the sample. The z-projection of the transmitted wave t(z) is given by :

$$t(z) = a_j^- e^{-ikz\sqrt{\theta_i^2 - \theta_c^2 - i\frac{\lambda}{2\pi}\mu}} \tag{1.73}$$

The intensity of the transmitted wave is equal to :

$$T(z) = |t(z)|^2 = |a_j^-|^2 e^{-ikz\frac{1}{\sqrt{2}}\sqrt{\sqrt{(\theta_i^2-\theta_c^2)^2 + (\frac{\lambda}{2\pi}\mu)^2} - (\theta_i^2 - \theta_c^2)}} \tag{1.74}$$

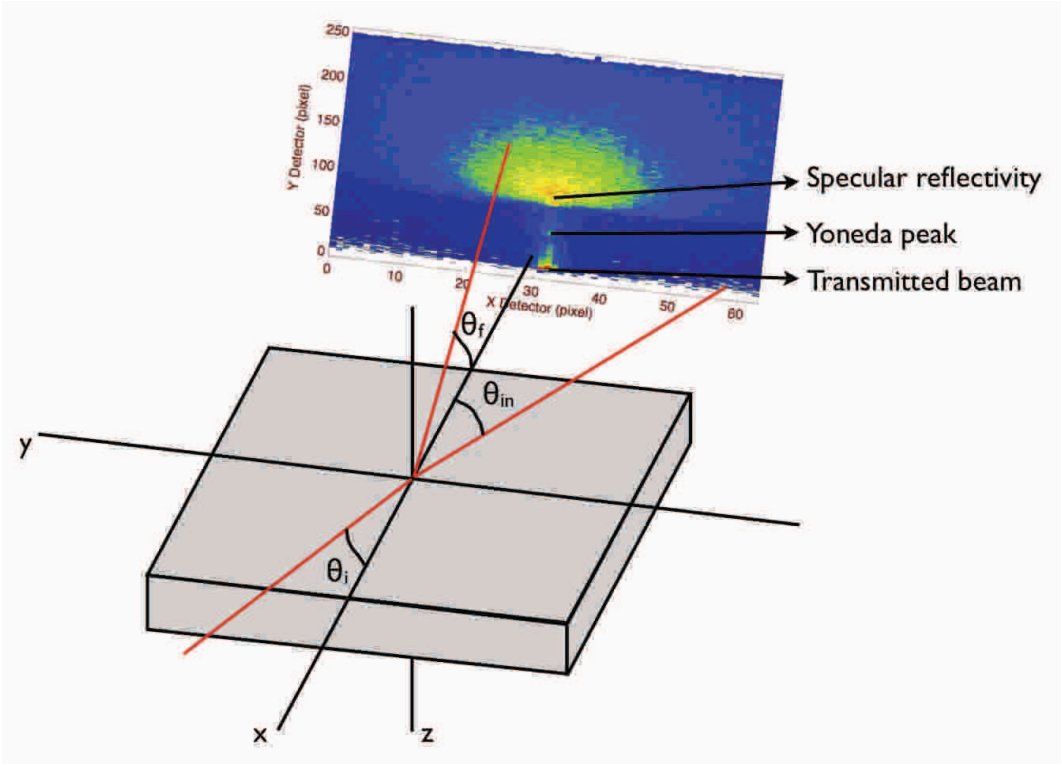

Figure 1.25: Grazing incidence scattering set-up. θ_i is the incidence ange, θ_f the outgoing angle and θ_{in} the in-plane angle.

We can identify the penetration depth in z-direction $z_{1/e}$ as :

$$z_{1/e} = \frac{\sqrt{2}\lambda}{4\pi}\sqrt{\sqrt{(\theta_i^2-\theta_c^2)^2+(\frac{\lambda}{2\pi}\mu)^2}-(\theta_i^2-\theta_c^2)} \tag{1.75}$$

The momentum transfers for a monochromatic incident wave of wavelength λ are given by :

$$q_x = \frac{2\pi}{\lambda}(\cos\theta_f\cos\theta_{in}-\cos\theta_i) \tag{1.76}$$

$$q_y = \frac{2\pi}{\lambda}(\cos\theta_f\cos\theta_{in}) \tag{1.77}$$

$$q_z = \frac{2\pi}{\lambda}(\sin\theta_i+\sin\theta_f) \tag{1.78}$$

For typical incident and outgoing angles in the order of one degree and wavelengths of several Ångströms, the observable structure in the y-direction and in the z-direction are between 1 nm to 1,000 nm. The form factor $F(q_xy)$ for a simple object located on a solid support can be calculated by :

$$F(q_{xy}) = F(q_{xy},q_z)+R(\alpha_i)F(q_{xy},p_z)+R(\alpha_f)F(q_{xy},-p_z) \tag{1.79}$$

$$+R(\alpha_i)R(\alpha_i)F(q_{xy},-q_z) \tag{1.80}$$

with $p_z = (\overrightarrow{k_i} + \overrightarrow{k_f})_z$, $q_{xy} = (q_x^2 + q_y^2)^{1/2}$ and the Fresnel reflection coefficients of the substrate $R(\alpha_i)$ and $R(\alpha_f)$. The differential cross section for diffuse scattering can be approximated for small roughnesses ($\sigma q_z \ll 1$) by the effective surface approach :

$$\left(\frac{d\sigma}{d\Omega}\right)_{diff} = \frac{A\pi^2}{\lambda^4}(1-n^2)^2|T_i|^2|T_f|^2 P(\overrightarrow{q}) \tag{1.81}$$

with A the illuminated surface area, T_i and T_f the Fresnel transmission functions and $P(\overrightarrow{q})$ the diffuse scattering factor, which contains the morphological information.

1.2.4 Neutron scattering and multilayer films

Neutron scattering measurements are of great interest for the study of polymers, due to the possibility to exchange hydrogen by deuterium in the polymers, which allows to study the internal structure of polymer films without changing their structure or chemistry.

Especially, the multilayer films of polyelectrolytes assembled by the Layer-by-Layer process are suitable for measurements of the structure perpendicular to the surface by neutron reflectometry, due to their stratified structure. Indeed, by using deuterated polyelectrolytes inside specific layers, it is possible to observe the alternation of the layers and to determine their structural properties, that is their thicknesses, SLDs and roughnesses (composed of the roughness and the interpenetration of the polyelectrolytes into the neighbouring layers). Several neutron reflectometry measurements were already performed on different multilayer films to study their structure and the effect of different parameters by analysing the specular reflectivity. The first neutron reflectometry measurements were performed by J. Schmitt *et al.* in 1993 [4] on films composed of PSS and PAH, and this study allowed them to demonstrate that the films prepared with the Layer-by-Layer process are stratified as assumed and are not composed of a mixture of the polyelectrolytes deposited. They have also shown that it is not possible to differentiate the PSS and PAH layers by neutron scattering, due to the interpenetration of the polyelectrolytes. Since then, various studies were carried out using neutron reflectometry on multilayer films with different compositions. Two kinds of studies were particularly interesting : the study of the influence of the build-up conditions and the influence of external stimuli on the deposited films. For example, M. Kolasinska *et al.* [69] studied the difference of structure of (PSS-PAH) films when prepared by dipping and by spraying, as well as the effect of the pH of the polyelectrolyte solutions. They also observed the difference of swelling when measuring the films at different humidity between the sprayed and dipped films. To give other examples, studies were also performed on the effect on (PSS-PAH) films of the polyelectrolyte solutions buffer [72], of the temperature of the solutions during the preparation of the films [78], of the salt concentration of the polyelectrolyte solutions [73] or of the dipping time [151]. Studies of the response

of multilayer films to the change of the external conditions were also carried out, like the effect of the increase of temperature on the structure of films composed of PSS and different polycations [152, 153] or the swelling of films depending on the humidity or in solutions [76, 119]. H. W. Jomaa *et al.* [5] studied for example the influence of the dipping of (PSS-PDADMAC) films into salt solutions (annealing) to observe the change of the structure with the time of annealing. Whereas the thickness of the films is slightly different, it was observed that the intensity of the Bragg peaks, present on the reflectivity curve of the film before the annealing due to the sequence of deuterated and non-deuterated layers, decreases with the time of annealing. This indicated an increase of the interpenetration of the polyelectrolytes into the neighbouring layers and so a reorganization of the polyelectrolytes in the films and a change of conformation of the chains.

No GISANS measurements on multilayer films assembled with the Layer-by-Layer process were performed until now to study the structure parallel to the surface. The most common studies performed on polymer films were studies of the general structure in the direction parallel to the surface, like the periodicity of patterns, the spacing between domains, for different materials, for example homopolymers [154] or diblock [155, 156] and triblock [157] copolymer films. The only study of the conformation of a polymer chain in a single film we found was reported by J. Kraus *et al.* [158]. They showed that it is possible to determine the radius of gyration in the direction parallel to the surface of a polystyrene chain in a polystyrene film of 300 nm thickness by performing GISANS measurements. So, it is possible to determine the conformation of a polymer, or a polyelectrolyte chain, in a multilayer film by combining GISANS (in-plane information) and neutron reflectometry, which allows to determine an average size of the polyelectrolyte chains in the direction perpendicular to the surface for multilayer films with a sequence of deuterated and protonated layers.

Chapter 2

Materials and methods

2.1 Materials

All products were used as received unless stated otherwise.

2.1.1 Polyelectrolytes

The chemical structures of the polyelectrolytes used for the build-up of the studied multilayer films are shown in Figure 2.1.

The following polyelectrolytes were purchased from Sigma-Aldrich (Saint-Louis, USA) : non-deuterated poly(styrene sulfonate) sodium salt (PSS_{h7}, M_w = 70,000 g/mol) and poly(allylamine hydrochloride) (PAH, M_w = 56,000 g/mol and M_w = 58,000 g/mol).

Deuterated poly(styrene sulfonate) sodium salt (PSS_{d7}, M_w = 80,800g/mol - PdI $\leq$ 1.20 and M_w = 78,300g/mol - PdI $\leq$ 1.20) was purchased from Polymer Standard Service (Mainz, Germany).

Branched poly(ethyleneimine) (PEI, Lupasol HF, M_w = 21,000 g/mol) was purchased from BASF (Ludwigshafen am Rhein, Germany).

PSS_{h7}, PSS_{d7} are polyanions and PEI, PAH are polycations.

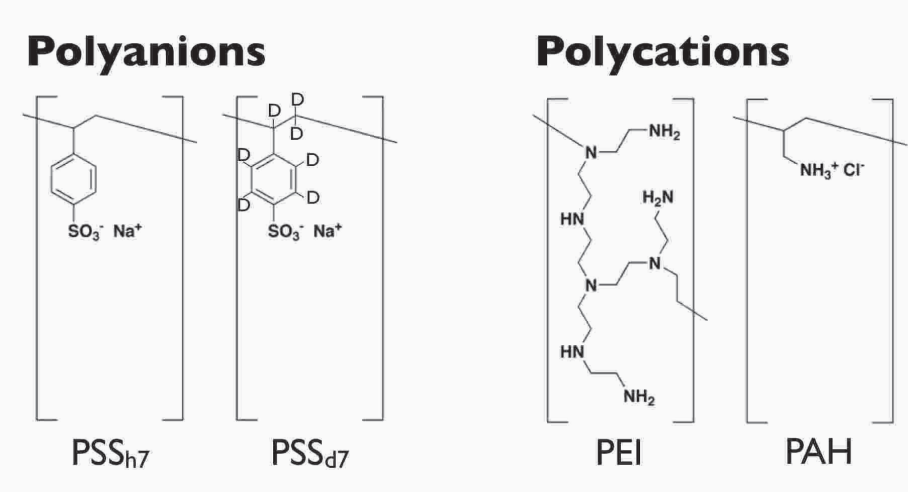

Figure 2.1: Chemical structures of the polyelectrolytes used for the build-up of LbL films.

2.1.2 Chemicals

Potassium chloride (KCl, $\geq 99\%$ pure) was purchased from Sigma-Aldrich (Saint-Louis, USA).

Sodium chloride (NaCl, $\geq 99.9\%$ pure) was purchased from Carl Roth GmbH (Karlsruhe, Germany).

The solutions and buffers were prepared with ultrapure water, MilliQ water (Milli-Q system, Millipore), with a resistivity of at least 18.2 MΩ.cm.

2.1.3 Substrates

Substrates used for the deposition of the multilayer films were silicon wafers with an orientation (100) and a thickness of 700-775 μm. They were purchased from Wafernet Inc. (San Jose, USA).

Before the deposition of the films, all silicon wafers were rinsed with ethanol and MilliQ water, followed by a drying step under compressed air. Then, they were treated with plasma in a plasma cleaner (PDC-002, Harrick Plasma, Ithaca, USA) for 3 min, to activate the surface. The activated wafers were used within hours.

2.2 Polyelectrolyte multilayer film build-up

All the films were deposited on silicon wafers activated by plasma, with a first PEI layer adsorbed on the surface by dipping the substrate into a 1 mg/mL (3 x 10^{-3} monomol/L) PEI solution for 15 min, followed by three rinsing steps of 2 min into pure MilliQ water, and dried under compressed air after the rinsing. Monomol corresponds to moles of the monomer repeat unit.

The films were prepared from solutions of 0.6 mg/mL (3 x 10^{-3} monomol/L) PSS_{h7} or PSS_{d7} and 0.27 mg/mL (3 x 10^{-3} monomol/L) PAH dissolved in MilliQ water containing 0.5 M NaCl, 2 M NaCl or 2 M KCl.

The films were deposited on the substrates by dipping, spraying or using the spin-assisted LbL assembly, as described below.

2.2.1 Deposition by dipping

The films prepared by dipping were deposited either by manual dipping, for the growth studies, or automated robot dipping, for neutron scattering studies.

The manual dipping process was the same for all samples. The silicon wafers covered with a PEI layer were immersed into the polyelectrolyte solutions for 15 min, followed by three rinsing steps of 2 min into pure MilliQ water. Every layer was dried under compressed air after the rinsing, to perform ellipsometry measurements.

Films build-up with the dipping robot (picture of the robot in Figure 2.2) were prepared by immersion of the substrates in the polyelectrolyte solutions for 12 min, with a lifting up of the samples out of the solutions every two minutes immediately followed by an immersion into the same solutions. This was done to induce a slight mixing of the solutions in order to improve the adsorption of the polyelectrolytes on the surface. The dipping in the polyelectrolyte solutions was followed by three rinsing steps of 2 min into pure MilliQ water. After one minute of dipping, a lifting up and down was also done for each rinsing step, to have a better rinsing. The samples were dried under compressed air every layer pair (after the polycation deposition) with an automated drying tool included on the robot.

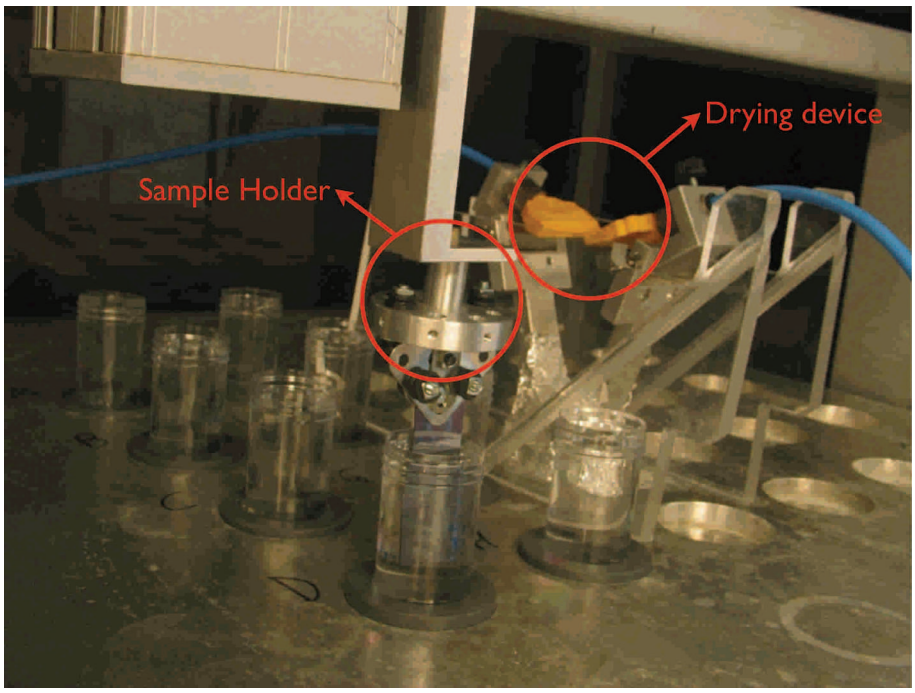

Figure 2.2: Picture of the dipping robot used for the automated dipping.

2.2.2 Deposition by spraying

The films prepared by spraying deposition were built-up by three different methods : the manual spray with Air-boy cans, the automated spray with Aztek airbrushes and the automated spray with a grazing incidence angle using stainless steel nozzles. The three methods are used by our team, the Air-boy cans and the Aztek airbrushes are used for spraying perpendicular to the surface, and the stainless teel nozzles are used for spraying at a grazing incidence angle with the surface, for orientation and alignment of nanoparticles like nanowires.

Air-boy cans were purchased from Carl Roth GmbH (Karlsruhe, Germany) and consist of containers with a manual pump to induce a pressure inside the solution chamber, allowing the spraying of the solutions. The nozzle has an internal diameter of 0.4 mm. Four different cans were used : one for the non-deuterated polyanions, one for the deuterated polyanions, one for the polycations and one for the water used to rinse the samples. A picture of an Air-boy can is shown in Figure 2.3.

The film deposition was performed at a distance of roughly 10 cm. Solutions were sprayed for 5 s, followed by a waiting time of 15 s. Then, the surfaces were rinsed with pure MilliQ water sprayed for 5 s, also followed by a waiting time of 15 s. The samples were dried under compressed air either every layer for ellipsometry measurements (thickness evolution studies) or at the end of the build-up of the films (neutron scattering measurements). As the pressure inside the cans was decreasing during the spraying, the cans were pumped every 2-3 spraying steps to keep a rather similar pressure during the whole build-up.

Figure 2.3: Picture of an Air-boy can.

Aztek airbrushes (model A4809) were purchased from Kit Discount (Roquebrune-sur-Argens, France) and are composed of a solution inlet, a gas inlet and different nozzles with different internal diameters. The solutions were injected with pumps, and the gas and solution flux were controlled. Three different pumps and airbrushes were used for the polyanions, the polycations and the rinsing water. Figure 2.4 shows an Aztek airbrush.

The solutions were sprayed at a flux of 15 mL/min with a gas flux of 10 L/min or 20 L/min perpendicularly on a vertical substrate. The gas used was compressed air and the spray was done at a distance of roughly 10 cm. The nozzle had a internal diameter of 0.3 mm. The spraying was done in the same conditions than the spray with Airboy cans : 5 s of spraying of the solutions followed by a waiting time of 15 s, then a rinsing step of 5 s with 15 s of waiting. The samples were dried under compressed air either every layer for ellipsometry measurements (thickness evolution studies), or at the end of the film build-up (neutron scattering measurements).

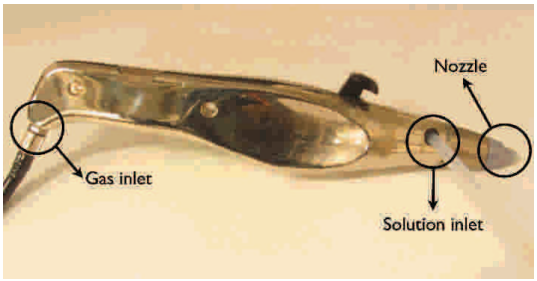

Figure 2.4: Picture of an Aztek airbrush.

Stainless steel nozzles (model 1/4J-316S+SU26-316SS) were purchased from Spraying Systems Co. (Wheaton, USA) and consist of a solution inlet, a gas inlet and a nozzle with a fixed internal diameter. The solutions were injected with pumps, and the gas and solution flux were controlled, with the same device as for the Aztek airbrushes. Three different pumps and airbrushes were used for the polyan-

ions, the polycations and the rinsing water. A picture of a stainless steel nozzle is shown in Figure 2.5

The solutions were sprayed at a flux of 5 mL/min, with a gas compressed air flux of 30 L/min on a vertical subtrate. The polyanion solution was sprayed at a distance of 2 cm with an angle of 15° between the surface of the samples and the spraying direction. The polycation solutions and the MilliQ water for the rinsing were sprayed at a distance of roughly 10 cm perpendicularly to the surface. The spraying was done as followed : 20 s of spraying of the solutions followed by a waiting time of 15 s, then a rinsing step of 20 s with 15 s of waiting. The samples were dried under compressed air either every layer for ellipsometry measurements (thickness evolution studies) or at the end of the build-up of the films (neutron scattering measurements).

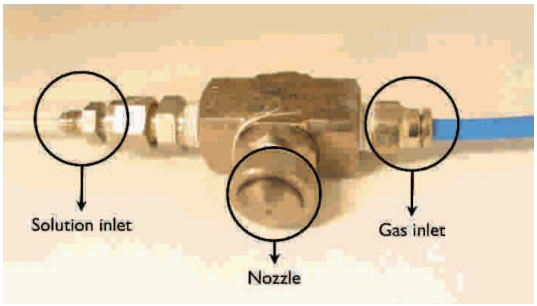

Figure 2.5: Picture of a stainless steel nozzle.

2.2.3 Deposition by using the spin-assisted LbL assembly

The spin-assisted LbL assembly was performed on a spin-coater WS-650-8B (picture in Figure 2.6) purchased from Laurell Technologie Corporation (North Wales, USA). The spin-assisted LbL assembly was carried out at a rotation speed of 4,000 rpm (rotation per minute) or 8,000 rpm. The films were built-up by depositing ten drops of the solutions with a pipette on the rotating substrates, immediately followed by a rinsing step with 1 mL of pure MilliQ water. Before the deposition of a new layer, the samples were left rotating until the removal of the solvent.

Figure 2.6: Picture of the spin-coater used for the films build-up by using the spin-assisted LbL assembly.

2.3 Instrumentation

2.3.1 Neutron scattering

Neutron scattering experiments (reflectometry and GISANS) were performed at several neutron institutions : the Institut Laue-Langevin (ILL) [159], Grenoble, France and the Forschungs-Neutronenquelle Heinz Maier-Leibnitz (FRMII) [160], Garching, Germany, which are neutron reactor sources.

The instruments used are described below and the setups are summarized in Table 2.1.

Setup reflectometry	Angle (degree)	Collimation slits (mm)	Wavelength (Å)	Angular resolution	Wavelength resolution
D17-1	0.7	0.4 / 0.7	2 - 27	$d\theta/\theta$ = 0.78%	Variable
	3.8	1.6 / 0.8			
D17-2	0.7	0.4 / 0.2	2 - 27	$d\theta/\theta$ = 0.78%	Variable
	2.8	1.6 / 0.8			
FIGARO-1	0.624	0.216 / 0.216	2 - 20	$d\theta/\theta$ = 0.9%	$d\lambda/\lambda$ = 0.82%
	2	0.7 / 0.216			
FIGARO-2	0.622	0.216 / 0.216	2 - 20	$d\theta/\theta$ = 0.9%	$d\lambda/\lambda$ = 0.82%
	2	0.7 / 0.216			
N-REX+	0.1 - 2.5	1	4.3	$\Delta\theta$ = 0.029°	$d\lambda/\lambda$ = 3%
SuperADAM	0 - 5	3	4.4	$\Delta\theta$ = 0.01°	$d\lambda/\lambda$ = 0.6%

Setup GISANS	Angle (degree)	Collimation slits (mm)	Wavelength (Å)	Sample-to-detector distance (mm)	Angular resolution	Wavelength resolution	Detector resolution
FIGARO-3	1	6.667 / 3.333	2 - 20	2831	$\Delta\theta_y$ = 0.118° $\Delta\theta_z$ = 0.134°	$d\lambda/\lambda$ = 7%	2 x 4.7 mm^2 (z x y)

Table 2.1: Setups used for the neutron reflectometry and GISANS measurements.

2.3.1.1 D17

D17 [22, 161], located at ILL, uses neutron reflection with a vertical sample surface geometry designed to study the surface structures at solid and solid/liquid interfaces. In time-of-flight mode it can access a wavelength range from 2 Å to 27 Å. A high flux of 9.6 x 10^9 n/s/cm^2 and a low background allow to measure reflectivities down to 10^{-7}. The wide angle multidetector, with a size of 30 x 48 cm^2, allows the simultaneous measurement of background and off-specular scattering, spanning from 4° at sample-detector distance of 3.1 m to 13° at 1.1 m. The detector resolution is 2.2 x 4.8 mm^2 and the detector allows specular and off-specular reflectivity measurements. Figure 2.3.1.1 shows a schematic drawing of the reflectometer.

We performed neutron reflectometry on D17, with the setups D17-1 and D17-2.

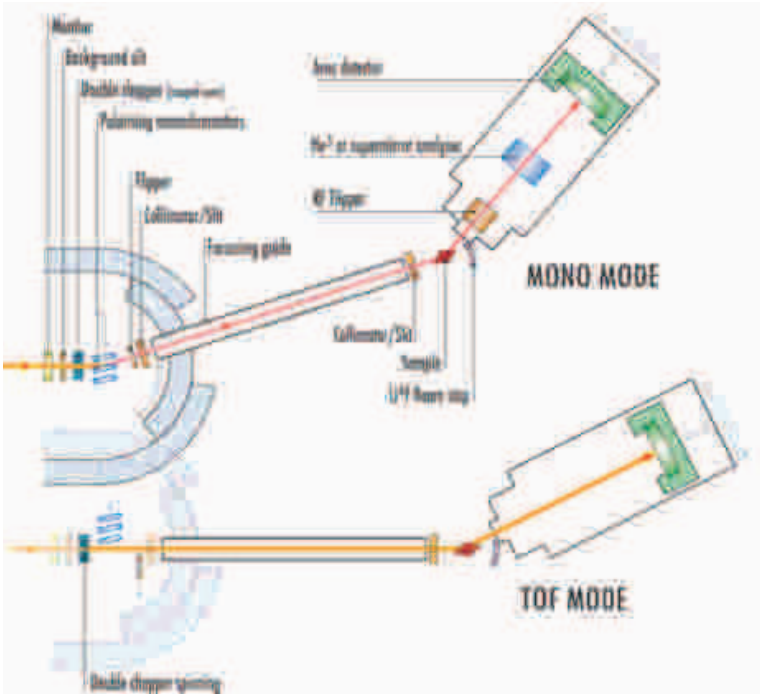

Figure 2.7: Schematic layout of the D17 reflectometer. Reproduced from reference [22].

2.3.1.2 FIGARO

FIGARO [23,162] (Fluid Interfaces Grazing Angles ReflectOmter) is located at ILL and designed for the study of horizontal surfaces like liquid/air or liquid/liquid interfaces. It is a time-of-flight reflectometer and can access a wavelength band between 2 Å and 30 Å, and incoming angles between 0.62° and 3.8°(for free liquid surfaces), which allows to achieve a q-range from 0.0045 $Å^{-1}$ to 0.42 $Å^{-1}$. A two dimensional multitube detector allows the measurement of specular and off-specular reflectivity, as well as the carrying out of GISANS measurements. The detector has a size of 30 x 48 cm^2 and a resolution of 2.2 x 4.8 mm^2. Figure 2.3.1.2 shows a schematic drawing of the reflectometer.

We used Figaro to perform neutron reflectometry and GISANS measurements, with the setups FIGARO-1, FIGARO-2 and FIGARO-3.

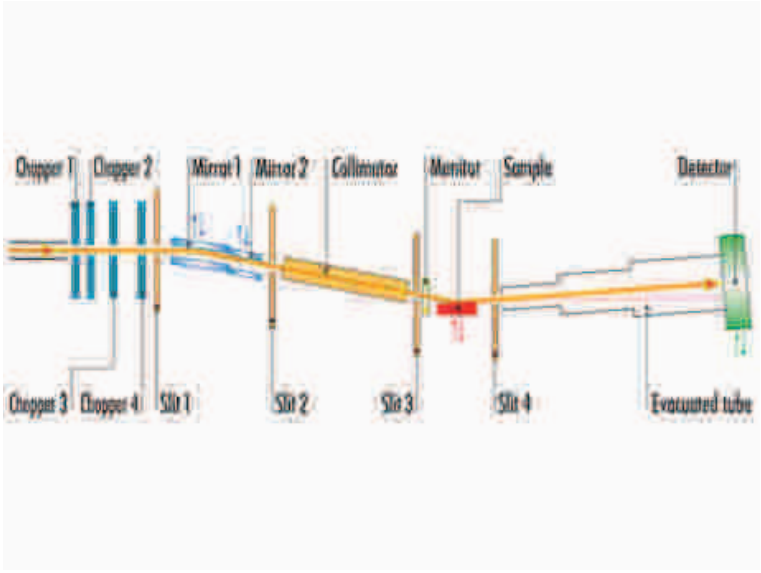

Figure 2.8: Schematic layout of the FIGARO reflectometer. Reprinted from reference [23].

2.3.1.3 N-REX+

N-REX+ [24] (Neutron reflectometer with X-ray option) is an angle dispersive fixed wavelength (4.4 Å) reflectometer located at FRMII with an horizontal sample surface geometry. It is optimized for structural and magnetic properties characterization of surfaces, interfaces and thin films. Neutrons are detected with a 20 x 20 cm^2 position sensitive or a pencil detector, with a lateral resolution of 3 mm. Specular and off-specular reflectivity are measured on this instrument. Figure 2.3.1.3 shows a schematic drawing of the reflectometer.

We carried out neutron reflectometry on N-REX+, with the setup N-REX+.

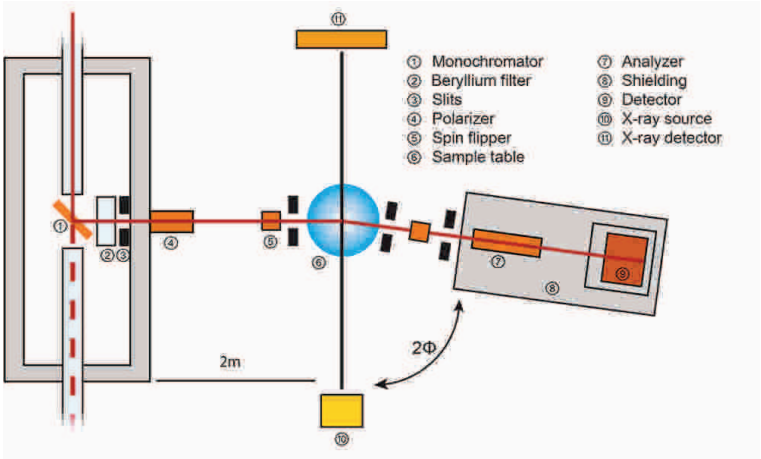

Figure 2.9: Schematic layout of the N-REX+ reflectometer. Reprinted from reference [24].

2.3.1.4 SuperADAM

SuperADAM [25, 163] (Advanced Reflectometer for the Analysis of Materials) is an angle dispersive reflectometer at a fixed wavelength of 4.4 Å with a vertical sample surface geometry, located at ILL. It can access scattering angles up to 85° which correspond to q values up to 2.1 $Å^{-1}$, useful to probe small length scales. The flexibility of the instrument permits the variation of the sample-detector and sample-monochromator distances in order to accomodate the specific requirements for incident and outgoing resolutions. The two dimensional position sensitive detector has an active area of 30 x 30 cm^2 and a resolution of 2.8 mm, and allows specular and off-specular reflectivity measurements. Figure 2.3.1.4 shows a schematic drawing of the reflectometer.

We performed neutron reflectometry on SuperADAM, with the setup SuperADAM.

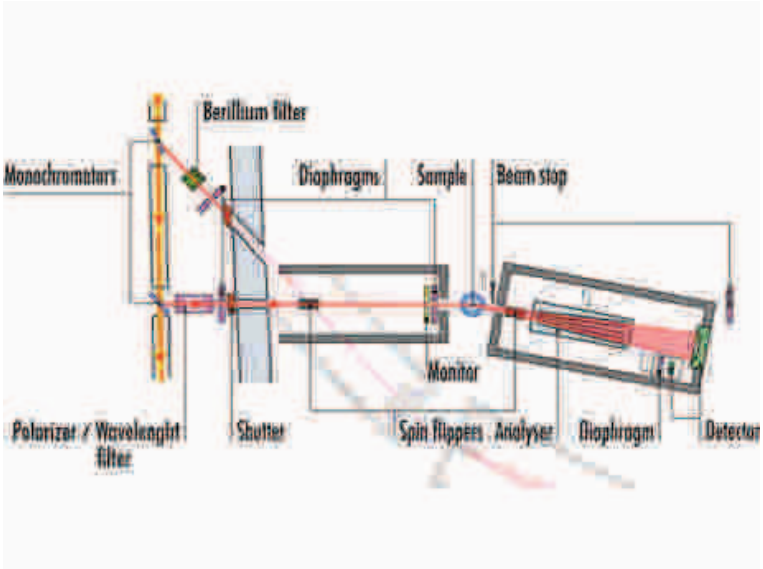

Figure 2.10: Schematic layout of the SuperADAM reflectometer. Reprinted from reference [25].

2.3.2 Ellipsometry

Ellipsometry is a non-destructive technique measuring the changes in the polarization of light after reflection on a surface and used to analyse and characterize thin films. This technique allows especially the determination of the thickness and refractive index of layers.

Principle [164]

The most common polarization of light is the elliptical polarization. Light is elliptically polarized when the electric field describes an elliptic trajectory in a plane perpendicular to the direction of propagation, as shown in Figure 2.11. It is characterized by the two angles ψ and Δ.

For monochromatic light wave travelling along the positive direction of the z axis of a Cartesian right-handed coordinate system (the z axis points to the reader in Figure 2.11), the electric vector is perpendicular to z and the components in x and y directions are given by :

$$E_x = X\cos(-\omega t + \delta_x) \tag{2.1}$$
$$E_y = Y\cos(-\omega t + \delta_y) \tag{2.2}$$

with ω the angular frequency, X and Y the amplitudes of the components in x and y directions, δ_x and δ_y the absolute phases in x and y directions at the initial time t = 0.

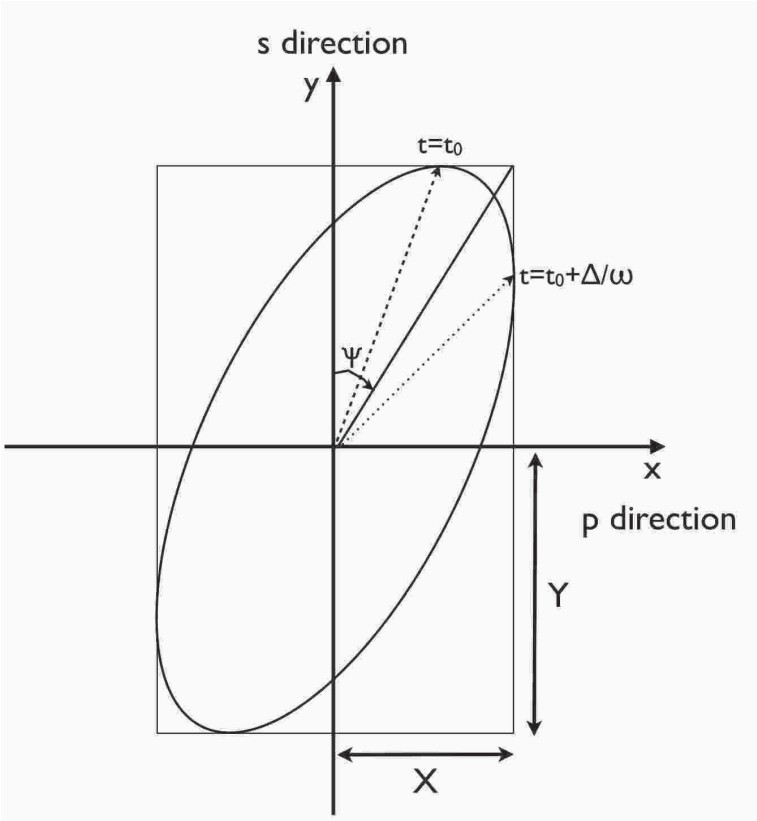

Figure 2.11: Elliptical polarization and parameters.

The ratio between the amplitudes of the electric field in the x direction (p direction) and the y direction (s direction), named respectively X and Y, is given by the following equation :

$$\tan\psi_{xy} = \frac{X}{Y} \qquad \psi \in \left(0, \frac{\pi}{2}\right) \tag{2.3}$$

At the initial time $t = t_0$, the electric field in the y direction is maximal (dashed arrow in Figure 2.11) and the electric field in the x direction is maximal at $t = t_0$

+ Δ/ω (dotted arrow). The phase shift Δ is defined by :

$$\Delta_{xy} = \delta_x - \delta_y \qquad \Delta \in (-\pi, \pi) \tag{2.4}$$

Let us consider the incidence of a monochromatic optical plane wave on a planar interface between two semi-infinite media with an incident angle of φ_1. The two media have two different complex refractive index N_1 and N_2. As shown in Figure 2.12, the light beam can be reflected with an angle φ_1 or transmitted with an angle φ_2.

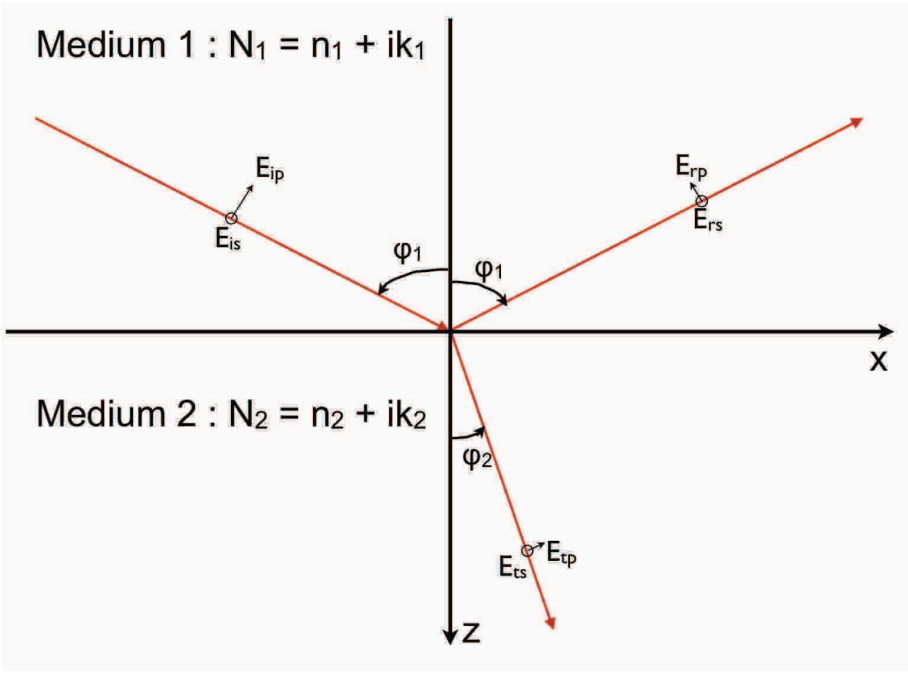

Figure 2.12: Interaction of a monochromatic electromagnetic wave with a planar interface between two media. E_i, E_r and E_t correspond to the components of the electric field vectors of the incident, reflected and transmitted light respectively.

The reflection coefficients in s and p directions are defined by the Fresnel equations :

$$r_s = \frac{E_{rs}}{E_{is}} = \frac{N_1 \cos\varphi_1 - N_2 \cos\varphi_2}{N_1 \cos\varphi_1 + N_2 \cos\varphi_2} \tag{2.5}$$

$$r_p = \frac{E_{rp}}{E_{ip}} = \frac{N_1 \cos\varphi_2 - N_2 \cos\varphi_1}{N_1 \cos\varphi_2 + N_2 \cos\varphi_1} \tag{2.6}$$

With the Snell-Descartes law ($N_1 \sin\varphi_1 = N_2 \sin\varphi_2$), we obtain the following

equations, which depend only on φ_1, N_1 and N_2 :

$$\begin{aligned} r_s &= \frac{\sin(\varphi_2 - \varphi_1)}{\sin(\varphi_2 + \varphi_1)} = \frac{N_1 \cos\varphi_1 - \sqrt{N_2^2 - N_1^2 \cos^2\varphi_1}}{N_1 \cos\varphi_1 + \sqrt{N_2^2 - N_1^2 \cos^2\varphi_1}} \\ &= \tan\psi_s e^{i\Delta_s} \end{aligned} \tag{2.7}$$

$$\begin{aligned} r_p &= \frac{\tan(\varphi_2 - \varphi_1)}{\tan(\varphi_2 + \varphi_1)} = \frac{N_1/\cos\varphi_1 - N_2/\sqrt{1 - (N_1/N_2)^2 \sin^2\varphi_1}}{N_1/\cos\varphi_1 + N_2/\sqrt{1 - (N_1/N_2)^2 \sin^2\varphi_1}} \\ &= \tan\psi_p e^{i\Delta_p} \end{aligned} \tag{2.8}$$

The multilayer films of polyelectrolytes correspond to a substrate-film-air system, with a homogeneous layer of thickness d_1 and refractive index N_1 placed between two semi-infinite media, the air with a refractive index n_a and the substrate with a refractive index N_0, as represented in Figure 2.13. In this case, the reflection coefficient is :

$$r = \frac{r_{12} + r_{10} e^{i2\theta}}{1 + r_{21} r_{10} e^{i2\theta}} \tag{2.9}$$

with θ the phase shift of multiple reflected waves given by :

$$\theta = \frac{2\pi}{\lambda} d_1 N_1 \cos\varphi_1 = \frac{2\pi}{\lambda} d_1 N_1 \sqrt{1 - \left(\frac{n_a \sin\varphi_2}{N_1}\right)^2}$$

During measurements by ellipsometry, the reflected/incident angle φ is known, as well as the refractive index of air, n_a, and the wavelength of the light beam. So the phase shift θ is only dependent on the thickness d_1 and the refractive index N_1 of the film.

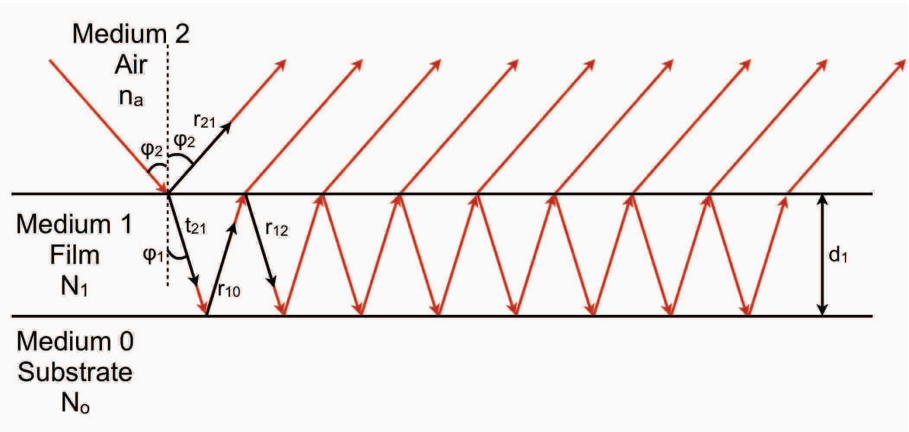

Figure 2.13: Interaction of an electromagnetic wave with a substrate-film-air system.

Ellipsometers

Two ellipsometers were used for our studies, a monochromatic ellipsometer (SD

2300, Plasmos) and a spectrometric ellipsometer (SENpro, SENTECH Instrument GmbH). The multilayer films of polyelectrolytes were considered as one layer for the ellipsometry measurements, as the refractive indexes of the polyelectrolytes used were similar. So, the thicknesses measured are the total thicknesses of the films deposited.

The monowavelength ellipsometer operated at a laser wavelength of 632.8 nm and a fixed angle of 70°, and the measurements were carried out on ten points to determine an average thickness of the films all over the surface and the standard devation. With fixed wavelength and angle, it is not possible to determine both the refractive index and the thickness of a film. Furthermore, for the multilayer films the refractive index is not constant over few hundreds of nanometers. So, the refractive index of the films was assumed to be equal to the refractive index of the silicon oxide layer, which is equal to 1.465 and is close to the refractive index of polymers, and only the thickness of the films was measured. Even if this assumption leads to slightly incorrect values of the thicknesses, this allows to perform quick measurements of the relative thicknesses and to compare the different films. This refractive index of 1.465 was used for the growth studies of the films, with measurements every layer. However, more accurate total film thicknesses were needed for the multilayer films measured by neutron scattering, to have good starting values of the thicknesses for the analysis of the reflectivity curves. Actually, the films were measured by ellipsometry after the build-up of the whole film to verify that the depositions were done correctly. We needed also a first average layer pair thickness to use for the analysis of the neutron reflectivities. So, for this films, a first measurement was done with the spectrometric ellipsometer to determine the average refractive index of each film. Then, the measurements of the thicknesses were performed on the monochromatic ellipsometer with the refractive indexes measured.

The spectrometric ellipsometer operated at a fixed angle of 70° and a wavelength range of 370 nm - 1050 nm, which allowed to determine the refractive indexes and the thicknesses of the films. The measurements were done on one point in the center of the samples.

2.3.3 X-ray Photoelectron Spectrometry (XPS)

X-ray Photoelectron Spectrometry (XPS) is a technique based on the measurement of the kinetic energy of electrons emitted by a sample under X-ray irradiation. This technique allows the determination of the composition of the surface of a material.

Principle [165, 166]

Upon irradiation with photons (light) of sufficient energy, any material emits electrons called photoelectrons. Since the energy levels of electrons of an atom are quantified, the kinetic energy of the photoelectrons emitted upon irradiation with monochromatic light (in our case X-ray) is also quantified. Each atom emits a set of photoelectrons with specific energies (the kinetic energy of the electron is equal to the energy of the photon received minus the energy of the orbital). So, each element has

a defined XPS spectrum. XPS looks at the core electrons of the elements, because of the high energy of X-rays. The energy of the photoelectrons emitted is therefore primarily defined by the nature of the element (large difference between the peaks of different elements). The chemical environment of the element also influences the position of the peaks, but the variations are small and often lead to convoluted peaks. While elemental analysis using XPS is straightforward, the identification of the different environments requires more practice. To summarize, XPS is a quantitative analysis technique that gives information about the composition, chemical state and electronic state of the elements at the surface of a material. While X-ray can easily go through the material, the photoelectrons emitted are quickly diffracted and absorbed by the material. Most of the electrons at the surface of the sample reach the detector, whereas at 10 nm of depth the electrons do not escape the material and cannot be analyzed (at 3 nm depth, the detection is already limited). XPS is therefore only sensitive and quantitative to the surface of the sample. In layered materials, the composition of the surface layer is over-represented compared to the other layers. Rough and porous surfaces are also difficult to analyze because the electrons in the holes may not reach the detector.

A schematic representation of the experimental setup of an XPS mesurement is shown in Figure 2.14. Typically an X-ray source shines monochromatic X-rays on a sample placed in ultra high vacuum. The photoelectrons emitted by the sample are collected, passed through an electron energy analyser and detected. An energy scan of the analyser provides via the electron detector an XPS spectrum.

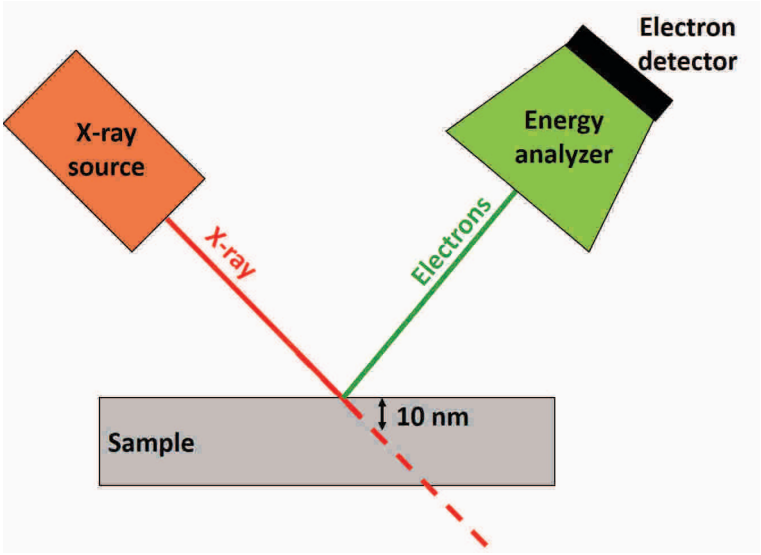

Figure 2.14: Schematic representation of an XPS measurement setup.

Spectrometer

The XPS measurements and analyses were carried out by Dr. Vasiliki Papaefthimiou in the Institut de Chimie et Procédés pour l'Energie, l'Environnement et la Santé (ICPEES) in Strasbourg.

The XPS measurements were carried out on a MULTILAB 2000 (THERMO VG) setup equipped with an AlKα X-ray source (hν=1486.6 eV). The CASA XPS pro-

gram with a Gaussian-Lorentzian mix function and Shirley background subtraction was employed to deconvolute the XP spectra. The % atomic ratios were calculated by the XPS core level peaks, properly normalized to the photoemission cross section and assuming a homogeneous distribution arrangement model.

2.4 Neutron scattering data analysis

Neutron scattering data were analysed with IgorPro 6 [167] and Motofit 3.2 [168, 169], which is a package of IgorPro.

The specular neutron reflectivity data were fitted using Motofit, which is designed for the analysis of neutron and X-ray reflectivity. This corresponds well to our multilayer films.

For the fitting of the reflectivity, we used a box model to describe our films, in which each box (slab or layer) was described by three structural parameters : the thickness, the SLD and the roughness. The iSLD correspond to the imaginary SLD, but it was neglected. Figure 2.15 shows the window where the structure of the film and the environment are described. We can differentiate three parts : the environment parameters, which described the media below the film (the substrate) and on top of the fiilm (in our case, it is air) ; the multilayer description, when the film is composed of a repetition of a sequence of layers with the same parameter values ; the individual layer description, for layers which are not repeated.

The environment was the same for all the multilayer films we studied. The films where deposited on a silicon wafer ("base") with a SLD of 2.07 x 10^{-6} $Å^{-2}$, which is the common value of the silicon crystal SLD, and a roughness ("baserough") of 4 Å, the common value used. The measurements were done in air, "top" medium, with a SLD of 0 $Å^{-2}$. The top and base media are considered as infinite by Motofit. The neutron background is described in the "bkg" box. Usually, a measurement of the background is done and removed from the reflectivity of the films, but some background may be still present and the background value is adjusted to optimize the fit. The layer value corresponds to the number of individual layers and the scale factor is used to correct the experimental data and normalize to total reflection of 1.

In all the films of polyelectrolytes measured by neutron reflectometry, two layers are on the silicon crystal : a silicon oxide layer (SiO_2 layer) and a PEI layer. The thicknesses of both layers were determined by ellipsometry and the thickness of the SiO_2 layer were adjusted to have a better fit, but with a maximum variation of 2-3 Å from the value determined by ellipsometry. The SLD and the roughness were fixed at 3.15 x 10^{-6} $Å^{-2}$ and 4 Å respectively, which are the common values used for the SiO_2 layer for this type of samples [11]. The SLD of the PEI layer was assumed to be identical to the SLD of the layer deposited on it, and was fitted with it. As there is no difference between the SLDs of the PEI layer and the layer above, the roughness of the PEI layer, which corresponds to the interface between the two layers, has no infuence on the fit and cannot be fitted. So it was fixed at 9 Å, as done previously

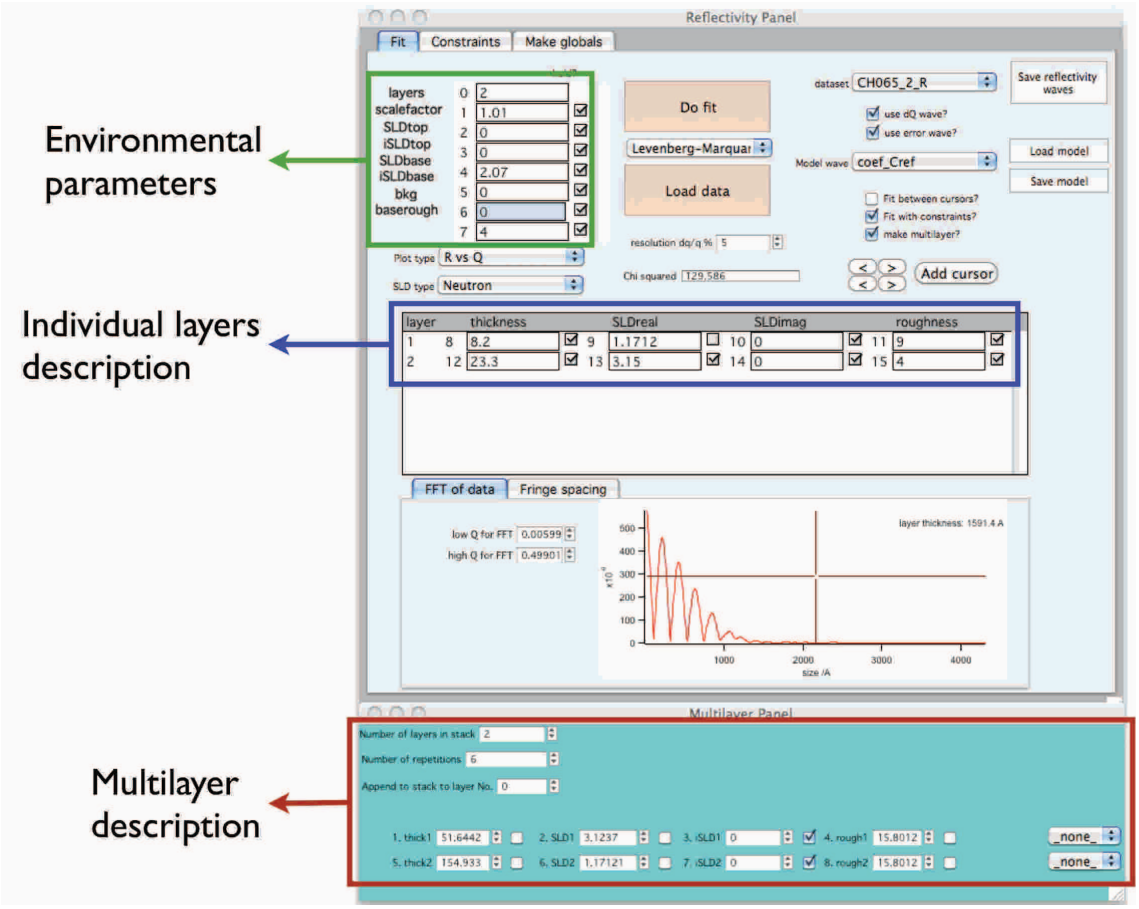

Figure 2.15: Motofit reflectivity panel, the window where the sample and the environment are described.

by our team [11]. In some films, other individual layers were described.

The "multilayer panel" corresponds to the description of the repeated layers of the films. In this part, two layers were described in each film, a layer corresponding to the deuterated layers and a layer describing the stacks of non-deuterated layers separating the deuterated layers. The parameter "Append to stack to layer No." corresponds to the position of the multilayer part in the film. The number correponds to the individual layer under which the multilayer is placed. The air corresponds to layer 0, the layer on the top of the "individual layers" is layer 1, and so on. For example, if the parameter "Append to stack to layer No." is set to 1, the multilayer part is placed between layer 1 and layer 2.

The starting values for the SLDs and roughnesses were determined from the average values found in the previous neutron reflectometry measurements on (PSS-PAH) films and the starting thicknesses were determined from measurements of the film thicknesses by ellipsometry. Then, the parameters were fitted manually, followed by a numerical fit using the Levenberg-Marquardt algorithm. Errors for non-fixed parameters were calculated using the "create local chi2map for requested parameter" option of Motofit. 2D Chi^2 maps were created for two correlated parameters (each non-fixed parameter was correlated to at least one other parameter) and

the maximal/minimal values for each parameter were determined for a 5% increase in Chi^2. Errors were the differences between the parameter values as determined by the fit and the maximal/minimal values determined from the 2D Chi^2 maps.

The GISANS data were analysed with the "Curve fitting" function of IgorPro. The equations used were entered manually and are described later in the thesis.

2.5 Influence of the temperature on the film growth - Comparison between dipping and spraying

Before the study of the internal structure of multilayer films by neutron scattering, we wanted to determine the influence of the temperature on the growth of our films. Indeed, it was already shown that the temperature of the polyelectrolyte solutions has an influence on the thickness of some films [45,170,171]. As the temperature was not controlled during the preparation of our films and room temperature measurements performed in the laboratories during one year showed a difference of about 10°C between the minimal and maximal temperatures, we decided to study the effect of the temperature on the thickness growth of our films, to know if the difference of the structure of the multilayer films could be due to the temperature or to the parameters studied.

Another interest of this study was to compare the dipping and spraying process. Actually, it is well known that there are differences between sprayed and dipped films (thickness, roughness, ...) [2, 172–174], but the reason of this difference was not determined yet. An idea we had is that the sprayed droplets of the solutions have a different temperature than the solutions at room temperature, which could be the cause of the difference of thickness. Hence we carried out temperature measurements of the solutions in both deposition processes and a comparison of dipped films at different temperatures and sprayed films.

2.5.1 Temperature measurements

Measurements of the room temperature, the temperature of static MilliQ water (dipping) and the temperature of MilliQ water droplets during spraying were measured with an alcohol thermometer with a precision of 1°C. The measurements where done the same day, in the same laboratory. Measurements of the temperature were done for the three spraying methods and were performed by spraying the water on the thermometer at a distance of 10 cm, with a water flux of 10 mL/min for the automated spray and different gas pressure (compressed air). The results are summarized in Table 2.2. The room temperature was 21°C.

We could see that the temperature of the water used for dipping is the same than the room temperature, as we could expect. We also observed that our assumption was true, the dynamic water (sprayed droplets) had a different temperature than the static water, and the sprayed droplets are 3°C to 7°C colder than the initial water. This cooling could be due to an evaporation of water of the droplets during

Deposition technique	Temperature
Dipping	21 ± 1°C
Spray with Air-Boy cans	18 ± 1°C
Spray with Aztek airbrushes	15-16 ± 1°C
Spray with industrial nozzles	14-15 ± 1°C

Table 2.2: Temperature of MilliQ water measured in different conditions.

the spray.

At this point, a study of the thickness evolution of dipped multilayer films with the temperature of the solutions was carried out to determine the influence of the temperature.

2.5.2 Temperature influence on multilayer films prepared by dipping

Multilayer films were prepared by dipping in PSS_{h7} solutions of concentration of 0.6 mg/mL and PAH solutions of concentration of 0.27 mg/mL. Both polyelectrolytes were dissolved in 0.5 M NaCl solutions. The films were built-up on silicon wafers coated with a first PEI layer deposited by immersion in a solution of concentration of 1 mg/mL of PEI for 15 min, followed by three rinsing steps in pure MilliQ water for 2 min and drying under compressed air. The PSS_{h7} and PAH layers were deposited by dipping in the polyelectrolyte solutions for 15 min, followed by three rinsing steps in pure MilliQ water for 2 min and drying under compressed air. Twenty (PSS_{h7}-PAH) layer pairs were deposited, and the films were prepared at different temperatures. This was done by putting all the polyelectrolyte and MilliQ water solutions to the right temperature using a polystat (Fisher Bioblock Scientific, Illkirch, France). Figure 2.16 shows the total thickness evolution of multilayer films composed of twenty (PSS_{h7}-PAH) layer pairs as a function of the temperature measured by ellipsometry on the monochromatic ellipsometer with a refractive index of 1.465.

We observed a linear increase with the temperature of 4.2 Å per degree for 20 layer pairs, which means an increase of 0.21 Å per degree for one layer pair. This corresponds to 0.67% of the thickness of a layer pair at 21°C (31.18 Å per layer pair). These differences are lower or in the order of the standard deviations measured with the ellipsometer for these samples for the deposition of 20 layer pairs or one layer pair. This effect can be neglected for a small room temperature variation (2-3°C) but can be important for higher variations, as the 10°C variation measured in our laboratory. This could explain the small differences in thickness which can be seen by neutron scattering for films prepared exactly in the same build-up conditions. We will explain further in this thesis how to minimize this effect of the temperature by fitting together reflectivity curves of several films prepared in the same conditions to determine average values of the structural parameters, using the "Global Fit" process of Motofit.

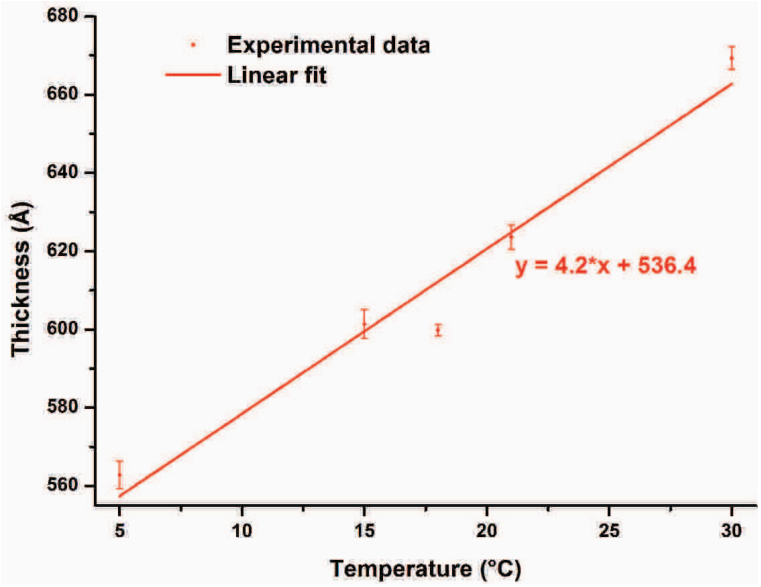

Figure 2.16: Evolution of the thickness of multilayer films composed of 20 layer pairs (PSS_{h7}-PAH) as a function of the temperature of preparation. The line corresponds to the linear fit of the curve.

2.5.3 Difference between dipped and sprayed films

To determine the exact influence of the temperature in the thickness difference between sprayed and dipped samples, seven multilayer films composed of PSS_{h7} and PAH were prepared and the thicknesses were measured every layer by ellipsometry (n = 1.465, on the monochromatic ellipsometer). These films were three dipped films prepared at 15°C (temperature of the droplets for the spray with Airboy cans), 18°C (temperature of the droplets for the spray with the Aztek airbrushes) and 21°C (room temperature), three sprayed films built-up with Aztek airbrushes at gas pressures of 1 bar, 3 bars and 5 bars, and one sprayed film with Airboy cans. The room temperature was 21°C for every sample. The increase of thickness with the number of layer pairs is shown in Figure 2.17 for the seven films.

All films were deposited on silicon wafers coated with a first PEI layer deposited as described before and the polyelectrolyte solutions were prepared in the same way.

The dipped films were prepared as described in the part above concerning the temperature influence study, with solution temperatures of 15°C, 18°C and 21°C.

The sprayed films prepared with Aztek airbrushes were built-up at a distance of 10 cm, on vertical substrates perpendicularly to the surface. The solutions were sprayed for 10 s at a flux of 10 mL/min, followed by a rinsing step with pure MilliQ water for 10 s. The pressures of the spraying gas (compressed air) were 1 bar, 3 bars and 5 bars, and the internal diameter of the nozzles was 0.7 mm. The preparation of the film prepared with Airboy cans was also done at a distance of 10 cm on a vertical substrate with spray perpendicular to the surface. The films were dried every layer under compressed air.

We observed that the three dipped films have the quicker film growth. The dipped films prepared at 15°C and 18°C had nearly the same thickness growth (29.67

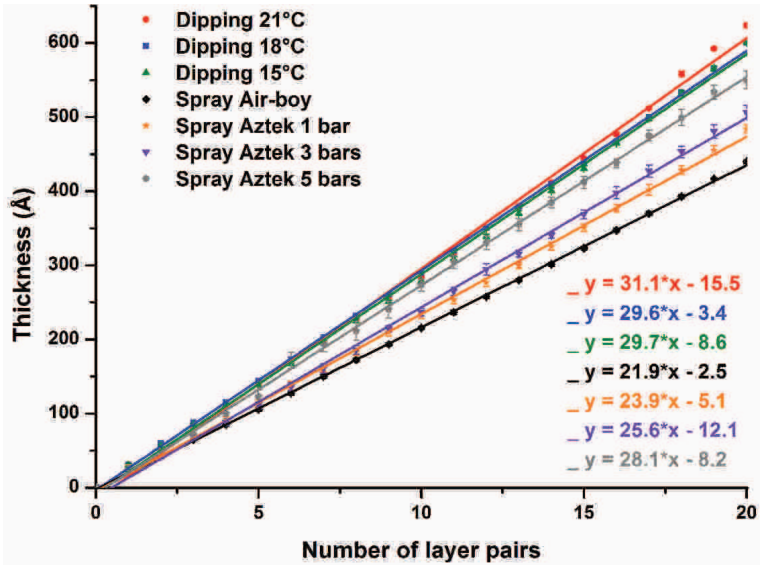

Figure 2.17: Evolution of the thickness of multilayer films composed of 20 layer pairs (PSS_{h7}-PAH) as a function of the number of layer pairs. Films prepared by dipping at different temperature and by spraying at different gas pressure are shown. Lines correspond to linear fits of the curves.

Å and 29.64 Å per layer pair) and the difference with the dipped film prepared at 21°C is of the order of 1.50 Å per layer pair. The film prepared by spraying with Airboy cans showed the smallest thickness increase and a bigger pressure for spraying with Aztek airbrushes gives a thicker film. We can see that the thickness differences between the dipped sample at room temperature (21°C) and the sprayed films, which is of the order of 3.00 Å to 9.20 Å per layer pair, are more important than the differences with the dipped films at the droplets temperatures (2 to 6.1 bigger difference in thickness). This means that, even if the temperature of preparation has an influence on the thickness of multilayer films, it is not the main parameter which causes the difference in structure between sprayed and dipped films. This difference is probably due to specific hydrodynamic effects that occur while spraying on a surface, which could explain the increase of thickness with the increase of the gas pressure of the spraying process.

2.5.4 Conclusions

We have seen that the thickness of multilayer films of polyelectrolytes prepared by dipping increases with the temperature of the solutions, but the thickness increase is small for a difference of 2-3°C. We have also observed a difference in temperature of the droplets of solutions during the spraying process, the temperature is 3°C to 7°C smaller than the room temperature. Nevertheless, even if the temperature of the solutions has an influence on the thickness of the films, it is negligible compared to the thickness difference between dipped and sprayed films. The increase of the thickness of sprayed films with the gas pressure of the spraying process would suggest that this difference is due to specific hydrodynamic effects that occur on the surface during the spraying.

Chapter 3

What is the structural evolution of multilayer films with time ?

Due to its general use for organic, polymeric, inorganic and biological materials and due to their simplicity of use, the multilayer films built-up by the LbL technique are studied in applied research in many domains, as biomedicine (tissue engineering, functionalization of implants, drug/gene delivery, biosensing, ...), electronics (conductivity, electroluminescent devices, lithium-ion-batteries), optics (anti-reflective coatings), corrosion protection, catalysis, microreactors, functionalization of nanoparticles [110, 175–180]. Several applications using LbL assembled films are developed or are already commercialized, and an important parameter is the life-time of the devices, their evolution with time. We studied the multilayer film ageing not for an industrial interest, but for a fondamental point of view to observe the evolution of the internal structure with time. This should give us an estimation of the time a film can be stored without changing the result of a structural measurement (in our case, using neutron scattering).

As far as we know, no studies of the ageing of multilayer films of polyelectrolytes are availablle, except one structural study done on (PSS-PAH) films by our team. Indeed, a first structural analysis was done on multilayer films by neutron reflectometry at Risø National Laboratory, Denmark, in 1993 [4] and a second set of neutron reflectometry measurements was performed at Dubna, Russian Federation, in 1995 [181], one of the samples having been measured in both studies. This sample is Sample B in reference [4] and the Sample 2 in reference [181], and has the following structure : $[(\mathrm{PSS}_{h7}\text{-PAH})/(\mathrm{PSS}_{d7}\text{-PAH})]_8$. The thickness values, determined from the fit of the specular neutron reflectivity, are summed up in Table 3.1. The thickness was determined in two ways. The total thickness was determined from the Kiessig fringes and the thickness of a repeat unit $[(\mathrm{PSS}_{h7}\text{-PAH})/(\mathrm{PSS}_{d7}\text{-PAH})]$ was calculated from the Bragg peaks, and both thickness are given for a better comparison. We observe that the total thickness determined from the Kiessig fringes is 1.09 times thicker after 2 years of storage, whereas the thickness of a repeat unit determined from the Bragg peaks is 1.05 thinner after 2 years. So, we can see a slight change in thickness for the multilayer film after 2 years, but unfortunately, the two ways of determining the thickness give contradictory results. We just know that, after 2 years, we have a change of thickness lower than 10.0%, but we do not

know if we have an increase or a decrease of the size. Thus, a new study of the effect of the storage on multilayer film structure has to be performed.

	Measurement in 1993	Measurement in 1995
Total thickness from Kiessig fringes (Å)	780.0	850.0
Repeat unit thickness from Bragg peaks (Å)	105.0	100.0

Table 3.1: Structural parameters determined from the fits of the specular reflectivities, measured after preparation of the film and after 2 years of storage.

As mentioned in the motivation paragraph at the beginning of this thesis, the effect of water during the storage was observed by M. Lösche *et al.* [10] on a multilayer film composed of PSS and PAH. This film was prepared by dipping during two days, and was stored in water during the night (around 12 h). Neutron reflectometry measurements showed that the three last layer pairs deposited before the storage in water were thinner than the other layers. This is shown on the scattering length density (SLD) profile of the film in Figure 3.1. This change of thickness is due to a plastification, a relaxation of the polyelectrolytes due to the water. We may assume a change of conformation of the polyelectrolyte chains.

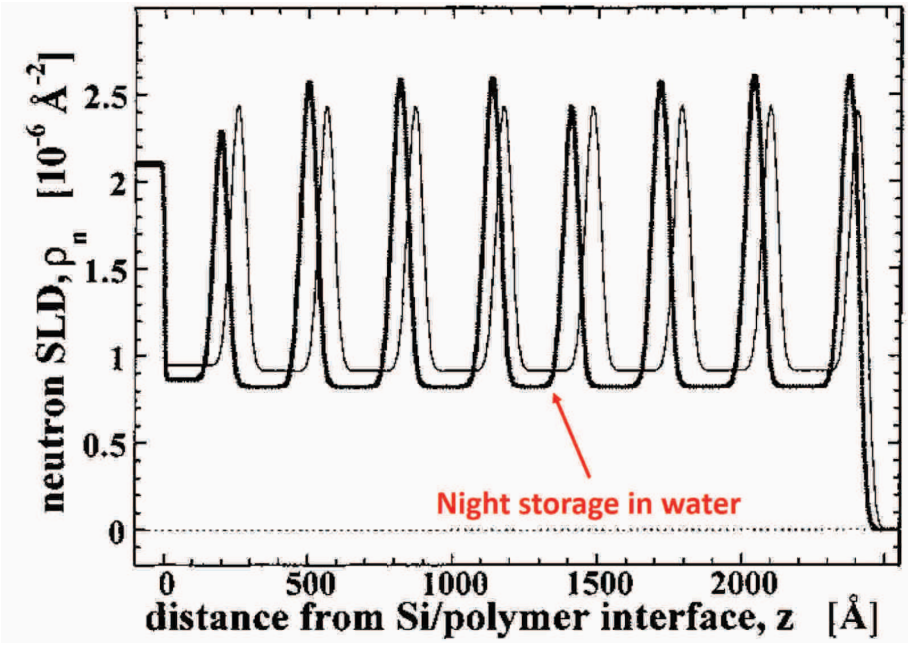

Figure 3.1: Scattering length density profile of a dipped multilayer film of PSS and PAH. The storage in water is indicated. Adapted from reference [10].

The films studied in this chapter being stored in the air, we can assume a similar evolution of their structures due to the humidity in the air, but at a lower proportion and for a longer time. These films are divided in two groups, the first one is constituted of multilayer films measured by neutron reflectometry at Risø National Laboratory, Denmark, in 1998 [10], and the second group is composed of films prepared and measured by neutron reflectometry at Laboratoire Léon Brillouin (LLB),

in Paris, France, in 2007 [11]. A part of these films were measured again at ILL in 2012-2013, which means 14-15 and 5-6 years after preparation, respectively. By comparing the internal structure of the films, we can determine their evolution with time.

3.1 Evolution of (PSS-PAH) films after 15 years

Nine multilayer films of polyelectrolytes were built up and measured at Risø National Laboratory in 1998 by our team [10]. Three of these films, Sample A1, A2 and A3 were stored to be measured again at ILL in 2012-2013, i.e. 14-15 years after their preparation.

3.1.1 Multilayer films preparation

As described in reference [10], the three films were composed of PSS_{h7} (M_w = 84,000 g/mol, $M_w/M_n \leq 1.1$), PSS_{d7} (M_w = 168,000 g/mol, $M_w/M_n \leq 1.1$) and PAH (M_w = 50,000 - 65,000 g/mol). The films were deposited on silicon wafers cleaned in $H_2O/H_2O_2/NH_3$ (5:1:1 v/v/v) at 80°C for 15 min, followed by rinsing with MilliQ water. The substrates were washed with methanol, methanol/toluene (1:1 v/v) and toluene and then a first layer of 4-Aminobutyldimethylmethoxysilane (ABS) was deposited on it from a 1 vol % solution of ABS for 16h. After the deposition, the substrates were washed with toluene, methanol/toluene (1:1 v/v) and methanol. The multilayer films were deposited by manual dipping alternately into deuterated or protonated PSS (3 x 10^-3 monomol/L, 3 mM HCl and 2 M NaCl) and PAH solutions (3 x 10^-3 monomol/L, 3 mM HCl and 2 M NaCl) for 20 min, followed by three rinsing steps into MilliQ water for 1 min. After the deposition of the whole film, the samples were dried under either a N_2 gas stream or a stream of pressurized, filtered air.

The three films were the following :

- Sample A1 : $[(PSS_{h7}\text{-PAH})/(PSS_{d7}\text{-PAH})]_8$
- Sample A2 : $[(PSS_{h7}\text{-PAH})_2/(PSS_{d7}\text{-PAH})]_8$
- Sample A3 : $(PSS_{d7}\text{-PAH})_{10}$

In Figures 3.2 are shown the representations of the structure of the multilayer films corresponding to the layer sequence deposition.

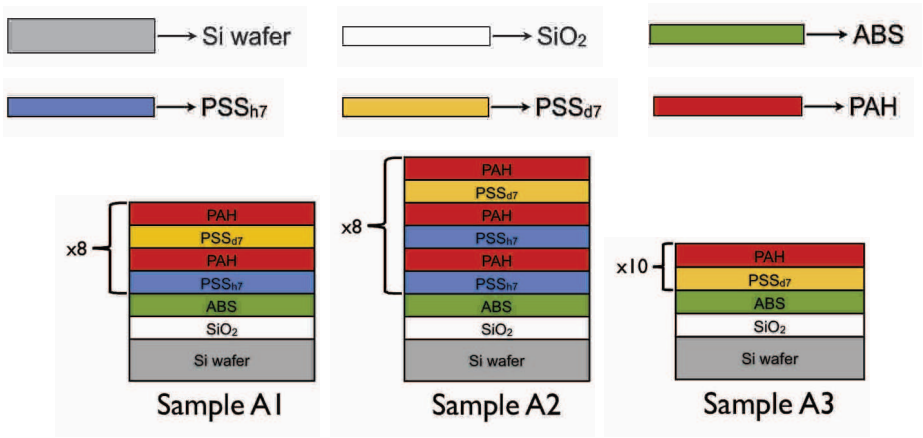

Figure 3.2: Layer sequences for Sample A1, A2 and A3. The proportions of the layer thicknesses are not kept.

3.1.2 Analysis of the measurements performed at Risø National Laboratory

The measurements were performed on the TAS7 reflectometer with a vertical scattering plane, at a fixed wavelength of 4.64 Å and varying angles, at ambient conditions.

The experimental data were not available, so we used the theoretical model described in the publication for our study. The analysis of the specular reflectivity curves was done by using a layer model and considering a homogeneity of the films in the direction perpendicular to the surface. The curves corresponding to the theoretical models are shown in Figure 3.3. Thicknesses of 20 Å and 30 Å and roughnesses of 5 Å and 9 Å were used for the SiO_2 and ABS layers respectively, the SLD of the SiO_2 layer was set to 3.15 x 10^{-6} $Å^{-2}$. As for the PEI layer, the SLD of the ABS layer was considered to be the same than the SLD of the layer adsorbed on it. The structural parameter values determined by the theoretical models are summarized in Table 3.2.

	Layer pair thickness (Å)	Protonated SLD (x 10^{-6} $Å^{-2}$)	Deuterated SLD (x 10^{-6} $Å^{-2}$)	Roughness (Å)
Sample A1	51.4	0.87	3.10	20.0
Sample A2	51.0	0.87	3.10	19.0
Sample A3	47.5	X	2.90	13.0

Table 3.2: Layer pair thicknesses, SLDs and roughnesses determined from the specular reflectivity fits of the Sample A1, A2 and A3 measured at Risø National Laboratory in 1998.

Sample A1 had a thickness per layer pair of 51.4 Å, Sample A2 a thickness per layer pair of 51.0 Å and Sample A3 a thickness per layer pair of 47.5 Å. Sample A3 had layer pairs 1.1 times thinner than Sample A1, which corresponds to 3.9 Å. The deuterated and non-deuterated SLDs were the same for Sample A1 and Sample A2, 3.10 x 10^{-6} $Å^{-1}$ and 0.87 x 10^{-6} $Å^{-1}$, but the SLD of Sample A3, which was

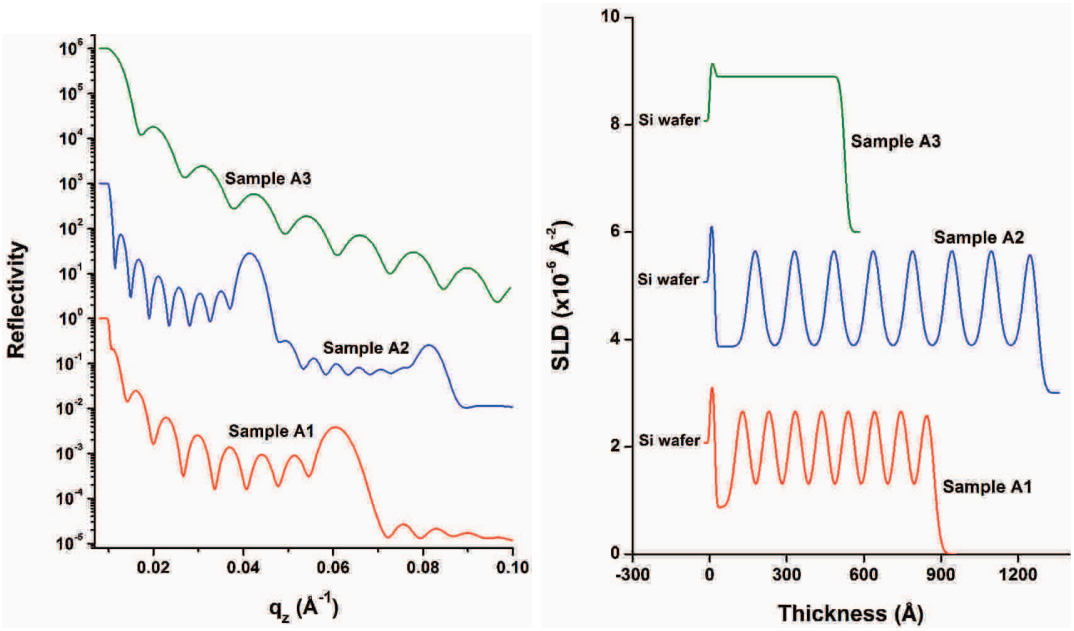

Figure 3.3: On the left, the theoretical models corresponding to the fit of the specular reflectivity curves of Sample A1, A2 and A3 measured at Risø National Laboratory in 1998. On the right, the SLD profiles extracted from the fits. The curves are shifted for clarity.

fully deuterated, was 1.07 times smaller, with a value of 2.90 x 10^{-6} Å^{-1}, that is a difference of 0.20 x 10^{-6} Å^{-1} with Sample A1 and Sample A2. Even if the thickness is smallest for Sample A3, its SLD is not bigger, but similar to the ones of Sample A1 and Sample A2. The roughnesses of Sample A1 and Sample A2 were similar, with respective values of 20.0 Å and 19.0 Å. The roughness at the surface was 13.0 Å for Sample A3, 1.5 times smaller than the roughness of Sample A1 (a difference of 7.0 Å).

The three films were then stored and measured at ILL in 2012-2013, that is 14-15 years later.

3.1.3 Structural evolution after 15 years

The three multilayer films were stored in non-controlled conditions, in an office where the variations of temperature and humidity were important. The box containing the samples was found opened, with dust inside, so contamination of the films may have occured.

Sample A1 and Sample A2 were measured on D17 with the setup D17-2 and Sample A3 on FIGARO with the setup FIGARO-1 (the setups are described in Part 2.3.1). The reflectivity curves of the three films are shown in Figure 3.4.

We can first see a difference of the gap between the Kiessig fringes depending on the films. As we know, the gap between two neighbouring fringes is dependent on the thickness and especially a smaller gap means a bigger thickness.

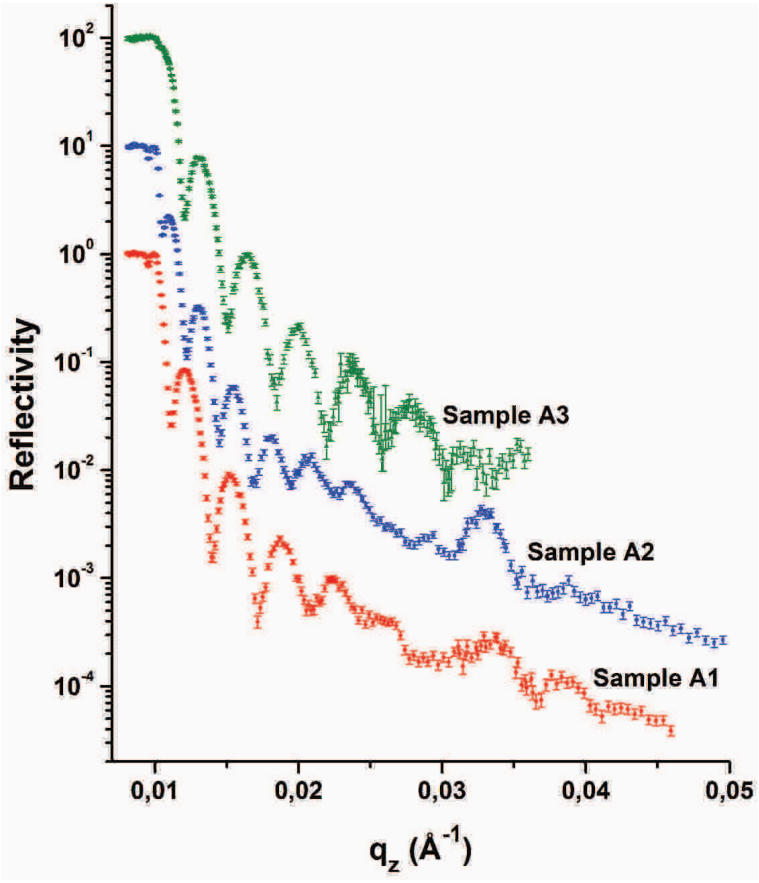

Figure 3.4: Specular reflectivity curves of Sample A1, A2 and A3 measured at ILL in 2012-2013. The curves are shifted for clarity.

To have a first idea of the changes undergone by the films, ellipsometry measurements were performed on the three films to have a first comparison of the thicknesses with the initial ones. The measurements were carried out with the monochromatic ellipsometer using refractive indexes measured with the spectroscopic elllipsometer. Table 3.3 gathers the refractive indexes and the thicknesses measured by ellipsometry as well as the total thicknesses of the films determined by neutron reflectometry in 1998.

	Refractive index	Total thickness in 2014 by ellipsometry (Å)	Total thickness in 1998 by reflectometry (Å)	Ratio between thickness in 2014 and in 1998
Sample A1	1.520	1962.1 ± 93.7	872.4	2.2
Sample A2	1.554	2529.2 ± 117.8	1274.0	2.0
Sample A3	1.582	1753.7 ± 17.6	525.0	3.3

Table 3.3: Total thicknesses of the three films measured by ellipsometry and the refractive indexes used for the measurements. On the right column are indicated the total thicknesses of the multilayer films as measured by neutron reflectometry at Risø National Laboratory in 1998.

The thicknesses of the films increased from 2.0 times to 3.3 times the initial thicknesses. This is a large increase, and we can see that the three films did not

thicken in the same proportions. The thickest film, Sample A2, thickened less than the thinnest film, Sample A3.

Initially, data were fitted using the same structural parameters values for the SiO_2 and PEI layers and the same structures than the ones determined in 1998, and only the values of the parameters of the (PSS-PAH) films were varied. We rapidly saw that the intial structures did not correspond to the structures after 15 years. So we decided to use different structures than the initial ones by making the following assumptions :

- An oxidation of the silicon substrate close to the silicon oxide layer, leading to a change of the SiO_2 layer parameters.
- An increase of interpenetration significant enoough to change the deuterated/protonated layered structure of Sample A1 by a monolayer (box) structure.
- An inhomogeneous change of the structure of the films in the direction perpendicular to the surface, leading to the transition from a one layer structure to a several layers structure for Sample A1 and Sample A3.

Figure 3.5 shows the specular reflectivity curves measured at ILL for Sample A1 and Sample A2, with the best fits we found, as well as the theoretical reflectivities determined in 1998 and the corresponding SLD profiles. The values of the structural parameters are summarized in Table 3.4. The thickness and roughness of the SiO_2 layer of Sample A3 were fixed to 55.0 Å and 35.0 Å respectively (similar to the values for the SiO_2 layer of Sample A1), because the numerical fit gave a really small value for the thickness (less than few angströms) and a really big value of the roughness (more than 100 Å).

We can first see that our assumption concerning an oxidation of the silicon substrate was correct. Indeed, the thickness of the SiO_2 layer increased from 20.0 Å to 55.8 Å for Sample A1 and from 20.0 Å to 55.0 Å for Sample A2, which corresponds to differences of 35.8 Å and 35.0 Å, and ratios of 2.8. This thickness increase went along with a decrease of the SLD from 3.15 x 10^{-6} $Å^{-2}$ to 2.91 x 10^{-6} $Å^{-2}$ for Sample A1 or 2.65 x 10^{-6} $Å^{-2}$ for Sample A3. The SLD is 1.08 times bigger for Sample A1 and 1.20 times bigger for Sample A3. This is probably due to an appearence of porosity in the layer. Finally, the roughness was 7.0 times bigger for Sample A1 (from 5.0 Å to 35.2 Å) and 7.0 times bigger for Sample A3 (from 5.0 Å to 35.0 Å) than the initial roughness.

Then we observed an increase of the total thicknesses of the two films, from 852.4 Å to 1619.3 Å for Sample A1 (1.9 times bigger) and from 505.0 Å to 1538.2 Å for Sample A3 (3.0 times bigger). We can see that the change of thickness was not the same for the two films. This is in agreement with the ellipsometry measurements. Furthermore, the change in the films was not homogeneous, as assumed. We had a two layers structure instead of a one layer structure for both films. This manifested as a first small layer, which include the ABS layer, and a second larger. For Sample A1, the first layer had a thickness of 220.8 Å, which corresponds to 13.6% of the total

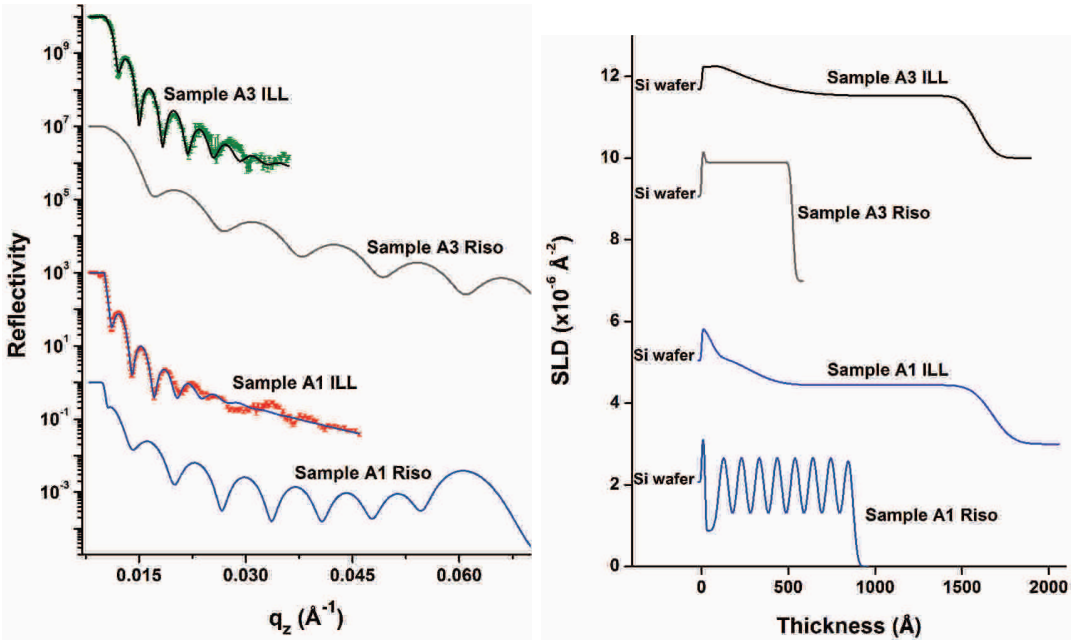

Figure 3.5: On the left, the experimental specular reflectivity curves (points) of Sample A1 and Sample A3 measured at Risø National Laboratory in 1998 and ILL in 2012-2013 and the corresponding theoretical models (line). On the right, the SLD profiles extracted from the fits. The curves are shifted for clarity.

	Sample A1				Sample A3			
	Layer pair thickness (Å)	Protonated SLD (x 10^{-6} Å^{-2})	Deuterated SLD (x 10^{-6} Å^{-2})	Roughness (Å)	Layer pair thickness (Å)	Protonated SLD (x 10^{-6} Å^{-2})	Deuterated SLD (x 10^{-6} Å^{-2})	Roughness (Å)
(PSS-PAH) film	51.4	0.87	3.10	20.0	47.5	X	2.90	13.0
	Thickness (Å)	SLD (x 10^{-6} Å^{-2})		Roughness (Å)	Thickness (Å)	SLD (x 10^{-6} Å^{-2})		Roughness (Å)
ABS	30.0	0.87		9.0	30.0	2.90		9.0
SiO_2	20.0	3.15		5.0	20.0	3.15		5.0

	Sample A1			Sample A3		
	Thickness (Å)	SLD (x 10^{-6} Å^{-2})	Roughness (Å)	Thickness (Å)	SLD (x 10^{-6} Å^{-2})	Roughness (Å)
Layer 2	1398.5 ± 71.5	1.44 ± 0.07	94.2 ± 30.7	1446.8 ± 11.8	1.53 ± 0.03	74.1 ± 5.8
Layer 1	220.8 ± 105.8	2.20 ± 0.22	135.4 ± 51.6	91.4 ± 14.0	2.84 ± 0.02	297.0 ± 7.4
SiO_2	55.8 ± 30.3	2.91 ± 0.59	35.2 ± 24.3	55.0 (fixed)	2.65 ± 0.15	35.0 (fixed)

Table 3.4: Layer thicknesses, SLDs and roughnesses determined from the specular relfectivity fits of Sample A1 and Sample A3 measured at Risø National Laboratory in 1998 (top table) and at ILL in 2012-2013 (bottom table).

thickness of the film, and the second layer a thickness of 1398.5 Å, that is say 86.4% of the thickness. For Sample A3, the thickness of the first layer was 91.4 Å, 5.9%

of the total thickness, and the thickness of the second layer was 1446.8 Å, 94.1% of the total thickness. This increase went along with a decrease of the SLD for the top layer of the films, the SLD of the first layer being similar to the average SLD of the initial films. For Sample A1, the initial SLDs were 0.87 x 10^{-6} Å^{-2} and 3.1 x 10^{-6} Å^{-2}, we can assume an average value of 1.99 x 10^{-6} Å^{-2} for the initial film with a homogeneous mixture of the deuterated and protonated polyelectrolytes inside the films and the same thickness. The SLD of the first layer of Sample A1 was similar to this value with 2.20 x 10^{-6} Å^{-2}, which corresponds to a 1.11 times bigger SLD. However, the SLD of the second layer was 1.38 times smaller than the initial average value, going from 1.99 x 10^{-6} Å^{-2} to 1.44 x 10^{-6} Å^{-2}. Sample A3 had a similar behaviour : a first layer with a SLD similar to the initial one, 1.02 times smaller (from 2.90 x 10^{-6} Å^{-2} to 2.84 x 10^{-6} Å^{-2}), and a second layer with a SLD 1.90 times smaller than the initial SLD, going from 2.90 x 10^{-6} Å^{-2} to 1.53 x 10^{-6} Å^{-2}. This decrease of the SLDs is in agreement with the increase of the thicknesses, if we consider a decrease of the density. But, as the proportions of the thickness increases and SLDs decreases are not the same, we may have also a change of composition of the film. An assumption is an oxidation of the polyelectrolytes, a contamination of the films or a water uptake from the humidity in the ambient air with the time. The difference between the two layers is probably due to the proximity of the silicon wafer next to the first layer, which may have a protective effect on the bottom of the film. Indeed, it is possible that the change of the films began at the top and went deeper in the film with time. The large roughnesses between the two layers, 135.4 Å for Sample A1 and 297.0 Å for Sample A2, would suggest a large interface between the top and the bottom layers where the structure changed partially.

We were not able to fit the specular reflectivity curve for Sample A2, but we can see a Bragg peak on the reflectivity curve shown in Figure 3.6, at a position q = 0.0330 Å^{-1}. This indicates that we still have a layered structure as for the initial films, but the film had probably undergone an inhomogeneous change depending on the depth inside the film, as observed for Sample A1 and Sample A3. Finally, the increase of the polyelectrolyte interpenetration was limited in distance after 15 years of storage and even with a non-controlled storage, the film still exhibited a layered structure.

The neutron reflectometry measurements gave us the off-specular reflectivity signals of the films in addition to the specular reflectivity. Figure 3.7 shows the 2D pictures of the off-specular reflectivity signals of Sample A1 and Sample A2 after treatment and normalization.

The pictures are composed of two signals interesting for us : the specular reflectivities and the Bragg sheets. The specular reflectivities correspond to the vertical signal on which we can see the Kiessig fringes and the Bragg peak of Sample A2. This signal is the one we fit to determine the internal structure of the multilayer films. The second signal, the Bragg sheets, corresponds to the inclined signal, which crosses the specular reflectivity signal at the Bragg peaks. We did not perform a quantitative analysis of the off-specular reflectivities, but some conclusions may be drawn by observing the 2D pictures. First of all, the presence of Bragg sheets indicated that there was some correlation between the roughness profiles at the interfaces inside the films. This is possible only for several interfaces, if the films have a

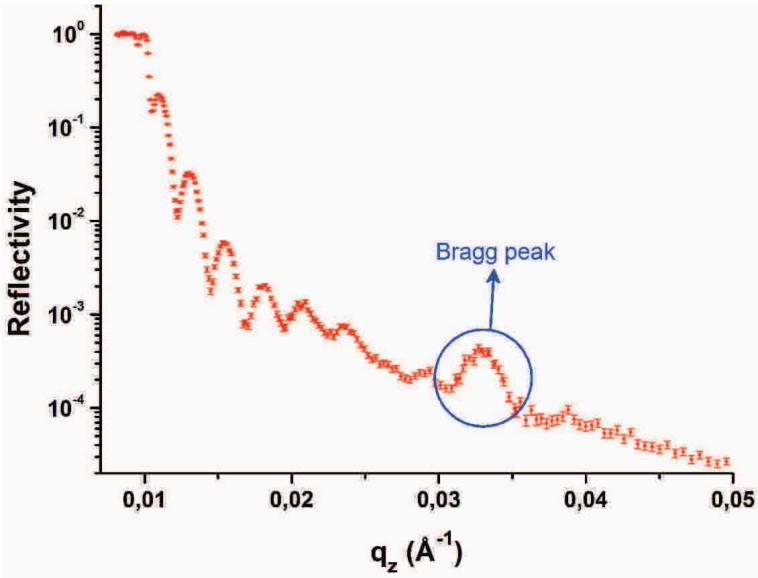

Figure 3.6: Experimental specular reflectivity curve of Sample A2 measured at ILL in 2012-2013.

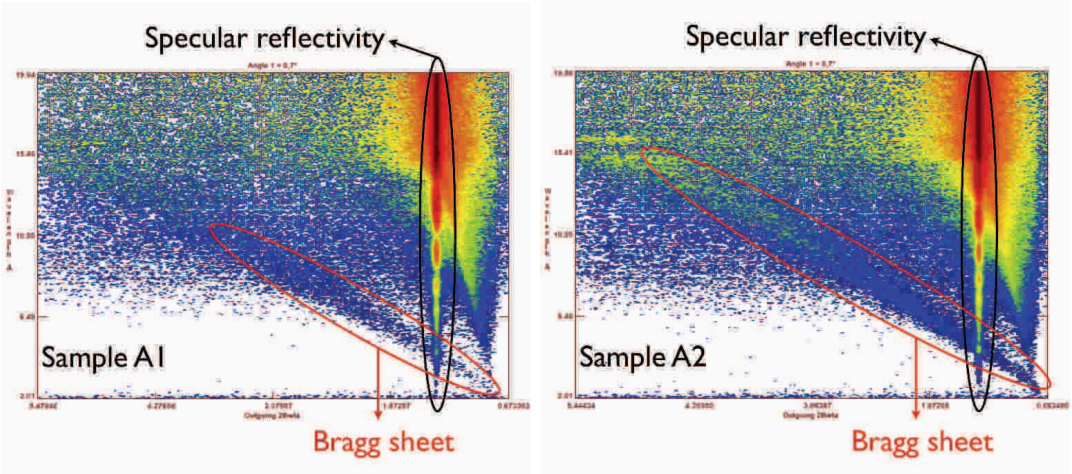

Figure 3.7: 2D pictures of the off-specular reflectivity signals for Sample A1 (on the left) and Sample A2 (on the right) measured at ILL in 2013-2014.

multilayered structure (in our case, an alternation of deuterated and non-deuterated stacks). For Sample A2, we already saw the Bragg peak on the specular reflectivity curve, indicating a multilayered structure. For Sample A1, we did not expect the presence of Bragg sheets, as we observed a two boxes structure. But as we also see a Bragg sheet on the 2D picture, this means there were interfaces inside the film, with a multilayered structure. The intersection between the specular reflectivity and the Bragg sheet corresponds to a wavelength of $\lambda = 4.56$ Å, that is $q = 0.0337$ Å^{-1}, from which we can deduce that the peak circled on the reflectivity curve drawn in Figure 3.8 is a Bragg peak. But the intensity of the peak is very low and even not captured by the fit. A possibility is that there were inhomogeneous thickness increases of the films depending on the positions on the surfaces, i.e. there were spots where

the thickness increased more or less, giving inclined interfaces, which smear out the specular reflectivity signal but not the off-specular signal.

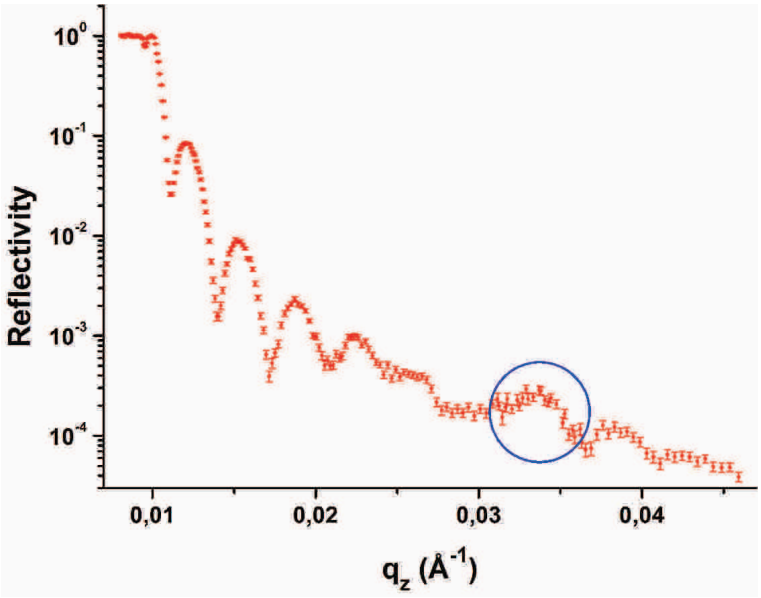

Figure 3.8: Experimental specular reflectivity curve of Sample A1 measured at ILL in 2012-2013.

3.1.4 Conclusion

To conclude, we have seen that after 15 years, the three multilayer films showed an important structural change. The films had a thickness which is at least twice the initial thickness and exhibited a decrease of the SLDs. This change of structure was inhomogeneous in the direction perpendicular to the surface. Despite this big changes, there is still a residue of the typical signal of a multilayered structure. We have here reached the limit of interpretation of the reflectivity curve analysis. These changes may be due to an oxidation of the polyelectrolytes, a contamination of the films, a water uptake from the humidity in the ambient air or a rearrangement of the polyelectrolytes in the films with time.

After 15 years, we have reach the limit of storage of multilayer films. So, we have studied the evolution of the multilayer film structure for a lower time of storage, that is 5 years.

3.2 Evolution of (PSS-PAH) films after 5 years

Eighteen samples were prepared in 2007 by our team and were measured by neutron reflectometry at LLB the same year [11]. We decided to measured again six of these samples, the ones described in the publication, by neutron reflectometry at ILL in 2012 and 2013 to observe the evolution of the internal structure after 5-6 years of storage.

3.2.1 Multilayer films preparation

A detailed description of the sample preparation is available in reference [11], and we will give here a summary of what is written in the publication.

Mutlilayer films composed of deuterated as well as non-deuterated PSS (M_w = 80,800 g/mol and M_w = 70,000 g/mol respectively) and PAH (M_w = 70,000 g/mol) were deposited on silicon wafers cleaned by a 30 min long immersion in a mixed solution of methanol and hydrochloric acid (1:1, v/v) followed by a storage in a concentrated sulfuric acid solution for at least one night. Then the wafers were rinsed in Milli-Q water and used the same day for the film buid-up. A first layer of PEI (M_w = 25,000 g/mol) was deposited by dipping the wafers in a solution with a concentration of 1 mg/mL (in pure MilliQ water) during 5 min, then rinsed in MilliQ water and dried under nitrogen. Then, the films were deposited on the substrates either by manual spraying (Air-boy cans) or by dipping. The deposition by spraying was carried out by spraying the polyelectrolyte solutions during 5 s, with a contact time of 15 s following the spraying, then by rinsing with pure MilliQ water during 5 s and by waiting 15 s before depositing the next layer. The dipping deposition was done by dipping the substrate in the solution for 20 min, followed by three rinsing steps of 100 s, 100 s and 120 s. The solutions used for all the films were the same, the concentrations of PSS_{h7} and PSS_{d7} being 0.6 mg/mL, the one of PAH was 0.27 mg/mL and all the polyelectrolytes were dissolved in 0.5 M NaCl solutions.

The eighteen multilayer films prepared were differentiated by the deposition method (dipping or spraying) and by the layer sequence, as described below (for easier comparison with the publication, the names of the samples were kept the same) :

- Sample A : $(PSS_{h7}\text{-}PAH)_{10}$ by spraying
- Sample B : $(PSS_{d7}\text{-}PAH)_{10}$ by spraying
- Sample C : $[(PSS_{h7}\text{-}PAH)_3/(PSS_{d7}\text{-}PAH)]_6/(PSS_{h7}\text{-}PAH)_3$ by spraying
- Sample D : $[(PSS_{h7}\text{-}PAH)_5/(PSS_{d7}\text{-}PAH)]_6/(PSS_{h7}\text{-}PAH)_5$ by spraying
- Sample E : $[(PSS_{h7}\text{-}PAH)_4/(PSS_{d7}\text{-}PAH)]_8/(PSS_{h7}\text{-}PAH)_4$ by spraying
- Sample F : $[(PSS_{h7}\text{-}PAH)_4/(PSS_{d7}\text{-}PAH)]_8/(PSS_{h7}\text{-}PAH)_4$ by dipping
- Sample G : $[(PSS_{h7}\text{-}PAH)_4/(PSS_{d7}\text{-}PAH)_2]_6/(PSS_{h7}\text{-}PAH)_4$ by spraying
- Sample H : $[(PSS_{h7}\text{-}PAH)_3/(PSS_{d7}\text{-}PAH)_3]_6/(PSS_{h7}\text{-}PAH)_3$ by spraying
- Sample I : $[(PSS_{h7}\text{-}PAH)_2/(PSS_{d7}\text{-}PAH)_4]_6/(PSS_{h7}\text{-}PAH)_2$ by spraying
- Sample J : $[(PSS_{h7}\text{-}PAH)/(PSS_{d7}\text{-}PAH)_5]_6/(PSS_{h7}\text{-}PAH)$ by spraying
- Sample K : $[(PSS_{h7}\text{-}PAH)_5/(PSS_{h7}\text{-}PAH)]/[(PSS_{h7}\text{-}PAH)_5/(PSS_{d7}\text{-}PAH)]_4/(PSS_{h7}\text{-}PAH)_5$ or $(PSS_{h7}\text{-}PAH)_{11}/[(PSS_{d7}\text{-}PAH)/(PSS_{h7}\text{-}PAH)_5]_4$ by spraying

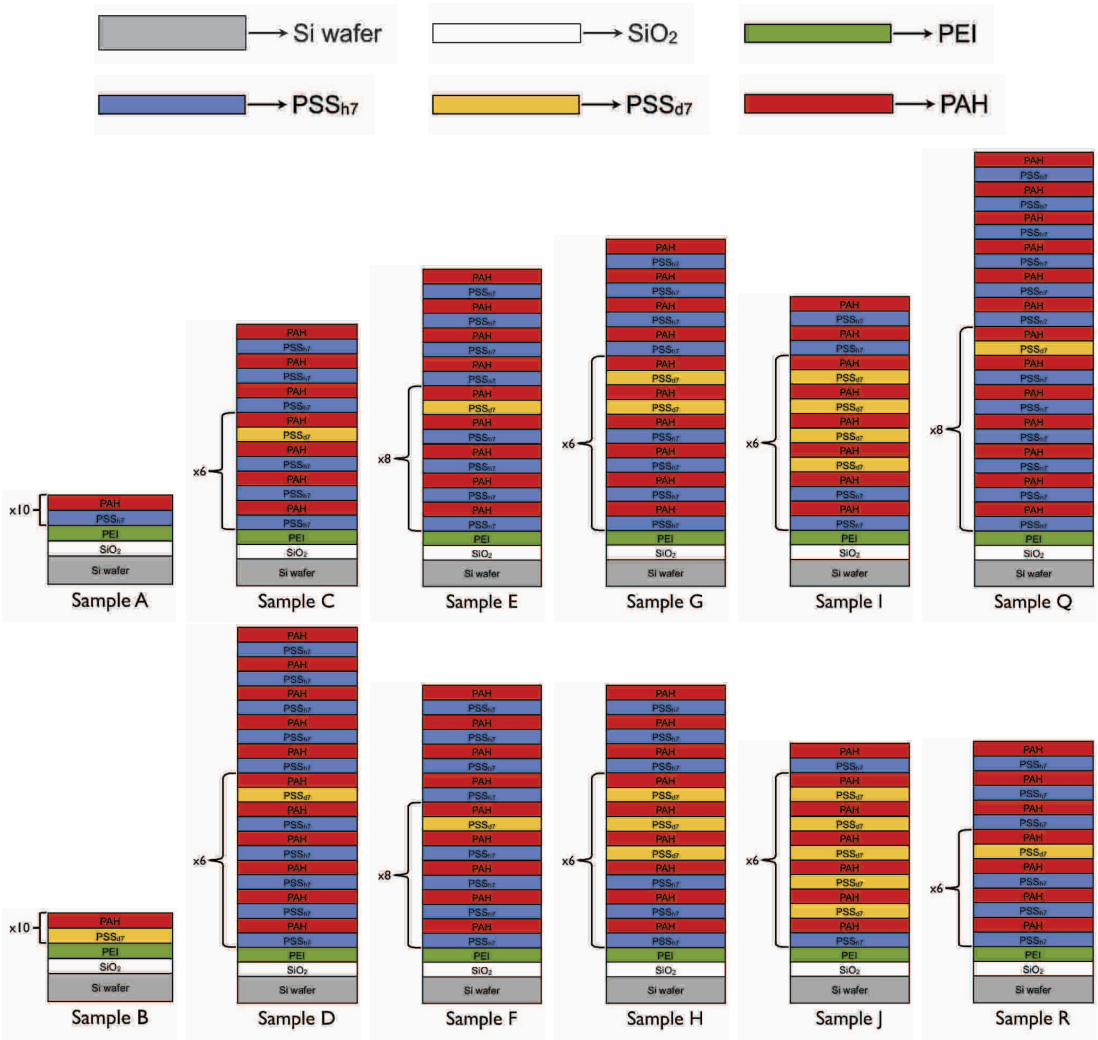

Figure 3.9: Layer sequences for Sample A, B, C, D, E, F, G, H, I, J, Q and R. The proportions of the layer thicknesses are not kept.

- Sample L : $[(PSS_{h7}\text{-}PAH)_5/(PSS_{d7}\text{-}PAH)]/[(PSS_{h7}\text{-}PAH)_5/(PSS_{h7}\text{-}PAH)]_4/(PSS_{h7}\text{-}PAH)_5$ or $(PSS_{h7}\text{-}PAH)_5/(PSS_{d7}\text{-}PAH)/(PSS_{h7}\text{-}PAH)_{29}$ by spraying
- Sample M : $[(PSS_{h7}\text{-}PAH)_5/(PSS_{d7}\text{-}PAH)]_2/[(PSS_{h7}\text{-}PAH)_5/(PSS_{h7}\text{-}PAH)]/[(PSS_{h7}\text{-}PAH)_5/(PSS_{d7}\text{-}PAH)]_2/(PSS_{h7}\text{-}PAH)_5$ or $[(PSS_{h7}\text{-}PAH)_5/(PSS_{d7}\text{-}PAH)]_2/(PSS_{h7}\text{-}PAH)_{11}/[(PSS_{d7}\text{-}PAH)/(PSS_{h7}\text{-}PAH)_5]_2$ by spraying
- Sample N : $[(PSS_{h7}\text{-}PAH)_5/(PSS_{h7}\text{-}PAH)]_2/[(PSS_{h7}\text{-}PAH)_5/(PSS_{d7}\text{-}PAH)]/[(PSS_{h7}\text{-}PAH)_5/(PSS_{h7}\text{-}PAH)]_2/(PSS_{h7}\text{-}PAH)_5$ or $(PSS_{h7}\text{-}PAH)_{17}/(PSS_{d7}\text{-}PAH)/(PSS_{h7}\text{-}PAH)_{17}$ by spraying
- Sample O : $[(PSS_{h7}\text{-}PAH)_5/(PSS_{d7}\text{-}PAH)]_4/[(PSS_{h7}\text{-}PAH)_5/(PSS_{h7}\text{-}PAH)]/(PSS_{h7}\text{-}PAH)_5$ or $[(PSS_{h7}\text{-}PAH)_5/(PSS_{d7}\text{-}PAH)]_4/(PSS_{h7}\text{-}PAH)_{11}$ by spraying
- Sample P : $[(PSS_{h7}\text{-}PAH)_5/(PSS_{h7}\text{-}PAH)]_4/[(PSS_{h7}\text{-}PAH)_5/(PSS_{d7}\text{-}PAH)]/(PSS_{h7}\text{-}PAH)_5$ or $(PSS_{h7}\text{-}PAH)_{29}/(PSS_{d7}\text{-}PAH)/(PSS_{h7}\text{-}PAH)_5$ by spraying

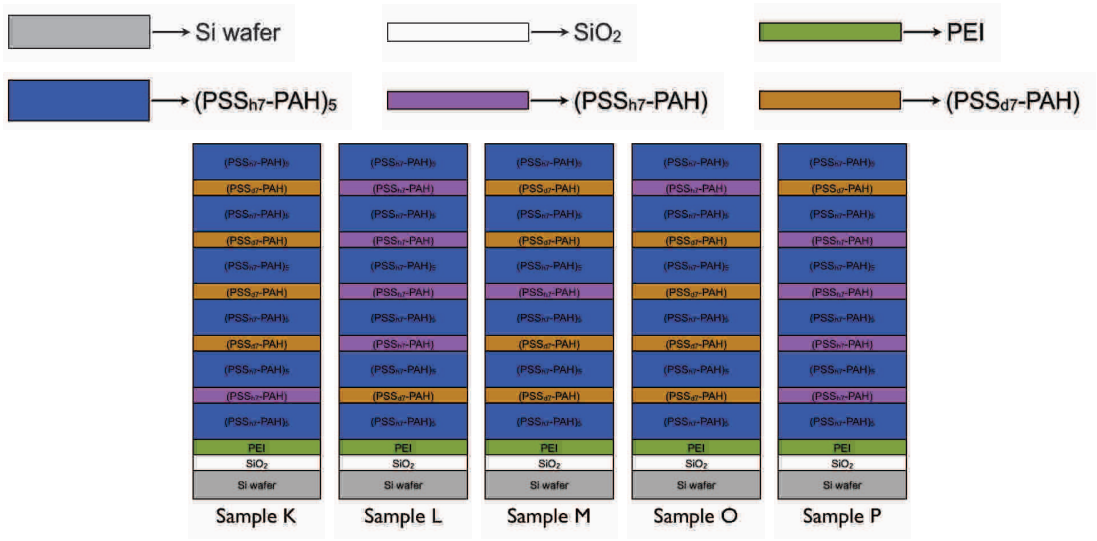

Figure 3.10: Layer sequences for Sample K, L, M, N, O and P. The proportions of the layer thicknesses are not kept.

- Sample Q : $[(\mathrm{PSS}_{h7}\text{-PAH})_6/(\mathrm{PSS}_{d7}\text{-PAH})]_8/(\mathrm{PSS}_{h7}\text{-PAH})_6$ by spraying
- Sample R : $[(\mathrm{PSS}_{h7}\text{-PAH})_3/(\mathrm{PSS}_{d7}\text{-PAH})]_6/(\mathrm{PSS}_{h7}\text{-PAH})_3$ by dipping

Figures 3.9 and 3.10 show the schematic representations of the structure of the multilayer films corresponding to the layer sequence deposition.

3.2.2 Analysis of the LLB measurements

Neutron reflectometry measurements were performed at LLB in 2007 on the eighteen multilayer films described above and the analysis of six of the samples (Sample A to Sample F) was reported in reference [11]. The measurements were carried out on the TOF reflectometer EROS. The measurements were done at a fixed angle of 0.93° with wavelengths from 2.5 Å to 25 Å and a wavelength resolution $\mathrm{d}\lambda/\lambda = 0.025$. Collimation slits of 2 mm and 1 mm were used, leading to an angular resolution of $\mathrm{d}\theta/\theta = 0.045$.

The analysis of the obtained specular reflectivity curves, done with Motofit by O. Félix *et al.* was carried out by considering that the structural parameters are the same for different films prepared in the same conditions, i.e., in our case, the sprayed films have the same structural parameters and the dipped films have the same parameters, because the solutions are the same for all samples. They also considered a homogeneity of the structure inside the films, that means that the layer thickness, the SLDs, as well as the roughness are constant in the films, whatever the position of the layers in the multilayer films is. They determined the layer thickness, the SLDs of the protonated and deuterated parts, and the roughness of the sprayed films from Sample A and Sample B, to 25.4 Å, 1.11 x 10^{-6} $Å^{-2}$, 2.75 x 10^{-6} $Å^{-2}$ and 13.0 Å, respectively. However, they noticed slightly thicker layers for Sample E, with a value of 26.2 Å per layer, and this was attributed to the fact

that this sample was prepared several months after the build-up of the other films. Indeed, ambient conditions are not controlled and can be different in the laboratory depending on the period of the year. Finally, the layer thickness and the roughness of dipped samples were determined from Sample F, the SLDs beeing kept the same like the ones determined for sprayed samples. The layer thickness was calculated by multiplying the layer thickness of Sample E by 1.321, the proportion between the thicknesses of the two samples determined by ellipsometry, and was equal to 34.6 Å. The roughness was calculated with the fit and was 18.0 Å.

For the ageing study, we decided to fit again the specular reflectivities of the samples, but by doing individual fits for all the samples. The reason for this is to have exact values for all the structural parameters fo each sample, to be able to compare accurately the "old" and "new" structures.

Analysis was performed on the specular reflectivity curves by using Motofit. The two first layers, the SiO_2 and the PEI layers, had fixed thicknesses, determined by O. Félix *et al.* by ellipsometry, namely 12.5 Å and 11.5 Å, respectively. The SLD of the SiO_2 layer was set to 3.15 x 10^{-6} $Å^{-2}$ and the roughness at the interface SiO_2/PEI to 4.0 Å. The SLD of the PEI layer was assumed to be identical to the SLD of the layer deposited on it and the roughness of the PEI layer was fixed at 9.0 Å, as it was done by O. Félix and al. *et al.* This roughness has no influence on the fitting process, due to the fact that the SLD of the PEI layer is the same as that of the above layer one, which means that the layers cannot be differenciate and their is no interface between the two layers a seen by neutrons. This is why this value was not changed. Finally, the resolution dq/q was set to 5%. As O. Félix *et al.* did, we considered that the film is homogeneous in the direction perpendicular to the surface, i.e. the layer thicknesses, the protonated and deuterated SLDs and the roughnesses at the interfaces of each film are identical. In Figures 3.11, 3.12 and 3.13 are shown the experimental specular curves with the corresponding fitting curves, as well as the SLD profiles extracted from the fits. The structural parameters values of the films (thickness, SLD, roughness) are summarized in Table 3.5. During the fit, the roughnesses of Sample H and Sample R went down to zero, which, on one hand, is not physically possible as we have interpenetration and, on the other hand, causes some errors in Motofit stopping the fit. For this reason, the roughnesses of these two films were fixed at 10 Å (as indicated in Table 3.5), a value for which the fit is good. One average error estimation of each parameter was calculated for all the films.

We noticed a big difference in the SLDs of Sample R compared to the others : the SLD of the deuterated layers is < 1.9 x 10^{-6} $Å^{-2}$ whereas it is > 2.4 x 10^{-6} $Å^{-2}$ for the other samples. We saw a similar behavior for the SLD of the non-deuterated layers, the SLD beeing lower in this case. It is possible that there was a problem during the preparation of Sample R, as for example a contamination of the film, that could explain the difference of structure.

We observed a similar layer pair thickness for the sixteen samples prepared by spraying, going from 24.3 Å to 27.4 Å per layer pair, corresponding to a difference of 3.1 Å and a proportion of 1.1. Even if the samples were prepared with the same solutions and in the same spraying conditions, some parameters were not controlled.

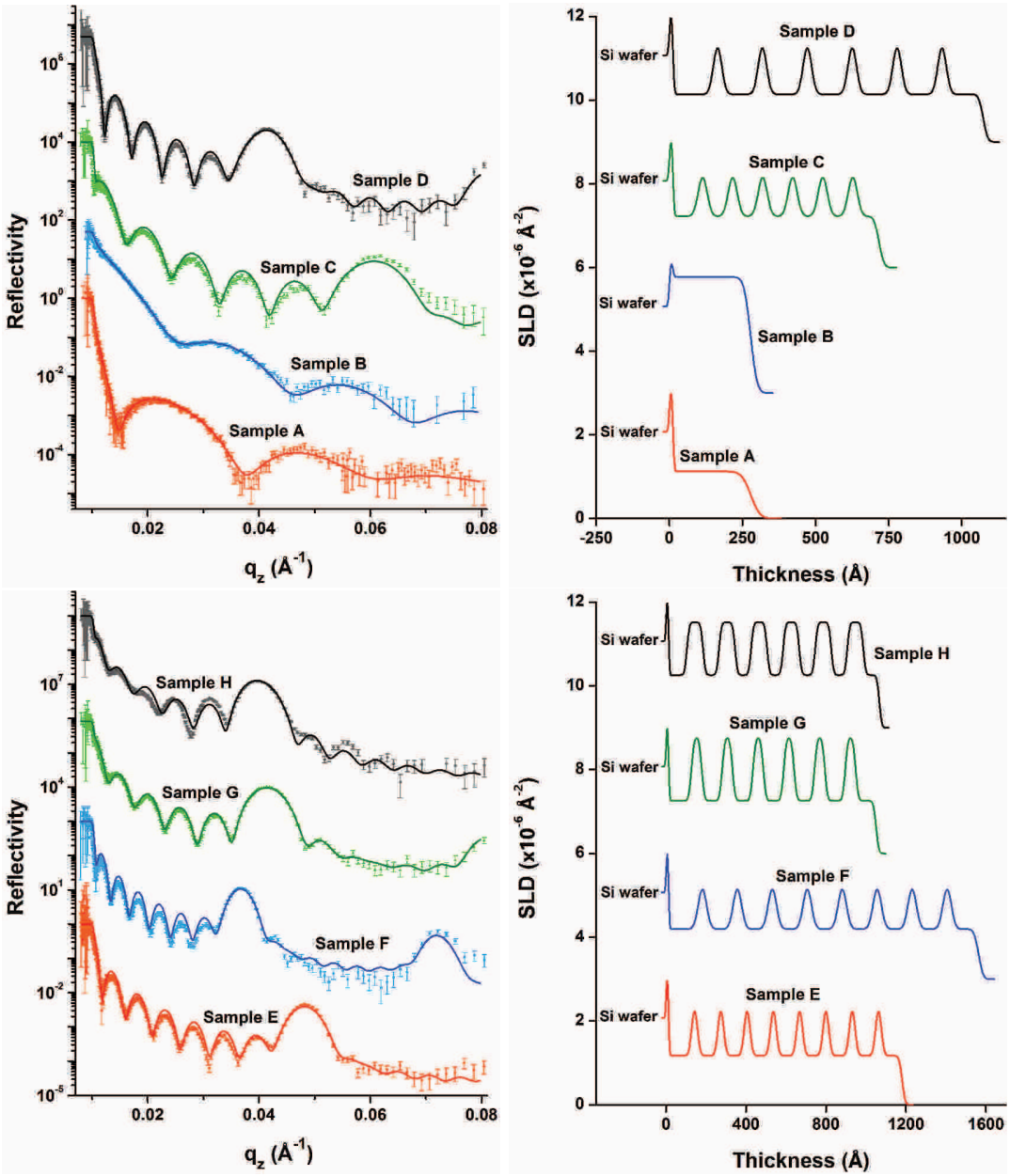

Figure 3.11: On the left, the experimental specular reflectivity curves (points) measured at LLB in 2007 and the corresponding theoretical models (line). On the right, the SLD profiles extracted from the fits. Data for Sample A, B, C, D, E, F, G and H are shown. The curves are shifted for clarity.

We already mentioned that the temperature during the build-up has an influence on the thickness of the mutilayer films of polyelectrolytes and we observed variations of the ambient temperature in the laboratories depending on the seasons and the weather, which could explain the difference observed for the layer pair thickness. Of course, the thicknesses of Sample F and Sample R are larger as these two samples were prepared by dipping, but there is also a difference in thickness between these dipped samples, in the order of 4.6 Å per layer pair. Except for Sample R, the SLDs are quite similar, with an interval of 0.27 x 10^{-6} Å^{-2} (from 1.02 x 10^{-6}

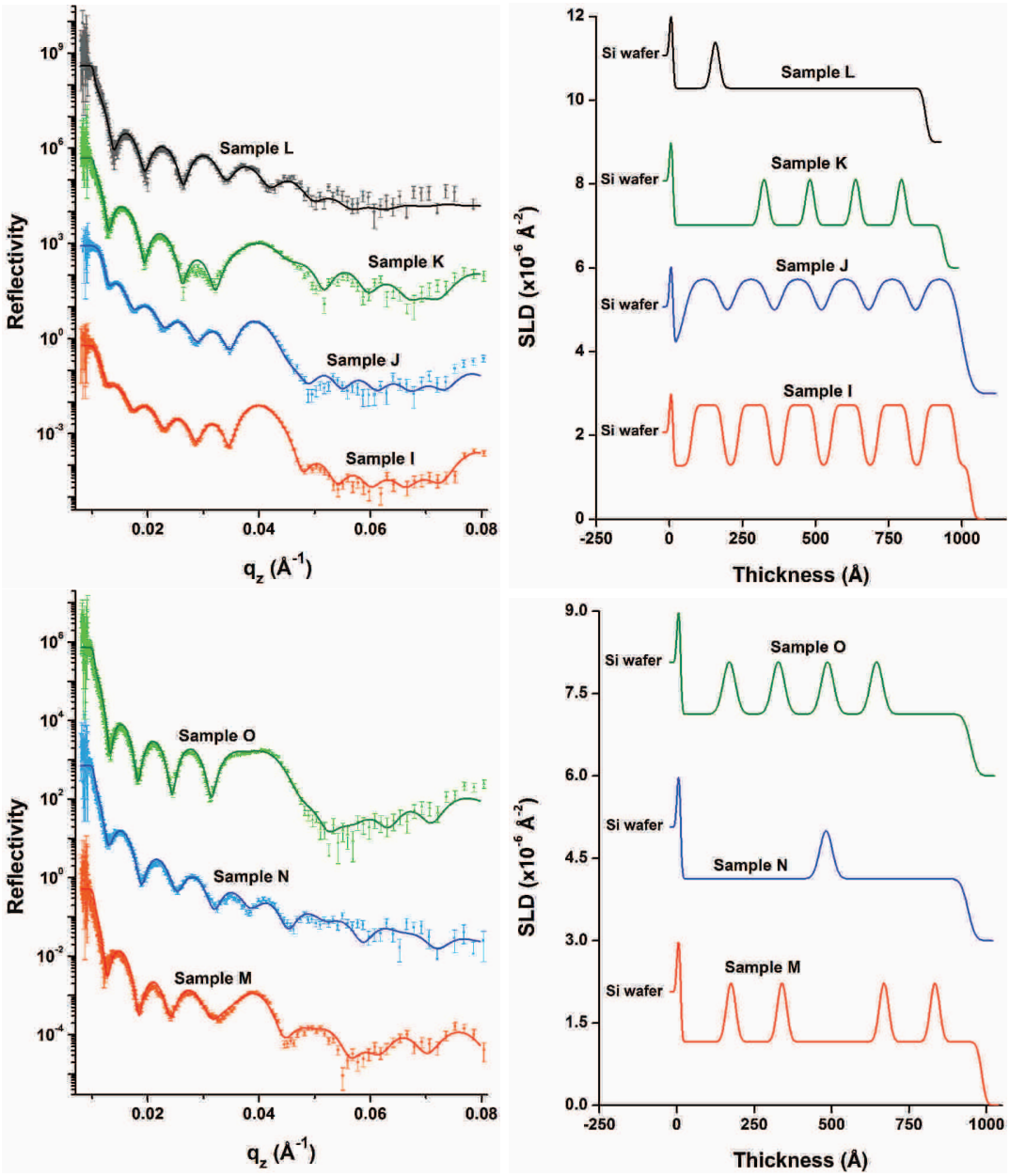

Figure 3.12: On the left, the experimental specular reflectivity curves (points) measured at LLB in 2007 and the corresponding theoretical models (line). On the right, the SLD profiles extracted from the fits. Data for Sample I, J, K, L, M, N and O are shown. The curves are shifted for clarity.

Å^{-2} to 1.29 x 10^{-6} Å^{-2}) for the SLDs of the protonated parts and an interval of 0.44 x 10^{-6} Å^{-2} (from 2.46 x 10^{-6} Å^{-2} to 2.90 x 10^{-6} Å^{-2}) for the deuterated fractions. This corresponds to a proportion of 1.25 for the protonated SLDs and 1.18 for the deuterated SLDs. As the SLD is dependent on the composition and the density of the layers, and as a change of the composition was not expected since the polyelectrolyte solutions were the same, we expect a difference in density in the same proportion than the difference in thickness. Finally, we observed roughnesses from 10 Å to 24.8 Å, which means a difference of 14.8 Å and a proportion of 2.5.

If we compare the films to each other in detail, we can see that the proportions

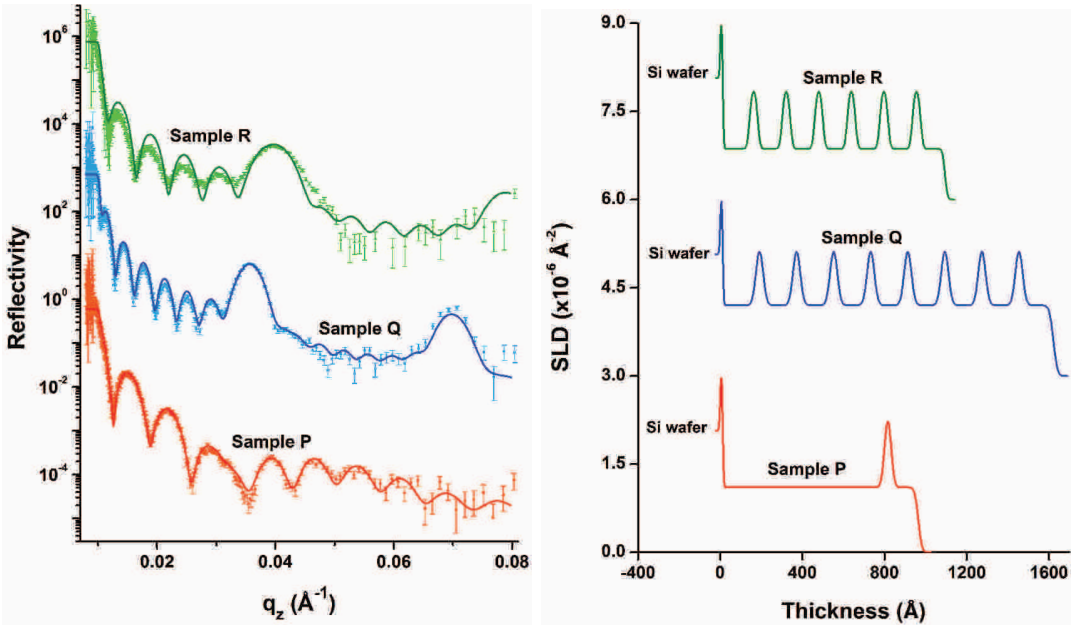

Figure 3.13: On the left, the experimental specular reflectivity curves (points) measured at LLB in 2007 and the corresponding theoretical models (line). On the right, the SLD profiles extracted from the fits. Data for Sample P, Q and R are shown. The curves are shifted for clarity.

	Layer pair thickness (Å)	Protonated SLD (x 10^{-6} Å^{-2})	Deuterated SLD (x 10^{-6} Å^{-2})	Roughness (Å)
Sample A	25.4 ± 2.5	1.12 ± 0.22	X	24.8 ± 10.5
Sample B	25.4 ± 2.5	X	2.77 ± 0.57	17.8 ± 10.5
Sample C	25.7 ± 2.5	1.22 ± 0.22	2.63 ± 0.57	13.5 ± 10.5
Sample D	25.6 ± 2.5	1.14 ± 0.22	2.71 ± 0.57	12.4 ± 10.5
Sample E	26.3 ± 2.5	1.18 ± 0.22	2.62 ± 0.57	12.0 ± 10.5
Sample F	35.0 ± 2.5	1.20 ± 0.22	2.62 ± 0.57	18.3 ± 10.5
Sample G	25.7 ± 2.5	1.26 ± 0.22	2.78 ± 0.57	11.1 ± 10.5
Sample H	26.7 ± 2.5	1.26 ± 0.22	2.52 ± 0.57	10.0 (fixed)
Sample I	26.5 ± 2.5	1.28 ± 0.22	2.73 ± 0.57	10.6 ± 10.5
Sample J	26.8 ± 2.5	1.04 ± 0.22	2.73 ± 0.57	23.6 ± 10.5
Sample K	26.1 ± 2.5	1.02 ± 0.22	2.46 ± 0.57	11.3 ± 10.5
Sample L	24.3 ± 2.5	1.29 ± 0.22	2.84 ± 0.57	11.6 ± 10.5
Sample M	27.4 ± 2.5	1.16 ± 0.22	2.60 ± 0.57	12.2 ± 10.5
Sample N	26.2 ± 2.5	1.13 ± 0.22	2.81 ± 0.57	18.7 ± 10.5
Sample O	26.4 ± 2.5	1.13 ± 0.22	2.90 ± 0.57	18.0 ± 10.5
Sample P	27.0 ± 2.5	1.10 ± 0.22	2.80 ± 0.57	14.2 ± 10.5
Sample Q	25.8 ± 2.5	1.20 ± 0.22	2.77 ± 0.57	16.0 ± 10.5
Sample R	39.6 ± 2.5	0.86 ± 0.22	1.88 ± 0.57	10.0 (fixed)

Table 3.5: Layer pair thicknesses, SLDs and roughnesses determined from the specular reflectivity fits of the eighteen films measured at LLB in 2007.

between the thicknesses, the SLDs and the roughnesses are not the same. Let us take an example, comparing Sample C and Sample I. Sample I had 1.03 times

thicker layer pairs than Sample C, so we could expect smaller SLDs for Sample I than for Sample C. But the protonated SLD of Sample I is 1.05 times bigger than the one of Sample C and the deuterated SLD of Sample I 1.04 times bigger. So we can conclude not only that the SLDs are higher for the thicker film, but also that the proportion between the non-deuterated SLDs of Sample C and Sample I and the proportion between the deuterated SLDs of the two films are not the same. And yet, we would have expected a homogeneous change in SLDs, and therefore in density, in the whole films. Finally, we observe a 1.3 times smaller roughness for Sample I. We see similar behaviours for the other films, the proportions are not the same and we cannot determine a clear trend for the differences of the structural parameters between the eighteen multilayer films.

Surely, all parameters deduced from the fitting of experimental curves have a certain error. Indeed, the values calculated by fitting the experimental reflectivities are adjusted to have the best accordance (minimal chi^2) between the experimental and theoretical reflectivities. Moreover, the reflectivities included some errors coming from the scattering measurements and the fitting. We can assume that the thicknesses determined are accurate, the differences being due to the change in the non-controlled parameters. The differences of SLDs are probably due to fitting errors. Contrary, to what we supposed above, the differences of thicknesses probably do not have to be linked to a modification of density (so SLD), but a change of the adsorbed amount of polyelectrolyte. Concerning the roughness, we could expect similar values for films prepared in the same conditions, the values found are also probably not accurate, even if their are certainly rather correct. It seems that the roughness is the parameter which is the most adjusted to improve the fit by the numerical process, what would explain the large range of values for films prepared in the same conditions, and which have thickness per layer pair which are very similar. For this reason, an assumption is that the SLDs and the roughnesses should be the same or similar for the sixteen films prepared by spraying. A tool to determine if we could use exactly the same structural parameters for films prepared in the same way and to calculate the values of these parameters is the "Global Fit" process of Motofit. This is a function which allows to fit several specular reflectivity curves at the same time and to link parameters from the different films together. So we can fit, for example, the specular reflectivity by asking the "Global Fit" to have the same SLDs for all the films. This work is described in Part 4.1.

Finally, Sample F, prepared by dipping, had thicker layer pairs than the other films, prepared by spraying. But we can see that the SLDs of Sample F, 1.20 x 10^{-6} $Å^{-2}$ for the protonated SLD and 2.62 x 10^{-6} $Å^{-2}$ for the deuterated SLD, are in the range of the SLDs of the sprayed films. This would mean that the SLDs for dipped and sprayed multilayer films are close to each other or even the same. So, we could deduce that the change of thickness is due to a change of adsorbed amount of polyelectrolytes adsorbed and not due to a density change. We can also observe that the roughness of Sample F is in the range of the roughnesses of the sprayed films, what would mean that the interpenetration is similar for dippped and sprayed films, while, due to the charge compensation inside the film, we could assume an increase of the roughness with the increase of thickness.

Then, the films were stored during several years and measured again by neutron reflectometry to study the evolution of the multilayer films of polyelectrolytes with time.

3.2.3 Structural evolution after 5 years

The eighteen films prepared and measured in 2007 were stored in a laboratory without controlling the environment parameters (temperature, humidity, ...) in closed boxes. We could assume rather stable ambient parameters and no contamination.

Six multilayer films of the eighteen were measured by neutron reflectometry at ILL, in 2012 and 2013, that is 5-6 years after their preparation. These films were Sample A and Sample C measured on D17 with the setup D17-1, Sample B, D and F on D17 with the setup D17-2 and Sample E on FIGARO with the setup FIGARO-1 (the setups are described in Part 2.3.1). The specular reflectivity curves obtained are shown in Figures 3.14 and 3.15 with the corresponding fits and the SLD profiles extracted from the fits. For comparison, the specular reflectivity curves, fits and SLD profiles of the neutron reflectometry measurements of Samples A, B, C, D, E and F performed at LLB in 2007 are drawn on the figures.

We can immediately observe on the graphics a shift of the Kiessig fringes and Bragg peaks of the specular reflectivity curves to higher q values in respect to the measurements carried out in 2007. This indicates a decrease of the thicknesses, an it is confirmed by the SLD profiles. This behaviour is observed for the six films. The structural parameters determined from the fits of the measurements done at ILL are summarized in Table 3.6.

	LLB in 2007				ILL in 2012-2013			
	Layer pair thickness (Å)	Protonated SLD (x 10^{-6} Å^{-2})	Deuterated SLD (x 10^{-6} Å^{-2})	Roughness (Å)	Layer pair thickness (Å)	Protonated SLD (x 10^{-6} Å^{-2})	Deuterated SLD (x 10^{-6} Å^{-2})	Roughness (Å)
Sample A	25.4 ± 2.5	1.12 ± 0.22	X	24.8 ± 10.5	24.7 ± 0.4	1.25 ± 0.10	X	10.2 ± 4.0
Sample B	25.4 ± 2.5	X	2.77 ± 0.57	17.8 ± 10.5	24.7 ± 0.4	X	2.98 ± 0.06	13.2 ± 1.4
Sample C	25.7 ± 2.5	1.22 ± 0.22	2.63 ± 0.57	13.5 ± 10.5	24.4 ± 6.5	1.24 ± 0.14	2.97 ± 0.40	10.8 ± 7.1
Sample D	25.6 ± 2.5	1.14 ± 0.22	2.71 ± 0.57	12.4 ± 10.5	24.5 ± 0.6	1.22 ± 0.08	3.07 ± 0.37	13.0 ± 8.5
Sample E	26.3 ± 2.5	1.18 ± 0.22	2.62 ± 0.57	12.0 ± 10.5	23.9 ± 0.3	1.31 ± 0.04	3.27 ± 0.18	11.3 ± 10.1
Sample F	35.0 ± 2.5	1.20 ± 0.22	2.62 ± 0.57	18.3 ± 10.5	32.7 ± 1.1	1.27 ± 0.08	2.86 ± 0.43	15.6 ± 8.1

Table 3.6: Layer pair thicknesses, SLDs and roughnesses determined from the specular reflectivity fits of Sample A, B, C, D, E and F measured at LLB in 2007 and at ILL in 2012-2013.

The structural parmaters of the SiO_2 and PEI layers were kept the same than for the fits of the reflectivities measured at LLB. That is a thickness of 12.5 Å, a SLD of 3.15 x 10^{-6} Å^{-2} and a roughness of 4 Å for the SiO_2 layer, and a thickness of 11.5 Å and a roughness of 9 .0Å for the PEI layer, the SLD was determined by the fits, as we assumed, like before, the same SLD as for the following layer.

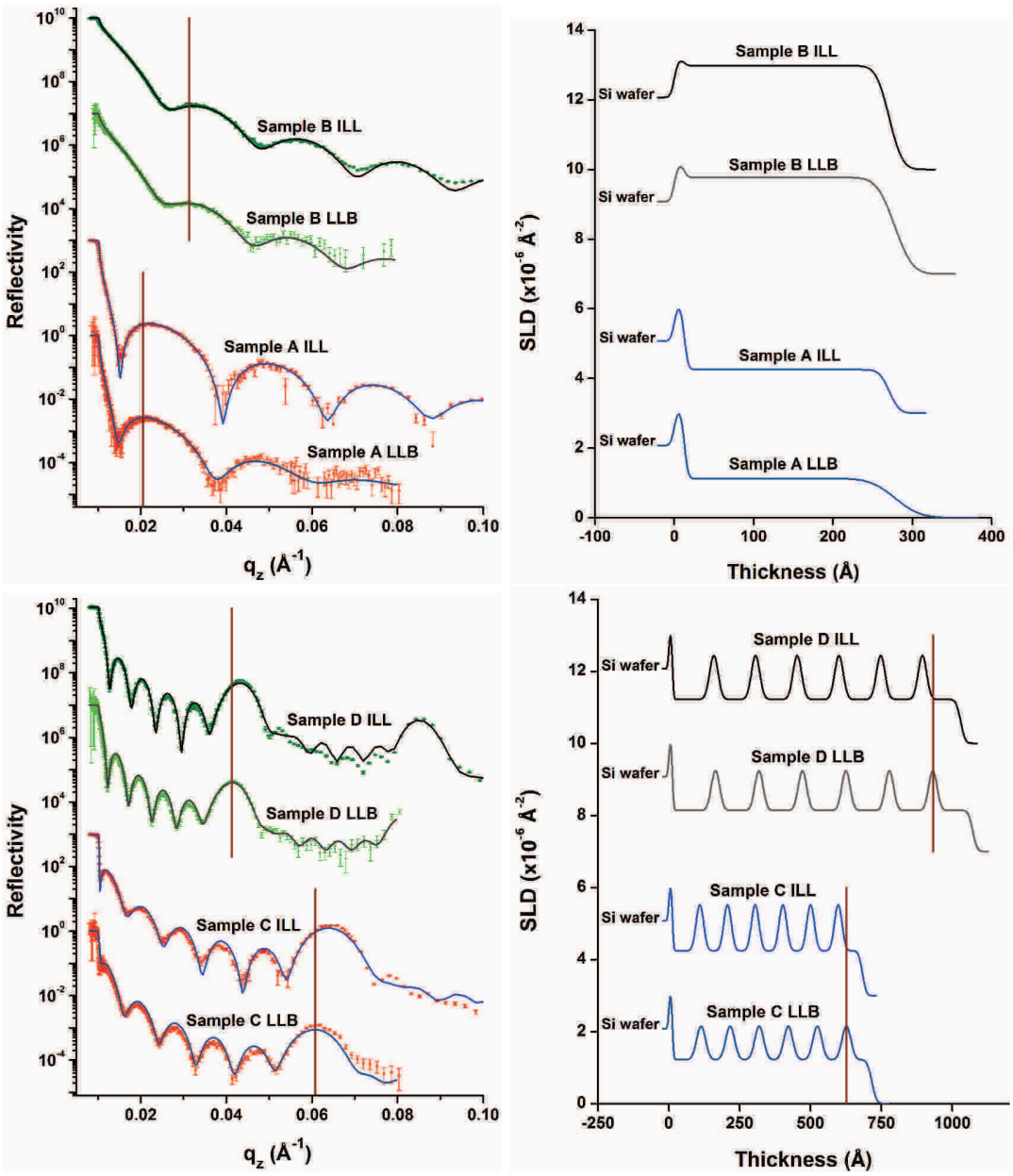

Figure 3.14: On the left, the experimental specular reflectivity curves (points) of Sample A, B, C and D measured at LLB in 2007 and ILL in 2012-2013 and the corresponding theoretical models (line). On the right, the SLD profiles extracted from the fits. The curves are shifted for clarity.

If we compare the structure of the films measured at ILL, we can observe that the parameters are similar for the five sprayed samples, as seen for the measurements at LLB. For the LLB measurements, the thinnest layer pair was 1.04 times thinner than the thickest one, the smallest protonated SLD was 1.09 times lower than the bigger one, the proportion was 1.06 for the deuterated SLDs and the smallest roughness was 2.1 times smaller than the highest roughness. These proportions are similar for the measurements performed in 2012-2013, except for the roughness. For the ILL measurements, the thinnest layer pair was 1.03 times thinner than the thickest one, the lower protonated SLD was 1.07 times smaller

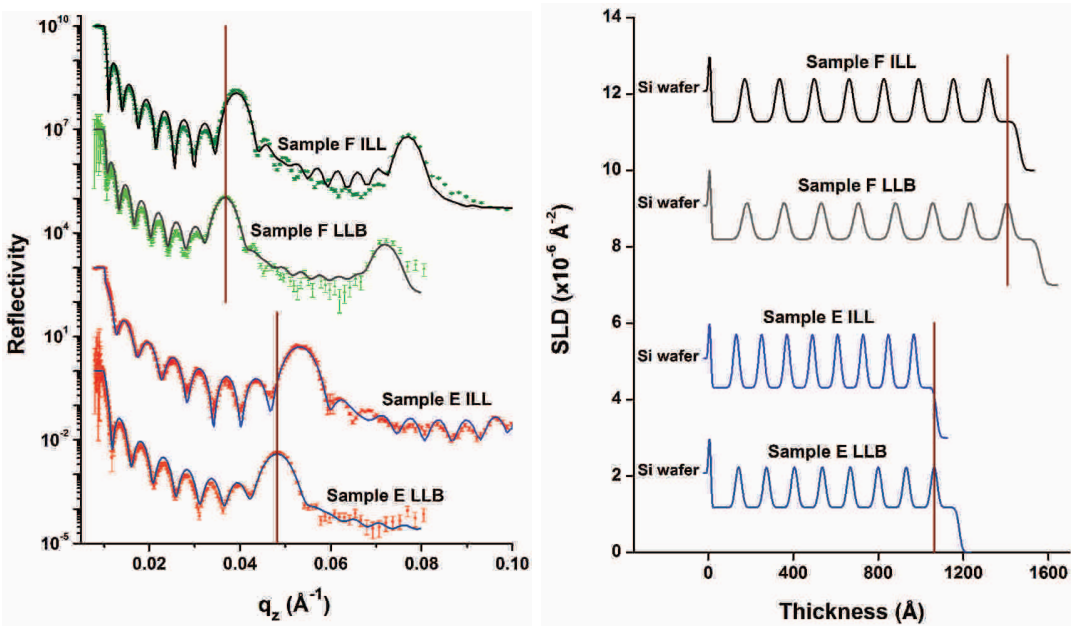

Figure 3.15: On the left, the experimental specular reflectivity curves (points) of Sample E and F measured at LLB in 2007 and ILL in 2012-2013 and the corresponding theoretical models (line). On the right, the SLD profiles extracted from the fits. The curves are shifted for clarity.

than the higher one, this proportion was 1.10 for the deuterated SLDs and the smallest roughness was 1.3 times smaller than the bigger one. As observed above, the SLDs and the roughness of the dipped film were similar to the ones of the sprayed films for the measurements at LLB as well as for the ones at ILL.

After 5 years, there was a decrease of the thicknesses, the films were 1.03 to 1.1 times thinner than the initial films. The initial thicknesses were from 25.4 Å to 26.3 Å per layer pair and after 5 years from 23.9 Å to 24.7 Å per layer pair for the sprayed films. This decrease of thickness went along with an increase of the SLDs, which were 1.02 to 1.12 times bigger for the protonated SLDs (1.12 x 10^{-6} Å^{-2} to 1.22 x 10^{-6} Å^{-2} in 2007 and 1.22 x 10^{-6} Å^{-2} to 1.31 x 10^{-6} Å^{-2} in 2012-2013) and 1.08 to 1.25 times bigger for the deuterated SLDs (2.62 x 10^{-6} Å^{-2} to 2.77 x 10^{-6} Å^{-2} in 2007 and 2.97 x 10^{-6} Å^{-2} to 3.27 x 10^{-6} Å^{-2} in 2012-2013). These values are similar to those found for the thicknesses, even if the deuterated SLDs had increased more. As we did not expect a contamination or a change in composition, we can deduce that the density increased with the decrease of the thickness. The more important change in the deuterated SLDs compared to the protonated SLDs may be due to mathematical errors of the fits. Finally, we see a decrease of the roughnesses, which are 1.1 to 1.9 times smaller than the initial ones (10.2 Å to 13.2 Å at ILL compared to the initial one, from 12.0 Å to 24.8 Å), except for Sample D, for which the thickness was 1.05 times larger than the one determined in 2007.

Concerning the dipped sample, Sample F, there was a decrease of 2.7 Å in thickness per layer pair, from 35.0 Å to 32.7 Å, i.e. Sample F was 1.1 times thinner in 2012-2013 than in 2007. At the same time, the SLDs increased of 0.07 x 10^{-6} Å^{-2} for the protonated layers (from 1.20 x 10^{-6} Å^{-2} to 1.27 x 10^{-6} Å^{-2}) and 0.24 x 10^{-6} Å^{-2} for the deuterated layers (from 2.62 x 10^{-6} Å^{-2} to 2.86 x 10^{-6} Å^{-2}),

which means they were 1.06 times and 1.09 times bigger than the initial SLDs. And again, we observe a decrease of the roughness, from 18.3 Å to 15.6 Å, a difference of 2.7 Å and a proportion of 1.2. These proportions are similar to the ones calculated for the sprayed films, what indicates that the dipped and sprayed films change in a similar way.

We could see that the proportion of the changes of the parameters after 5 years are similar for all the parameters : there was an decrease of thicknesses per layer pair and roughnesses of 1.03 to 1.1 times and 1.1 to 1.9 times respectively, and an increase of the SLDs of 1.02 to 1.12 times for the protonated layers and 1.08 to 1.25 times for the deuterated layers. Even if there are small differences between the proportions, we can assume that the change of the parameters were correlated, as the differences could be due to fitting uncertainties. These changes indicate a shrink of the films, which could be due to a slight rearrangement of the polyelectrolytes inside the films due to internal forces or an evaporation of remaining solvent with time.

In addition to the six samples measured by neutron reflectometry, we decided to measure the thicknesses of all the films by ellipsometry to compare them with the initial thicknesses. The measurements were done in 2014, 1-2 years after the neutron reflectometry measurements at ILL. The measurements were carried out on the monochromatic ellipsometer with a refractive index measured on the spectroscopic ellipsometer for each film, as explained in Part 2.3.2. The total thicknesses measured with the corresponding refractive indexes are summarized in Table 3.7. The thicknesses are the total thicknesses measured by ellipsometry, that is the thicknesses of the films with the PEI and the SiO_2 layers. For comparison, the total thicknesses, including the PEI and SiO_2 layers, determined by neutron reflectometry at LLB in 2007 are also shown.

As we can see in Table 3.7, all the films were thinner in 2014 than in 2007, except for Sample R. The thicknesses were 1.02 to 1.1 times smaller compared to the initial thicknesses. These proportions are similar for the films measured at ILL in 2012-2013 and the other films, we could probably assume that the changes in structure observed at ILL are the same for all the samples, in similar proportions, that is a decrease of thicknesses and roughnesses, and an increase of SLDs. The only exception was Sample R, for which the thickness measured in 2014 was 1.08 times bigger than the one determined by reflectometry in 2007. As we already mentioned, this films had very different SLDs compared to the seventeen other films. It is possible that there was a problem during the preparation of this film, a contamination for example, which could explain this increase instead of a decrease.

	Refractive index	Total thickness in 2014 by ellipsometry (Å)	Total thickness in 2007 by reflectometry (Å)	Ratio between thickness in 2007 and in 2014
Sample A	1.586	267.8 ± 1.1	278.4	1.0
Sample B	1.664	262.8 ± 0.7	277.6	1.1
Sample C	1.614	652.4 ± 2.6	716.7	1.1
Sample D	1.584	1008.1 ± 1.6	1072.7	1.1
Sample E	1.580	1096.0 ± 6.3	1181.0	1.1
Sample F	1.564	1457.4 ± 5.6	1563.8	1.1
Sample G	1.582	995.3 ± 2.0	1050.8	1.1
Sample H	1.582	1002.6 ± 3.5	1067.1	1.1
Sample I	1.585	952.6 ± 2.2	1030.9	1.1
Sample J	1.585	936.1 ± 1.8	1016.1	1.1
Sample K	1.595	857.0 ± 1.6	936.6	1.1
Sample L	1.596	859.1 ± 1.2	875.8	1.0
Sample M	1.594	870.8 ± 2.5	984.2	1.1
Sample N	1.593	862.3 ± 1.6	940.2	1.1
Sample O	1.591	875.8 ± 2.2	948.7	1.1
Sample P	1.592	891.3 ± 2.6	964.5	1.1
Sample Q	1.564	1548.3 ± 8.2	1622.0	1.1
Sample R	1.554	1183.8 ± 48.6	1094.2	0.9

Table 3.7: Total thicknesses of the eighteen samples measured by ellipsometry in 2014 and the refractive indexes used for the measurements. On the right column are indicated the total thicknesses of the multilayer films as measured by neutron reflectometry at LLB in 2007.

3.2.4 Conclusion

To conclude, we observed a slight change of the films after 5 years, a shrink, which presented as a decrease of the thicknesses and roughnesses, and an increase of the SLDs of the films. This could be due to a slight relaxation, plastification of the polyelectrolytes in the films due to the humidity in the air.

3.2.5 Effect of the temperature and the humidity

It was already shown that the temperature and the humidity have an effect on the multilayer films of polyelectrolytes [152, 182–185], and especially on the thickness of the films. So we can wonder whether the slight changes observed for the eighteen films could be due to a difference of the ambient conditions, particularly a difference of temperature and humidity, for the measurements performed in 2007 and in 2012-2013. Indeed, even if the ambient conditions are rather stable in the neutron guide halls, they are not strictly controlled and there are variations of this conditions. What should be done, to be sure to measure the samples at the same conditions, would be to use an environmental chamber, where the conditions can be controlled. Both at the LLB and at the ILL measurements were done at ambient conditions, i.e. without control of temperature and humidity. We did not perform a systematic study of the influence of the temperature and the humidity on the films we studied to know their exact effects, but we observed the influence of

the natural variations of the temperature and the humidity during one measurement.

A multilayer film composed of PSS_{h7}, PSS_{d7} and PAH was built up by alternation of dipping with the dipping robot into solutions of 0.6 mg/mL for the two PSS and 0.27 mg/mL for PAH dissolved in 2M NaCl solutions, for 12 min. Three rinsing steps of 2 min in pure MilliQ water were done after each polyelectrolyte deposition and the film was dried every two layers (after the PAH deposition steps). The film was deposited on a silicon wafer with a first layer of PEI. The structure of the film was three (PSS_{h7}-PAH) layer pairs alternated with one (PSS_{d7}-PAH) layer pair, this stack repeated six times : $Si/SiO_2/PEI/[(PSS_{h7}\text{-}PAH)_3/(PSS_{d7}\text{-}PAH)]_6$. This film was measured by neutron reflectometry on SuperADAM with the setup described in Part 2.3.1 and the specular reflectivity was measured twice for the q range from 0.0055 $Å^{-1}$ to 0.05^{-1} during the same day, once in the morning and once in the afternoon. The two specular reflectivity curves are show in Figure 3.16.

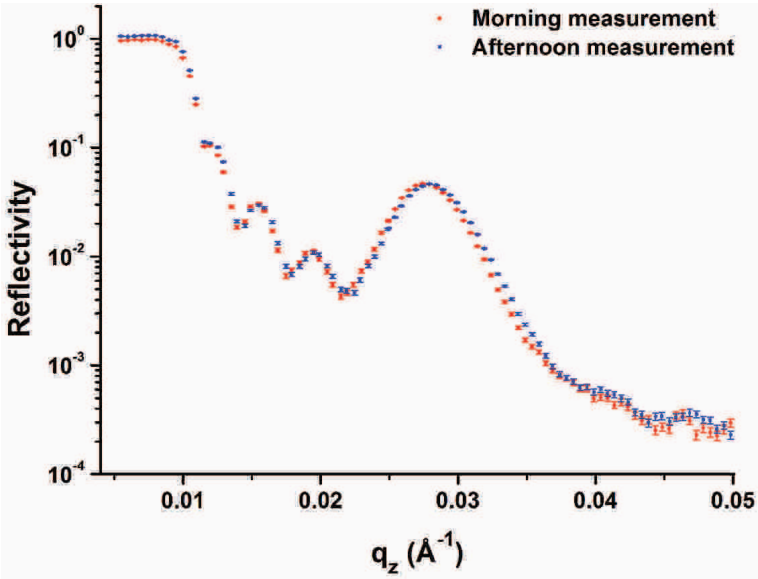

Figure 3.16: Experimental specular reflectivity curve of the dipped film (described above) measured at ILL in the morning and in the afternoon.

We immediately saw that there was a slight shift of the specular reflectivity curve measured in the afternoon to higher q values, what indicates a slight decrease of the film. The conditions were of lower temperature and higher humidity in the morning as compared to the afternoon, but the exact values of the parameters were not noted. In Figure 3.17 are shown the two specular reflectivity curves with the corresponding fits, as well as the SLD profils determined from the fits. The stuctural parameter values are summarized in Table 3.8.

The fits were done by considering a homogeneity of the film along the direction perpendicular to the surface of the sample, i.e. we considered the same thickness per layer pair in the whole film, the same SLD for the protonated layers, the same SLD for the deuterated layers and the same roughness at the interfaces. The thickness of the SiO_2 and PEI layers were measured by ellipsometry and fixed at 8

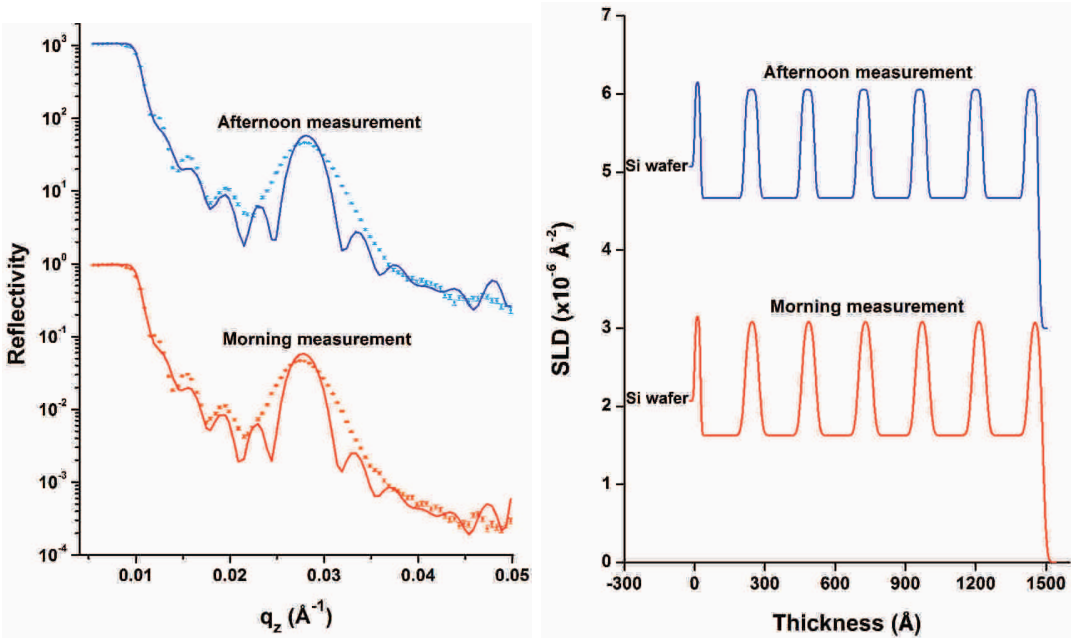

Figure 3.17: On the left, the experimental specular reflectivity curves (points) of the dipped film measured at ILL in the morning and in the afternoon and the corresponding theoretical models (line). On the right, the SLD profiles extracted from the fits. The curves are shifted for clarity.

	Layer pair thickness (Å)	Protonated SLD (x 10^{-6} Å^{-2})	Deuterated SLD (x 10^{-6} Å^{-2})	Roughness (Å)
Morning measurement	60.5 ± 5.6	1.63 ± 0.15	3.10 ± 0.43	12.4 ± 10.9
Afternoon measurement	59.8 ± 6.2	1.67 ± 0.40	3.05 ± 0.40	7.3 ± 15.4
	Layer thickness (Å)	SLD (x 10^{-6} Å^{-2})		Roughness (Å)
PEI layer	8.0 (fixed)	1.63 ± 0.15 / 1.67 ± 0.14		9.0 (fixed)
SiO_2 layer	25.0 (fixed)	3.15 (fixed)		4.0 (fixed)

Table 3.8: Layer pair thicknesses, SLDs and roughnesses determined from the fit of the specular reflectivities measured at ILL in the morning and in the afternoon.

Å for the PEI layer and 25 Å for the SiO_2 layer, after a slight adjustment of a few Ångströms of the measured value of the silicon oxide thickness to improve the fits. The SLD and the roughness of the SiO_2 layer and the roughness of the PEI layer were set at the common values of 3.15 x 10^{-6} Å^{-2}, 4 Å and 9 Å respectively. The values of all these parameters were the same for both fits. The SLD of the PEI layer was considered as the same of the layer adsorbed on it and was fitted with the other parameters.

As determined above, the film was thinner for the measurement done in the afternoon. The thickness per layer pair was 60.5 Å during the morning and 59.8 Å during the afternoon, i.e. the film was 1.01 times thinner during the afternoon. This corresponds to a loss of thickness of 1.1% from the morning to the afternoon. The roughness also changed from 12.4 Å in the morning to 7.3 Å in the afternoon, the film had 1.7 times rougher interfaces during the afternoon, which means a decrease of 41.1% of the roughness. This percentage is much higher than the

one for the thickness, but we can't really distinguish the effect of roughness in this limited q-range. The protonated SLD was 1.03 times higher in the afternoon (an increase from 1.63 x 10^{-6} Å^{-2} to 1.67 x 10^{-6} Å^{-2}), which corresponds to an increase of 2.5% of the SLD from the morning to the afternoon, and the deuterated SLD was 1.02 times lower in the afternoon (a decrease from 3.10 x 10^{-6} Å^{-2} to 3.05 x 10^{-6} Å^{-2}), which means a decrease of 1.6% of the SLD from the morning to the afternoon. With a decrease of the thickness, we could expect an increase of the SLDs due to an increase of the density, which was the case for the protonated SLD but the inverse behaviour happened for the deuterated SLD. The theoretical models does not correspond perfectly to the experimental specular reflectivity curves. In Part 4.2, we describe how we can improve the fits by considering more complex structures while the uncertainty in SLDs and roughness is too high to allow definite conclusions. The thicknesses, which are determined from the gap between the Kiessig fringes and the Bragg peaks, can be considered as accurate since the fringes and peaks of the experimental specular reflectivity curves and the theoretical models are aligned.

To conclude, we have seen that just the change of weather (temperature and humidity) had an influence on the structure determined by fitting the specular reflectivity of the multilayer films of polyelectrolytes. A slight decrease of the thickness was observed between two measurements of the same film at different moments. So, at least a part of the difference observed between the films measured at 5 years interval is probably due to a difference of ambient environments during the measurements performed at LLB in 2007 and at ILL in 2012-2013. To have an accurate comparison of the structure of the films, an environmental chamber, where the ambient conditions are strictly controlled, should be used to carry out neutron reflectometry measurements on multilayer films of polyelectrolytes. Although these chambers are available at the ILL, the size of the substrates was not adapted to the dimensions of the chamber.

3.3 General conclusion

We have seen that after 15 years, multilayer films showed an important structural change, a thickness increase and a SLDs decrease, which was inhomogeneous in the direction perpendicular to the surface. Despite this big changes, there is still a residue of the typical signal of a multilayered structure. We have here reached the limit of interpretation of the reflectivity curve analysis. One explanation of this expansion is an oxydation of the polyelectrolytes. To have a first estimation of this possibility, we performed XPS measurements on three (PSS-PAH) films, 6 months, 5 years and 15 years after their preparation. The measurements and the analysis of the data were carried out by Dr. Vasiliki Papaefthimiou. The proportions of carbon, nitrogen and oxygen in the films are shown in Table 3.9.

The decrease of carbon and nitrogen, and the increase of oxygen after 15 years seems to indicate an oxydation of the polyelectrolytes. As the XPS measurements probe only the surface of the films (a deepth of several nanometers), this trend may

Time after preparation	% C	% N	% O
6 months	68.1	8.7	17.6
5 years	68.2	7	19.7
15 years	64.6	6.6	23.5

Table 3.9: Proportions of carbon, nitrogen and oxygen in 6 months, 5 years and 15 years old multilayer films, as measured by XPS.

not be present in the whole film. But this preliminary result indicates that it is a possibility and other mesurements of the composition of the film, not limited to the surface, have to be carried out to have a better understanding of the structural change after 15 years. Contamination and water uptake in addition to oxydation are not excluded.

We have also observe that a storage of 5 years causes a slight shrink of the films. This is due to a plastification of the polyelectrolytes in the films caused by the humidity in the aire. The structral change is so low that we can consider no change of multilayer films after several months. So we were able to measure the conformation of polyelectrolyte chains in multilayer films even after several months of storage.

Chapter 4

Neutron reflectometry analysis - Global fit and non-homogeneous structures

In this chapter, we describe the "Global Fit" process of Motofit [169], a way to determine average thicknesses, SLDs and roughnesses of several multilayer films prepared in the same conditions. We show the advantages and drawbacks of this process compared to individual fits of the specular reflectivities and we analyse the reproducibility of the films.

We also compare multilayer films prepared in different conditions and determine the structural features of both homogeneous and non-homogeneous structures.

4.1 Global fit

In Part 3.2, we saw that multilayer films prepared exactly in the same conditions with the same solutions have slightly different structural parameter values. We assumed that these differences can come from the non-controlled preparation conditions, as temperature, and from mathematical uncertainties of the fitting process. In order to determine whether films prepared in the same conditions lead to the same structure and to study the reproducibility of the film build-up, we decided to use the "Global Fit" process of Motofit. O. Félix *et al.* [11] already investigated this idea by determining the structural parameter values from two films either fully deuterated or fully protonated. They observed that it is possible to use structural values of some other films prepared in the same conditions, but not for all them. In our case, we went further by using the "Global Fit" process, which allows to fit several reflectivity curves at the same time, with the possibility to link the parameters of the different films together, so that one value of the parameters is calculated for all the films. For example, it is possible to determine one value of the thickness per layer pair for all the films. Then, by comparing the global fit results with the individual fits, it is possible to determine if the parameters are the same for all the films or not.

For this study, we analysed the specular reflectivity curves measured at LLB in 2007 for the sixteen multilayer films prepared by spraying in the same conditions :

- Sample A : $(PSS_{d7}\text{-}PAH)_{10}$ by spraying
- Sample B : $(PSS_{h7}\text{-}PAH)_{10}$ by spraying
- Sample C : $[(PSS_{h7}\text{-}PAH)_3/(PSS_{d7}\text{-}PAH)]_6/(PSS_{h7}\text{-}PAH)_3$ by spraying
- Sample D : $[(PSS_{h7}\text{-}PAH)_5/(PSS_{d7}\text{-}PAH)]_6/(PSS_{h7}\text{-}PAH)_5$ by spraying
- Sample E : $[(PSS_{h7}\text{-}PAH)_4/(PSS_{d7}\text{-}PAH)]_8/(PSS_{h7}\text{-}PAH)_4$ by spraying
- Sample G : $[(PSS_{h7}\text{-}PAH)_4/(PSS_{d7}\text{-}PAH)_2]_6/(PSS_{h7}\text{-}PAH)_4$ by spraying
- Sample H : $[(PSS_{h7}\text{-}PAH)_3/(PSS_{d7}\text{-}PAH)_3]_6/(PSS_{h7}\text{-}PAH)_3$ by spraying
- Sample I : $[(PSS_{h7}\text{-}PAH)_2/(PSS_{d7}\text{-}PAH)_4]_6/(PSS_{h7}\text{-}PAH)_2$ by spraying
- Sample J : $[(PSS_{h7}\text{-}PAH)/(PSS_{d7}\text{-}PAH)_5]_6/(PSS_{h7}\text{-}PAH)$ by spraying
- Sample K : $[(PSS_{h7}\text{-}PAH)_5/(PSS_{h7}\text{-}PAH)]/[(PSS_{h7}\text{-}PAH)_5/(PSS_{d7}\text{-}PAH)]_4/(PSS_{h7}\text{-}PAH)_5$ or $(PSS_{h7}\text{-}PAH)_{11}/[(PSS_{d7}\text{-}PAH)/(PSS_{h7}\text{-}PAH)_5]_4$ by spraying
- Sample L : $[(PSS_{h7}\text{-}PAH)_5/(PSS_{d7}\text{-}PAH)]/[(PSS_{h7}\text{-}PAH)_5/(PSS_{h7}\text{-}PAH)]_4/(PSS_{h7}\text{-}PAH)_5$ or $(PSS_{h7}\text{-}PAH)_5/(PSS_{d7}\text{-}PAH)/(PSS_{h7}\text{-}PAH)_{29}$ by spraying
- Sample M : $[(PSS_{h7}\text{-}PAH)_5/(PSS_{d7}\text{-}PAH)]_2/[(PSS_{h7}\text{-}PAH)_5/(PSS_{h7}\text{-}PAH)]/[(PSS_{h7}\text{-}PAH)_5/(PSS_{d7}\text{-}PAH)]_2/(PSS_{h7}\text{-}PAH)_5$ or $[(PSS_{h7}\text{-}PAH)_5/(PSS_{d7}\text{-}PAH)]_2/(PSS_{h7}\text{-}PAH)_{11}/[(PSS_{d7}\text{-}PAH)/(PSS_{h7}\text{-}PAH)_5]_2$ by spraying
- Sample N : $[(PSS_{h7}\text{-}PAH)_5/(PSS_{h7}\text{-}PAH)]_2/[(PSS_{h7}\text{-}PAH)_5/(PSS_{d7}\text{-}PAH)]/[(PSS_{h7}\text{-}PAH)_5/(PSS_{h7}\text{-}PAH)]_2/(PSS_{h7}\text{-}PAH)_5$ or $(PSS_{h7}\text{-}PAH)_{17}/(PSS_{d7}\text{-}PAH)/(PSS_{h7}\text{-}PAH)_{17}$ by spraying
- Sample O : $[(PSS_{h7}\text{-}PAH)_5/(PSS_{d7}\text{-}PAH)]_4/[(PSS_{h7}\text{-}PAH)_5/(PSS_{h7}\text{-}PAH)]/(PSS_{h7}\text{-}PAH)_5$ or $[(PSS_{h7}\text{-}PAH)_5/(PSS_{d7}\text{-}PAH)]_4/(PSS_{h7}\text{-}PAH)_{11}$ by spraying
- Sample P : $[(PSS_{h7}\text{-}PAH)_5/(PSS_{h7}\text{-}PAH)]_4/[(PSS_{h7}\text{-}PAH)_5/(PSS_{d7}\text{-}PAH)]/(PSS_{h7}\text{-}PAH)_5$ or $(PSS_{h7}\text{-}PAH)_{29}/(PSS_{d7}\text{-}PAH)/(PSS_{h7}\text{-}PAH)_5$ by spraying
- Sample Q : $[(PSS_{h7}\text{-}PAH)_6/(PSS_{d7}\text{-}PAH)]_8/(PSS_{h7}\text{-}PAH)_6$ by spraying

The individual fits are described in Part 3.2, the structural parameters are summarized in Table 4.1 below.

We performed three different global fits, by considering that only one of the parameters is the same for all the samples (thickness, SLDs or roughness). One average error estimation of each parameter was calculated for all the films and for the three global fits.

	Layer pair thickness (Å)	Protonated SLD ($\times 10^{-6}$ Å^{-2})	Deuterated SLD ($\times 10^{-6}$ Å^{-2})	Roughness (Å)
Sample A	25.4 ± 2.5	1.12 ± 0.22	X	24.8 ± 10.5
Sample B	25.4 ± 2.5	X	2.77 ± 0.57	17.8 ± 10.5
Sample C	25.7 ± 2.5	1.22 ± 0.22	2.63 ± 0.57	13.5 ± 10.5
Sample D	25.6 ± 2.5	1.14 ± 0.22	2.71 ± 0.57	12.4 ± 10.5
Sample E	26.3 ± 2.5	1.18 ± 0.22	2.62 ± 0.57	12.0 ± 10.5
Sample G	25.7 ± 2.5	1.26 ± 0.22	2.78 ± 0.57	11.1 ± 10.5
Sample H	26.7 ± 2.5	1.26 ± 0.22	2.52 ± 0.57	10.0 (fixed)
Sample I	26.5 ± 2.5	1.28 ± 0.22	2.73 ± 0.57	10.6 ± 10.5
Sample J	26.8 ± 2.5	1.04 ± 0.22	2.73 ± 0.57	23.6 ± 10.5
Sample K	26.1 ± 2.5	1.02 ± 0.22	2.46 ± 0.57	11.3 ± 10.5
Sample L	24.3 ± 2.5	1.29 ± 0.22	2.84 ± 0.57	11.6 ± 10.5
Sample M	27.4 ± 2.5	1.16 ± 0.22	2.60 ± 0.57	12.2 ± 10.5
Sample N	26.2 ± 2.5	1.13 ± 0.22	2.81 ± 0.57	18.7 ± 10.5
Sample O	26.4 ± 2.5	1.13 ± 0.22	2.90 ± 0.57	18.0 ± 10.5
Sample P	27.0 ± 2.5	1.10 ± 0.22	2.80 ± 0.57	14.2 ± 10.5
Sample Q	25.8 ± 2.5	1.20 ± 0.22	2.77 ± 0.57	16.0 ± 10.5

Table 4.1: Layer pair thicknesses, SLDs and roughnesses determined from the specular reflectivity fits of the sixteen sprayed films measured at LLB in 2007.

4.1.1 Effect on the thickness per layer pair

In this part, we carried out a global fit by linking the thicknesses per layer pair so that they are the same for all the films. The SLDs and roughnesses were kept independent. The initial parameters were set to the values calculated by the individual fits except for the layer pair thickness, which was set to 25.4 Å for all the films as a first guess (value determined for Sample A and Sample B by individual fitting). Five consecutive numerical fits were done using a Levenberg-Marquardt algorithm, without changing the values between the fits, to obtain more accurate values. For Sample L, G and H, the fitting routine was not sensitive to their roughnesses after the first fit for Sample L and after the second fit for Sample G and H. So the roughness values were kept constant at the values determined when the problem occured, that is 0.9 Å for Sample L, 2.6 Å for Sample G and 0.1 Å for Sample H.

The experimental reflectivity curves and the theoretical models determined after the fifth fit are shown in Figures 4.1 and 4.2. The values of the structural parameters extracted from the fits are summarized in Table 4.2.

We can observe that in some cases, the experimental specular reflectivity curve and the theoretical model are shifted, the Kiessig fringes and the Bragg peaks being not well aligned. This is due to the differences between the thicknesses per layer pair calculated with the global fit and the ones determined with the individual fits. We have calculated a thickness of 26.3 Å per layer pair with the global fit, whereas the minimum thickness determined by the individual fits was 24.3 Å per layer pair (Sample L) and the maximum thickness was 27.4 Å per layer pair (Sample M). This corresponds to a difference of 7.6% (2 Å per layer pair) from 26.3 Å to 24.3 Å and 4,2% (1.1 Å per layer pair) from 26.3 Å to 27.4 Å. We observe that the structure

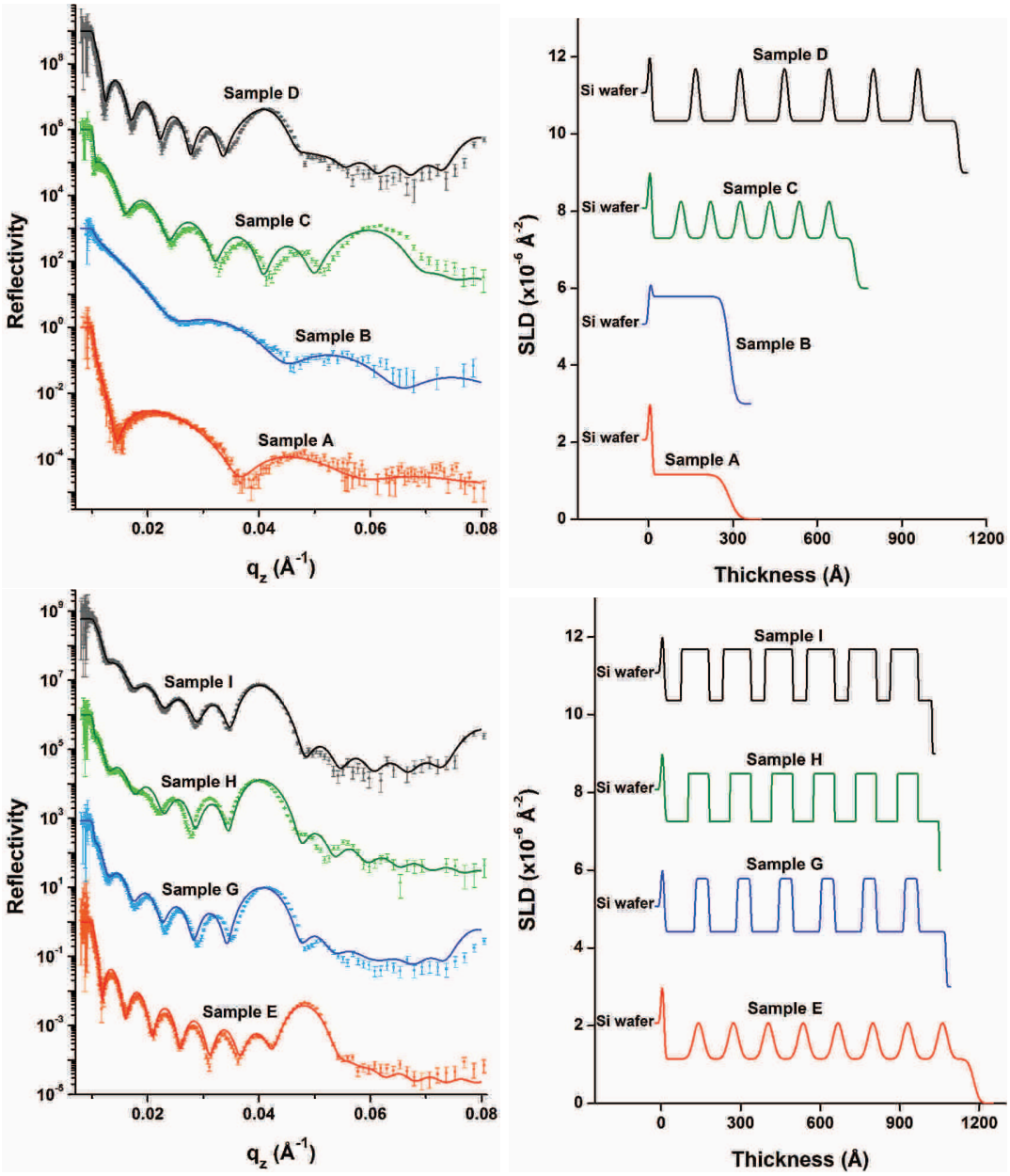

Figure 4.1: On the left, the experimental specular reflectivity curves (points) measured at LLB in 2007 and the corresponding theoretical models (line). On the right, the SLD profiles extracted from the fits. Data for Sample A, B, C, D, E, G, H and I are shown. The curves are shifted for clarity.

of Sample L was not kept, the deuterated layers had an SLD of 1.35 x 10^{-6} Å^{-2} instead of 2.84 x 10^{-6} Å^{-2} and the protonated layers a SLD of 1.62 x 10^{-6} Å^{-2} instead of 1.29 x 10^{-6} Å^{-2}. The deuterated SLD is really low, the value corresponds to the average value of the protonated SLDs, and is smaller than the protonated SLD of Sample L. As there is no Bragg peak, this difference of SLD does not have a particularly visible effect on the reflectivity curve, but does not correspond to the real structure. Except for Sample L, the protonated SLDs had values from 0.95 x 10^{-6} Å^{-2} to 1.41 x 10^{-6} Å^{-2} and the deuterated SLDs had values from 2.35 x

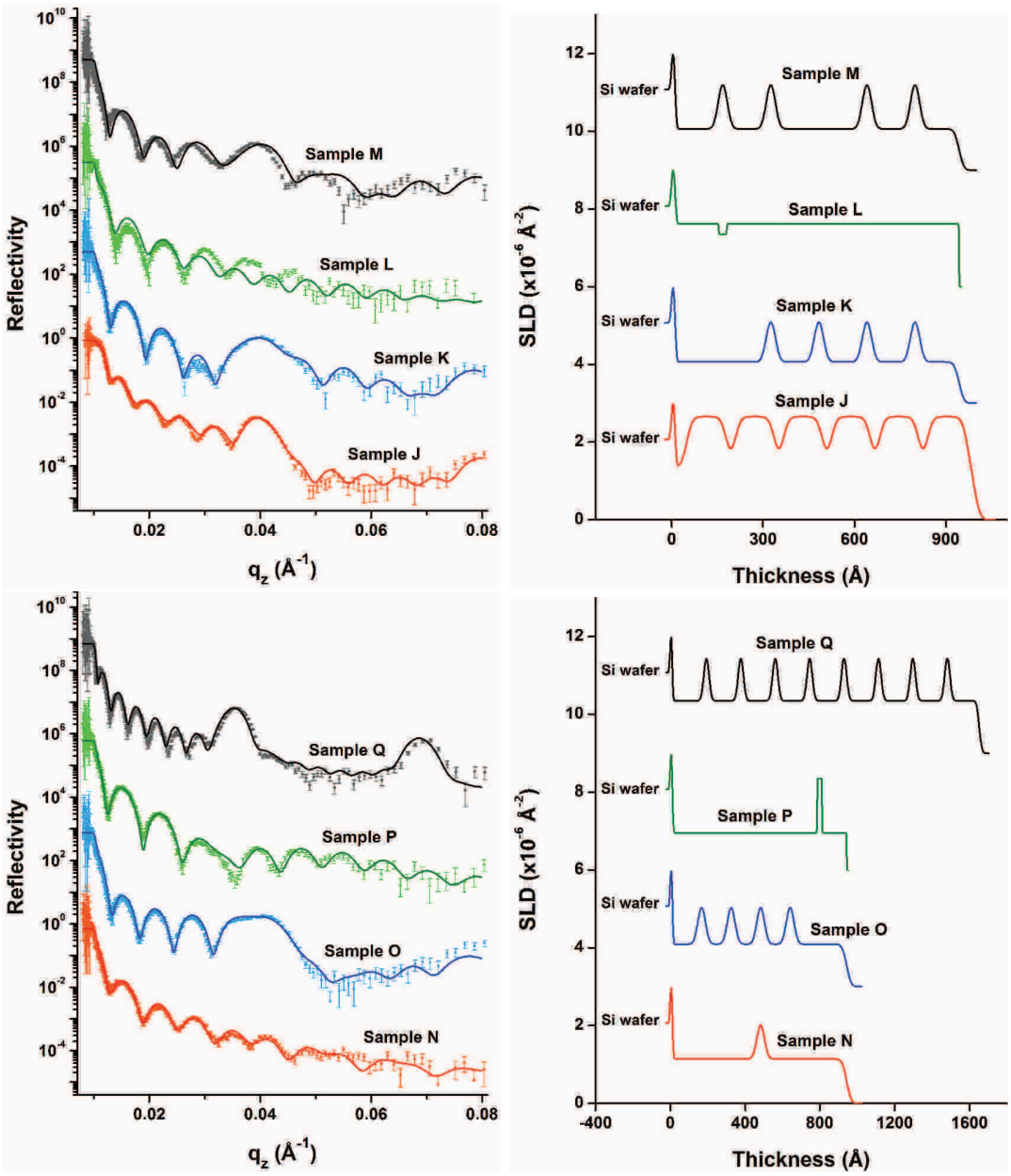

Figure 4.2: On the left, the experimental specular reflectivity curves (points) measured at LLB in 2007 and the corresponding theoretical models (line). On the right, the SLD profiles extracted from the fits. Data for Sample J, K, L, M, N, O, P and Q are shown. The curves are shifted for clarity.

10^{-6} Å^{-2} to 2.93 x 10^{-6} Å^{-2}. These values are similar to those calculated with the individual fits (from 1.02 x 10^{-6} Å^{-2} to 1.29 x 10^{-6} Å^{-2} for the protonated SLDs and from 2.46 x 10^{-6} Å^{-2} to 2.90 x 10^{-6} Å^{-2} for the deuterated SLDs). Finally, the roughnesses determined with the global fit, from 0.1 Å to 26.8 Å, have maximal values similar to those determined by individual fitting, 24.8 Å, but have a much smaller minimal value than that from the individual fits, 10.0 Å. These differences of SLDs and roughnesses values between the global fits and the individual fits are due to a compensation of the errors induced by the differences of thicknesses per

	Layer pair thickness (Å)	Protonated SLD (x 10^{-6} Å^{-2})	Deuterated SLD (x 10^{-6} Å^{-2})	Roughness (Å)
Sample A	26.3 ± 4.0	1.16 ± 0.35	X	26.8 ± 16.5
Sample B		X	2.78 ± 0.65	17.6 ± 16.5
Sample C		1.30 ± 0.35	2.46 ± 0.65	9.8 ± 16.5
Sample D		1.34 ± 0.35	2.75 ± 0.65	6.5 ± 16.5
Sample E		1.14 ± 0.35	2.77 ± 0.65	16.7 ± 16.5
Sample G		1.41 ± 0.35	2.78 ± 0.65	2.6 (fixed)
Sample H		1.26 ± 0.35	2.48 ± 0.65	0.1 (fixed)
Sample I		1.36 ± 0.35	2.68 ± 0.65	1.1 ± 16.5
Sample J		1.34 ± 0.35	2.65 ± 0.65	15.0 ± 16.5
Sample K		1.06 ± 0.35	2.54 ± 0.65	12.9 ± 16.5
Sample L		1.62 ± 0.35	1.35 ± 0.65	0.9 (fixed)
Sample M		1.06 ± 0.35	2.67 ± 0.65	12.6 ± 16.5
Sample N		1.14 ± 0.35	2.83 ± 0.65	18.9 ± 16.5
Sample O		1.09 ± 0.35	2.93 ± 0.65	19.0 ± 16.5
Sample P		0.95 ± 0.35	2.35 ± 0.65	1.3 ± 16.5
Sample Q		1.35 ± 0.35	2.78 ± 0.65	11.3 ± 16.5

Table 4.2: Layer pair thicknesses, SLDs and roughnesses determined from the specular reflectivity fits of the sixteen sprayed films measured at LLB in 2007.

layer pair.

The values of the thicknesses determined by individual fitting are close to those determined by global fitting, but we can see a visible difference on the fits. This suggests that the thickness differences determined by the individual fits of the specular reflectivity curves are not due to the uncertainty of the fitting routine, but this difference is probably a real difference of thickness due to non-controlled parameters during the preparation of the films.

4.1.2 Effect on the SLDs

In this part, we carried out a global fit by linking the SLDs (deuterated and protonated) so that they have the same value for all the films. The thicknesses and roughnesses were kept independent. The initial parameters were set to the values calculated by the individual fits except for the SLDs, which were set to 1.12 x 10^{-6} Å^{-2} for the protonated SLDs and 2.77 x 10^{-6} Å^{-2} for the deuterated SLDs for all the films (values determined for Sample A and Sample B). Five consecutive numerical fits were done using a Levenberg-Marquardt algorithm, without changing the values between the fits, to obtain more accurate values.

The experimental reflectivity curves and the theoretical models determined after the fifth fit are shown in Figures 4.3 and 4.4. The values of the structural parameters extracted from the fits are summarized in Table 4.3.

We can see that the theoretical models produce good fits for the specular reflectivity curves, which indicates that the values determined for the protonated and deuterated SLDs, which are the same for the sixteen films, are accurate values for

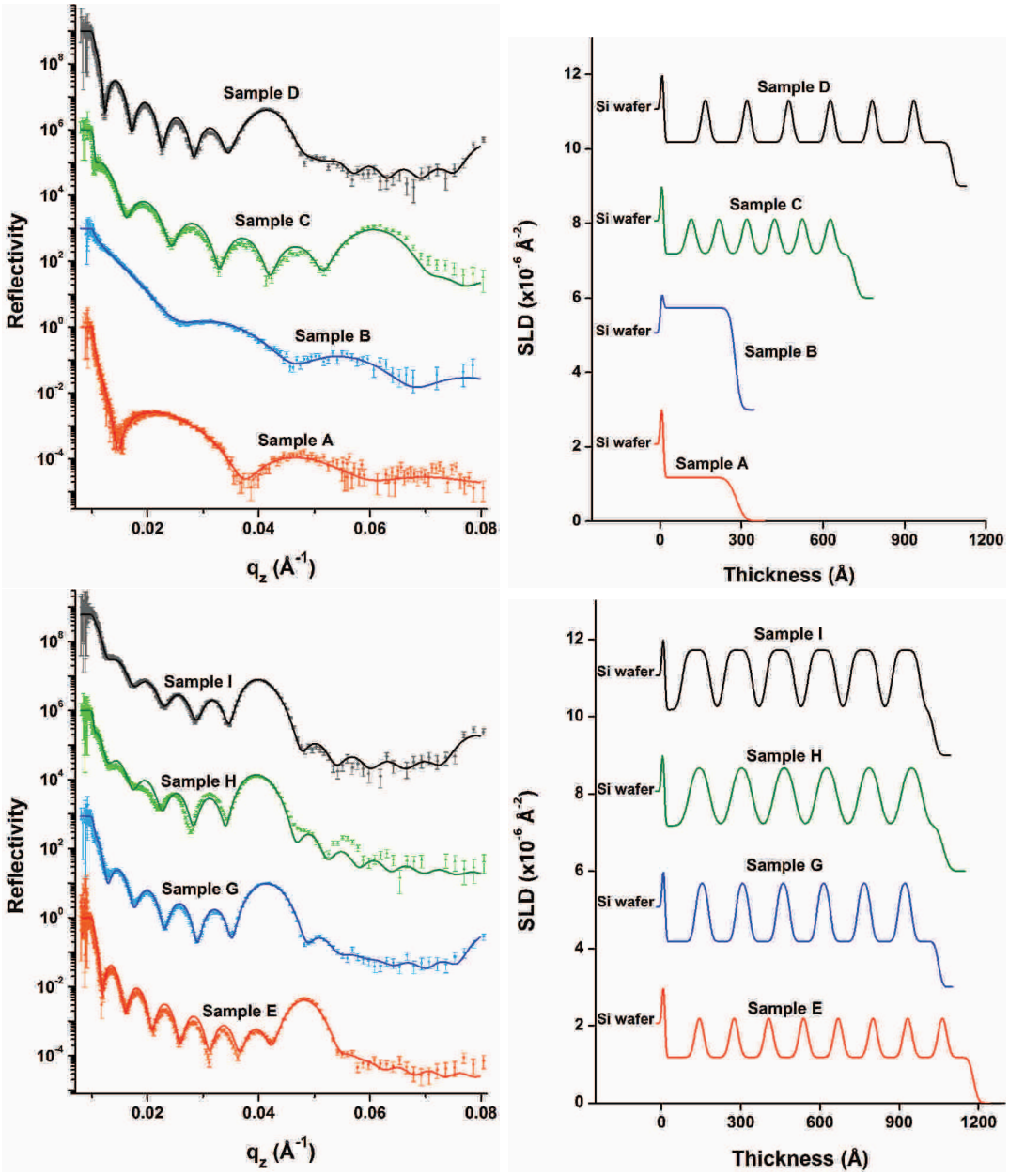

Figure 4.3: On the left, the experimental specular reflectivity curves (points) measured at LLB in 2007 and the corresponding theoretical models (line). On the right, the SLD profiles extracted from the fits. Data for Sample A, B, C, D, E, G, H and I are shown. The curves are shifted for clarity.

the structure of the films. This indicates that the differences between the SLDs calculated individually are due to mathematical errors and we can assume that the SLDs, and the densities, are the same for multilayer films prepared in the same conditions, even if differences of thicknesses are observed. This indicates that the thickness differences are going along with a difference of polyelectrolyte quantity adsorbed and not a difference of density. The protonated SLD had a value of 1.18 x 10^{-6} Å^{-2}, which gives a difference of 13.6% (0.16 x 10^{-6} Å^{-2}) with the minimal value of 1.02 x 10^{-6} Å^{-2} determined by individual fitting and a difference of 9.3%

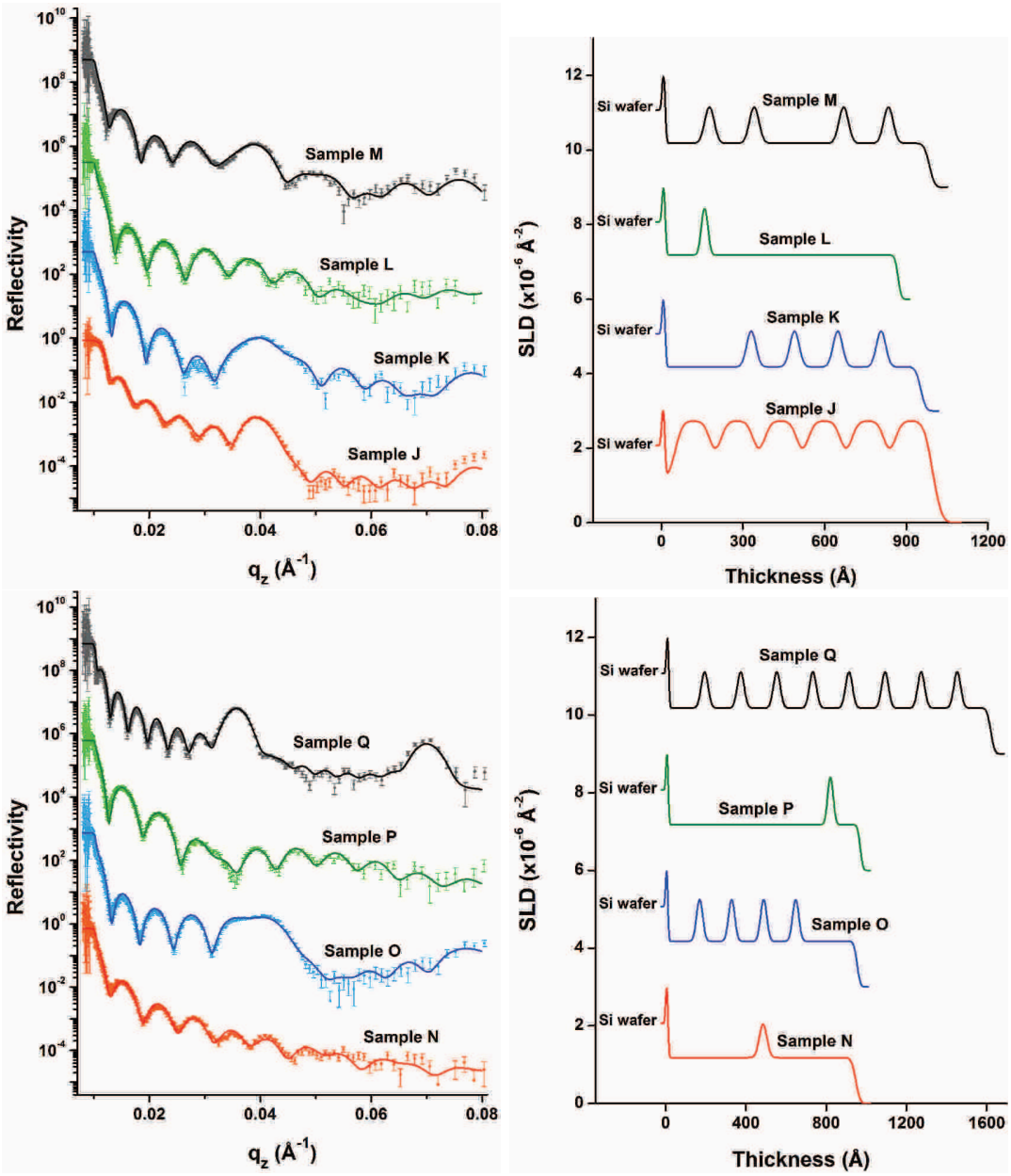

Figure 4.4: On the left, the experimental specular reflectivity curves (points) measured at LLB in 2007 and the corresponding theoretical models (line). On the right, the SLD profiles extracted from the fits. Data for Sample J, K, L, M, N, O, P and Q are shown. The curves are shifted for clarity.

(0,11 x 10^{-6} Å^{-2}) with the maximal value of 1.29 x 10^{-6} Å^{-2}. The deuterated SLD was 2.73 x 10^{-6} Å^{-2}, which corresponds to a difference of 9.9% (0.27 x 10^{-6} Å^{-2}) with the minimal value of 2.46 x 10^{-6} Å^{-2} and 6.2% (0.17 x 10^{-6} Å^{-2}) with the maximal value of 2.90 x 10^{-6} Å^{-2}. The thicknesses calculated by global fitting were similar to those determined by individual fitting, with a range of 24.1 Å to 27.4 Å instead of 24.3 Å to 27.4 Å. We observe the same behaviour for the roughnesses with values from 9.3 Å to 25.2 Å for the global fit compared to 10.0 Å to 24.8 Å for the individual fits.

	Layer pair thickness (Å)	Protonated SLD (x 10^{-6} Å^{-2})	Deuterated SLD (x 10^{-6} Å^{-2})	Roughness (Å)
Sample A	25.7 ± 4.0	1.18 ± 0.35	X	25.2 ± 16.5
Sample B	25.2 ± 4.0	X	2.73 ± 0.65	15.8 ± 16.5
Sample C	25.6 ± 4.0	1.18 ± 0.35	2.73 ± 0.65	15.1 ± 16.5
Sample D	25.6 ± 4.0			11.7 ± 16.5
Sample E	26.3 ± 4.0			14.0 ± 16.5
Sample G	25.6 ± 4.0			11.7 ± 16.5
Sample H	26.8 ± 4.0			19.4 ± 16.5
Sample I	26.5 ± 4.0			14.0 ± 16.5
Sample J	26.7 ± 4.0			21.5 ± 16.5
Sample K	26.5 ± 4.0			15.1 ± 16.5
Sample L	24.1 ± 4.0			9.3 ± 16.5
Sample M	27.4 ± 4.0			15.4 ± 16.5
Sample N	26.4 ± 4.0			17.3 ± 16.5
Sample O	26.6 ± 4.0			13.1 ± 16.5
Sample P	27.0 ± 4.0			11.0 ± 16.5
Sample Q	25.7 ± 4.0			15.3 ± 16.5

Table 4.3: Layer pair thicknesses, SLDs and roughnesses determined from the specular reflectivity fits of the sixteen sprayed films measured at LLB in 2007.

Finally, we can consider the same SLDs for multilayer films prepared in the same conditions, the differences observed by fitting individually are probaby within the error of the fit. We also determined that the differences of thickness go along with a difference of amount of polyelectrolytes adsorbed and not a difference of density.

4.1.3 Effect on the roughness

In this part, we carried out a global fit by linking the roughnesses so that they are the same for all the films. The thicknesses and SLDs were kept independent. The initial parameters were set to the values calculated by the individual fits except for the roughnesses, which were set to 14.9 Å, the average value of the roughnesses. Five consecutive numerical fits were done using a Levenberg-Marquardt algorithm, without changing the values between the fits, to obtain more accurate values.

The experimental reflectivity curves and the theoretical models determined after the fifth fit are shown in Figures 4.5 and 4.6. The values of the structural parameters extracted from the fits are summarized in Table 4.4.

As for the SLDs, the theoretical models fit nicely the specular reflectivity curves when we consider the same roughness for the sixteen sprayed films. So, the value of roughness calculated by global fitting is very likely the real roughness at the interfaces even if there are differences with the individual fits. Like for the SLDs, these differences are probably due to fitting uncertainties and not to a real difference in roughness. The roughness value was 13.8 Å for the global fitting and 10.0 Å for the minimal roughness determined by individual fitting, that is a difference of 27.5% (3.8 Å), and 24.8 Å for the maximal roughness, which means a

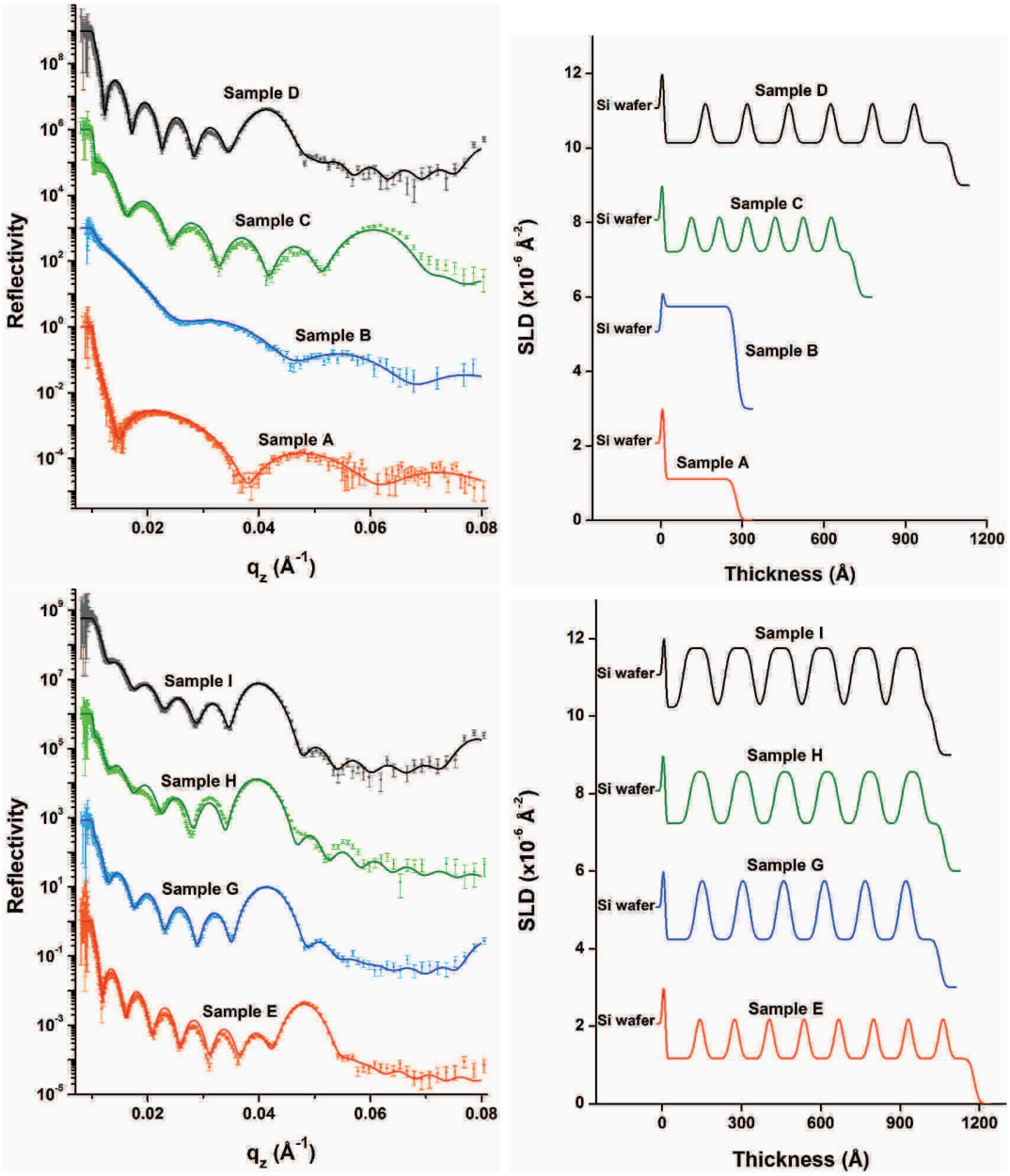

Figure 4.5: On the left, the experimental specular reflectivity curves (points) measured at LLB in 2007 and the corresponding theoretical models (line). On the right, the SLD profiles extracted from the fits. Data for Sample A, B, C, D, E, G, H and I are shown. The curves are shifted for clarity.

difference of 79.7% (11.0 Å). The thicknesses were the same or nearly the same for the global fit and the individual fits, with a range of 24.3 Å to 27.4 Å calculated by global fitting and by individual fitting. The protonated SLDs were from 1.02 x 10^{-6} Å^{-2} to 1.35 x 10^{-6} Å^{-2} for the global fit and from 1.02 x 10^{-6} Å^{-2} to 1.29 x 10^{-6} Å^{-2} for the individual fits, while values for the deuterated SLD were included in the ranges 2.53 x 10^{-6} Å^{-2} to 2.88 x 10^{-6} Å^{-2} calculated by global fitting and 2.46 x 10^{-6} Å^{-2} to 2.90 x 10^{-6} Å^{-2} determined by individual fitting. The values are also close to each other.

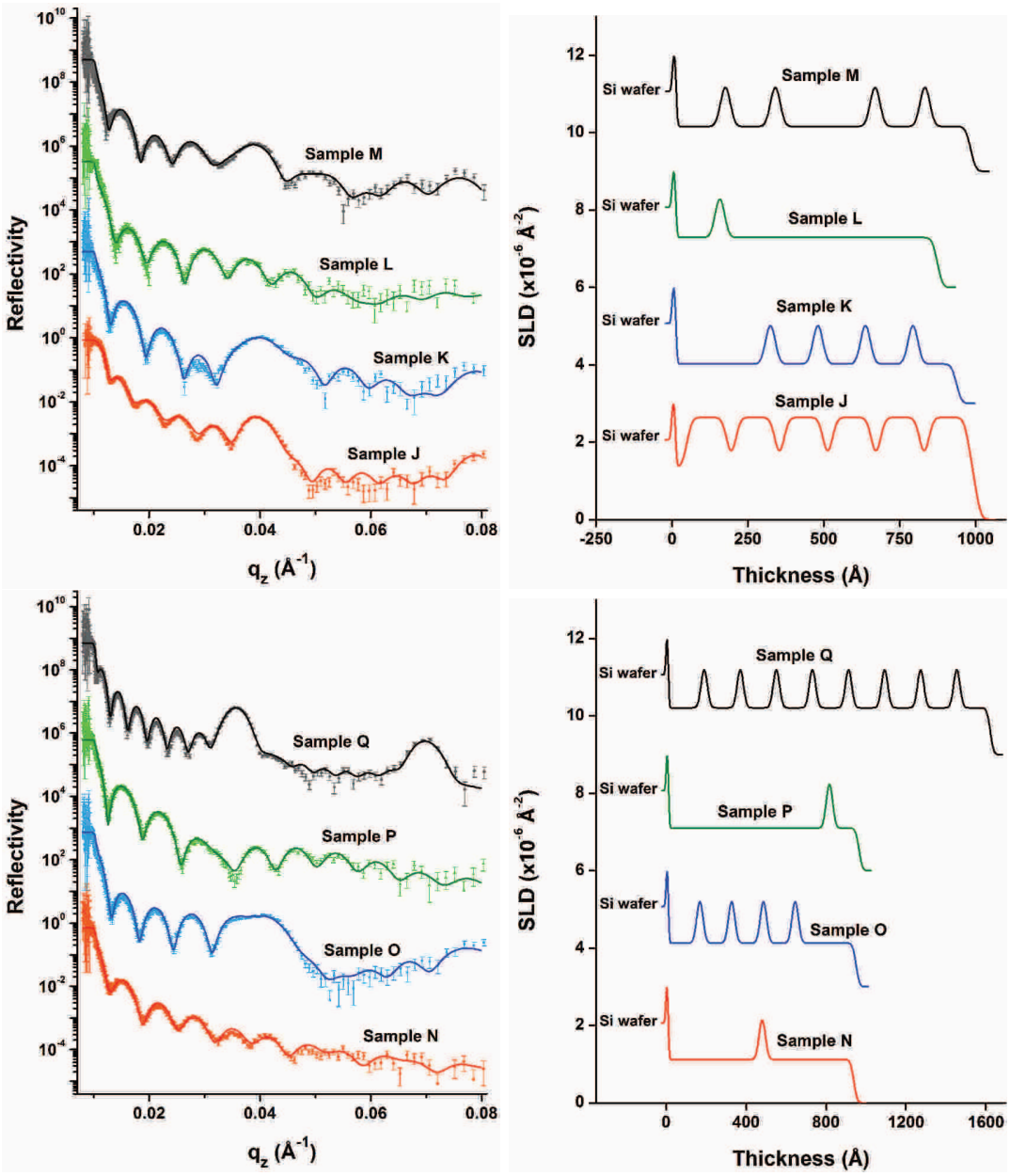

Figure 4.6: On the left, the experimental specular reflectivity curves (points) measured at LLB in 2007 and the corresponding theoretical models (line). On the right, the SLD profiles extracted from the fits. Data for Sample J, K, L, M, N, O, P and Q are shown. The curves are shifted for clarity.

Like for the SLDs, we can conclude that the roughnesses are the same for multilayer films prepared in the same conditions and the differences observed with the individual fitting come from uncertainties of the fitting process.

	Layer pair thickness (Å)	Protonated SLD (x 10^{-6} Å^{-2})	Deuterated SLD (x 10^{-6} Å^{-2})	Roughness (Å)
Sample A	25.3 ± 4.0	1.11 ± 0.35	X	13.8 ± 16.5
Sample B	25.3 ± 4.0	X	2.75 ± 0.65	
Sample C	25.7 ± 4.0	1.22 ± 0.35	2.64 ± 0.65	
Sample D	25.6 ± 4.0	1.14 ± 0.35	2.76 ± 0.65	
Sample E	26.3 ± 4.0	1.16 ± 0.35	2.70 ± 0.65	
Sample G	25.7 ± 4.0	1.24 ± 0.35	2.85 ± 0.65	
Sample H	26.8 ± 4.0	1.23 ± 0.35	2.57 ± 0.65	
Sample I	26.5 ± 4.0	1.23 ± 0.35	2.76 ± 0.65	
Sample J	26.5 ± 4.0	1.35 ± 0.35	2.64 ± 0.65	
Sample K	26.1 ± 4.0	1.02 ± 0.35	2.53 ± 0.65	
Sample L	24.3 ± 4.0	1.29 ± 0.35	2.88 ± 0.65	
Sample M	27.4 ± 4.0	1.16 ± 0.35	2.64 ± 0.65	
Sample N	26.2 ± 4.0	1.12 ± 0.35	2.66 ± 0.65	
Sample O	26.5 ± 4.0	1.13 ± 0.35	2.74 ± 0.65	
Sample P	26.9 ± 4.0	1.10 ± 0.35	2.79 ± 0.65	
Sample Q	25.8 ± 4.0	1.21 ± 0.35	2.72 ± 0.65	

Table 4.4: Layer pair thicknesses, SLDs and roughnesses determined from the specular reflectivity fits of the sixteen sprayed films measured at LLB in 2007.

4.1.4 Conclusion

To conclude, we have seen that we have the same values of SLDs and roughness for multilayer films prepared in the same conditions and that we can determine an average value by using the global fit process. The differences of the values calculated by individual fitting are due to uncertainties of the fitting process. However, the differences of thickness observed with the individual fits are real. We already assumed that these differences of thickness are probably due to non-controlled parameters during the build-up of the films, as the temperature.

4.2 Non-homogeneous structures

Nine multilayer films composed of PSS and PAH were built up in different conditions and measured by neutron reflectometry to compare their structures. We observed that considering a homogeneous structure does not give the best fit and that we have to use non-homogeneous structures.

4.2.1 Multilayer films build-up

Nine multilayer films were prepared by alternating PSS_{h7}, PSS_{d7} and PAH depositions and had the same layer sequence, an alternation of three layer pairs (PSS_{h7}-PAH) with one layer pair (PSS_{d7}-PAH), repeated six times : $[(PSS_{h7}\text{-PAH})_3/(PSS_{d7}\text{-PAH})]_6$. The films were deposited on silicon wafers coated with a first PEI layer, as explained in Paragraph 2.2. Seven of these films were prepared from solutions of

PSS_{h7} or PSS_{d7} with a concentration of 0.6 mg/mL and of PAH with a concentration of 0.27 mg/mL, dissolved in 2 M NaCl solutions. The deposition was done by dipping, spraying or using the spin-assisted LbL assembly. The films were :

- **Dip-2MNaCL** prepared by dipping
- **Spin-4000** prepared by using the spin-assisted LbL assembly at a rotation speed of 4,000 rpm
- **Spin-8000** prepared by using the spin-assisted LbL assembly at a rotation speed of 8,000 rpm
- **Spray-Air-boy** prepared by spraying with Air-boy cans
- **Spray-10** prepared by spraying with Aztek airbrushes at an air flux of 10 L/min
- **Spray-20** prepared by spraying with Aztek airbrushes at an air flux of 20 L/min
- **Spray-Grazing** prepared by spraying with stainless steel nozzles at a grazing incidence angle

Two other films were prepared by dipping in solutions of 0.6 mg/mL of PSS_{h7} or PSS_{d7} and of 0.27 mg/mL of PAH, dissolved in 0.5 M NaCl or 2 M KCl solutions. The films were :

- **Dip-0.5MNaCL** prepared by dipping in solutions with 0.5 M NaCl
- **Dip-2MKCL** prepared by dipping in solutions with 2 M KCl

The build-up processes are described in Paragraph 2.2. The dipped films were prepared with the automated dipping robot with 12 min of dipping into the polyelectrolyte solutions, rinsing into pure MilliQ water and drying steps every two layers (after the PAH deposition). The films prepared by spin coating were deposited on silicon wafers rotating at speeds of 4,000 rpm or 8,000 rpm. The films sprayed with Aztek airbrushes were deposited with an air flux of 10 L/min or 20 L/min.

4.2.2 Analysis of the structure of the films

The films were measured by neutron reflectometry on N-REX+ at FRMII with the setup N-REX+ and on FIGARO at ILL with the setup FIGARO-2 for the sample Spray-Grazing.

We first fitted the specular reflectivity curves by considering a homogeneous structure of the films along the direction perpendicular to the surface, that is the layer pairs have the same thickness, the SLDs of the protonated layers are the same, the SLDs of the deuterated layers are the same and the interfaces have the same roughness in each films. The SLD and roughness of the SiO_2 layers were set to 3.15

x 10^{-6} $Å^{-1}$ and 4 Å respectively and the roughness of the PEI layer was fixed at 9 Å. The SLD of the PEI layer was considered the same as the layer deposited on it, the thicknesses of the SiO_2 and PEI layers were measured by ellipsometry and are summarized in Table 4.5. The specular reflectivity curves with the corresponding fits as well as the SLD profiles are shown in Figure 4.7. The structural parameter values are summarized in Table 4.6. During the fit, the roughnesses of the films Spray-Air-boy and Spray-Grazing increased a lot, which had the effect to remove the Kiessig fringes and Bragg peaks. For this reason, the roughnesses of these two films were fixed at 30.0 Å and 20.0 Å respectively (as indicated in Table 3.5), values for which the fits look good.

	SiO_2 layer thickness (Å)	PEI layer thickness (Å)
Dip-0.5MNaCl	18.0 ± 0.9	8.6 ± 1.3
Dip-2MNaCl	23.3 ± 3.0	8.2 ± 1.6
Dip-2MKCl	21.0 ± 0.9	7.5 ± 1.2
Spin-4000	18.0 ± 1.1	8.9 ± 1.1
Spin-8000	23.7 ± 1.1	6.9 ± 1.2
Spray-Air-boy	18.0 ± 1.1	7.6 ± 1.8
Spray-10	15.0 ± 0.7	8.4 ± 1.2
Spray-20	15.0 ± 0.5	8.8 ± 0.7
Spray-Grazing	16.0 ± 2.8	11.4 ± 1.0

Table 4.5: Thicknesses of the SiO_2 and PEI layers used for the fit of the specular reflectivities of the nine films measured at FRMII and ILL.

	Layer pair thickness (Å)	Protonated SLD (x 10^{-6} $Å^{-2}$)	Deuterated SLD (x 10^{-6} $Å^{-2}$)	Roughness (Å)
Dip-0.5MNaCl	28.8 ± 7.7	1.49 ± 0.25	3.03 ± 0.64	12.8 ± 9.3
Dip-2MNaCl	51.6 ± 6.7	1.17 ± 0.32	3.12 ± 0.42	15.8 ± 8.7
Dip-2MKCl	65.0 ± 7.1	1.22 ± 0.37	3.29 ± 0.37	24.2 ± 18.0
Spin-4000	33.2 ± 2.7	1.42 ± 0.14	2.72 ± 0.25	16.6 ± 13.9
Spin-8000	34.0 ± 6.1	1.68 ± 0.17	2.80 ± 0.67	14.2 ± 13.7
Spray-Air-boy	39.5 ± 16.2	1.33 ± 0.22	2.20 ± 0.38	30.0 (fixed)
Spray-10	37.9 ± 5.0	1.35 ± 0.16	2.63 ± 0.44	25.7 ± 15.1
Spray-20	40.0 ± 5.7	1.34 ± 0.21	2.53 ± 0.65	26.4 ± 15.3
Spray-Grazing	43.1 ± 11.4	1.25 ± 0.18	2.22 ± 0.25	20.0 (fixed)

Table 4.6: Layer pair thicknesses, SLDs and roughnesses determined from the specular reflectivity fits of the nine films measured at FRMII and ILL with a homogeneous structure.

We can immediately see that the experimental and theoretical thickness oscillations are rather well aligned, but the intensity and the width of the fringes and the peaks are not the same for experimental and theoretical curves, except for the films Dip-0.5MNaCl and Dip-2MNaCl, for which the theoretical curves give a good match with the experimental curves. This indicates that the calculated thicknesses are quite accurate but the SLDs and the roughnesses contain some errors.

To improve the fits, we decided to make the assumption that the structural parameters are different for the layers next to the substrate and the ones next to the

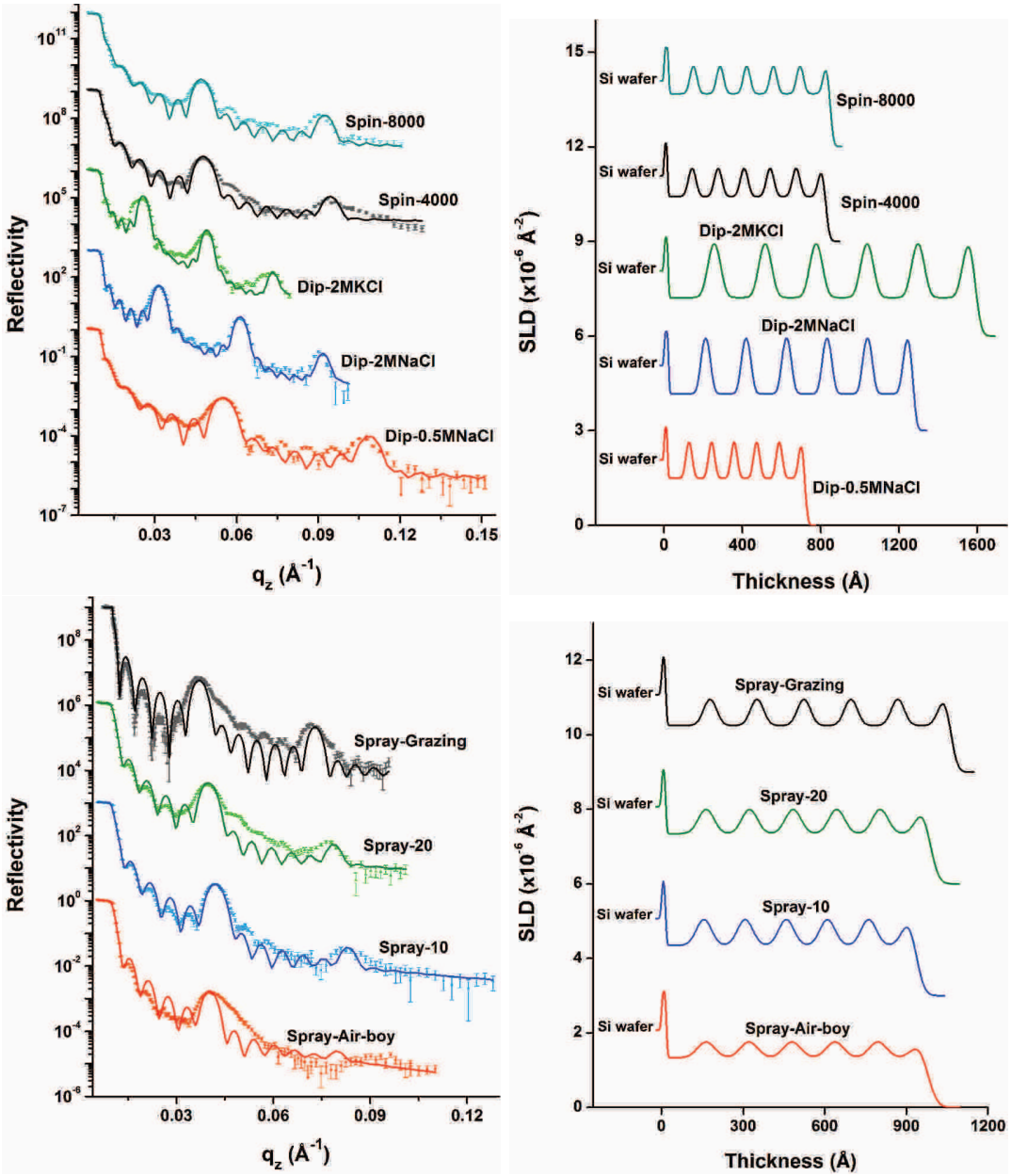

Figure 4.7: On the left, the experimental specular reflectivity curves (points) of the nine multilayer films measured at FRMII and ILL with the corresponding theoretical models (line) for a homogeneous structure. On the right, the SLD profiles extracted from the fits. The curves are shifted for clarity.

surface, due to a difference of environment. Indeed, it was already observed that the three to four first layer pairs, the layers next to the silicon wafer, show a slightly lower growth than the layers above. This is probably due to the proximity of the strong, inorganic wafer which changes the environment around the polyelectrolytes compared to the "bulk" layers, where the environment is only composed of polyelectrolytes. This probably results in a slightly different structure of the polyelectrolytes, and then a different thickness of the layers, compared to the layers in bulk. This trend is shown in Figure 4.8, where the thickness growth of three films is drawn.

These films were built up from solutions of 0.6 mg/mL of PSS_{h7} and 0.27 mg/mL of PAH, dissolved in 2 M NaCl, and were deposited by using the spin-assisted LbL assembly at a rotation speed of 8,000 rpm, spraying with Air-boy cans or spraying with Aztek airbrushes at an air flux of 20 L/min. The thicknesses were measured by ellipsometry with the monochromatic ellipsometer at a fixed refractive index of 1.465. We also assume that the presence of air at the surface of the films has an effect on the structure of the layers at the top of the films.

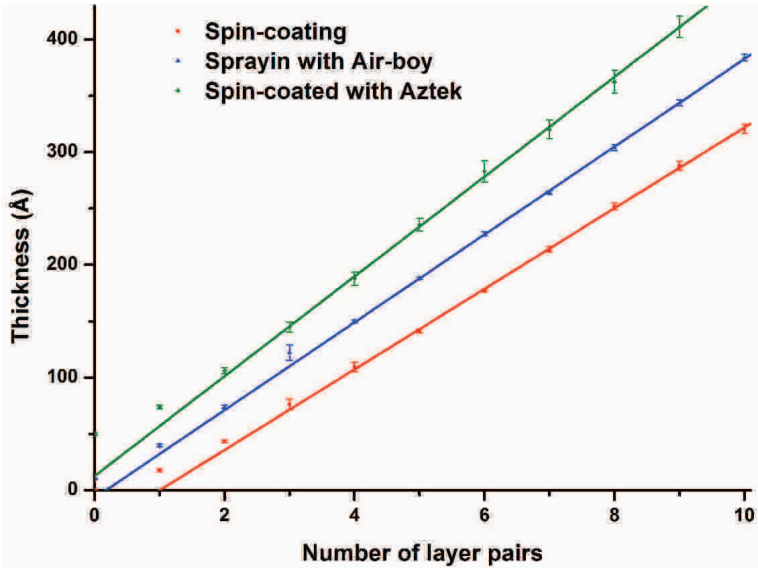

Figure 4.8: Evolution of the thickness of multilayer films composed of 10 layer pairs (PSS_{h7}-PAH) as a function of the number of layer pairs. Films prepared by using the spin-assisted LbL assembly, spraying with Air-boy cans and spraying with Aztek airbrushes are shown. The curves are shifted for clarity and the linear lines are used as guidelines.

We performed new fits of the specular reflectivity curves by considering an inhomogeneous structure, by separating the films in three parts, the "bottom layers" next to the silicon substrate, the "top layers" next to the surface and the "bulk layers" in the middle of the films. The bottom layers part of the films is composed of the three first (PSS_{h7}-PAH) layer pairs, deposited on the PEI layer. We assumed that these layers have a smaller thickness per layer pair than the bulk layers and a smaller roughness at the interfaces. The top layers part is composed of the last (PSS_{d7}-PAH) layer pair. The bulk layer part is composed of the rest of the film, that is $[(PSS_{d7}\text{-PAH})/(PSS_{h7}\text{-PAH})]_5$. The structure is considered homogeneous in the direction perpendicular to the surface in this bulk layers part, which means that the thickness per layer pairs, the SLDs and the roughnesses are the same for all the layers. The structural parameters of the SiO_2 and PEI layers are the same than those used for the fits with a homogeneous structure, summarized in Table 4.5. Figure 4.9 shows the specular reflectivity curves of the nine films with the best fits we found by considering an inhomogeneous structure composed of three parts. The corresponding SLD profils are also drawn and the structural parameter values used are summarized in Table 4.7 and 4.8. During the fit, the bottom layer roughness of the film Spin-4000 went down to zero, which caused some errors in Motofit stopping the fit. For this reason, the roughness of this film was fixed at 0.1 Å(as indicated in

Table 3.5).

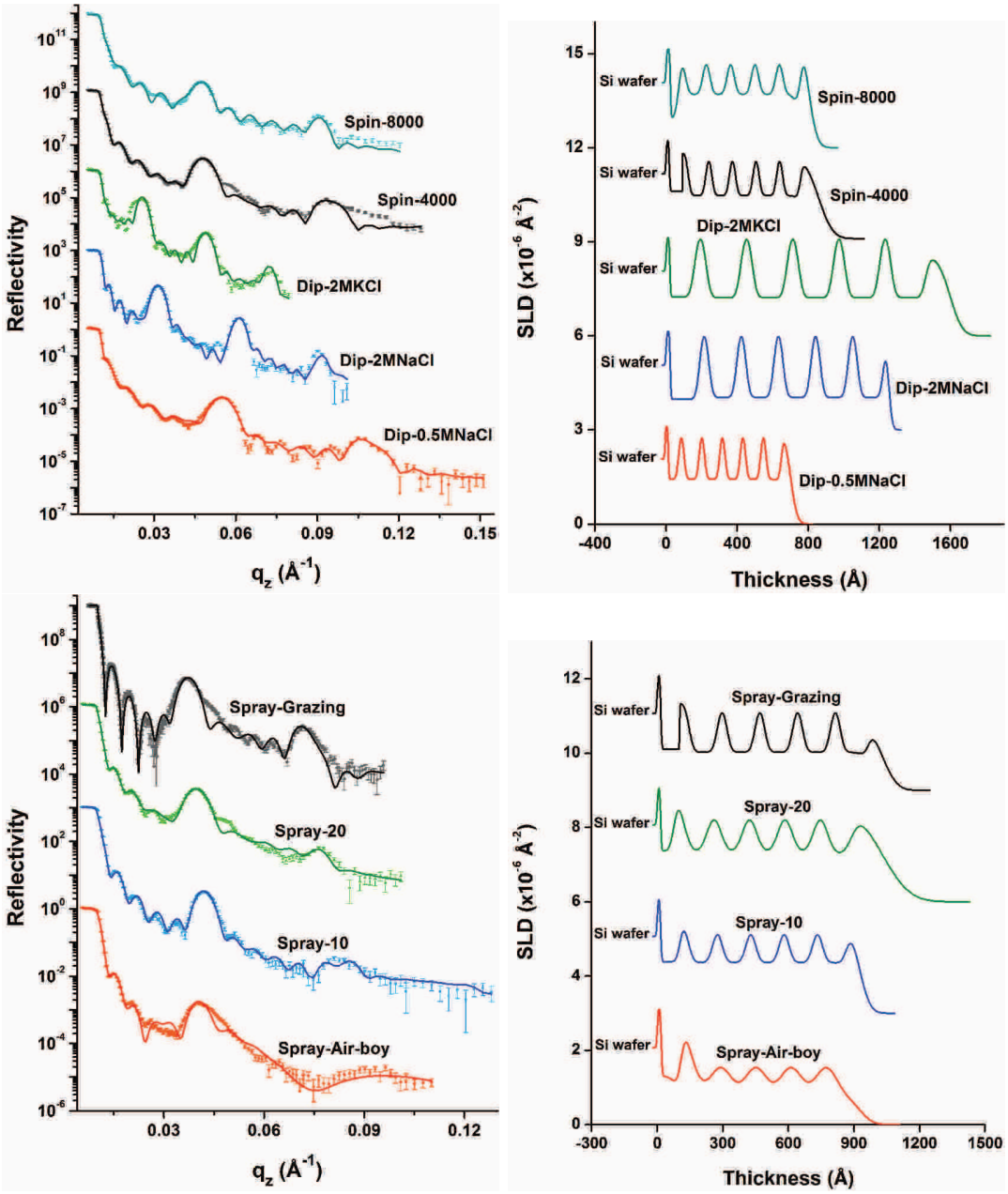

Figure 4.9: On the left, the experimental specular reflectivity curves (points) of the nine multilayer films measured at FRMII and ILL with the corresponding theoretical models (line) for an inhomogeneous structure. On the right, the SLD profiles extracted from the fits. The curves are shifted for clarity.

We can immediately see an improvement of the fits, there is a better match between the experimental and theoretical curves with the inhomogeneous structure. As for the homogeneous structure, the fringes and peaks of the experimental and theoretical curves are well aligned, but contrary to the homogeneous structure, the intensity and width of the fringes and peaks of the theoretical curves have a good match with the ones of the experimental curves.

If we compare the different parts composing the films, we can see that the

		Layer pair thickness (Å)	Protonated SLD ($\times 10^{-6}$ Å^{-2})	Deuterated SLD ($\times 10^{-6}$ Å^{-2})	Roughness (Å)
Dip-0.5MNaCl	Top layers	46.9 ± 14.1	X	3.21 ± 0.95	29.5 ± 11.6
	Bulk layers	28.9 ± 7.0	1.43 ± 0.28	3.08 ± 0.41	11.6 ± 5.9
	Bottom layers	16.0 ± 5.7	1.36 ± 0.41	X	11.6 ± 8.2
Dip-2MNaCl	Top layers	10.3 ± 8.9	X	7.78 ± 3.48	18.2 ± 9.1
	Bulk layers	52.2 ± 2.1	1.04 ± 0.29	3.28 ± 0.33	17.4 ± 9.7
	Bottom layers	52.2 ± 5.8	0.98 ± 0.42	X	17.5 ± 15.5
Dip-2MKCl	Top layers	137.2 ± 39.2	X	2.56 ± 0.65	55.4 ± 38.6
	Bulk layers	65.0 ± 5.3	1.21 ± 0.38	3.33 ± 0.36	20.9 ± 12.0
	Bottom layers	43.9 ± 9.2	1.24 ± 0.33	X	20.9 ± 18.9
Spin-4000	Top layers	103.5 ± 29.0	X	2.60 ± 0.29	63.0 ± 17.2
	Bulk layers	33.2 ± 2.7	1.38 ± 0.18	2.73 ± 0.17	13.0 ± 9.3
	Bottom layers	21.3 ± 1.9	1.52 ± 0.11	X	0.1 (fixed)
Spin-8000	Top layers	36.5 ± 13.5	X	4.43 ± 0.82	41.6 ± 7.3
	Bulk layers	34.2 ± 5.0	1.70 ± 0.18	3.08 ± 0.37	17.2 ± 13.9
	Bottom layers	13.8 ± 2.7	0.92 ± 0.30	X	17.2 ± 12.7

Table 4.7: Layer pair thicknesses, SLDs and roughnesses determined from the specular reflectivity fits of the dipped and spin-coated films measured at FRMII and ILL with an inhomogeneous structure.

		Layer pair thickness (Å)	Protonated SLD ($\times 10^{-6}$ Å^{-2})	Deuterated SLD ($\times 10^{-6}$ Å^{-2})	Roughness (Å)
Spray-Air-boy	Top layers	0.5 ± 0.3	X	32.9 ± 1.55	48.7 ± 8.2
	Bulk layers	40.2 ± 8.6	0.68 ± 0.33	3.33 ± 0.49	48.8 ± 8.2
	Bottom layers	27.9 ± 3.9	1.32 ± 0.24	X	16.4 ± 9.2
Spray-10	Top layers	57.7 ± 20.2	X	2.45 ± 0.85	39.1 ± 17.1
	Bulk layers	38.1 ± 3.8	1.36 ± 0.12	2.47 ± 0.35	19.3 ± 15.7
	Bottom layers	26.7 ± 3.3	1.39 ± 0.16	X	13.3 ± 12.0
Spray-20	Top layers	142.7 ± 45.3	X	2.52 ± 0.30	98.6 ± 31.6
	Bulk layers	40.6 ± 2.6	1.32 ± 0.08	3.09 ± 0.18	30.2 ± 10.2
	Bottom layers	17.8 ± 2.9	1.37 ± 0.17	X	16.6 ± 7.2
Spray-Grazing	Top layers	65.9 ± 20.6	X	1.78 ± 0.34	52.3 ± 8.5
	Bulk layers	43.2 ± 2.7	1.03 ± 0.11	2.35 ± 0.10	16.9 ± 7.6
	Bottom layers	24.9 ± 2.2	1.11 ± 0.14	X	1.3 ± 14.2

Table 4.8: Layer pair thicknesses, SLDs and roughnesses determined from the specular reflectivity fits of the sprayed films measured at FRMII and ILL with an inhomogeneous structure.

bottom layers are thinner than the bulk layers, as expected. The biggest difference in layer pair thickness is observed for the sample Spin-8000, for which the bottom layer pairs are 2.5 times thinner than the bulk layer pairs, and the sample Spray-10 has the smallest difference with bottom layer pairs 1.4 times thinner than the bulk layer pairs. There is one exception : the sample Dip-2MNaCl shows the same thickness per layer pair for the bottom and the bulk layers. This difference of proportion of thickness between the bottom and bulk layers depending on the films could be due to an effect of the build-up conditions, each set of preparation conditions would show a different proportion of thickness between the bottom and

bulk layers. It may also be due to fit effects as observed for the multilayer films measured at LLB in 2007, the parameters are mathematically the best for the fits but are not physically completely accurate. Except for the samples Spin-8000 and Spray-Air-boy, the protonated SLDs of the bottom and bulk layers are rather similar, and we could probably assume that the SLDs are the same, the differences being again due to fitting errors. This suggests that the densities of the bottom and bulk layers are the same and that the difference of thickness is due to a difference of amount of polyelectrolytes adsorbed. For the film Spin-8000, the protonated SLD of the bottom layers is 1.8 times smaller than the bulk layers one and is 1.9 time bigger for the film Spray-Air-boy. The protonated SLDs of the bulk layer are particularly low for the sample Spray-Air-boy and high for the sample Spin-8000. This could be due to particularly bigger mathematical uncertainties compared to the other films or to a lower quality of the films. But we could certainly assume the same trend for the nine films. Finally, the roughnesses of the bottom and bulk layers are the same for the samples Dip-0.5MNaCl, Dip-2MNaCl, Dip-2MKCl and Spin-8000, and are 1.5 to 3.0 times smaller for the films Spray-Air-boy, Spray-10 and Spray-20. The roughnesses of the films Spin-4000 and Spray-Grazing are clearly too small and are not physical. At this point of the studies, it is not possible to determine if the roughnesses of the bottom layers are the same or smaller than those of the bulk layers.

Concerning the top layers, we observe a thickness per layer pair which is 1.1 to 3.5 times bigger than the thickness per layer pair of the bulk layers, except for the film Dip-2MNaCl for which the thickness per layer pair of the top layers is 5.1 times smaller than the one of the bulk layers and for the film Spray-Air-boy for which the thickness per layer pair of the top layer is 80.4 times smaller than the one of the bulk layers. This difference of thickness of the top layers was not observed by ellipsometry and the differences are too big. These values are probably not physically true. The SLDs of the top layers are 1.0 to 9.9 times bigger than the deuterated SLDs of the samples Dip-0.5MNaCl, Dip-2MNaCl, Spin-8000 and Spray-Air-boy, 1.1 to 1.3 times smaller for the films Dip-2MKCl, Spin-4000, Spray-20 and Spray-Grazing, or the same for the film Spray-10. As there is less polyelectrolytes for interpenetration for the top layers, since there is no layer above, we could expect a lower density, hence a smaller SLD for the top layers. Again, the fact that there is bigger and smaller SLDs is certainly due to mathematical uncertainties of the fits, but the values are not accurate. Finally, the roughnesses are 1.0 to 4.8 times bigger for the top layers than for the bulk layers, except for the film Spray-Air-boy, for which the roughnesses are the same. We can probably assume that the roughness at the surface is bigger than the one inside the film, but the values may not be accurate as we already mentioned that the roughness is the parameter which is the most adjusted to improve the fits. What could be interesting to do is to perform neutron reflectometry on several films for each build-up conditions to carry out a global fit on the specular reflectivities and to have average values of the parameters which are more accurate. We can also probably assume that the structure we used is not the best, and structures with more layers on the top and the bottom parts may be more accurate.

Finally, if we compare the parameters of the bulk layers with the parameters of the homogeneous structure, we can see that the values are similar in most

cases. The thicknesses per layer pair are very close ; the protonated SLDs for the inhomogeneous structures are up to 1.2 times lower or higher and the deuterated SLDs up to 1.2 times lower or higher, whic is rather similar, except for the film Spray-Air-boy for which the protonated SLD is 2.0 times smaller and the deuterated one 1.5 times bigger for the inhomogeneous structure. Finally, the roughnesses are 1.1 to 1.6 times bigger or smaller for the inhomogeneous structure compared to the homogeneous structure. As the parameters are similar for both structures, the fits with a homogeneous structure are good enough to determine the values of the structural parameters for the bulk part, which corresponds to the most part of the films.

Let us compare the film structures to see the influence of the preparation conditions. The comparison is done on the basis of the structural parameters of the bulk layers. We can first observe the influence of the salt nature and concentration on dipped films. The thickness per layer pair for 2 M KCl is 1.2 times bigger than for 2 M NaCl, the protonated SLD is 1.2 times bigger, the deuterated SLD the same within errors and the roughness 1.2 times higher. The thickness per layer pair is 1.8 times smaller for 0.5 M NaCl than for 2 M NaCl, the protonated SLD 1.4 times bigger, the deuterated SLD 1.1 times smaller and the roughness 1.5 times lower. So the films prepared from solutions of polyelectrolytes with KCl are thicker than the films with NaCl and the thickness increases with the increase of the salt concentration. It seems that a bigger thickness for dipped films due to different salt nature and concentration goes along with a bigger roughness. However, whereas the SLDs are bigger for KCl than for NaCl, which corresponds to a higher density, the protonated SLD is higher and the deuterated one lower for lower NaCl concentration, which implies higher density for protonated layers and lower density for deuterated layers. It is possible that these differences are really due to the difference of salt nature and concentration, but it is more likely to be within the error of th fits and the density may be the same, just the thickness and the roughness change.

The spin-coated films are 1.5 to 1.6 times thinner than the dipped film prepared with the same solutions. The rotation speed does not have a big impact on the thickness, the thicknesses per layer pair for a speed of 4,000 rpm and 8,000 rpm are nearly the same. The protonated SLDs are 1.3 to 1.6 times higher for the spin-assisted LbL assembly than for dipping and the deuterated SLDs 1.1 to 1.2 times smaller. The SLDs are bigger for a speed of 8,000 rpm than for 4,000 rpm, what would mean that the films are denser for a higher speed. Finally, the roughnesses for spin-coated films are up to 1.3 times smaller than for dipped films and the roughness increases with the rotation speed.

Sprayed films are 1.2 to 1.4 times thinner than dipped films, with roughnesses 1.4 to 2.3 times bigger or 1.1 to 1.2 times smaller. The increase of the air flux for films sprayed with Aztek airbrushes gives thicker films, the spraying with Air-boy shows a film with a thickness between the ones for Aztek spraying with air flux of 10 L/min and 20 L/min and the spraying with stainless steel nozzles at a grazing incidence angle gives the thicker film. The roughness seems to increase with the increase of the air flux of the Aztek spraying, whereas the spraying with Air-boy

gives the biggest roughness and the spraying with stainless steel nozzles at a grazing incidence angle the smallest roughness. The protonated SLDs are 1.3 to 1.3 times bigger and the deuterated SLDs 1.1 to 1.3 times smaller for the Aztek spraying compared to the dipping. The protonated SLD for Air-boy spraying is 1.5 times smaller than for dipping and the deuterated one the same within the fitting errors, whereas for spraying with stainless steel nozzles, the protonated SLD is the same than for dipping and the deuterated one is 1.4 times lower. There is not a clear trend visible when comparing the difference of SLDs of the sprayed and the dipped samples.

Finally, we can clearly see the influence of the build-up conditions on the thicknesses per layer pair of the films, but no clear trend for the difference of the SLDs and the roughnesses can be observed.

4.2.3 Conclusion

To conclude, we have seen that (PSS-PAH) multilayer films do not show a homogeneous structure in the direction perpendicular to the surface, but there is some influence of the silicon wafer and the air on the layers next to them. The structure determined can be optimized, but we show that a fit with a homogeneous structure gives good values for the main part of the films, the bulk layers.

We have also compared the influence of the preparation conditions on the structural parameters and have seen a clear influence on the thicknesses. Unfortunately, no clear trend on the difference in SLDs and roughnesses could be extracted from the comparison of the parameters, due to the mathematical uncertainties of the fits. As a perspective, it could be interesting to do is neutron reflectometry measurements on several multilayer films for each build-up condition to be able to perform global fits and to obtain more accurate values of the structural parameters, and so a better comparison of the structures.

Chapter 5

Study of the polyelectrolyte conformation in multilayer films

The conformation of polyelectrolyte chains in multilayer films is highly important for understanding the properties of the films, but no study of the conformation has been reported so far on multilayer films. The only studies by neutron scattering on multilayer films reported are studies on the structure of the films by neutron reflectometry (see for example references [6,119,186,187]). However, it is possible to determine an average size of the polyelectrolyte chains in the direction perpendicular to the surface from the analysis of specular reflectivity and an average radius of gyration in the direction parallel to the surface from GISANS measurements.

We showed above that we can consider that the structures determined for multilayer films of polyelectrolytes prepared during the thesis can be considered as the original ones, after the preparation, even if the measurements were done after several months or few years during the thesis. We assumed that it is also the case for the conformation observed below.

5.1 Conformation of PSS chains in dipped films

We performed the first study of the polyelectrolyte chain conformation on a dipped multilayer film using neutron reflectometry and GISANS.

5.1.1 Multilayer films preparation

Two multilayer films composed of PSS_{h7}, PSS_{d7} and PAH were prepared by dipping the polyelectrolytes on silicon wafers coated with a first PEI layer using the automated dipping robot as described in Paragraph 2.2. The films were dipped for 12 min into solutions of 0.6 mg/mL of PSS_{h7} or PSS_{d7} and of 0.27 mg/mL of PAH, dissolved in 2 M NaCl solutions, rinsed in pure MilliQ water and dried every two layers, after the deposition of the PAH layers.

One film was composed of alternating deuterated and non-deuterated layers for neutron reflectometry measurements, with the following sequence : three (PSS_{h7}-PAH) layer pairs alternated with one (PSS_{h7}-PAH) layer pair, repeated six times, $[(PSS_{h7}\text{-PAH})_3/(PSS_{d7}\text{-PAH})]_6$. The second film was an alternation of layers composed of a mixure of 50% PSS_{h7} and 50% PSS_{d7} with PAH layers, $(PSS_{50-50}\text{-PAH})_{53}$. Fifty-three layers were deposited to obtain a film with a thickness bigger than 300 nm and the film was measured by GISANS.

5.1.2 Polyelectrolyte chain size in the direction perpendicular to the surface

The film composed of alternating deuterated and non-deuterated layers was measured by neutron reflectometry on N-REX+ at FRMII. The analysis of the specular reflectivity curve was already described in Paragraph 4.2 and corresponds to the film Dip-2MNaCl. Here, we will use the inhomogeneous structure, which better described the data, for the determination of the chain size. The specular reflectivity curve with the corresponding fit are shown in Figure 5.1, as well as the SLD profile. The structural parameter values are summarized in Table 5.1.

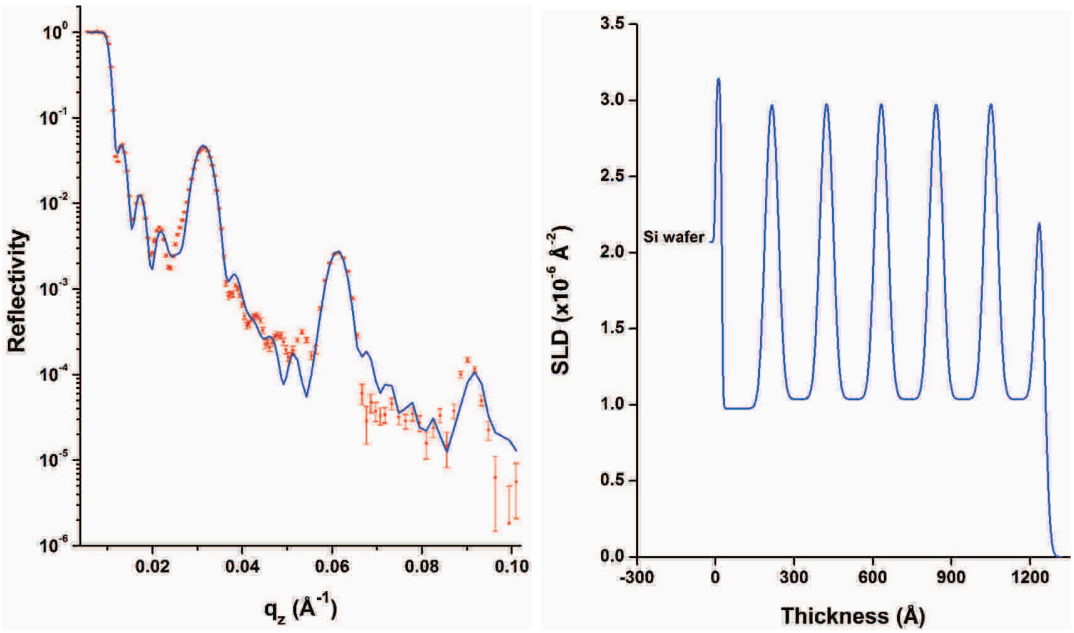

Figure 5.1: On the left, the experimental specular reflectivity curve (points) and the corresponding theoretical model (line). On the right, the SLD profile extracted from the fit.

From specular reflectivity it is not possible to calculate the individual size of a polyelectrolyte chain perpendicular to the surface of the film, but it was possible to determine an average maximal size of a PSS chain, which corresponds to the maximal distance of extension of the polyelectrolyte in the out-of-plane direction. This distance, D, is the distance between the most distant points of the polyelectrolyte chains composing the layer as represented in Figure 5.2.

	Layer pair thickness (Å)	Protonated SLD (x 10^{-6} Å^{-2})	Deuterated SLD (x 10^{-6} Å^{-2})	Roughness (Å)
Top layers	10.3 ± 8.9	X	7.78 ± 3.48	18.2 ± 9.1
Bulk layers	52.2 ± 2.1	1.04 ± 0.29	3.28 ± 0.33	17.4 ± 9.7
Bottom layers	52.2 ± 5.8	0.98 ± 0.42	X	17.5 ± 15.5

Table 5.1: Layer pair thickness, SLDs and roughness determined from the specular reflectivity fit.

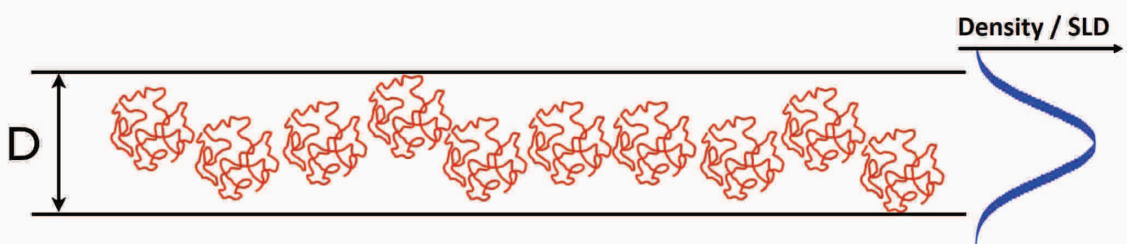

Figure 5.2: Schematic representation of a polyelectrolyte layer in a LbL film. D is the distance between the most distant points of the polyelectrolyte chains composing the layer.

As the fitted roughness is composed of the interface roughness and the polymer interpenetration, we can determine D using the neutron reflectivity analysis. In Figure 5.3, the peaks correspond to the deuterated PSS layers, each one composed of only one layer. We can consider that the maximal elongation, D, of the PSS chains is equal to the width of the peak, which includes the thickness and most part of the interpenetration. The gradient at the interfaces is described by an error function with the standard deviation, σ, equal to the roughness calculated by the fits, and D was chosen to include 99.7% of the gaussian distributed material of the layer in question. This means that D is equal to the thickness per layer pair, d, plus three times the roughness :

$$D = d + 3\sigma \tag{5.1}$$

In an ideal film, the center of the polyelectrolytes chains would be aligned and they would interpenetrate into the neighbouring layers within the same distance. But the polyelectrolyte chains in one layer can be more or less shifted from each other due to the roughness, so D is clearly an upper limit of the size of a polyelectrolyte chain in the direction perpendicular to the surface and we will use it to have a first comparison with the size in the direction parallel to the surface. For the dipped film studied here, the maximal diameter of a PSS chain with a molecular weight of 80,800 g/mol is 10.4 nm. We can calculate the radius of gyration of a polylectrolyte chain, R_g, from the end-to-end distance of the chain, δ :

$$R_g = \frac{\delta}{\sqrt{6}} \tag{5.2}$$

The radius of gyration error, $R_{g,err}$, is given by :

$$R_{g,err} = \sqrt{d_{err}^2 + 3 \times \sigma_{err}^2} \tag{5.3}$$

with d_{err} the thickness error and σ_{err} the roughness error.

So, from the maximal end-to-end distance D, we can calculate the maximal radius of gyration of a PSS chain (M_w = 80,000 g/mol) in the direction perpendicular to the surface, R_{gz}(max), which is equal to 4.3 ± 1.7 nm.

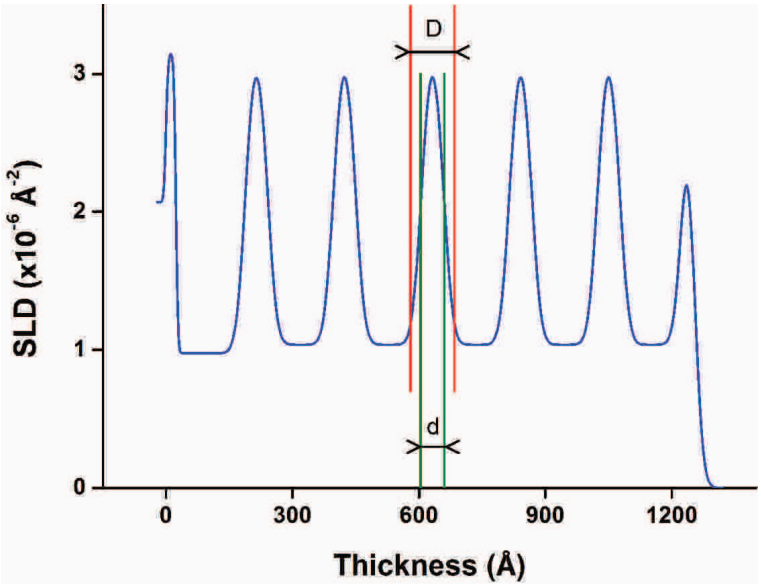

Figure 5.3: SLD profile of the dipped film.

We have determined that the general structure of multilayer films of polyelectrolytes does not change after several months or few years. We can also observe the influence of the ageing on the out-of-plane size of a PSS chain for Sample C, D, E and F studied in Chapter 3. The maximal out-of-plane radii of gyration for the four films in 2007 and five years after are summarized in Table 5.2. We can see a radius decrease of 0 Å to 0.5 Å, which is below the accuracy of the polyelectrolyte in-plane and out-of-plane sizes we can get with the methods used here. So we can assume that there is no change of the polyelectrolyte chain conformation even if the films were measured several months after their preparation.

	Sample C	Sample D	Sample E	Sample F
R_{gz}(max) in 2007 (nm)	2.7 ± 1.8	2.6 ± 1.8	2.5 ± 1.8	3.7 ± 1.8
R_{gz}(max) in 2012-2013 (nm)	2.3 ± 1.4	2.6 ± 1.5	2.4 ± 1.7	3.2 ± 1.4

Table 5.2: Maximal out-of-plane radii of gyration of PSS chains in Sample C, D, E and F in 2007 and five years after, in 2012-2013. The film preparation and the neutron reflectometry measurements are described in Chapter 3.

5.1.3 Radius of gyration of a polyelectrolyte chain in the direction parallel to the surface

We followed here the work of J. Kraus *et al.* [158], who studied the radius of gyration of polystyrene chains in films of polystyrene by GISANS measurements. The film composed of layers with a mixure of 50% deuterated and 50% non-deuterated PSS was measured by GISANS at ILL on FIGARO with the setup FIGARO-3. Figure 5.4 shows the detector picture of the GISANS pattern of the dipped film at a wavelength of 3.2 Å.

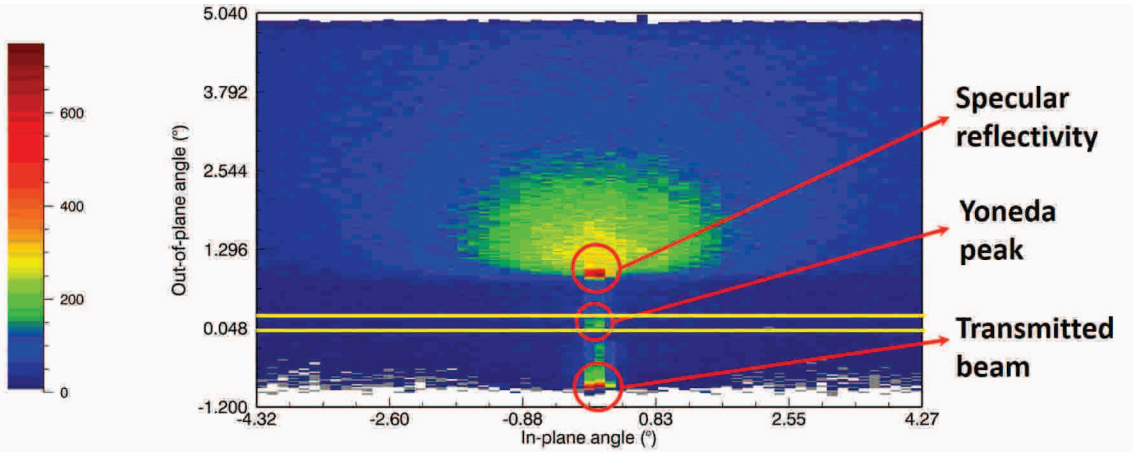

Figure 5.4: GISANS pattern of the dipped film.

As the measurement was done in TOF mode, data were treated for every wavelength individually. Data were treated to remove the background and the signal of the substrate so that we could analyze only the signal of the film. Then, we performed an horizontal cut (in the y direction, parallel to the surface) at the height of the Yoneda peak, as shown in Figure 5.4. We obtained good data at three wavelengths : 4 Å (integration over 3.6 - 4.4 Å), 5 Å (integration over 4.5 - 5.5 Å) and 7 Å (integration over 6.3 - 7.7 Å). The experimental curves for the three wavelengths as well as the theoretical model are shown in Figure 5.5.

The experimental curves follow a Debye function [12, 13, 188] :

$$I = \frac{2}{q_y^2 R_{gy}^2}\left[1 - \frac{1}{q_y^2 R_{gy}^2}\left(1 - \exp(-q_y^2 R_{gy}^2)\right)\right] \tag{5.4}$$

with I the intensity and R_{gy} the radius of gyration in the y direction.

The experimental data were fitted together with the global fit function of IgorPro, so that the radius of gyration calculated for the three wavelengths is the same. We found that the radius of gyration in the direction parallel to the surface is 15.6 nm ± 1.8 nm for a PSS chain with a molecular weight of 80,800 g/mol.

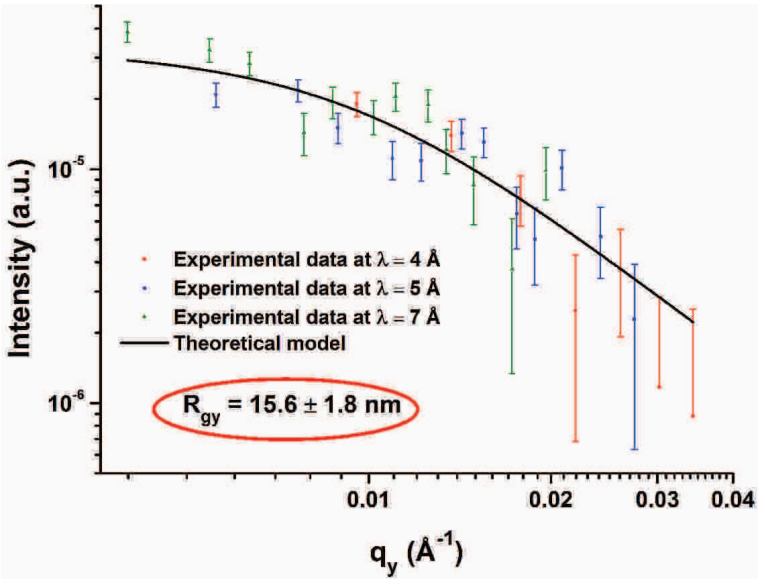

Figure 5.5: Out-of-plane scans of the multilayer film containing 50% deuterated PSS. The experimental data (points) for wavelengths of 5 Å, 7 Å and 9 Å, and the corresponding Debye function (line) are shown.

5.2 Comparison of the conformation in a multilayer film, in a complex or in solution

We calculated that the radius of gyration of a PSS chain in the direction parallel to the surface is equal to 15.6 nm ± 1.8 nm whereas the maximal radius of gyration in the direction perpendicular to the surface is equal to 4.3 nm. Even if it was not possible to calculate the exact radius in the direction perpendicular to the surface, we can see that the radius in the direction perpendicular to the surface is 3 times smaller than the radius of gyration in the direction parallel to the surface. This means that the PSS chains with a molecular weight of 80,800 g/mol in the dipped film prepared in the conditions described above have a flattened coil conformation. This is in agreement with the fact that the layers in multilayer films are smaller than the polyelectrolyte size in solutions.

In comparison, M. Z. Markarian *et al.* have studied the size of PSS chains in complexes of polyelectrolytes [33]. They prepared complexes composed of PSS and PDADMAC and measured the radius of gyration of PSS chains in different solutions by SANS. They observed radii of gyration of 2.5 nm to 2.72 nm for NaCl solutions of 0.1 M to 1.5 M for PSS with a molecular weight of 14,000 g/mol and radii of gyration of 10.5 nm to 11.0 nm for PSS with a molecular weight of 104,000 g/mol. For PSS with a molecular weight of 104,000 g/mol, which is the closest to the PSS we used (M_w = 80,800 g/mol), the radius of gyration is a bit smaller than the one we determined in multilayer films in the direction parallel to the surface and bigger than the size perpendicular to the surface. Since the PSS coils in the complexes are rather spherical and the PSS chains have a flattened coil conformation in multilayer films, we could expect that, compared to the size of the PSS in the polyelectrolyte complexes, the size of the PSS chains is smaller in

the direction perpendicular to the surface (flattened) and bigger in the direction parallel to the surface. This is in agreement with the results observed by neutron scattering.

SANS measurements were also performed by other groups on solutions of PSS to determine the radius of gyration of a PSS spherical coil depending on the polyelectrolyte and salt concentration [39–41]. Unfortunately, the solutions they studied did not have the same polyelectrolyte and salt concentration used here. To obtain an estimation of the size of the PSS coils in the solutions used to build up our multilayer films, we can use the study of the conformation of PSS coils in solution of NaBr by M.-N. Spiteri [42]. On page 84, the radius of gyration for PSS coils with a molecular weight of 150,000 - 170,000 g/mol in solutions of NaBr with different concentrations are shown. These sizes are included between 10.1 nm and 19.7 nm for concentration of NaBr from 0 M to 3 M and concentration of PSS of 0.17 monomol/L and 0.34 monomol/L. We can see an increase of the radius of gyration with the decrease of the polyelectrolyte and the salt concentrations. Our solutions of PSS contained 2 M NaCl and 1 x 10^{-3} monomol/L of PSS. Let us take as a starting point the radii of gyration of the PSS in solution for 1.5 M NaCl and 3 M NaCl with a concentration of PSS of 0.17 monomol/L, that is 13.5 nm and 10.6 nm. As we have a lower concentration of PSS, we can assume a radius of gyration lower than 13.5 nm. This is smaller than the radius of gyration in the direction parallel to the surface of the PSS in the multilayer film.

To conclude, we have determined that the conformation of a PSS chain in a dipped multilayer film is a flattened coil, and this is in agreement with the small thickness of the layers compared to the sizes of polyelectrolytes in solutions. This conformation was compared to the radius of gyration of spherical PSS coils in PSS-PDADMAC complexes and we have seen that the size of PSS chains in multilayer films is bigger in the direction parallel to the surface and smaller in the direction perpendicular to the surface, compared to the radius of gyration of PSS in complexes. Finally, it seems that the radius of gyration of the spherical PSS coil in the solutions used for the build up of the films is smaller than the radius of gyration of the PSS chain in the films in the direction parallel to the surface.

5.3 Perspectives

We have demonstrated the possibility to determine the conformation of polyelectrolyte chains in multilayer films using neutron reflectometry and GISANS. It is also possible to measure the in-plane radius of gyration by Small Angle Neutron Scattering (SANS), which consists to measure the scattering of an incident beam perpendicular to the surface of the film. We get the same information than for GISANS, but we have the possibility to determine the in-plane radius of gyration in several directions. So we could determine the conformation for anisotropic objects, like deformed polyelectrolyte chains. First SANS tests performed are promising, so SANS measurements should be carried out in the future.

As we have succeed to measure the conformation of PSS chains in one film, we should now measure the conformation of polyelectrolyte chains in other films. First, it would be useful to determine the influence of the build-up parameters on the conformation of the polyelectrolyte. Second it would be interesting to measure the conformation of polyelectrolyte chains in films showing a particular structure. Three examples of interesting films are described below.

5.3.1 The brush-like structure

The "grafting from" technique consists of grafting molecules on a surface and to polymerize on this initiator to form a polymer layer attached to the surface. The team of Jürgen Rühe studied the preparation of such kind of attached layer for several polyelectrolytes or polymers : poly(methyl methacrylate) (PMMA) [189, 190], poly(styrene) (PS) [191,192], poly(4-vinyl-N-n-butylpyridinium) (BuPVP) [193], etc ... By controlling the grafting density and the polymerization degree, it is possible to control the thickness of the layer [194]. With a high grafting density, the polyelectrolytes take a brush conformation, since they are vertically elongated, due to the charge repulsion.

The team of J. Rühe showed the possibility to deposit a polyelectrolyte layer on top of the polyelectrolyte brush layers using the Layer-by-Layer process (cf. Figure 5.6).

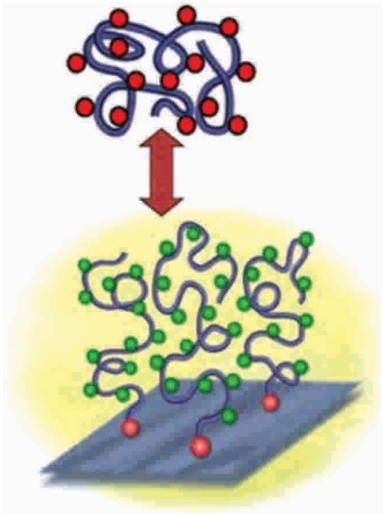

Figure 5.6: Representation of the adsorption of a polyelectrolyte on an oppositely charged polyelectrolyte brush.

Two cases were observed, the deposition of strong polyelectrolytes and the deposition of weak polyelectrolytes. H. Zhang *et al.* [195] showed that the deposition of a PSS layer on a poly(4-vinyl-N-methylpyridinium) iodide (PMeVP) brush layer with a swollen thickness of 660 nm leads to a collapse of the film to a thickness of 19 nm in solution, which corresponds to the thickness of the dried brush layer plus the thickness of a PSS (strong polyelectrolytes) layer which is in the order of magnitude of a PSS layer in the linear regime. But an interesting behavior was observed for

weak polyelectrolytes (see for example references [26, 196]). It was shown that the thickness of the layer deposited on the attached layer is dependent on the thickness of this first layer. In Figure 5.7, we can see a linear dependence of the thickness of a PMAA layer and a PMeVP layer deposited on a PMeVP brush layer and a PMAA brush layer respectively. The thickness of the second layer is in the same order of magnitude than the one for the first layer, even for thicknesses of 200 nm.

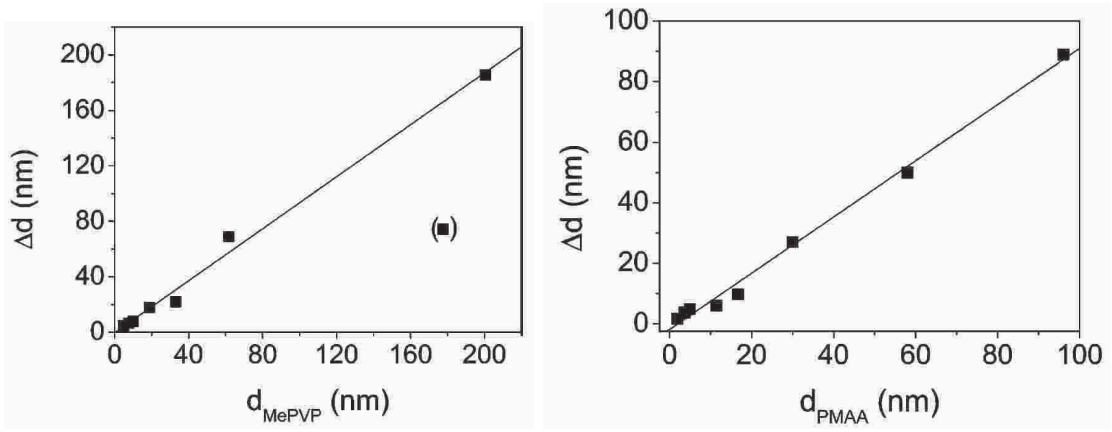

Figure 5.7: On the right, layer thickness increase of PMeVP layers adsorbed on PMAA brushes as a function of the thickness of the PMAA brushes. On the left, layer thickness increase of PMAA layers adsorbed on PMeVP brushes as a function of the thickness of the PMeVP brushes. The solid lines represent linear fits. Reproduced from reference [26].

Furthermore, this is not limited to one layer but this thickness template is observed for at least 5 layers deposited on the brush layer. This behaviour is shown in Figure 5.8, on which the total thickness of (PMAA-PMeVP) multilayer films deposited on PMAA brush layers is drawn as a function of the number of layers, for different thicknesses of the first layer. We say that the films have a brush-like structure.

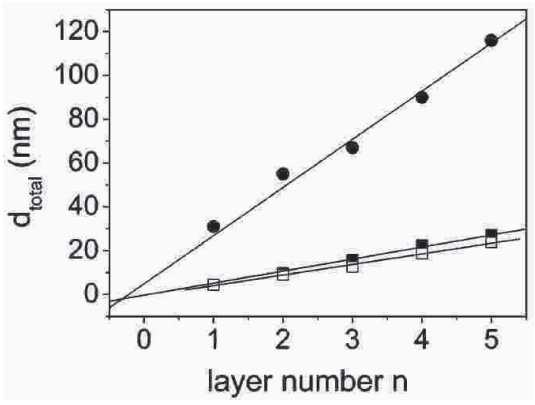

Figure 5.8: Thickness growth with the number of layers for (PMAA-PMeVP) films deposited on 5 nm (■ ellipsometry data, □ X-ray reflectivity data) and 31 nm (●) PMAA brushes. The solid lines represent linear fits. Reproduced from reference [26].

For now, the mechanisms of formation for such films are not understood. A way

to better understand how these films can be formed is to study the conformation of the polyelectrolyte chains. Indeed, two cases can be assumed : a coil conformation and a brush conformation, as represented in Figure 5.9.

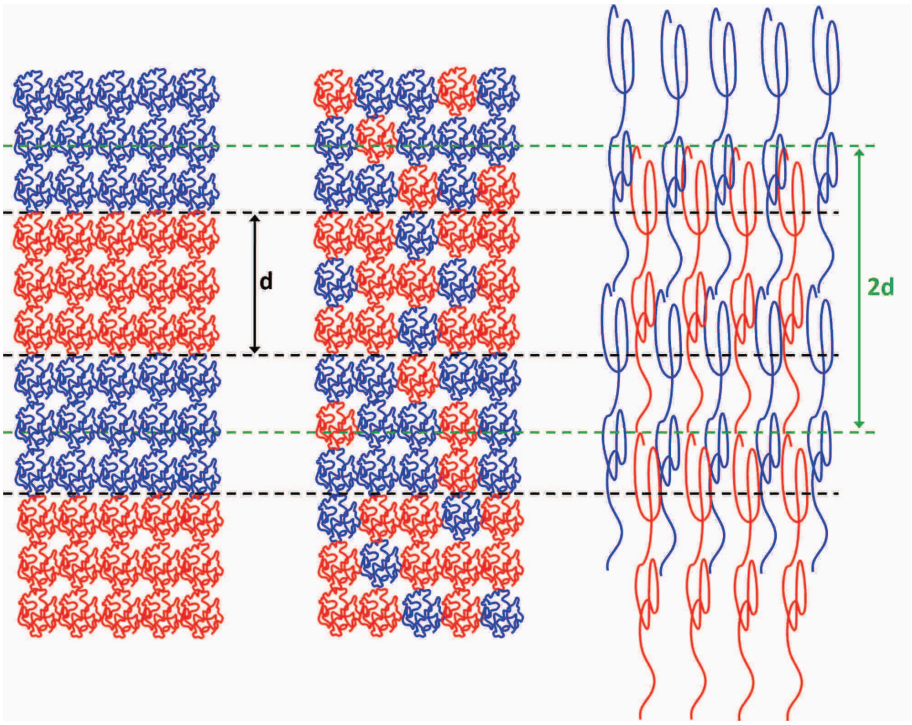

Figure 5.9: Oversimplified representation of the three possible conformations of the polyelectrolyte chains in a film with a brush-like structure. On the left, the coil conformation with a layered structure, in the middle, the coil conformation without a layered structure, and on the right, the brush conformation. "d" is the thickness of a layer.

In the case of the coil conformation with the layered structure, one layer is not composed of a monolayer of polycations or polyanions as for regular LbL films, but of a stack of several layers of polycations or polyanions in a coil conformation (spherical or non-spherical). This means that there is no microscopic pairing of a charge with the opposite charge, but there is a macroscopic compensation of the charges (neutral object). For the coil conformation without a layered structure, the film is composed of a mixture of polyanions and polycations and the layered structure is lost. In this case, there is a microscopic pairing of the charges.

For the brush conformation, we have monolayers of elongated polyanions or polycations, and the polyelectrolytes interpenetrate in the neighboring layers. So, in this case, there is a microscopic pairing of a charge with the opposite charge. The out-of-plane size of the polyelectrolyte chains should be at least twice the thickness of a layer. Therefore, in the study performed by H. Zhang *et al.* [26] and described above, the size of a fully elongated polyelectrolyte has to be at least 400 nm for the thickest layers build-up. The PMAA used had a molecular weight M_w = 990,000 g/mol and a fully elongated size of around 2,875 nm, and the PMeVP a molecular weight M_w = 431,800 g/mol and a maximal size of 437 nm. So the brush conformation is a realistic assumption.

5.3.2 Spherical coil conformation - Effect of salt on polyelectrolyte interdiffusion

H. Jomaa *et al.* [5] studied the influence of the annealing by salt on a multilayer film of PSS and PDADMAC. Indeed, they measured by neutron reflectometry the film, with the structure $[(\text{PDADMAC-PSS}_{h7})_4/(\text{PDADMAC-PSS}_{d7})]_5(\text{PDADMAC-PSS}_{h7})$, as-deposited and after annealing in salt solution for different times to observe the effect on the internal structure of the film. We can see in Figure 5.10 the evolution of the reflectivity curve with the time of annealing.

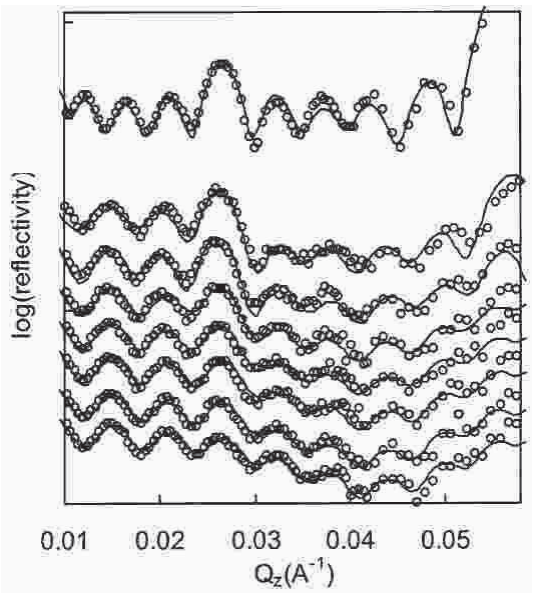

Figure 5.10: Reflectivity curves for a (PSS-PDADMAC) multilayer film. The open circles represent the experimental data, the solid lines the fits. Uppermost curve : as-deposited film measured in ambient conditions. Lower curves, measured under argon, from top to bottom : after annealing in 0.8 M NaCl for 10, 25, 55, 110, 170 and 260 min. Lowest curve : final annealing in 1 M NaCl for 120 min. Reproduced from reference [5].

Whereas there are Kiessig fringes and a well defined Bragg peak for the film before the annealing, due to the alternation of deuterated and non deuterated layers, the intensity of the Bragg peak decreases with time of annealing until its complete disappearance, indicating that it is not possible to differentiate the deuterated and non-deuterated layers anymore. H. Jomaa *et al.* determined that the annealing had the effect of slightly decreasing the thickness of the layers, but the roughness, or the interpenetration, increased a lot, 7.5 times the initial roughness. This indicates an expansion of the polyelectrolyte chains in the out-of-plane direction, so a change of their out-of-plane size and of their conformation. A question is to know how the in-plane size of the polyelectrolyte chains evolved. Indeed, we could assume that the initial conformation of the PSS chains in the (PSS-PDADMAC) film is a flattened coil, as in the (PSS-PAH) film studied above. If we assume that the in-plane size of the chains did not really change with the annealing, due to lateral constraints, the increase of the out-of-plane size would indicate a change of the conformation to a spherical, or more spherical, coil. It would be interesting to verify this assumption

by performing the same experiment than H. Jomaa *et al.*, but carrying out also GISANS measurements to determine the conformation of the polyelectrolyte chains.

5.3.3 Alignement by spraying at a grazing incidence angle

A new geometry of spray is developed in our team and consists of spraying the solution at a grazing incidence angle. It was shown that this geometry allows the alignment of anisotropic nanoparticles in the direction of spraying, as shown in Figure 5.11. This is a SEM picture of a layer composed of silver nanowires deposited using the grazing incidence spraying technique and we can see the alignment of the nanowires.

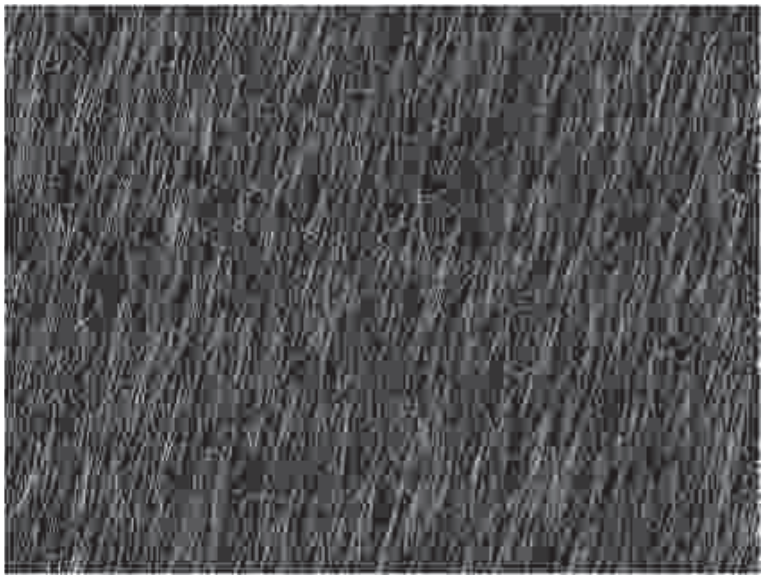

Figure 5.11: SEM picture of a layer of aligned silver nanowires prepared by grazing incidence spraying by Hebing Hu. Thesis in progress.

As the spray at a grazing incidence angle can aligne nanowires, a question is to know if we can observe a deformation of polyelectrolyte chains in LbL films using this geometry, due to the shear forces. This could be determined by using neutron scattering measurements to study the polyelectrolyte chain conformation, and especially by comparing the in-plane sizes in the direction of the spraying and perpendicular to the spraying to see if they are different.

Chapter 6

Conclusions and outlook

We have shown in these studies that the neutron scattering is a powerful technique for the study of the internal structure of multilayer films of polyelectrolytes.

We have shown the evolution of (PSS-PAH) films with time and observed an important expansion after a storage of 15 years. This expansion went along with aan inhomogeneous change in the structure depending on the depth in the film, which indicated an effect of the substrate on the layers next to it. Even if the 15 years old films were stored in non-controlled conditions, they still presented a stratified structure. The limits of the storage and the reflectivity curve analyis was observed here. The change of the film structure could be due to an oxydation.

For a storage of 5 years, a slight shrink of the films was observed. This is probably due to a plastification of the films by the humidity in the air. We determine that the structure of (PSS-PAH) multilayer films can be considered as stable during several months to few years.

We also pointed out that the control of ambient conditions is important. What should be done in future neutron scattering measurements is to measure the films in an environmental chamber, with fixed ambient conditions, to have an accurate comparison of the internal structure of the multilayer films.

In the second part, we have seen the big advantage to measure several films prepared in the same conditions and the use of a global fit process to determine average values of the structural parameters. We observed that the SLDs and the roughnesses of several films prepared in the same conditions are the same. This indicates that the density and composition of the films are the same (same SLD) and the interpenetration of the polyelectrolytes within the neighbouring layers has the same amplitude (same roughness). However, the thickness determined by individual fitting are accurate and we could observe a difference of thickness for the films, probably due to non-controlled build-up parameters, as the temperature.

We also determined than the films have an inhomogeneous structure in the direction perpendicular to the surface with thinner layers near the substrate and an effect of the proximity of the air on the top layers. This is more or less pronounced depending on the build-up conditions and the structure used for the fit can be

probably improved.

Finally, we showed that it is possible to determine an average conformation of the polyelectrolyte chains in the films by combining neutron reflectometry and GISANS measurements. We have particularly determined that PSS chains in (PSS-PAH) multilayer films prepared by dipping have a flattened coil conformation, that is a smaller size in the direction perpendicular to the surface than in the direction parallel to the surface. This is in agreement with the fact that the thickness per layer of "trapped polyelectrolytes" is smaller than the size of the polyelectrolytes in solutions. Further studies should be performed to compare the conformation of the polyelectrolytes chains depending on the build-up conditions, as for example the difference between dipping, spraying and spin-assisted LbL assembly. The study of the conformation of the polyelectrolytes chains of other systems would also be really interesting, and especially on films in which we expect different conformations, as for example in "brush" films, in which we assume a brush conformation, or in films with mobile polyelectrolyte, in which the chains have probably a spherical conformation.

Bibliography

[1] G. Decher. *Science*, 277:1232–1237, **1997**.

[2] A. Izquierdo, S. S. Ono, J.-C. Voegel, P. Schaaf, and G. Decher. *Langmuir*, 21:7558–7567, **2005**.

[3] F. Fadhillah, S. M. J. Zaidi, Z. Khan, M. Khaled, F. Rahman, and P. Hammond. *J. Appl. Polym. Sci.*, 126:1468–1474, **2012**.

[4] J. Schmitt, T. Grünewald, G. Decher, P. S. Pershan, K. Kjaer, and M. Lösche. *Macromolecules*, 26:7058–7063, **1993**.

[5] H. W. Jomaa and J. B. Schlenoff. *Macromolecules*, 38:8473–8480, **2005**.

[6] G. J. Kellogg, A. M. Mayes, W. B. Stockton, M. Ferreira, and M. F. Rubner. *Langmuir*, 12:5109–5113, **1996**.

[7] A.-J. Dianoux and G. Lander. *Neutron Data Booklet*. OCP Science, Philadelphia, **2003**.

[8] J. Daillant and A. Gibaud. *X-Ray and Neutron Reflectivity : Principles and Applications*. Springer-Verlag, Berlin Heidelberg, **2009**.

[9] A. Hexemer and P. Müller-Buschbaum. *IUCrJ*, 2:106–125, **2015**.

[10] M. Lösche, J. Schmitt, D. Decher, W. G. Bouwman, and K. Kjaer. *Macromolecules*, 31:8893–8906, **1998**.

[11] O. Félix, Z. Zheng, F. Cousin, and G. Decher. *C. R. Chimie*, 12:225–234, **2009**.

[12] B. Hammouda. Probing nanoscale structures – The SANS toolbox. http://www.ncnr.nist.gov/staff/hammouda/the_SANS_toolbox.pdf, **2010**.

[13] P.-G. De Gennes. *Scaling Concepts in Polymer Physics*. Cornell University Press, Ithaca, **1979**.

[14] A. Pallandre, A. Moussa, B. Nysten, and A. M. Jonas. *Adv. Mater.*, 18:481–486, **2006**.

[15] F. Carnal, S. Ulrich, and S. Stoll. *Macromolecules*, 43:2544–2553, **2010**.

[16] S. Uyaver and C. Seidel. *J. Phys. Chem. B*, 108:18804–18814, **2004**.

[17] J. van der Gucht, E. Spruijt, M. Lemmers, and M. C. Cohen Stuart. *J. Colloid Interface Sci.*, 361:407–422, **2011**.

[18] G. Decher and J. B. Schlenoff. *Multilayer Thin Films: Sequential Assemble of Nanocomposite Materials*. Wiley-VCH, Weinheim, **2003**.

[19] P. Lavalle, C. Gergely, F. J. G. Cuisinier, G. Decher, P. Schaaf, J.-C. Voegel, and Picart C. *Macromolecules*, 35:4458–4465, **2002**.

[20] M. Salomäki, P. Tervasmäki, S. Areva, and J. Kankare. *Langmuir*, 20:3679–3683, **2004**.

[21] D. Kovacevic, S. van der Burgh, A. de Keizer, and M. A. Cohen Stuart. *Langmuir*, 18:5607–5612, **2002**.

[22] http://www.ill.eu/instruments-support/instruments-groups/instruments/d17.

[23] http://www.ill.eu/instruments-support/instruments-groups/instruments/figaro.

[24] http://www.mlz-garching.de/nrex.

[25] http://www.ill.eu/instruments-support/instruments-groups/instruments/superadam.

[26] H. Zhang and J. Rühe. *Macromolecules*, 38:10743–10749, **2005**.

[27] Y. Zhang, J. F. Douglas, B. D. Ermi, and E. J. Amis. *J. Chem. Phys.*, 114:3299–3313, **2001**.

[28] S. G. Starodubtsev, T. V. Laptinskaya, A. S. Yesakova, A. R. Khokhlov, E. V. Shtykova, K. A. Dembo, and V. V. Volkov. *Polymer*, 51:122–128, **2010**.

[29] N. Girbasova, V. Aseyev, S. Saratovsky, I. Moukhina, H. Tenhu, and A. Bilibin. *Macromol. Chem. Phys.*, 204:2258–2264, **2003**.

[30] B. Jachimska, T. Jasiński, P. Warszyński, and Z. Adamczyk. *Colloids Surf. A*, 355:7–15, **2010**.

[31] Z. Adamczyk, K. Jamroży, P. Batys, and M. Aneta. *J. Colloid Interface Sci.*, 435:182–190, **2014**.

[32] C. Heitz, M. Rawiso, and J. François. *Polymer*, 40:1637–1650, **1999**.

[33] M. Z. Markarian, H. H. Hariri, A. Reisch, V. S. Urban, and J. B. Schlenoff. *Macromolecules*, 45:1016–1024, **2012**.

[34] F. Boué, F. Cousin, J. Gummel, J. Oberdisse, G. Carrot, and A. El Harrak. *C. R. Physique*, 8:821–844, **2007**.

[35] E. Spruijt, F. A. M. Leermakers, R. Fokkink, R. Schweins, A. A. van Well, M. A. Cohen Stuart, and J. van der Gucht. *Macromolecules*, 46:4596–4605, **2013**.

[36] J. Gummel, F. Cousin, and F. Boué. *Macromolecules*, 41:2898–2907, **2008**.

[37] S. P. Strand, S. Danielsen, B. E. Christensen, and K. M. Vårum. *Biomacromolecules*, 6:3357–3366, **2005**.

[38] A. Drogoz, L. David, C. Rochas, A. Domard, and T. Delair. *Langmuir*, 23:10950–10958, **2007**.

[39] E. Dubois and F. Boué. *Macromolecules*, 34:3684–3697, **2001**.

[40] Y. Takahashi, N. Matsumoto, S. Iio, H. Kondo, and I. Noda. *Langmuir*, 15:4120–4122, **1999**.

[41] M. Nierlich, F. Boué, A. Lapp, and R. Oberthür. *J. Physique*, 46:649–655, **1985**.

[42] M.-N. Spiteri. *Conformation et corrrélations spatiales dans les solutions de polyélectrolytes: étude par Diffusion de Neutrons aux Petits Angles*. PhD thesis, Université de Paris-Sud Orsay, **1997**.

[43] U. Voigt, W. Jaeger, G. H. Findenegg, and R. v. Klitzing. *J. Phys. Chem. B*, 107:5273–5280, **2003**.

[44] N. G. Hoogeveen, M. A. Cohen Stuart, and G. J. Fleer. *Langmuir*, 12:3675–3681, **1996**.

[45] K. Büscher, K. Graf, H. Ahrens, and C. A. Helm. *Langmuir*, 18:3585–3591, **2002**.

[46] P. J. Flory. *Principles of Polymer Chemistry*. Cornell University Pres, Ithaca, **1953**.

[47] M. Rubinstein and R. H. Colby. *Polymer Physics*. Oxford University Press, Oxford and New York, **2003**.

[48] D. I. Bower. *An Introduction to Polymer Physics*. Cambridge University Press, Cambridge and New York, **2002**.

[49] C. Williams, F. Brochard, and H. L. Frisch. *Ann. Rev. Phys. Chem.*, 32:433–451, **1981**.

[50] H. J. Butt, K. Graf, and M. Kappl. *Physics and Chemistry of Interfaces*. Wiley-VCH, Weinheim, **2003**.

[51] T. Radeva. *Physical Chemistry of polyelectrolytes*. Marcel Dekker, Inc., New York, **2001**.

[52] J.-L. Barrat and J.-F. Joanny. *Europhys. Lett.*, 24:333–338, **1993**.

[53] D. Baigl, M. Sferrazza, and C. E. Williams. *Europhys. Lett.*, 62:110–116, **2003**.

[54] R. Schweins and K. Huber. *Macromol. Symp.*, 211:25–42, **2004**.

[55] M. N. Spiteri, C. E. Williams, and F. Boué. *Macromolecules*, 40:6679–6691, **2007**.

[56] H. L. Bungenberg de Jong and W. J. Klaar. *Trans. Faraday Soc.*, 28:27–68, **1932**.

[57] J. T. G. Overbeek and M. J. Voorn. *J. Cell. Comp. Physiol.*, 49:7–26, **1957**.

[58] V. A. Kabanov. *Russ. Chem. Rev.*, 74:3–20, **2005**.

[59] E. Tsuchida and K. Abe. *Adv. Polym. Sci.*, 45:1–119, **1982**.

[60] B. Philipp, H. Dautzenberg, K.-J. Linow, J. Kötz, and W. Dawydoff. *Prog. Polym. Sci.*, 14:91–172, **1989**.

[61] A. A. Lazutin, A. N. Semenov, and V. V. Vasilevskaya. *Macromol. Theory Simul.*, 21:328–339, **2012**.

[62] A. F. Thünemann, M. Müller, H. Dautzenberg, J.-F. Joanny, and H. Löwen. *Adv. Polym. Sci.*, 166:113–171, **2004**.

[63] H. Dautzenberg. *Macromolecules*, 30:7810–7815, **1997**.

[64] P. M. Biesheuvel and M. A. Cohen Stuart. *Langmuir*, 20:2785–2791, **2004**.

[65] G. Decher, J. D. Hong, and J. Schmitt. *Thin Solid Films*, 210/211:831–835, **1992**.

[66] G. B. Sukhorukov, H. Möhwald, Decher. G., and Y. M. Lvov. *Thin Solid Films*, 284-285:220–223, **1996**.

[67] J. B. Schlenoff, S. T. Dubas, and T. Farhat. *Langmuir*, 16:9968–9969, **2000**.

[68] P. Schaaf, J.-C. Voegel, L. Jierry, and F. Boulmedais. *Adv. Mater.*, 24:1001–1016, **2012**.

[69] M. Kolasinska, R. Krastev, T. Gutberlet, and P. Warszynski. *Langmuir*, 25:1224–1232, **2009**.

[70] G. Mertz, J. Bour, V. Toniazzo, D. Ruch, and V. Ball. *Colloids Surf. A*, 415:77–85, **2012**.

[71] M. Lefort, G. Popa, E. Seyrek, R. Szamocki, O. Félix, J. Hemmerlé, L. Vidal, J.-C. Voegel, F. Boulmedais, G. Decher, and P. Schaaf. *Angew. Chem. Int. Ed.*, 49:10110–10113, **2010**.

[72] E. Kharlampieva, V. Kozlovskaya, J. Chan, J. F. Ankner, and V. V. Tsukruk. *Langmuir*, 25:14017–14024, **2009**.

[73] R. Steitz, V. Leiner, R. Siebrecht, and R. v. Klitzing. *Colloids Surf. A*, 163:63–70, **2000**.

[74] C. C. Buron, C. Filiâtre, F. Membrey, C. Bainier, L. Buisson, D. Charraut, and A. Foissy. *Thin Solid Films*, 517:2611–2617, **2009**.

[75] K. Glinel, A. Moussa, A. M. Jonas, and A. Laschewsky. *Langmuir*, 18:14081412, **2002**.

[76] R. Köhler, I. Dönch, P. Ott, A. Laschewsky, A. Fery, and R. Krastev. *Langmuir*, 25:11576–11585, **2009**.

[77] M. Elzbieciak, S. Zapotoczny, P. Nowak, R. Krastev, M. Nowakowska, and Warszyński. *Langmuir*, 25:3255–3259, **2009**.

[78] M. Gopinadhan, O. Ivanova, H. Ahrens, J.-U. Günther, R. Steitz, and C. A. Helm. *J. Phys. Chem. B*, 111:8426–8434, **2007**.

[79] J. M. C. Lourenço, P. A. Ribeiro, A. M. Botelho do Rego, and M. Raposo. *J. Colloid Interface Sci.*, 313:26–33, **2007**.

[80] G. Decher, Y. Lvov, and J. Schmitt. *Thin Solid Films*, 244:772–777, **1994**.

[81] C. Picart, J. Mutterer, L. Richert, Y. Luo, G. D. Prestwich, P. Schaaf, J.-C. Voegel, and P. Lavalle. *Proc. Natl. Acad. Sci. U.S.A.*, 99:12531–12535, **2002**.

[82] R. v. Klitzing. *Phys. Chem. Chem. Phys.*, 8:5012–5033, **2006**.

[83] R. v. Klitzing, J. E. Wong, W. Jaeger, and R. Steitz. *Curr. Opin. in Colloid & Interf. Sci.*, 9:158–162, **2004**.

[84] J. Lyklema and L. Deschênes. *Adv. in Colloid & Interf. Sci.*, 168:135–148, **2011**.

[85] J. J. Cerdà, B. Qiao, and C. Holm. *Soft Matter*, 5:4412–4425, **2009**.

[86] S. A. Sukhishvili, E. Kharlampieva, and V. Izumrudov. *Macromolecules*, 39:8873–8881, **2006**.

[87] P. Lavalle, J.-C. Voegel, D. Vautier, B. Senger, P. Schaaf, and V. Ball. *Adv. Mater.*, 23:1191–1221, **2011**.

[88] N. Laugel, C. Betscha, M. Winterhalter, J.-C. Voegel, P. Schaaf, and V. Ball. *J. Phys. Chem. B*, 110:19443–19449, **2006**.

[89] R. Steitz, W. Jaeger, and R. v. Klitzing. *Langmuir*, 17:4471–4474, **2001**.

[90] S. T. Dubas and J. B. Schlenoff. *Macromolecules*, 32:8153–8160, **1999**.

[91] J. Choi and M. F. Rubner. *Macromolecules*, 38:116–124, **2005**.

[92] P. Bieker and M. Schönhoff. *Macromolecules*, 43:5052–5059, **2010**.

[93] S. S. Shiratori and M. F. Rubner. *Macromolecules*, 33:4213–4219, **2000**.

[94] G. Ladam, P. Schaad, J.-C. Voegel, P. Schaaf, G. Decher, and F. Cuisinier. *Langmuir*, 16:1249–1255, **2000**.

[95] A. Laschewsky, E. Wischerhoff, S. Denzinger, H. Ringsdorf, A. Delcorte, and P. Bertrand. *Chem. Eur. J.*, 3:34–38, **1997**.

[96] W. B. Stockton and M. F. Rubner. *Macromolecules*, 30:2717–2725, **1997**.

[97] L. Wang, Y. Fu, Z. Wang, Y. Fan, and X. Zhang. *Langmuir*, 15:1360–1363, **1999**.

[98] M. E. Buck, J. Zhang, and D. M. Lynn. *Adv. Mater.*, 19:3951–3955, **2007**.

[99] G. Rydzek, J.-S. Thomann, N. B. Ameur, L. Jierry, P. Mésini, A. Ponche, C. Contal, A. E. El Haitami, J.-C. Voegel, B. Senger, B. Frisch, and F. Boulmedais. *Langmuir*, 26:2816–2824, **2010**.

[100] A. E. El Haitami, J.-S. Thomann, L. Jierry, A. Parat, J.-C. Voegel, P. Schaaf, B. Senger, F. Boulmedais, and B. Frisch. *Langmuir*, 26:12351–12357, **2010**.

[101] T. Serizawa, K. Nanameki, K. Yamamoto, and M. Akashi. *Macromolecules*, 35:2184–2189, **2002**.

[102] T. Serizawa, K. Hamada, T. Kitayama, N. Fujimoto, K. Hatada, and M. Akashi. *J. Am. Chem. Soc.*, 122:1891–1899, **2000**.

[103] T. Serizawa, K. Hamada, T. Kitayama, K. Katsukawa, K. Hatada, and M. Akashi. *Langmuir*, 16:7112–7115, **2000**.

[104] T. Serizawa, H. Yamashita, T. Fujiwara, Y. Kimura, and M. Akashi. *Macromolecules*, 34:1996–2001, **2001**.

[105] K. Hamada, T. Serizawa, T. Kitayama, N. Fujimoto, K. Hatada, and M. Akashi. *Langmuir*, 17:5513–5519, **2001**.

[106] J. J. Iturri Ramos, S. Stahl, R. P. Richter, and S. E. Moya. *Macromolecules*, 43:9063–9070, **2010**.

[107] K. Haberska and T. Ruzgas. *Bioelectrochemistry*, 76:153–161, **2009**.

[108] J. Schmitt, G. Decher, W. J. Dressick, S. L. Brandow, R. E. Geer, A. Shashidhar, and J. M. Calvert. *Adv. Mater.*, 9:61–65, **1997**.

[109] E. Song, W. Han, H. Xu, Y. Jiang, D. Cheng, Y. Song, and M. T. Swihart. *Chem. Eur. J.*, 20:14642–14649, **2014**.

[110] D. Dontsova, V. Keller, N. Keller, P. Steffanut, O. Félix, and G. Decher. *Macromol. Rapid Commun.*, 32:1145–1149, **2011**.

[111] P. Podsiadlo, S. Paternel, J.-M. Rouillard, Z. Zhang, J. Lee, J.-W. Lee, E. Gulari, and N. A. Kotov. *Langmuir*, 21:11915–11921, **2005**.

[112] S. Sunny, N. Vogel, C. Howell, T. L. Vu, and J. Aizenberg. *Adv. Funct. Mater.*, 24:6658–6667, **2014**.

[113] Z.-D. Qi, T. Saito, Y. Fan, and A. Isogai. *Biomacromolecules*, 13:553–558, **2012**.

[114] S. A. Camacho, P. H. B. Aoki, C. J. L. Constantino, R. F. Aroca, and A. M. Pires. *J. Alloy Compd*, 541:365–371, **2012**.

[115] Y. Lvov, H. Haas, G. Decher, and H. Möhwald. *Langmuir*, 10:4232–4236, **1994**.

[116] G. Decher, B. Lehr, K. Lowack, Y. Lvov, and J. Schmitt. *Biosensors & Bioelectronics*, 9:677–684, **1994**.

[117] Y. Zou, L. Xie, S. Carroll, M. Muniz, H. Gibson, W.-Z. Wei, H. Liu, and G. Mao. *Biomacromolecules*, 15:3965–3975, **2014**.

[118] G. Decher, M. Eckle, J. Schmitt, and B. Struth. *Curr. Opin. in Colloid & Interf. Sci.*, 3:32–39, **1998**.

[119] S. Singh, A. Junghans, M. J. Waltman, A. Nagy, R. Iyer, and J. Majewski. *Soft Matter*, 8:11484–11491, **2012**.

[120] G. Schneider and G. Decher. *Nano Lett.*, 4:1833–1839, **2004**.

[121] B. Schwarz and M. Schönhoff. *Langmuir*, 18:2964–2966, **2002**.

[122] S. C. Chang, R. P. Slopek, B. Condon, and J. C. Grunlan. *Ind. Eng. Chem. Res.*, 53:3805–3812, **2014**.

[123] E. V. Pasco, H. Shi, I. Xagoraraki, S. A. Hashsham, K. N. Parent, M. L. Bruening, and V. V. Tarabara. *J. Membr. Sci.*, 469:140–150, **2014**.

[124] X. Liu and M. L. Bruening. *Chem. Mater.*, 16:351–357, **2004**.

[125] H. H. Rmaile and J. B. Schlenoff. *J. Am. Chem. Soc.*, 125:6602–6603, **2003**.

[126] H. Schönhoff, V. Ball, A. R. Bausch, C. Dejugnat, N. Delorme, K. Glinel, R. v. Klitzing, and R. Steitz. *Colloids Surf. A*, 303:14–29, **2007**.

[127] D. V. Andreeva, D. Fix, H. Möhwald, and D. G. Shchukin. *Adv. Mater.*, 20:2789–2794, **2008**.

[128] J. Chluba, J.-C. Voegel, G. Decher, P. Erbacher, P. Schaaf, and J. Ogier. *Biomacromolecules*, 2:800–805, **2001**.

[129] T. R. Farhat and P. T. Hammond. *Adv. Funct. Mater.*, 15:945–954, **2005**.

[130] M. Matsusaki, H. Ajiro, T. Kida, T. Serizawa, and M. Akashi. *Adv. Mater.*, 24:454–474, **2012**.

[131] K. Glinel, C. Déjugnat, M. Prevot, B. Schöler, M. Schönhoff, and R. v. Klitzing. *Colloids Surf. A*, 303:3–13, **2007**.

[132] E. Kharlampieva, V. Kozlovskaya, and S. A. Sukhishvili. *Adv. Mater.*, 21:3053–3065, **2009**.

[133] www.ncnr.nist.gov/resources/n-lengths.

[134] F. Cousin, C. Genix, I. Grillo, J. Jestin, and J. Oberdisse. *JDN 17 - Neutrons et Matière Molle*. EDP Sciences, Les Ullis, **2010**.

[135] P. Müller-Buschbaum. *Polymer Journal*, 45:34–42, **2013**.

[136] R. K. Thomas. *Curr. Opin. in Solid State & Mater. Sci.*, 1:636–644, **1996**.

[137] S. Holbein, P. Steffens, T. Finger, A. C. Komarek, Y. Sidis, P. Link, and M. Braden. *Phys. Rev. B*, 91:014432, **2015**.

[138] A. Das, G. D. Dwivedi, P. Kumari, P. Shahi, H. D. Yang, A. K. Ghosh, and S. Chatterjee. *J. Magn. Magn. Mater.*, 379:6–8, **2015**.

[139] L. Keller, J. S. White, M. Frontzek, P. Babkevich, M. A. Susner, Z. C. Sims, A. S. Sefat, H. M. Rø nnow, and C. Rüegg. *Phys. Rev. B*, 91:020409, **2015**.

[140] P. Gutfreund, M. Wolff, M. Maccarini, S. Gerth, J. F. Ankner, J. Browning, C. E. Halbert, H. Wacklin, and H. Zabel. *J. Chem. Phys.*, 134:064711, **2011**.

[141] M. Wolff, P. Gutfreund, A. Rühm, B. Akgun, and H. Zabel. *J. Phys.: Condens. Matter*, 23:184102, **2011**.

[142] M. Wolff, R. Steitz, P. Gutfreund, N. Voss, S. Gerth, M. Walz, A. Magerl, and H. Zabel. *Langmuir*, 24:11331–11333, **2008**.

[143] K. Nishida, H. Urakawa, K. Kaji, B. Gabrys, and J. S. Higgins. *Polymer*, 38:6083–6085, **1997**.

[144] M. N. Spiteri, F. Boué, A. Lapp, and J. P. Cotton. *Phys. Rev. Lett.*, 77:5218–5220, **1996**.

[145] M. M. Malwitz, S. Lin-Gibson, E. K. Hobbie, P. D. Butler, and G. Schmidt. *J. Polym. Sci. Part B*, 41:3237–3248, **2003**.

[146] M. M. Malwitz, A. Dundigalla, V. Ferreiro, P. D. Butler, M. C. Henk, and G. Schmidt. *Phys. Chem. Chem. Phys.*, 6:2977–2982, **2004**.

[147] Y. Kamata, A. J. Parnell, P. Gutfreund, M. W. A. Skoda, A. J. C. Dennison, R. Barker, S. Mai, J. R. Howse, A. J. Ryan, N. Torikai, M. Kawaguchi, and R. A. L. Jones. *Macromolecules*, 47:8682–8690, **2014**.

[148] V. Rondelli, G. Fragneto, S. Motta, E. Del Favero, and L. Cantù. *J. Phys. Conf. Ser.*, 340:012083, **2012**.

[149] P. Callow, G. Fragneto, R. Cubitt, D. J. Barlow, and M. J. Lawrence. *Langmuir*, 25:4181–4189, **2009**.

[150] M. Born and E. Wolf. *Principles of Optics,*. Pergamon Press, Oxford, 4th edition, **1970**.

[151] O. Soltwedel, O. Ivanova, P. Nestler, M. Müller, R. Köhler, and C. A. Helm. *Macromolecules*, 43:7288–7293, **2010**.

[152] R. Steitz, V. Leiner, K. Tauer, V. Khrenov, and R. v. Klitzing. *Appl. Phys. A*, 74:S519–S521, **2002**.

[153] M. Tarabia, H. Hong, D. Davidov, S. Kirstein, R. Steitz, R. Neumann, and Y. Avny. *J. Appl. Phys.*, 83:725–732, **1998**.

[154] P. Müller-Buschbaum, E. Metwalli, J.-F. Moulin, V. Kudryashov, M. Haese-Seiller, and R. Kampmann. *Eur. Phys. J. Special Topics*, 167:107–112, **2009**.

[155] Korolkov D., P. Busch, L. Willner, E. Kentzinger, U. Rücker, A. Paul, H. Frielinghaus, and T. Brückel. *Appl. Cryst.*, 45:245–254, **2012**.

[156] P. Müller-Buschbaum, J. S. Gutmann, R. Cubitt, and W. Petry. *Pysica B*, 350:207–210, **2004**.

[157] P. Müller-Buschbaum, E. Maurer, E. Bauer, and R. Cubitt. *Langmuir*, 22:9295–9303, **2006**.

[158] J. Kraus, P. Müller-Buschbaum, T. Kuhlmann, D. W. Schubert, and M. Stamm. *Europhys. Lett.*, 49:210–216, **2000**.

[159] http://www.ill.eu.

[160] http://www.frm2.tum.de/en.

[161] R. Cubitt and G. Fragneto. *Appl. Phys. A*, 74:329–331, **2002**.

[162] R. A. Campbell, H. P. Wacklin, I. Sutton, R. Cubitt, and G. Fragneto. *Eur. Phys. J. Plus*, 126(107), **2011**.

[163] A. Devishvili, K. Zhernenkov, A. J. C. Dennison, B. P. Toperverg, M. Wolff, B. Hjörvarsson, and H. Zabel. *Rev. Sci. Instrum.*, 84(025112), **2013**.

[164] H. G. Tompkins and E. A. Irene. *Handbook of elllipsometry*. Williams Andrew Publishing, Norwich - Springer-Verlag, Heidelberg, **2005**.

[165] J. M. Hollander and W. L. Jolly. *Accounts Chem. Res.*, 3:193–200, **1970**.

[166] J. F. Moulder, W. F. Stickle, P. E. Sobol, and K. D. Bomben. *Handbook of X-ray Photoelectron Spectroscopy*. Physical Electronics, Inc, Eden Prairie, **1995**.

[167] http://www.wavemetrics.com.

[168] A. Nelson. *J. Appl. Cryst.*, 39:273–276, **2006**.

[169] A. Nelson. Motofit. http://motofit.sourceforge.net/manual/motofit/motofitmanual.pdf, **2007**.

[170] M. Westwood, A. P. Gunning, and R. Parker. *Macromolecules*, 43:10582–10593, **2010**.

[171] M. Salomäki, I. A. Vinokurov, and J. Kankare. *Langmuir*, 21:11232–11240, **2005**.

[172] P. H. B. Aoki, P. Alessio, D. Volpati, F. V. Paulovich, A. Riul Jr., O. N. Oliveira Jr., and C. J. L. Constantino. *Mater. Sci. Eng. C*, 41:363–371, **2014**.

[173] C. Elosua, D. Lopez-Torres, M. Hernaez, I. R. Matias, and F. J. Arregui. *Nanoscale Res. Lett.*, 8:539–548, **2013**.

[174] J. Hong and H. S. Park. *Colloids Surf. A*, 381:7–12, **2011**.

[175] P. Bertrand, A. Jonas, A. Laschewsky, and R. Legras. *Macromol. Rapid Commun.*, 21:319–348, **2000**.

[176] P. T. Hammond. *Curr. Opin. in Colloid & Interf. Sci.*, 4:430–442, **2000**.

[177] Z. Tang, Y. Wang, Podsiadlo. P., and N. A. Kotov. *Adv. Mater.*, 18:3203–3224, **2006**.

[178] A. A. Argun, J. N. Ashcraft, and P. T. Hammond. *Adv. Mater.*, 20:1539–1543, **2008**.

[179] K. Ariga, J. P. Hill, and Q. Ji. *Phys. Chem. Chem. Phys.*, 9:2319–2340, **2007**.

[180] A. P. R. Johnston, C. Cortez, A. S. Angelatos, and F. Caruso. *Curr. Opin. in Colloid & Interf. Sci.*, 11:203–209, **2006**.

[181] D. Korneev, Y. Lvov, G. Decher, J. Schmitt, and S. Yaradaikin. *Physica B*, 213-214:954–956, **1995**.

[182] S. Yang, Y. Zhang, Y. Guan, S. Tan, J. Xu, S. Cheng, and X. Zhang. *Soft Matter*, 2:699–704, **2006**.

[183] K. E. Secrist and A. J. Nolte. *Macromolecules*, 44:2859–2865, **2011**.

[184] J. E. Wong, F. Rehfeldt, P. Hänni, M. Tanaka, and R. v. Klitzing. *Macromolecules*, 37:7285–7289, **2004**.

[185] T. J. Halthur, P. M. Claesson, and U. M. Elofsson. *J. Am. Chem. Soc.*, 126:17009–17015, **2004**.

[186] R. Bijlsma, A. A. van Well, and M. A. Cohen Stuart. *Physica B*, 234-236:254–255, **1997**.

[187] C. Delajon, T. Gutberlet, H. Möhwald, and R. Krastev. *Colloids Surf. B*, 74:462–467, **2009**.

[188] P. Lindner and T. Zemb. *Neutrons, X-rays and Light: Scattering Methods Applied to Soft Condensed Matter*. Elsevier Science B. V., Amsterdam, **2002**.

[189] A. Ramakrishnan, R. Dhamodharan, and J. Rühe. *Macromol. Rapid Commun.*, 23:612–616, **2002**.

[190] A. Ramakrishnan, R. Dhamodharan, and J. Rühe. *J. Polym. Sci. Part A*, 44:1758–1769, **2006**.

[191] O. Prucker and J. Rühe. *Langmuir*, 14:6893–6898, **1998**.

[192] O. Prucker and J. Rühe. *Macromolecules*, 31:592–601, **1998**.

[193] M. Biesalski and J. Rühe. *Macromolecules*, 32:2309–2316, **1999**.

[194] M. Biesalski, D. Johannsmann, and J. Rühe. *Macromol. Symp.*, 145:113–124, **1999**.

[195] H. Zhang and J. Rühe. *Macromolecules*, 36:6593–6598, **2003**.

[196] H. Zhang and J. Rühe. *Macromol. Rapid Commun.*, 24:576–579, **2003**.

Christophe HIGY

Conformation des polyélectrolytes dans des films nanométriques assemblés couche-par-couche

Résumé

L'assemblage couche-par-couche permet de fabriquer des films multimatériaux aux propriétés variées présentant une structure stratifiée. Ce travail décrit les études structurelles des films multicouches de polyélectrolytes à l'aide de mesures de diffusion de neutrons.

L'effet du vieillissement des films a été déterminé par réflectométrie des neutrons. Nous avons observé un léger tassement des films après 5 ans et une forte expansion après 15 ans.

Nous avons aussi montré que le substrat et l'air en surface ont une influence sur la structure des couches proches des extrémités des films, conduisant à une structure inhomogène perpendiculairement à la surface.

Nous avons finalement étudié la conformation des chaînes de polyélectrolytes dans les films multicouches ; nous avons déterminé que les chaînes de PSS dans des films préparés par trempage ont une conformation en pelotes aplaties, contrairement aux chaînes de polyélectrolytes en solution qui présentent une conformation sphérique.

Mots-clés : Multicouches de polyélectrolytes ; Conformation ; Réflectométrie des neutrons ; GISANS ; Vieillissement ; Structure stratifiée ; Structure inhomogène ; Fit global

Résumé en anglais

The Layer-by-Layer assembly allows the build-up of multimaterial films with various properties showing a stratified structure. This work describes the structural strudies of multilayer films of polyelectrolytes with neutron scattering measurements.

Ageing effect on films was determined by neutron reflectometry. We observed a slight shrink of the films after 5 years and a strong expansion after 15 years.

We also showed that the proximity of the substrate and the air at the surface have an influence on the structure of the layers at the extremities of the films, leading to an inhomogeneous structure perpendicularly to the surface.

Finally, we studied the conformation of polyelectrolyte chains in the multilayer films ; we determined that PSS chains in dipped films have a flattened coil conformation, whereas the polyelectrolyte chains in solution have a spherical conformation.

Keywords : Polyelectrolyte multilayers ; Conformation ; Neutron reflectometry ; GISANS ; Ageing ; Stratified structure ; Inhomogeneous structure ; Global fit